Title
Behavior of Non-Ductile Beam-Slab Systems under Support Failure Scenarios /

Author
Prasad, Saurabh

Publication Date
2014

Peer reviewed|Thesis/dissertation

UNIVERSITY OF CALIFORNIA, SAN DIEGO

Behavior of Non-Ductile Beam-Slab Systems under Support Failure Scenarios

A dissertation submitted in partial satisfaction of the
requirements for the degree
Doctor of Philosophy

in

Structural Engineering

by

Saurabh Prasad

Committee in charge:

Professor Tara C. Hutchinson, Chair
Professor Jośe I. Restrepo
Professor David T. Sandwell
Professor Peter M. Shearer
Professor Benson Shing

2014

The dissertation of Saurabh Prasad is approved, and it is acceptable in quality and form for publication on microfilm and electronically:

Chair

University of California, San Diego

2014

Dedication

To my parents, for their love and support in my pursuit of higher education.

Table of Contents

Signature Page iii

Dedication iv

Table of Contents v

List of Symbols x

List of Figures xiii

List of Tables xxiii

Acknowledgements xxiv

Vita xxvii

Abstract of the Dissertation xxix

Chapter 1: Introduction 1

1.1 Background 1
1.2 Motivation for the Present Work 4
1.3 Research Objectives 5
1.4 Organization of Dissertation 6

Chapter 2: Literature Review 8

2.1 Progressive Collapse 8
2.1.1 Experimental Studies on Progressive Collapse 9
2.1.2 Code-Based Approach to Progressive Collapse 13
2.2 Capacity of Reinforced Concrete Slab 15
2.2.1 Experimental Studies 18
2.3 Summary Remarks 23

Chapter 3: Experimental Program 25

3.1 Overview 25
3.2 Specimen 1 Details 26

3.2.1 Reinforcement Details 29
3.2.2 Material Properties 34
3.2.2.1 Concrete Material Properties 34
3.2.2.2 Steel Material Properties 35
3.2.3 Loading Protocol and Test Setup 36
3.2.3.1 Loading Protocol 36
3.2.3.1 Test Setup 38
3.3 Specimen 1 - Test Results 40
3.3.1 Uniform Gravity Load 40
3.3.1.1 Load Distribution at Support Locations 40
3.3.1.2 Physical Observations 43
3.3.2 Pattern Loads 44
3.3.2.1 Load Distribution at Supports 45
3.3.2.2 Physical Observations 47
3.3.3 Column Removal Scenario 49
3.3.3.1 Load-Deflection Relation 49
3.3.3.2 Load Redistribution 53
3.3.3.3 Physical Observations 60
3.3.3.4 Deflection Profiles 63
3.4 Specimen 2 Details 65
3.4.1 Reinforcement Details 68
3.4.2 Material Properties 72
3.4.2.1 Concrete Material Properties 72
3.4.2.2 Steel Material Properties 72
3.4.3 Loading Protocol and Test Setup 73
3.4.3.1 Loading Protocol 73
3.4.3.2 Test Setup 74
3.5 Specimen 2-Test Results 77
3.5.1 Uniform Gravity Load 77
3.5.1.1 Load Distribution at Support Locations 77

3.5.1.2 Physical Observations ... 80
3.5.2 Column Removal Scenario ... 81
3.5.2.1 Load-Deflection Relation ... 81
3.5.2.2 Load Distribution at Supports ... 85
3.5.2.3 Physical Observations ... 90
3.5.2.4 Deflection Profiles ... 94
3.6 Conclusions ... 97
3.6.1 Overview ... 97
3.6.2 Findings ... 98
Chapter 4: Numerical Modeling and Validation ... 101
4.1 Introduction ... 101
4.2 Description of LS DYNA Model ... 102
4.2.1 Geometric Model ... 103
4.2.1.1 Concrete Model ... 103
4.2.1.2 Rebar Model ... 109
4.2.1.3 Beam and Solid Element Interface ... 112
4.2.1.4 Load Cell and Actuator Model ... 113
4.2.1.5 Concrete and Load Cell Interface Definition ... 117
4.2.2 Elements used in LS DYNA ... 118
4.2.2.1 Eight Node Solid Elements ... 118
4.2.2.2 Two Node Beam Elements ... 120
4.2.2.3 Four Node Shell Elements ... 121
4.2.3 Material Models in LS DYNA ... 122
4.2.3.1 Steel Material Model ... 122
4.2.3.2 Concrete Material Model ... 125
4.2.3.3 Elastic Material Model ... 128
4.2.4 Boundary Condition and Loading Protocol ... 129
4.3 Results Comparison ... 130
4.3.1 Gravity Test: 90 psf Uniform load ... 131
4.3.2 Column Removal at Corner Support Locations ... 136

4.3.2.1 Push Test 1 (beam-beam corner) 136
4.3.2.2 Push Test 2 (slab-slab corner) 145
4.3.2.3 Push Test 3 (beam-slab corner) 153
4.4 Summary Remarks 161
Chapter 5: Parametric Study 166
5.1 Overview 166
5.2 Model Description 167
5.2.1 Baseline Structure and LS-DYNA Model 168
5.2.1.1 Description of the baseline structure 168
5.2.1.2 LS-DYNA Model of the Baseline Structure 174
5.2.1.2.1 Geometric Model 175
5.2.1.2.2 Support column model 179
5.2.1.2.3 Loading Protocol and Boundary Conditions 181
5.2.1.2.4 Material Properties and Models in LS-DYNA 182
5.2.2 Description of the Parameters Varied 184
5.3 Results from the Parametric Study 188
5.3.1 Results from the Baseline Model 188
5.3.1.1 Load-Deflection Behavior 188
5.3.1.2 Load Redistribution at Supports 189
5.3.1.3 Observed Tensile Strain Concentration 192
5.3.3 Comparison of the Various Parametric Cases with Baseline 195
5.3.3.1 Load-Deflection Behavior 195
5.3.3.2 Comparison with Yield Line Theory Estimates 206
5.3.3.3 Redistribution of Loads to Adjacent Supports 210
5.4 Approximate Method for Determining Stiffness and Strength under Corner Column Failure Scenario 215
5.4.1 Approximation of Initial Stiffness 215
5.4.2 Estimation of Vertical Load Capacity under Corner Support Failure Considering Membrane Forces 218
5.5 Effect of Bond-Slip between Concrete and Rebar 224

5.6 Concluding Remarks 230

Chapter 6: Conclusions and Future Work 232

6.1 Motivation 232
6.2 Experimental Program 233
6.3 Numerical Investigation 235
6.4 Suggestions for Future Work 238

REFERENCES 241

APPENDIX A : Summary of Previous Tests on RC Slabs 251

APPENDIX B : Yield Lines from Experiment 257

APPENDIX C : LS-DYNA Steel Stress-Strain Input Curve 259

List of Symbols

Notation	Definition
A_i	Cross-section area of i^{th} column
$A_{i,Rebar}$	Area of i^{th} slab rebar crossing yield line
b_{Beam}	Width of spandrel beam
b_i	Width of support column *i*
C_{Conc}	Total compression in slab concrete along the yield line
$C_{Beam,j}$	Axial compression in i^{th} spandrel beam
D_i	Perpendicular distance to i^{th} slab section of the yield line from the corner support location
D_j	Perpendicular distance to the plastic hinge on j^{th} beam from the corner support location
DL	Additional dead load on beam-slab system in addition to its self-weight
d_{Beam}	Depth of spandrel beam
$E_{Elastic}$	Initial elastic modulus of steel material
E_i	Elastic modulus of support column *i*
E_r	Elastic modulus ratio of model to prototype structure
$f'c$	Concrete compressive strength
F_{Slab}	In-plane force in the slab along the yield line
$f_{y,i}$	Yield stress of i^{th} rebar crossing yield line
I_g	Gross moment of inertia of column
I_i	Moment of inertia of i^{th} column
$(K_A)_i$	Axial stiffness of support column *i*
$(K_{LF})_i$	Lateral and flexural stiffness of support column *i*
$K_{Calculated}$	Calculated system stiffness using simplified model
$K_{Parametric}$	System stiffness from non-linear parametric model
$K_{Experiment}$	System stiffness from experiment
L_d	Development length of rebar based on ACI-318 (2011)
ΔL_i	Length of i^{th} slab section of the yield line

Notation	Definition
L_r	Ratio of model to prototype dimension scale
LL	Total live load on beam-slab system
L_{Span}	Span length or center to center distance between adjacent supports
m_i	Moment capacity per unit length of i^{th} slab section of yield line
m_i^{Dir}	Moment capacity per unit length of i^{th} slab section of the yield line in direction *Dir*, where *Dir* is X or Y.
M_{Cap}	Ultimate flexural capacity of spandrel beam considering axial compression
M_j	Moment capacity of j^{th} spandrel beam
M_y	Ultimate flexural capacity of spandrel beam without axial compression
n	Stiffness reduction factor to account for cracking in elastic column
$P_{Analytical}$	Ultimate capacity of beam-slab system from simplified analytical method
$P_{Experiment}$	Ultimate capacity of beam-slab system from experiment
P_{Sim}	Ultimate capacity of beam-slab system from numerical simulation
P_{Ult}	Ultimate capacity of beam-slab system considering membrane forces
P_{YLT}	Ultimate capacity of beam-slab system using Yield Line Theory
$S_{beam,i}$	Out of plane shear in i^{th} spandrel beam
T_{Rebar}	Total tension in slab rebar along the yield line
t_{Slab}	Thickness of slab
W_{Ext}	Work done by external loads, including self-weight, per unit displacement at test location
ΔM_{PM}	Increase in ultimate flexural capacity of spandrel beam due to axial compression
Δ_{NA}	Distance between slab and beam centroidal axis
ε_{Eff}	Effective plastic strain
ε_{Engg}	Engineering strain ($=\Delta L/L$)
ε_{True}	True strain
ε_{Yield}	Yield strain
ρ_{Beam}	Longitudinal reinforcement ratio in spandrel beam

Notation	Definition
ρ_m	Mass density of model structure
ρ_p	Mass density of prototype structure
ρ_{Slab}	Longitudinal reinforcement ratio in slab
σ_{Engg}	Engineering stress
σ_{True}	True stress
θi	Angle of the i^{th} yield line with the X axis

List of Figures

Figure 1.1: Partial collapse of Kaiser Permanente office building after 1994 Northridge earthquake. 1
Figure 1.2: Collapse of a concrete structure during the 1999 Izmit earthquake, Turkey (photo courtesy: Halil Sezen). 2
Figure 1.3: Shear failure of columns at the Imperial County Services Building during the Imperial Valley earthquake, 1979 (photo courtesy: Vitelmo V Bertero)........ 3
Figure 1.4: Shear failure in columns at the Van Nuys Holiday Inn during the 1994 Northridge earthquake, 1994; (photo courtesy: Peter W. Clark)........ 3
Figure 2.1: Rebar rupture at bottom of the beam next to the joint where column was removed (from Yi et al. 2008). 9
Figure 2.2: Baptist Memorial Hospital, Tennessee (from Sasani and Sagiroglu, 2010)... 10
Figure 2.3: Tests conducted at NIST on beam-column frame showing the reinforcing details of the intermediate moment frame specimen designed for seismic category C. (from Lew et al., 2011)........ 11
Figure 2.4: Slab specimen showing different components of the test setup (from Qian and Li, 2012)........ 12
Figure 2.5: Category of tie forces required to prevent progressive collapse in a structure (from DoD UFC 2005). 14
Figure 2.6: Location of column removal in a frame structure (from DoD UFC 2005)..... 14
Figure 2.7: Membrane forces acting in a slab, (a) compressive membrane forces at small deflection, and (b) tensile membrane forces at large deflections. 17
Figure 2.8: Crack patterns on the nine panel beam-slab specimen at the end of the test, (a) top surface, (b) bottom surface. (from Hopkins and Park, 1971)........ 19
Figure 2.9: Schematic of the test specimen with two slab panels tested under uniform gravity loads. Additional stiffness was provided on two ends using thickened slab sections (from Park, 1971)........ 20

Figure 2.10: Schematic of the two slab strips tested by Vecchio and Tang (1990), showing different support conditions provided at the end of the slab strips (from Vecchio and Tang, 1990)..22
Figure 3.1: Region of building modeled for the study 27
Figure 3.2: Plan view of the first test specimen...28
Figure 3.3: Elevation view of the sections from Figure 3.2, (a) section 1-1, and (b) section 2-2. 29
Figure 3.4: Beam reinforcement, (a) elevation view, (b) cross section view. 30
Figure 3.5: Top slab reinforcement in N-S direction using Grade 40 - #3 bars................31
Figure 3.6: Slab top reinforcement in E-W direction using Grade 40 - #3 bars. 31
Figure 3.7: Slab bottom reinforcement in N-S direction using Grade 40 - #3 bars. 32
Figure 3.8: Slab bottom reinforcement in E-W direction using Grade 40 - #3 bars. 32
Figure 3.9: Drop panel reinforcement at support locations, (a) plan view, ...33
Figure 3.10: Stress-strain response of the reinforcement provided, (a) Grade 40 - #3 slab reinforcement, and (b) Grade 60 - #4 beam longitudinal reinforcement. 35
Figure 3.11: Different loading patterns imposed on the slab; A= 90 psf and B=38 psf. ..37
Figure 3.12: Schematic of the test setup specimen 1: (a) Plan view of the experimental setup, and (b) NS view of the test setup. Note: LC1 through LC5 are multi-axis load cells and LC6 through LC9 are axial only load cells. Direction of positive forces in NS and EW directions are also shown in part (a)...39
Figure 3.13: Resolved forces at the support locations due to applied uniform gravity loads 42
Figure 3.14: Schematic of cracking on specimen 1 after uniform gravity load application, (a) bottom and sides of the specimen, (b) top of the specimen. Black - cracks after 38 psf and blue- cracks after 90 psf. 43
Figure 3.15: Negative moment cracks at support LC2 at 38 psf uniform load.................44
Figure 3.16: Resolved forces at the support locations due to pattern load case 1.............46
Figure 3.17: Observed cracks on the specimen at the end of pattern load tests, (a) bottom surface, and (b) top surface of specimen..47

Figure 3.18: Load vs. displacement relation during the test at three corner locations on specimen 1 (SW = self-weight). 50
Figure 3.19: Load distribution at supports at maximum load during test at beam-beam corner on specimen 1 54
Figure 3.20: Load distribution at supports at maximum load during test at slab-slab corner of specimen 1 56
Figure 3.21: Localized failure near LC5 during test at slab-slab corner of specimen 1. .. 57
Figure 3.22: Load distribution at supports at maximum load during test at beam-slab corner. 59
Figure 3.23: Cracking on the specimen at the end of tests on specimen 1, (a) cracks on the top surface, and (b) cracks on the bottom surface and edges. *are the location of compressive failure shown in Figure 3.24. 61
Figure 3.24: Local failure and concrete spalling at beam support locations: (a) E-W beam at support LC1, (b) N-S beam at support location LC2... 62
Figure 3.25: Rebar buckling and concrete spalling in EW-beam at support LC1 at the end of the test at the beam-beam corner on specimen 1... 63
Figure 3.26: Deflection profile during test at beam-beam corner on specimen 1: (a) location of linear potentiometers, (b) deflection profile at sensor locations............ 64
Figure 3.27: Change in deflection recorded by linear potentiometers during test at slab-slab corner and beam-slab corner on specimen 1... 65
Figure 3.28: Region of building modeled for specimen 2.. 66
Figure 3.29: Schematic of the second specimen, (a) plan view, and (b) section A-A. 67
Figure 3.30: Schematic of beam reinforcement of specimen 2, (a) profile view of the beam reinforcement, and (b) cross-section view of the spandrel beam showing detailing along the length of the beam. 68
Figure 3.31: Top slab reinforcement in the NS direction.. 69
Figure 3.32: Top slab reinforcement in the EW direction... 69
Figure 3.33: Bottom slab reinforcement in the NS direction. 70
Figure 3.34: Bottom slab reinforcement in the EW direction. 70

Figure 3.35: Schematic of the extra reinforcement provided at drop panel locations, (a) plan view, and (b) cross section view. 71
Figure 3.36: Stress-strain curve of the steel reinforcement, (a) Grade 40 - #3 slab reinforcement, and (b) Grade 60 - #4 beam longitudinal reinforcement. 73
Figure 3.37: Plan view of the experimental setup showing load cell and test locations. Direction of positive NS and EW force resultants is shown. 75
Figure 3.38: E-W view showing setup for push down location 1 and 2. 76
Figure 3.39: N-S view showing setup for push down location 1. Direction of positive vertical load is shown. 76
Figure 3.40: Resolved forces at the support locations due to applied uniform gravity loads on specimen 2 79
Figure 3.41: Cracking in the specimen 2 after uniform gravity load of 90 psf, (a) Bottom and sides of the specimen, (b) Top of the specimen 80
Figure 3.42: Load vs. displacement relation during the test at two edge locations on specimen 2. 82
Figure 3.43: Local failure at beam edge push location creating large torsion in the beam. 84
Figure 3.44: Load distribution at supports at maximum load during the test at the slab edge on specimen 2 87
Figure 3.45: Load distribution at supports at maximum load during the test at the beam edge on specimen 2 89
Figure 3.46: Schematic of the observed damage on the specimen at the end of push tests on specimen 2, (a) cracks on top surface of the specimen at the end of the test, and (b) cracks observed on bottom surface and sides of the specimen at end of the test. 91
Figure 3.47: Photograph of concrete breakout at two ends of the spandrel beam during the test at beam edge on specimen 2, (a) at support LC1, and (b) at support LC2. 93
Figure 3.48: Concrete spalling and rebar bond failure at push location during test at beam edge on specimen 2. 93
Figure 3.49: Displacement profile at linear-potentiometers during test at slab edge........ 95
Figure 3.50: Displacement profile at linear-potentiometers during test at beam edge 96

Figure 4.1: Isometric views of the concrete model implemented in LS DYNA. (a) top surface, and (b) bottom surface. Different concrete components are shown in different color, red-drop panels, green-slab deck, and blue-spandrel beams.......... 105
Figure 4.2: Top view of the concrete model implemented in LS DYNA for modeling push at the beam-beam corner. Total of 112,058 solid elements. 106
Figure 4.3: Top view of the concrete model implemented in LS DYNA for modeling push at the slab-slab corner. Total of 93,531 solid elements................................. 107
Figure 4.4: Top view of the concrete model implemented in LS DYNA for modeling push at the beam-slab corner. Total of 96,957 solid elements............................... 108
Figure 4.5: Side view of the drop panels, (a) staircase mesh provided at locations with non-linear behavior... 109
Figure 4.6: Isometric view of the beam rebar, red-#4 longitudinal rebar, and green-#2 shear stirrups. An outline of the concrete model is shown in grey. 110
Figure 4.7: Isometric view of the slab bottom mat, red - EW #3 rebar, and green - NS #3 rebar. An outline of the concrete model is shown in grey. 111
Figure 4.8: Isometric view of the slab top mat, red - EW #3 rebar, and green - NS #3 rebar. An outline of the concrete model is shown in grey. 111
Figure 4.9: Isometric view of the extra reinforcement provided in the slab, red - #3 cage at support locations, and green - extra #3 rebar at push locations. An outline of the concrete model is shown in grey... 112
Figure 4.10: Mesh provided in an individual load cell. Four parts of the load cell are shown, green-top plate, red-steel pipe, blue-bottom plate, and black-connecting bolts.. 115
Figure 4.11: Isometric view of the specimen showing the multi-axis load cells with the connecting bolts. An outline of the concrete specimen is shown in grey. 115
Figure 4.12: Nodal rigid body definition at one of the axial load cell locations. All the nodes behave as a part of rigid body, thus transferring rotation and translation..... 116
Figure 4.13: Connection detail between the multi-axis load cell and test specimen. 117
Figure 4.14: Two of the twelve hourglass modes in 8 node solid elements with one integration point. 119

Figure 4.15: Comparison between stress-strain response from the rebar tension tests and the LS DYNA model 125
Figure 4.16: Concrete stress strain curve for 6500 psi concrete implemented in LS-DYNA. Compressive stress and strains are shown as negative value. 127
Figure 4.17: Location of single point constraints on the load cells. 130
Figure 4.18: Comparison of change in support loads at the end of 90 psf uniform load on specimen 1 132
Figure 4.19: Deflection comparison between the test and the numerical model in LS DYNA 135
Figure 4.20: Comparison of the load deflection relation during the test at beam-beam corner location. 137
Figure 4.21: Comparison of change in support loads at 4.5 in. vertical deflection during the test at the beam-beam corner location on specimen 1 140
Figure 4.22: Comparison of deflection profiles at linear-potentiometer locations vs the tip deflection at the beam-beam corner push location 142
Figure 4.23: Comparison of the observed damage on the top surface of the specimen during the test at beam-beam corner. 144
Figure 4.24: Comparison of the observed damage on the bottom surface of the specimen during the test at beam-beam corner. 145
Figure 4.25: Comparison of the load deflection relation during the test at slab-slab corner location. 146
Figure 4.26: Comparison of change in support loads at 9 in. vertical deflection during the test at slab-slab corner location 148
Figure 4.27: Localized failure near LC5 during test at slab-slab corner. 149
Figure 4.28: Comparison of deflection profiles at linear-potentiometer locations vs the tip deflection at the slab-slab push location 150
Figure 4.29: Comparison of the observed damage on the bottom surface of the specimen during the test at the slab-slab corner 152
Figure 4.30: Comparison of the observed damage on the bottom surface of the specimen during the test at the slab-slab corner 153

Figure 4.31: Comparison of the load deflection relation during the test at the beam-slab corner location. 154
Figure 4.32: Comparison of change in support loads at 9 in. vertical deflection during the test at the beam-slab corner location. 156
Figure 4.33: Comparison of deflection profiles at linear-potentiometer locations vs the tip deflection at the beam-slab push location. 158
Figure 4.34: Comparison of the observed damage on the top surface of the specimen during the test at the beam-slab corner. 160
Figure 4.35: Comparison of the observed damage on the bottom surface of the specimen during the test at the beam-slab corner. 161
Figure 5.1: Schematic of the overall structure with the modeled region shown by shaded area. 169
Figure 5.2: Plan view of the LS-DYNA model. Push location on the top left corner is identified as "Push Location". For the baseline model: LSpan = 30ft. and dBeam=64in. 170
Figure 5.3: Cross-section view of the baseline structure, (a) section 1-1, and (b) section 2-2. For the baseline model: LSpan = 30ft. and dBeam=64in. 171
Figure 5.4: Schematic of the top rebar mat provided in the baseline model. LSpan = 30ft. for the baseline model. 172
Figure 5.5: Schematic of the bottom rebar mat provided in the baseline model. LSpan = 30ft. for the baseline model. 173
Figure 5.6: Cross section of the beam showing the beam longitudinal and shear reinforcement. dBeam = 64in. for the baseline model. 174
Figure 5.7: Cross section view of the columns showing the rebar arrangement in the columns. 174
Figure 5.8: Isometric views of the model implemented in LS DYNA. 176
Figure 5.9: Isometric view of the beam rebar along the spandrel beams. Note: an outline of the concrete model is shown in grey. Elastic columns are not shown. 177
Figure 5.10: Isometric view of the slab top rebar top mat in two directions. Note: an outline of the concrete model is shown in grey. Elastic columns are not shown. 177

Figure 5.11: Isometric view of the slab bottom rebar mat in two directions. Note: an outline of the concrete model is shown in grey. Elastic columns are not shown.... 178
Figure 5.12: Isometric view of the support rebar provided at each support location. Note: an outline of the concrete model is shown in grey. Elastic columns are not shown. 178
Figure 5.13: Nodal rigid body definition at one of the support locations. All the nodes behave as a part of rigid body, thus transferring rotation and translation.............. 181
Figure 5.14: Stress-strain plot of the 6000 psi concrete material model implemented in LS-DYNA for the base line model. 183
Figure 5.15: Schematic of additional restraints provided for the special case to model the presence of in-plane restraint provided by additional panels. 185
Figure 5.16: Schematic of the special case model where only the edge beams are modeled. The slab is not incorporated in this model........ 186
Figure 5.17: Load deflection behavior of the baseline model. Initial negative load at zero deflection is the support reaction due to the self-weight and uniform gravity load applied on the model. 189
Figure 5.18: Distribution of loads at supports at peak load (142 kips) during the push at the corner support C1 190
Figure 5.19: Plot of the principal strain (tension) on the top surface at end of simulation (i.e. corner deflection of 34.5 in.). 193
Figure 5.20: Plot of the principal strain (tension) on the bottom surface at end of simulation (i.e. corner deflection of 34.5 in.)........ 194
Figure 5.21: Plot of the principal strain (tension) on the side of the spandrel beam at end of simulation (i.e. corner deflection of 34.5 in.). C1 is the location of push. It is noted that the deflected shape of the specimen is not shown. 195
Figure 5.22: Load deflection comparison between the base line case and the two special cases, one with additional restraints and another without the slab. 196
Figure 5.23: Load-deflection behavior comparison between baseline model and no slab model........ 197

Figure 5.24: Observed rebar fracture near column C2 during push at corner support in no-slab model at 25 in. vertical deflection. Note that only the beam longitudinal rebar are shown in the inset. 198
Figure 5.25: Load deflection relation for models with different beam depth. It is noted that total beam longitudinal reinforcement is same between different models. 199
Figure 5.26: Load deflection relation for models with different beam reinforcing ratios. 201
Figure 5.27: Load deflection relation for models with different slab reinforcing ratios. 202
Figure 5.28: Load deflection relation for models with different span length. 204
Figure 5.29: Load deflection relation for models with different concrete compressive strengths. 205
Figure 5.30: Load deflection comparison due to change in column stiffness at support locations. 206
Figure 5.31: Yield line definition characterizing the location and orientation of the yield line on the slab. The location of plastic hinges that form in the beam are also shown. 207
Figure 5.32: Comparison of yield line theory estimates with the calculated ultimate load capacities from the nonlinear finite element model. 209
Figure 5.33: Discretization of two-way slab into equivalent beams along the column and middle strip........ 216
Figure 5.34: Schematic of the beam-slab system under vertical deflection (a) deformed shape of the beam-slab system, and (b) in-plane internal forces along section 1-1. Part b does not show the vertical forces and moments........ 219
Figure 5.35: In-plane force balance in edge beam. Internal forces which affect the beam axial forces are shown, other forces in the beam and the slab are omitted for clarity. 220
Figure 5.36: Schematic showing the profile view of the additional moment demand due to the offset between beam and slab center lines. 222
Figure 5.37: Comparison of ultimate load capacity estimates from the analytical model and the values obtained from the non-linear finite element analysis. 223

Figure 5.38: Load deflection relation comparison with the baseline model and the model with slab rebar curtailed by their respective development length. 226
Figure 5.39: Schematic showing the slab rebar that intersect the slab failure surface due to the push at corner location. 227
Figure 5.40: Load deflection relation comparison with the baseline model and the relaxed rebar beam-slab model. 228
Figure 5.41: Load-deflection relation comparison between the no-slab model and the respective relaxed rebar model. 229
Figure B.1: Idealized yield line for the three corner tests locations on specimen 1. The crack pattern on the top surface is shown. All yield lines are negative, i.e. tension occurs on the top surface. 257
Figure B.2: Idealized yield line for the two push tests at center edge location on specimen 2. The crack pattern on the top surface is shown. Solid lines are yield lines with tension on top, while dashed lines are positive yield lines. 258

List of Tables

Table 3.1: Concrete unconfined compression test results 35
Table 3.2: Comparison between experimental and YLT load capacities for the tests performed at three corner support locations on specimen 1. 52
Table 3.3: Concrete cylinder compressive strength 72
Table 3.4: Comparison between experimental and YLT load capacities for the tests conducted at two edge support locations on specimen 2. 84
Table 4.1: Beam section parameter for rebar defined using *SECTION_BEAM 120
Table 4.2: Beam section parameter for axial load cells and actuator defined using *SECTION_BEAM... 121
Table 4.3: Shell section parameter for multi-axis load cell using *SECTION_SHELL. 122
Table 4.4: Values for the parameters as input to the LS DYNA steel model 124
Table 4.5: Concrete material parameters for *MAT_CSCM_CONCRETE.................. 128
Table 4.6: Elastic material parameters for *MAT_ELASTIC 128
Table 5.1: List of different design parameters considered for the parametric study. The values changes are highlighted 187
Table 5.2: Summary of forces at column C2 after gravity load and maximum load condition during the column failure simulation at support C1. 212
Table 5.3: Comparison of initial stiffness obtained from the simplified model (Figure 5.33) and the nonlinear model implemented in LS DYNA 217
Table 5.4: Comparison of initial stiffness obtained from the simplified model and the two test specimens (Chapter 3)... 218
Table A.1: Summary of experiments conducted on reinforced concrete slabs............... 252

Acknowledgements

The research in this dissertation on the behavior of beam-slab systems under support failure was conducted in the Department of Structural Engineering, University of California, San Diego. I would like to gratefully acknowledge those who have been instrumental to my completion of this dissertation.

First, I would like to acknowledge my Dissertation Committee Members: Professors Tara Hutchinson, Jośe Restrepo, David Sandwell, Peter Shearer and Benson Shing for their guidance and suggestions. In particular, Prof. Tara Hutchinson, who as my advisor, provided guidance and support throughout my graduate studies.

Second, I would like to acknowledge the input of the professional practice committee, composed of Professor Jack Moehle, Bill Holmes, Elie Elkhoury, Michael Mehrain, and Nabih Youssef on their input during the design phase of the two test specimen.

Third, I would like to acknowledge the laboratory staff at the University of California, San Diego Charles Lee Powell Components Laboratory. In particular, Mr. Andrew Gunthardt, Mr. Paul Greco; Mr. Noah Aldrich; Mr. Darren Mckay and Mr. Chris Latham for their technical assistance during the tests.

Fourth, I would like to acknowledge my fellow students at UCSD, including: Dr. Richard Woods, Xiang Wang, Dr. Weian Liu, Dr. Nicholas Trombetta, Chris Trautner, Dong-Won Kim, and Kyungtae Kim.

Finally, I would like to thank all of my family and friends for their love and support.

******

This study was supported through the National Science Foundation (NSF) - NEESR project (grant number CMMI-0618804) titled: Mitigation of Collapse Risk in Vulnerable Concrete Buildings, where Professor Jack P. Moehle (University of California, Berkeley) was the Principal Investigator.

******

Figures in Chapter 1 were obtained from the National Information Service for Earthquake Engineering (NISEE) website. In addition, portions of following publication, for which the author was the principal researcher and author, are contained in Chapter 3 and 4:

- Prasad, S. and Hutchinson, T. C. (201X), “Evaluation of Older Reinforced Concrete Floor Slabs under Edge Support Failure", ACI Structural Journal, (In review).
- Prasad, S. and Hutchinson, T. C. (2014), “Evaluation of Older Reinforced Concrete Floor Slabs under Corner Support Failure", ACI Structural Journal, Vol. 111, No. 4, pp 839-850.
- Prasad, S. and Hutchinson, T. (2014), "Experimental Evaluation of a 1/3rd scale Lightly Reinforced Concrete Slab under Uniform and Pull Down Load: Edge Conditions (Version B)." Structural Systems Research Project (SSRP) Report No. 14/02, Department of Structural Engineering University of California, San Diego, 100 pp.
- Prasad, S. and Hutchinson, T. (2014), "Experimental Evaluation of a 1/3rd scale Lightly Reinforced Concrete Slab under Uniform and Pull Down Load: Edge Conditions (Version A)." Structural Systems Research Project (SSRP)

Report No. 14/01, Department of Structural Engineering University of California, San Diego, 85 pp.

- Prasad, S. and Hutchinson, T. (2013), “Behavior of Reinforced Concrete Flat Slab Systems under Corner and Center Support Failure Scenarios”, Proceedings of 10th International Conference on Urban Earthquake Engineering (CUEE), Tokyo, Japan, March.
- Prasad, S. and Hutchinson, T. (2012), "Experimental Evaluation of a 1/3rd scale Lightly Reinforced Concrete Slab under Uniform, Pattern and Concentrated Pull Down Load: Corner Conditions." Structural Systems Research Project (SSRP) Report No. 12/11, Department of Structural Engineering University of California, San Diego, 120 pp.

Portions of the following publication in preparation, for which author is the principal researcher and author, are contained in Chapter 4 and 5:

- Prasad, S. and Hutchinson, T. C., “Behavior of older reinforced concrete beam-slab systems considering a corner support failure scenario: model validation and parametric study” ACI Structural Journal.

Vita

2007	Bachelor of Technology, Indian Institute of Technology, Kanpur, India
2009	M.S., Structural Engineering, University of California, San Diego
2009-2014	Graduate Student Researcher, University of California, San Diego
2014	Ph.D., Structural Engineering, University of California, San Diego

PUBLICATIONS

Referred Technical Journal

Prasad, S. and Hutchinson, T. C. (201X), "Evaluation of Older Reinforced Concrete Floor Slabs under Edge Support Failure", ACI Structural Journal, ACI (In review).

Prasad, S. and Hutchinson, T. C. (2014), "Evaluation of Older Reinforced Concrete Floor Slabs under Corner Support Failure", ACI Structural Journal, Vol. 111, No. 4, pp 839-850.

Conference Proceedings

Prasad, S. and Hutchinson, T. C. (2013), "Behavior of Reinforced Concrete Flat Slab Systems under Corner and Center Support Failure Scenarios", Proceedings of 10th International Conference on Urban Earthquake Engineering (CUEE), Tokyo, Japan.

Prasad, S. and Hutchinson, T. C. (2011), "Attempts at simulating membrane effects in Slabs using Finite Element Analysis", Proceedings of 8th International Conference on Urban Earthquake Engineering (CUEE), Tokyo, Japan.

Technical Reports

Prasad, S. and Hutchinson, T. (2014), "Experimental Evaluation of a $1/3^{rd}$ scale Lightly Reinforced Concrete Slab under Uniform and Pull Down Load: Edge Conditions (Version B)." Structural Systems Research Project (SSRP) Report No. 14/02, Department of Structural Engineering University of California, San Diego, 100 pp.

Prasad, S. and Hutchinson, T. (2014), "Experimental Evaluation of a $1/3^{rd}$ scale Lightly Reinforced Concrete Slab under Uniform and Pull Down Load: Edge Conditions (Version A)." Structural Systems Research Project (SSRP) Report No. 14/01, Department of Structural Engineering University of California, San Diego, 85 pp.

Prasad, S. and Hutchinson, T. (2012), "Experimental Evaluation of a $1/3^{rd}$ scale Lightly Reinforced Concrete Slab under Uniform, Pattern and Concentrated Pull Down Load: Corner Conditions." Structural Systems Research Project (SSRP) Report No. 12/11, Department of Structural Engineering University of California, San Diego, 120 pp.

ABSTRACT OF THE DISSERTATION

Behavior of Non-Ductile Beam-Slab Systems under Support Failure Scenarios

by

Saurabh Prasad

Doctor of Philosophy in Structural Engineering

University of California, San Diego, 2014

Professor Tara C. Hutchinson, Chair

Non-ductile reinforced concrete structures built prior to the introduction of seismic codes are susceptible to severe structural damage during an earthquake. Past earthquakes have demonstrated, for example, the high likelihood of shear failure of non-ductile columns. Failure of a column within a building system creates a discontinuous load path due to loss of axial load carrying capacity. When this occurs, the system has to redistribute loads to other load bearing members to prevent progressive collapse. Although several studies have been conducted to understand the behavior of the beam-

column frame system under support failure, the role of the beam-slab system under such failure scenarios has observed much less attention in the literature.

Large-scale experiments were conducted on two one-third scale reinforced concrete beam-slab models to investigate their behavior under different support failure scenarios. Test results demonstrate that the beam-slab system was able to continue to carry large vertical forces despite the occurrence of a simulated column failure, while redistributing the loads to the adjacent support locations. Compared to predictions using Yield Line Theory, an enhancement in load capacity of more than 50% was observed. This reserve capacity is largely attributed to the presence of in-plane forces that develop as the system redistributes load.

A nonlinear finite element model is implemented and its property selection and model protocol parameters evaluated by comparing its response to that observed in the tests. Subsequently, the validated finite element model is used to conduct a parametric analysis varying the different design parameters to common ranges found in practice. The emphasis of this aspect of the study is on characterizing the ultimate load carrying capacity of the system under the more critical corner support failure scenario. Results from the parametric analysis on the beam-slab system numerical model further corroborate observations from the experimental phase of the study. Namely the presence of in-plane membrane forces and increased load carrying capacity on average by 50% compared to the Yield Line Theory estimates. An analytical model is presented, which proves to increase the reliability of estimating the ultimate load carrying capacity of the system by considering the in-plane membrane forces that occur due to the presence of the slab.

Chapter 1: Introduction

1.1 Background

Anagnos et al. (2012) predict that about 8000 non-ductile concrete buildings exist in 30 California cities. Five thousand of these buildings are predicted to be the city of Los Angeles and San Francisco alone. Similarly, the Concrete Coalition (Comartin et al., 2011) suggests that about 16000-17000 such buildings exist in 23 counties in the state of California. These structures, built prior to the introduction of new seismic design codes, are vulnerable to collapse during an earthquake event as they lack the ability to deform inelastically without causing severe damage to component(s), therefore reducing the integrity and safety of the entire structure (e.g. Figures 1.1 and 1.2).

Figure 1.1: Partial collapse of Kaiser Permanente office building after 1994 Northridge earthquake.

Figure 1.2: Collapse of a concrete structure during the 1999 Izmit earthquake, Turkey (photo courtesy: Halil Sezen).

Reinforced concrete (RC) columns are especially susceptible to shear failure during seismic events (e.g. Figures 1.3 and 1.4) due to their inadequate design. This in turn could result in significant and abrupt reduction in axial load carrying capacity. When a column loses its load carrying capacity, the structural system must redistribute the loads and create new load paths to prevent progressive collapse. Beam-slab systems, being an integral load transfer component in a structure, have the potential to mitigate collapse by redistributing these loads in the event of a support failure. This would reduce the risk of partial or total collapse of the structure.

Figure 1.3: Shear failure of columns at the Imperial County Services Building during the Imperial Valley earthquake, 1979 (photo courtesy: Vitelmo V Bertero).

Figure 1.4: Shear failure in columns at the Van Nuys Holiday Inn during the 1994 Northridge earthquake, 1994; (photo courtesy: Peter W. Clark)

1.2 Motivation for the Present Work

Since the partial collapse of Alfred P. Murrah Building in Oklahoma City in 1995 and the collapse of the World Trade Center Towers in New York in 2001, extensive research has been conducted to understand the potential for progressive collapse of structures under column failure scenarios (e.g. Sasani et al. 2007; Yi et al., 2008; Sasani and Sagiroglu 2010; Lew et al. 2011; Qian and Li, 2012). Importantly, understanding the potential of a component to redistribute the loads will be integral to characterizing the system-level impacts of support failures.

While prior studies have been conducted on progressive collapse potential of structures, at both the system and component level, previous research has failed to analyze the contribution of beam-slab systems in load redistribution. Most prior experimental and numerical efforts have either focused on the behavior of the entire structure, or the structural frames (i.e. beams and columns only) with very limited studies have looked at the performance of slab or beam-slab systems under support failure scenarios (e.g. Qian and Li, 2012 and 2013; Dat and Hai 2013; Qian et al, 2014). Hawkins and Mitchell (1979) and Mitchell and Cook (1984), for example, suggest that the slab may act as secondary load carrying mechanism in the event of support failure due to their enhanced load capacity in the event that in-plane membrane forces develop. One could certainly imagine that, in particular, the beam-slab system, being an integral load transfer component in a structure, could mitigate collapse by providing load redistribution. Embellishing load redistribution via the slab aligns with the intent of recent design guidelines (e.g. ASCE-7, 2010) – however an accurate assessment of its load carrying capacity and ensuing deformation and damage pattern is needed before the slab can be confidently used in this fashion.

1.3 Research Objectives

To study the behavior of beam-slab systems under support failure and assess the additional load demands on neighboring members, this dissertation incorporates three primary research tasks:

- Experimental investigation of non-ductile reinforced concrete beam-slab systems under column failure scenarios. These tests allow assessment of any load enhancement observed as compared to the yield line theory.
- A numerical parametric study to investigate the effect of design parameters on the overall behavior, e.g. stiffness, load deflection, strength etc., of the beam-slab system under a support failure scenario.
- Development of an analytical model to provide a simple method to account for any enhancement of the ultimate load capacity that might be observed due to the presence of in-plane forces in the system.

The first research effort is completed by performing two large-scale laboratory experiments at the Charles Lee Powell Structural Components Facility at the University of California, San Diego (UCSD). The first experiment is conducted to characterize the behavior of beam-slab systems under corner support failure scenarios. The second experiment analyzes the behavior of a similar system under edge column failure. For both experiments, importance is given to the systems ultimate capacity, load deflection behavior, and loads transferred to the adjacent columns.

The second and third research efforts are completed by performing three dimensional nonlinear analysis of a typical non-ductile beam-slab system under a corner column failure scenario. Several parameters, such as the reinforcing ratio, frame member size, concrete strength, span length etc., are selected and their values varied to account for a range that may be encountered in practice. Results from the parametric study of particular focus include the ultimate load capacity, load redistribution, and observed damage to the beam-slab system. The analyses also provide insight into the failure mechanism and a simplified method is proposed to calculate initial stiffness and ultimate load carrying capacity of the beam-slab system under corner support failure scenario.

1.4 Organization of Dissertation

This dissertation is organized into six chapters as follows:

- **Chapter 2** contains a review of the relevant literature in the field which provide background to the dissertation. The literature review is summarized into two categories: (1) progressive collapse, and (2) capacity of reinforced concrete slab.
- **Chapter 3** presents a detailed description and results from the test program. Two one-third scale beam-slab specimens were constructed and support removal tests were performed at corner and edge locations. Results are

presented in terms of load deflection behavior, redistribution of loads, and observed damage.

- **Chapter 4** presents the details of a finite element model of the first test specimen where corner support removal was simulated. The three dimensional models were implemented in LS-DYNA. Results obtained from the numerical models are then compared against the three push tests conducted on the first specimen.
- **Chapter 5** describes a parametric study, which was conducted using three dimensional numerical models implemented in LS-DYNA. In these analyses several design parameters were varied, namely: section dimensions, reinforcing ratio, span length, concrete strength, and support column stiffness. Results are similarly presented in terms of: load deflection behavior, ultimate load capacity, observed damage and load distribution. The ultimate load capacities are compared with yield line theory estimates and an analytical model is proposed to account for the load enhancement observed.
- **Chapter 6** provides summary and conclusions along with the suggestions for future work.

******

Figures 1.1 to 1.4 are obtained from the National Information Service for Earthquake Engineering (NISEE) online archives.

Chapter 2: Literature Review

The literature reviewed is categorized into two broad categories in this chapter: (1) progressive collapse, and (2) capacity of reinforced concrete slab. The relevant literature is briefly summarized in the following sections.

2.1 Progressive Collapse

Following the terrorist attack on the Murrah Federal Building in 1995 and the collapse of the World Trade Center in 2001, several studies were performed to assess and mitigate the potential for the progressive collapse of building structures. Most of this work has focused on frame structures absent floor slabs (e.g. Bao et al., 2008; Bazan, 2008; Sasani and Kropenlnicki, 2008; Mohamed, 2009; Su et al., 2009; Tan et al., 2010; Sadek et al., 2011; FarhangVesali et al., 2013). In addition, a few studies have been performed on older RC structures before their demolition (e.g. Sasani et al. 2007; Sasani, 2008; Sasani and Sagiroglu, 2010; Sasani et al., 2011; Morone, 2012; Morone and Sezen 2014). Although these studies demonstrate the generally positive structural response of the system under different column removal scenarios even for older construction, very limited research has been conducted on the slabs under such extreme events (e.g. Qian and Li, 2012 and 13; Dat and Hai, 2013; Qian et al., 2014).

2.1.1 Experimental Studies on Progressive Collapse

Of the several experimental studies that have been performed to study the progressive collapse potential of component and structures, four experimental studies are discussed below, which were carried out recently to understand the load carrying capacity of RC systems after support removal. In an experimental study by Yi et al. (2008), the potential for progressive collapse of an RC frame due to loss of a lower floor column was investigated. To simulate the column loss, the center column of the four bay beam-column specimen was removed and vertical load was applied gradually. During the initial part of the test, the beams experienced an increase in compression due to arching action. This compression was slowly relieved and the vertical load was carried through beam catenary action at large displacements. The final failure was due to the bottom beam rebar rupture near the center column location (beam above the removed column, Figure 2.1). The authors conclude that based on the performance of the specimen, the structure was safe against progressive collapse.

Figure 2.1: Rebar rupture at bottom of the beam next to the joint where column was removed (from Yi et al. 2008).

The study of Sasani and Sagiroglu (2010), focused on investigating the redistribution of gravity loads after sudden removal of an interior column on the first floor level of a building. In this effort, the performance of the Baptist Memorial Hospital in Memphis, Tennessee (Figure 2.2), was studied by removing the interior column using explosives. It was observed that the vertical deformation of the slab was largest at the floor where the column was removed and decreased progressively on higher floors. As the load redistributed, axial load increase was observed in adjacent columns at the ground floor level, while the columns directly above the removed column experienced a decrease in axial load due to extension. The loads were redistributed via the beam-slab system and the greatest moment increase was observed in the second floor beams, above the removed column. It was concluded that buildings with more floors were less susceptible to progressive collapse after failure of a single column, as the entire system redistributes the loads efficiently.

Figure 2.2: Baptist Memorial Hospital, Tennessee (from Sasani and Sagiroglu, 2010).

In the experimental work of Lew et al. (2011), two full-scale RC beam-column subassemblies were tested under column removal scenarios. The two specimens represent a portion of two RC frame structures, which were designed for seismic design category C and D. Figure 2.3 shows the reinforcing details of one of the specimens before testing. The overall load deflection behavior of the specimen was governed by arching at small deflections and catenary action at deflections larger than the depth of the beam. Two numerical models were also implemented; one detailed model using 3D solid elements and another simple stick model, both were implements in LS-DYNA. The numerical models were able to capture the key behavior of the specimen, including arching and catenary action observed during the tests.

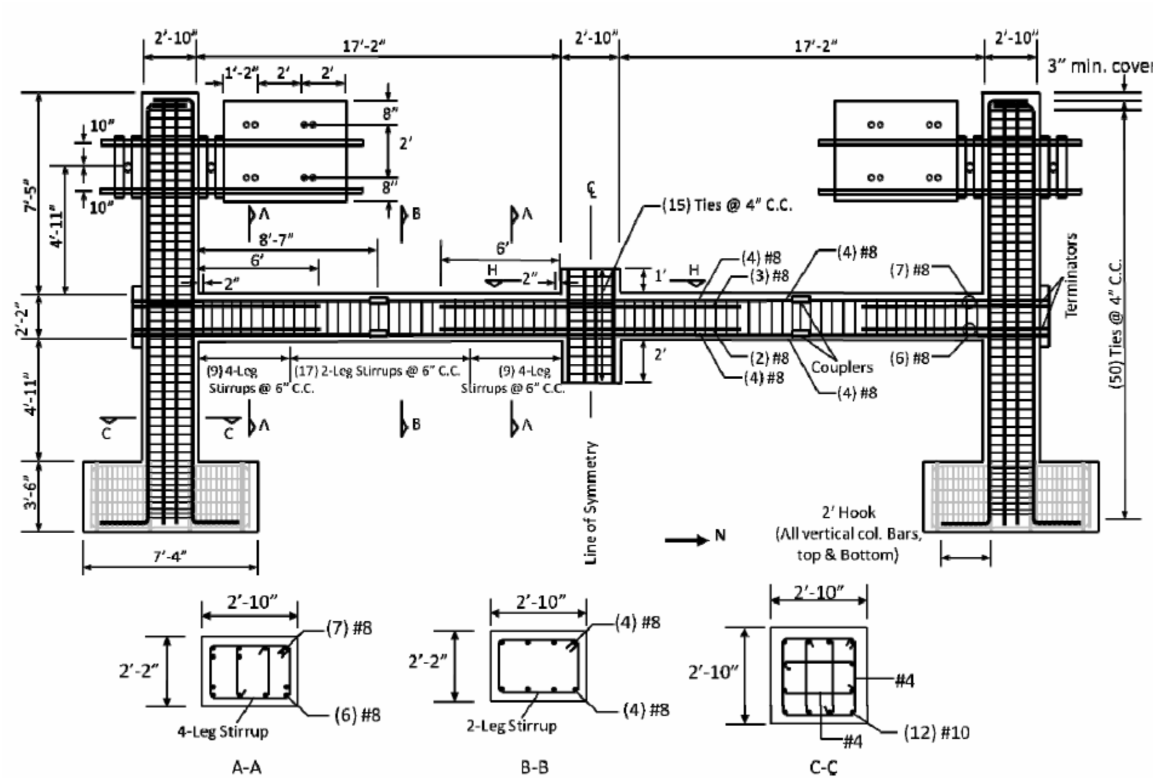

Figure 2.3: Tests conducted at NIST on beam-column frame showing the reinforcing details of the intermediate moment frame specimen designed for seismic category C. (from Lew et al., 2011)

In a recent study conducted by Qian and Li (2012), the contribution of slabs in preventing progressive collapse was investigated (Figure 2.4). The authors conducted corner column removal tests on six specimens, three beam-slab specimens and three beam only specimens. By comparing the results from the various tests, it was concluded that slabs contributed up to 40-60% of the overall strength under corner support failure scenarios. It was also observed that the non-seismically detailed specimens were able to reach only 55-75% of the required load capacity to prevent progressive collapse based on General Services Administration (GSA, 2003) requirements.

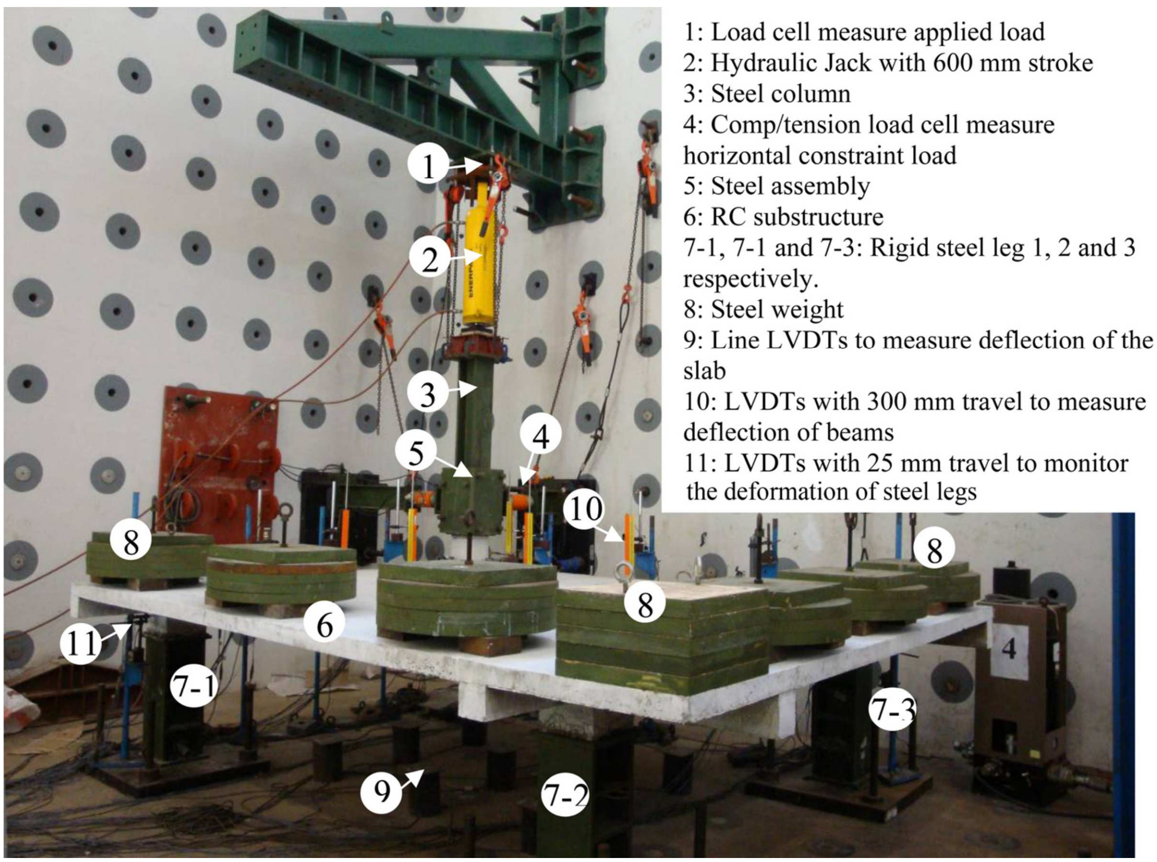

Figure 2.4: Slab specimen showing different components of the test setup (from Qian and Li, 2012).

2.1.2 Code-Based Approach to Progressive Collapse

In recent years, the Department of Defense (DoD) and General Services Administration (GSA) have proposed guidelines to address progressive collapse potential of new and existing structures. These codes provide direct and indirect analysis methods which could be utilized when analyzing the potential for progressive collapse in structures after initial damage (for example, failure of support due to an extreme event).

The Unified Facilities Criterion (2005) by DoD, for example provides three possible methods of design based on occupancy category of the structure. For example, for Low Level of Protection, a tie force approach can be used, where the structure should be able to develop tensile forces (termed tie forces) in various directions to ensure adequate redistribution of loads, while for a medium and high level of protection, an alternate path requirement must be satisfied, where the structure must be able to bridge over removed vertical load bearing members. The tie force approach categorizes the tie forces into four categories: (1) longitudinal horizontal ties, (2) transverse horizontal ties, (3) peripheral horizontal ties, and (4) vertical ties as shown in Figure 2.5. If the structure cannot provide the required tie forces, they either need to be redesigned/retrofitted or an alternate path requirement must be satisfied. For alternate path requirement, the code specifies several support removal locations (Figure 2.6), which must each be analyzed one at a time for each floor location. If the structure is able to bridge over the failed support it is deemed low risk of progressive collapse, otherwise it needs to be redesigned or retrofitted.

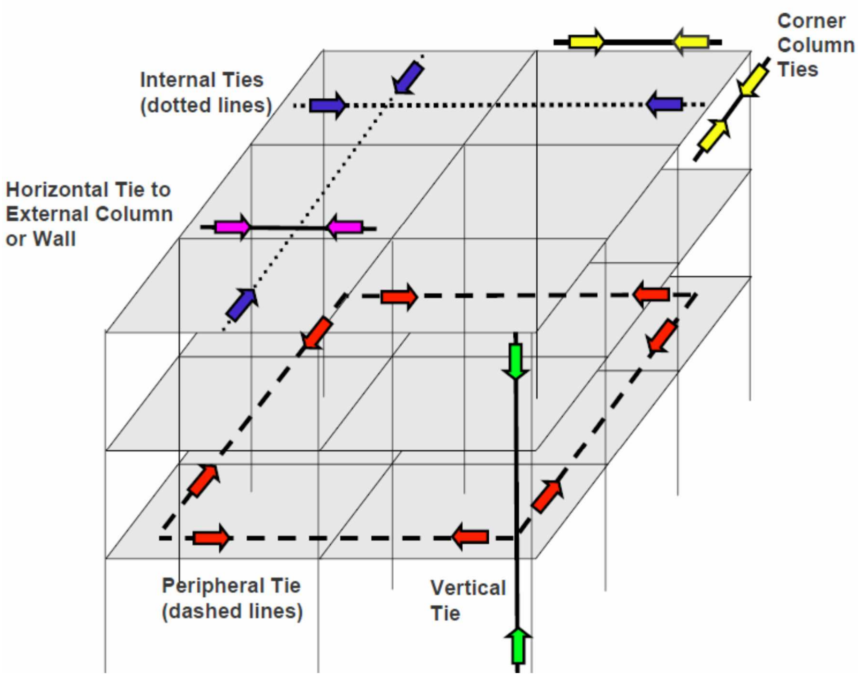

Figure 2.5: Category of tie forces required to prevent progressive collapse in a structure (from DoD UFC 2005).

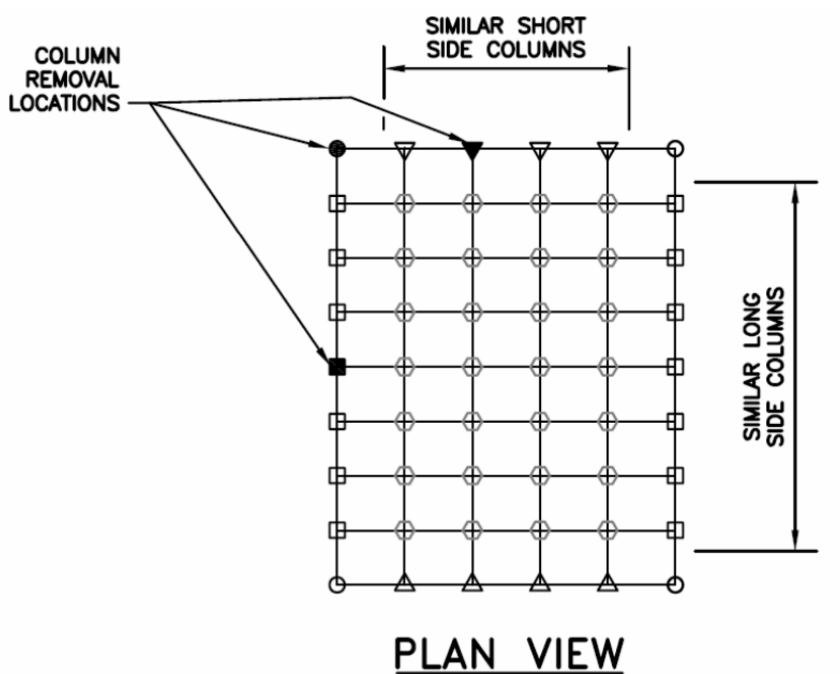

Figure 2.6: Location of column removal in a frame structure (from DoD UFC 2005).

In a similar approach proposed by General Services Administration (GSA, 2003), an alternate load path method is recommended to ensure the structure is able to bridge over the specified support locations after initial failure. In the suggested analysis process, the demand capacity ratio (DCR) of the structural elements are monitored for structural elements under gravity loads. Gravity loads are applied on the structure as either *(DL+LL)* or *2×(DL+0.25LL)* for dynamic and static analyses, respectively (where DL = dead load and LL = live load). During the analysis, any element, which exceeds DCR of 1.5 (for atypical structural configurations) or 2.0 (for typical structural configurations) are removed from the model (or replaced by a plastic hinge if the DRC exceeds in flexure). Once the component is removed, load carried by the failed components are redistributed to other nearby members and the analysis is continued until no component exceeds the DCR requirement. If the DCR values that exceeded during the analysis are outside the allowable collapse region, the structure is considered to have high potential for progressive collapse.

2.2 Capacity of Reinforced Concrete Slab

Owing to the importance of beam-slab system in load redistribution, it is important to understand its behavior and in particular, its ultimate load carrying capacity. Johansen Yield Line Theory (Johansen, 1962) has been widely used to predict the ultimate strength of reinforced concrete (RC) slabs under different loading and support conditions. Yield Line Theory (YLT) assumes the slab deformations are localized along predefined yield lines based on geometry, loading and boundary conditions.

Yield line theory assumes the failure of the system to be governed by flexure. As the loads are increased beyond the elastic limit, reinforcement yields in the region of high moment demand, forming plastic hinge(s) at these locations. As the load is further increased, the region(s) with a plastic hinge rotates, thus causing adjacent sections to yield. This force transfer and redistribution occurs until enough hinges have been formed to create a plastic mechanism, such that the system can then deform without any increase in the applied load. By equating the internal work done along these yield lines that form the plastic mechanism to the work done by the external force, an upper bound estimate can be found for the capacity of the system. Despite the widespread use of this method for estimating the ultimate load capacity of beam-slab systems due to its ease of use, ultimate capacity of the slabs is consistently shown to be underestimated. This increase in strength has been attributed to the presence of in-plane compressive and tensile membrane forces that develop in the slab at small and large vertical deflections, respectively (Figure 2.7). At small deflection amplitudes, compressive membrane forces or arching effects develop in laterally restrained slabs, increasing the moment capacity of the section (P-M interaction). At large deflections, the slab edges tend to move inward and the supports and adjacent panels provide lateral restraint, creating in-plane tensile forces. The vertical component of these tension forces provides additional capacity, resulting in higher ultimate loads.

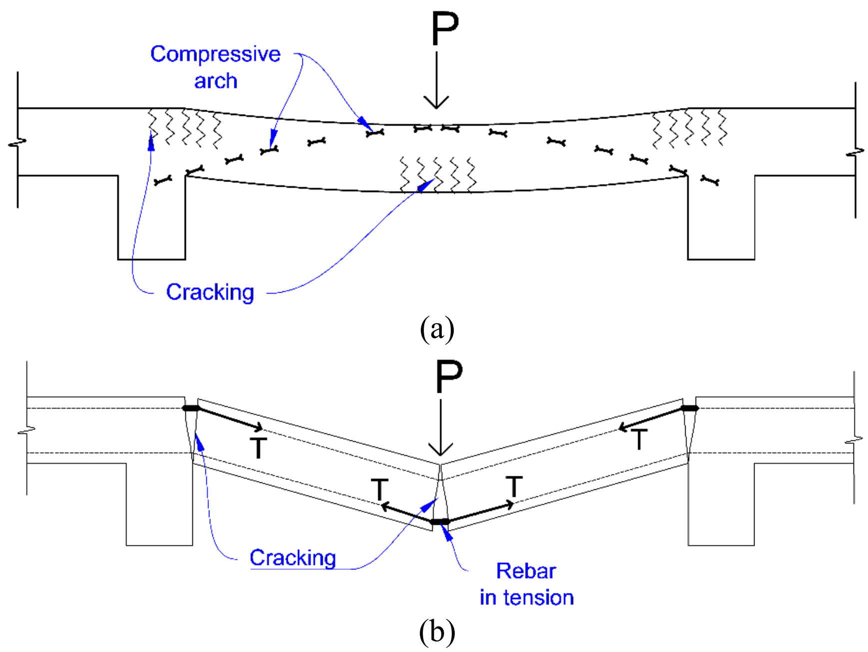

Figure 2.7: Membrane forces acting in a slab, (a) compressive membrane forces at small deflection, and (b) tensile membrane forces at large deflections.

To better understand the behavior of reinforced concrete beam-slab systems and the observed load enhancement, several experimental studies have been undertaken and a number of these provide comparison with YLT predictions (e.g. Park 1964; Hopkins, 1969; Keenan, 1969; Aoki and Seki 1971; Brotchie and Holley, 1971; Hopkins and Park, 1971; Hung and Nawy, 1971; Park, 1971; Tong and Batchelor, 1971; Christiansen and Frederickson, 1983; Guice and Rhomberg, 1988; Guice et al., 1989; Vecchio and Tang, 1990; Lahlouh and Waldron, 1992; Fang et al. 1994; Foster et al., 2004; Muthu et al., 2007; Bailey et al., 2008; Al-Hassani et al., 2009; Wang et al. 2011). In addition to these studies, several researchers have also investigated RC slab performance under fire (e.g. Bailey et al., 1999; Bailey 2001, 2002, 2004; Usmani and Cameron, 2003; Li et al., 2006) as fire loading mimics the progressive deflection of the slab and therefore generates similar membrane forces and could prevent collapse under fire loading conditions.

2.2.1 Experimental Studies

There have been many model slab tests conducted to investigate the capacity of slabs and beam-slab system as membrane forces develop. Perhaps earliest of these is the work of Hopkins and Park (1971), who tested a quarter-scale nine-panel RC beam-slab system under uniform load. In these analyses, the ultimate load capacity of each panel showed good correlation with the analytical model proposed by Park (1964), which accounts for membrane action in the slab. The center panel of the system observed the greatest load enhancement of about 2, due to fixity provided by adjacent panels. The center edge panels and the corner panels also experienced an enhancement of about 1.5 compared to theoretical YLT estimates. During the test, cracks radiating towards the beams were observed indicating the presence of membrane forces in the slab (Figure 2.8). At ultimate loads, severe cracking was observed in the panels and adjacent beams; these cracks also verified the formation of a plastic mechanism.

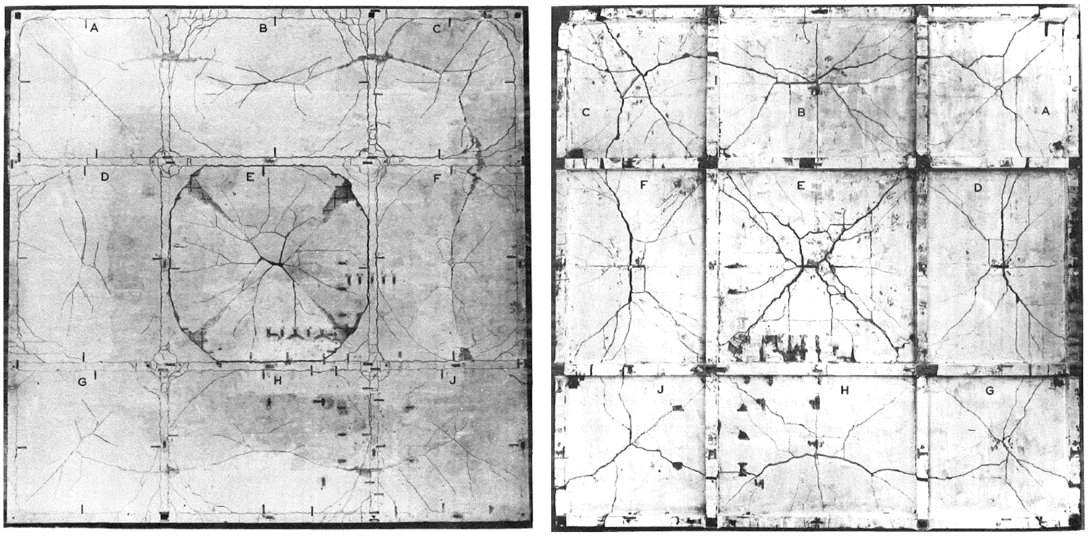

(a) (b)

Figure 2.8: Crack patterns on the nine panel beam-slab specimen at the end of the test, (a) top surface, (b) bottom surface. (from Hopkins and Park, 1971)

In a similar study performed by Park (1971), a quarter scale two-panel beam-slab system was tested to study membrane effects. Rigidity due to adjacent panels was simulated by stiffening the beams in the transverse direction as shown in Figure 2.9. Load was applied using air bags on the two panels. The experiment was performed in two stages, in the first stage, the slab was loaded to its service limit, and in the second stage it was loaded to failure. At service load, no cracking was observed on the bottom of the slab. At ultimate load, the slab was able to deform more than 3 times its thickness. The ultimate loads exceed the theoretical load estimates based on YLT by 65%-88%. The author conclude that the tensile membrane forces that developed in the slab at large deflections were balanced by large compressive forces induced in the beams.

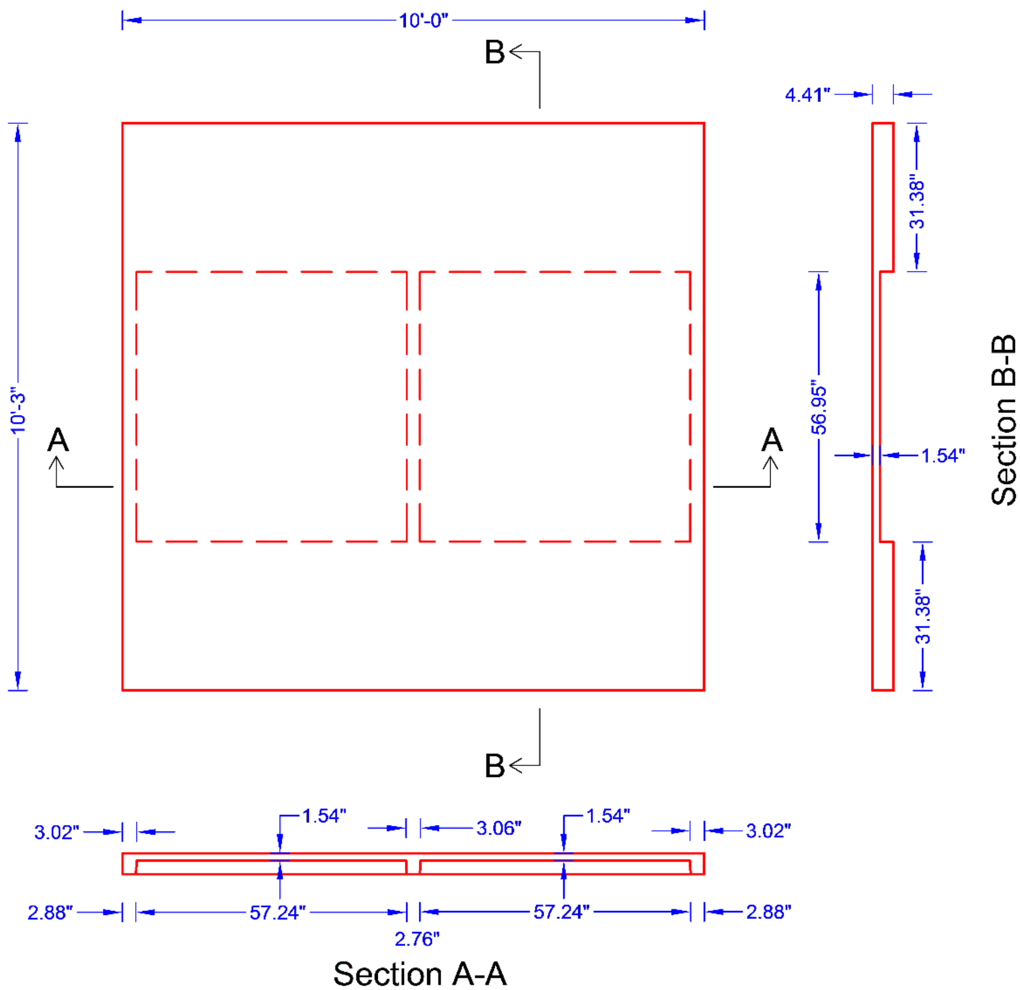

Figure 2.9: Schematic of the test specimen with two slab panels tested under uniform gravity loads. Additional stiffness was provided on two ends using thickened slab sections (from Park, 1971).

In the work by Hung and Nawy (1971), 29 isotropically reinforced concrete slab panels were tested under uniform loads using water bags. The panels varied in shape (60in.× 60in.×2.5in. to 42in.×60in.×2.5in.), slab reinforcing ratio (0.25 to 0.6%), and support conditions (i.e. number of fixed and hinged edges). Each panel was subjected to uniform surface load using water bags until failure. All panels failed in flexure and formed failure mechanisms with that suggested of YLT. However, when compared to

YLT, the ratio of ultimate load capacity to YLT predicted load ratio varied from 1.25 to 2.5. The authors observed that the load enhancement increased with increasing rigidity at the supports.

Christiansen and Frederiksen (1983) carried out tests on two-full scale RC slabs during demolition of a building using lead blocks to apply uniform load on each floor. During the in-situ tests on the building floor slab, first crack occurred at loads comparable with the yield line estimates, while the ultimate loads were 2.5 to 3 times higher than the load capacity predicted by YLT. Eleven laboratory tests on reinforced and unreinforced slabs with square and rectangular dimensions were also conducted. The slab specimens were tested under simulated uniform load by applying 16 point loads. Additional restraint was provided on the edge by providing additional reinforcement along the perimeter of each slab. The authors conclude that the load enhancement due to membrane forces, defined by the difference between the actual ultimate load and the load predicted by YLT, is not highly dependent on reinforcing ratio or the shape of the slab. It is concluded that the increase in total load carrying capacity of horizontally restrained slabs could be estimated by $h^2 \times f'_{Cyl}$ (where h is the slab thickness and f'_{Cyl} is the concrete cylinder compressive strength). By comparing the results from the test done by other researchers, authors conclude that this enhancement could be as high as $3 \times h^2 \times f'_{Cyl}$, depending on the level of edge restraint provided along the edge of the specimen.

In another experiment series by Vecchio and Tang (1990), two 4 in. thick, 60 in. wide slab strips (0.66% and 0.33% top and bottom rebar, respectively), were tested under concentrated load. The slab strip was supported by two columns, 10ft. apart. Both specimens were identical, except for the support conditions provided at the end of the strips; one specimen was supported by roller supports, while the other had end supports which were laterally restraint against horizontal movement as shown in Figure 2.10.

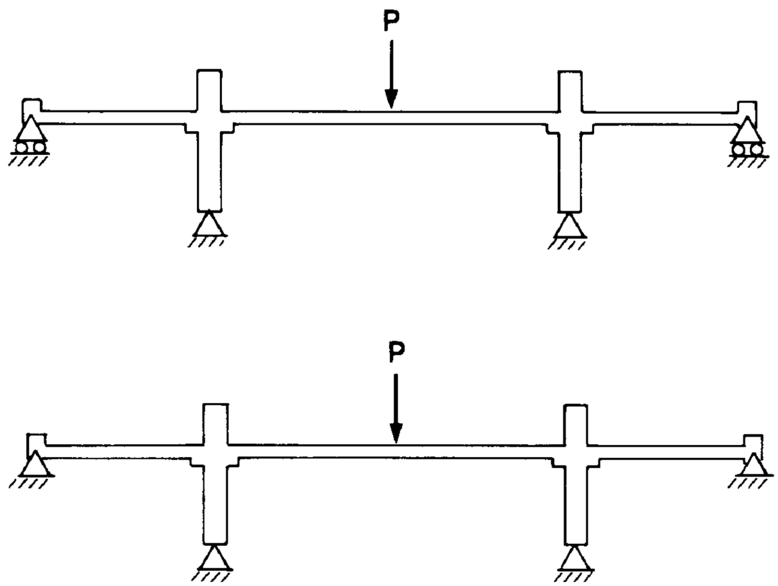

Figure 2.10: Schematic of the two slab strips tested by Vecchio and Tang (1990), showing different support conditions provided at the end of the slab strips (from Vecchio and Tang, 1990).

The results from the experimental program showed that the specimen with lateral restraint attained 40% higher load capacity compared to the unrestrained slab. This higher load capacity of the specimen with lateral restraint was attributed to the presence of compressive arching in the slab strip.

These and other experimental studies in the past (see Appendix A for summary of tests conducted on RC slabs) have consistently indicated that the presence of membrane forces could provide substantial beneficial load capacity enhancements compared with estimates predicted using YLT. These tests have shown that the ultimate capacity of the slab can be about 100 to 200% higher than the yield line theory estimates due to the presence of in-plane membrane forces. It has been suggested by researchers that this enhanced load capacity of the beam-slab system could act as a secondary load carrying mechanism in the event of initial support failure (e.g. Hawkins and Mitchell, 1979; Mitchell and Cook, 1984).

2.3 Summary Remarks

This chapter summarizes previous research activities related to progressive collapse under a support failure scenario, as well as the efforts made in understanding the behavior of slab and beam-slab system under various loading conditions. Slab tests have shown that the beam-slab system can experience more than 2 times the load enhancement due to the presence of arching and catenary action at small and large deflection levels.

Progressive collapse studies conducted on frame structures have also supported the fact that this load enhancement, due to arching and catenary action, provides a larger margin of safety against collapse. Although several studies have been conducted to understand the risk of progressive collapse in structures due to initial support failure scenario, most of this research has been conducted on beam-column subassemblies, or on behavior of entire structure, while only limited research has focused on the behavior of the slab and its contribution to the overall capacity under such support failure scenario (e.g. Qian and Li, 2012 and 2013; Dat and Hai, 2013; Qian et. al., 2014). The limited research in characterizing the role played by the slab in preventing progressive collapse after initial column failure, and the absence of simplified estimation method to account for the presence of slab on the overall capacity of the system warrants further study to ensure designers can amply determine a margin of safety against complete collapse.

Chapter 3: Experimental Program

3.1 Overview

This chapter summarizes the results obtained from large scale tests performed on two 1/3rd scale beam-slab specimens. Each beam-slab specimen was constructed in the laboratory at the University of California, San Diego (UCSD) and subjected to various support failure scenarios. The specimens were sequentially subjected to gravity load, pattern load (only first specimen), followed by column removal tests. Corner support failure scenarios were considered during the testing of the first specimen, while the second specimen considered the failure of interior edge supports.

To document this test program, the present chapter is arranged into five sections:

- **Section 3.2:** summarizes the details of the first specimen, including reinforcing details, material properties, test setup and loading protocol.
- **Section 3.3:** presents the results from the test conducted on the first specimen. For the gravity load tests, the results presented include, load distribution, and physical observations. For the column removal tests at the corner support locations, the results presented include: load-deflection relation at the push location, load distribution at supports, deflection profiles, and observed damage.
- **Section 3.4:** summarizes the details of the second specimen, including reinforcing details, material properties, test setup and loading protocol.

- **Section 3.5:** presents the results from the test conducted on the second specimen. For the gravity load tests, the results presented include, load distribution, and physical observations. For the column removal tests, the results presented include: load-deflection relation at the push location, load distribution at supports, deflection profiles, and observed damage.
- **Section 3.6:** provides concluding remarks from the test conducted on two specimens.

3.2 Specimen 1 Details

The test specimen was intended to model a section of the floor plan constructed according to detailing practices adopted for buildings prior to 1960s. Specific details were chosen by reviewing drawings of older reinforced concrete (RC) building, and in consultation with professional practice committee (personal correspondence, 2010-2011), and reviewing 1956 and 1963 ACI-318 design provisions. The test specimen was modeled to represent a portion of a floor plan, extending two panels from the building corner in each direction as shown in Figure 3.1. For cost and space practicality, the specimen was a 1/3rd scale model of the prototype structure.

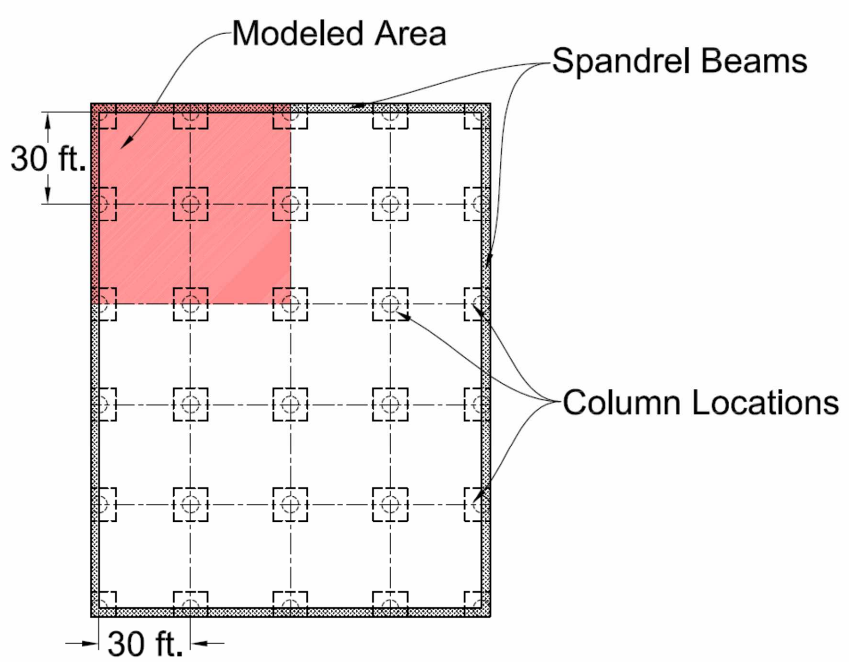

Figure 3.1: Region of building modeled for the study

The overall test specimen was 21'-2" in both directions, with equal span supports spaced 10 feet apart. The specimen has 12"x3" (height x width) spandrel beams along two exterior edges, a characteristic found to be common in structures from that era. The slab itself was 3 in. thick, therefore a model of 9 in. thick prototype slab. Lightly reinforced sloped drop panels, commonly used in slab construction of that era were provided at each support location. The specimen was supported on 200-kip commercially available axial load cells at four corner support locations, while the other five supports were provided by custom built multi-axis load cells constructed using steel pipe sections (Prasad and Hutchinson, 2012). Figure 3.2 and 3.3 provide schematics of the test specimen and the location of different test locations.

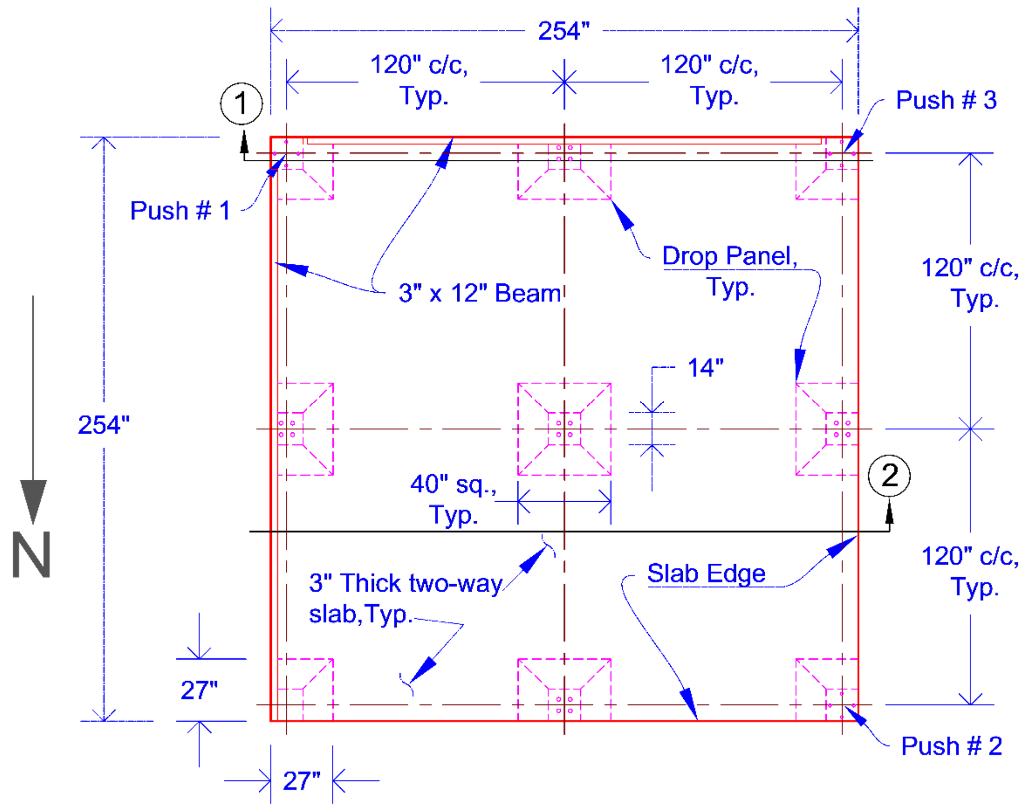

Figure 3.2: Plan view of the first test specimen.

Three support failure locations at the corner of the specimen are identified, namely (i) push 1 - beam-beam corner, (ii) push 2 - slab-slab corner and (iii) push 3 - beam-slab corner; these location are identified in Figure 3.2 as "Push 1", "Push 2" and "Push 3". It is noted that since no additional boundary constraints were provided along the two slab edges of the specimen that would be present in a multi-panel system, “Push 2” and “Push 3” do not correspond to an actual location in a structure.

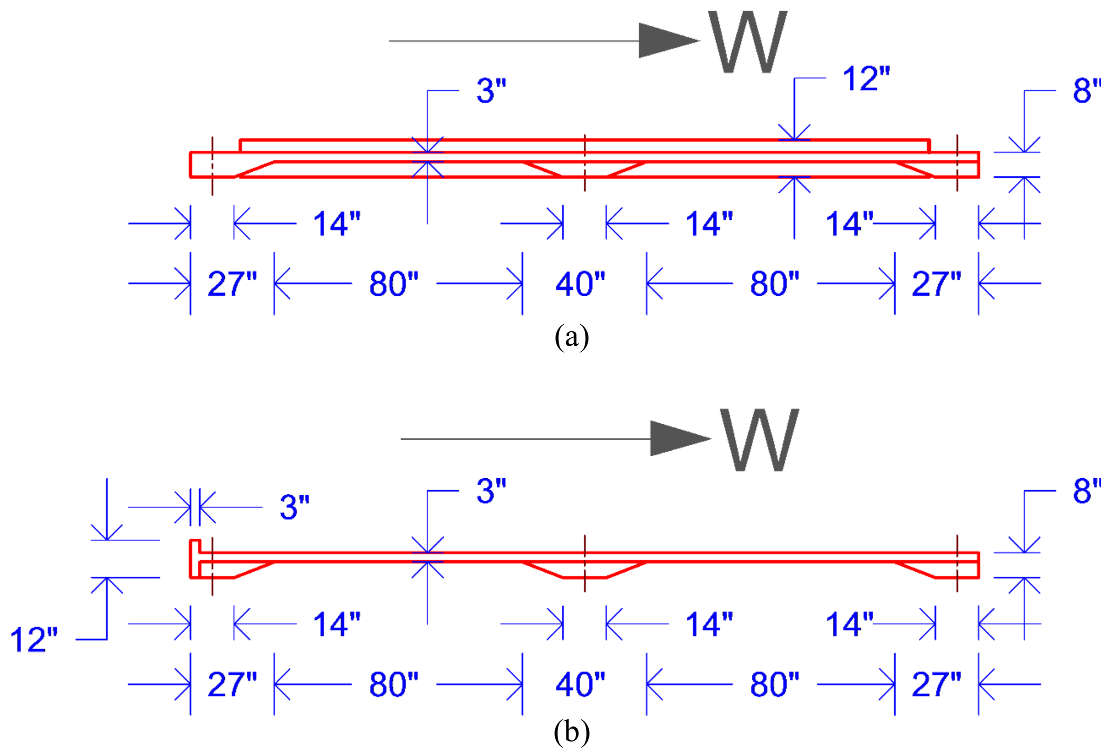

Figure 3.3: Elevation view of the sections from Figure 3.2, (a) section 1-1, and (b) section 2-2.

3.2.1 Reinforcement Details

Reinforcement details were based on drawings of pre-60's building provided by Nabih Youssef and Associates and in consultation with a professional practice committee (2010-2011). As the specimen was a scaled model of the prototype structure, smaller size rebar were used to maintain similar reinforcing ratios as found in the prototypical situation, while satisfying rebar spacing and concrete cover requirements of ACI-318 (1956). Grade-40 #3 (0.375 in. nominal diameter) rebar were used for the slab reinforcement and Grade-60 #4 (0.5 in. nominal diameter) rebar were used to provide longitudinal reinforcement in the spandrel beams. Grade A36 #2 smooth rebar were used to provide shear stirrups in the spandrel beams. Schematics of the reinforcement in the specimen are shown in Figures 3.4 through 3.8. Other reinforcing details including, minimum spacing; embedment length; concrete cover, were selected based on ACI-318 (1956).

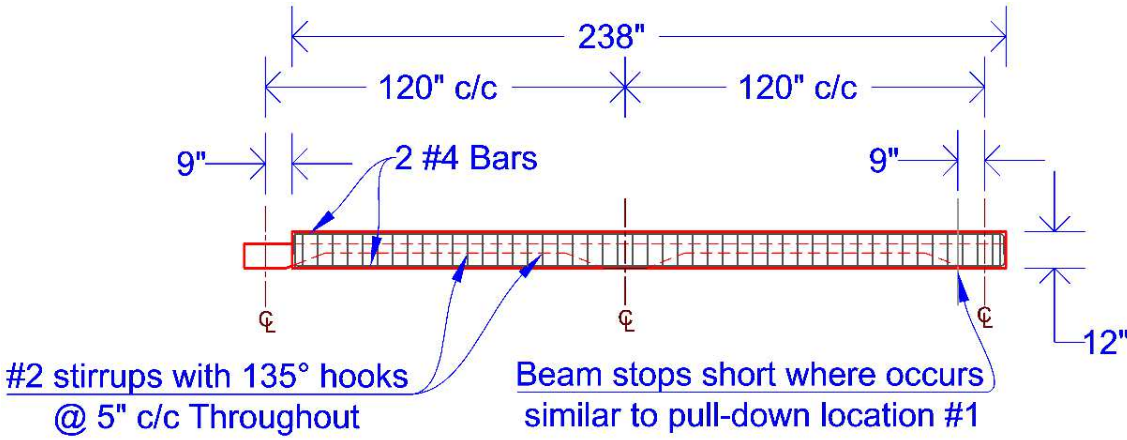

(a)

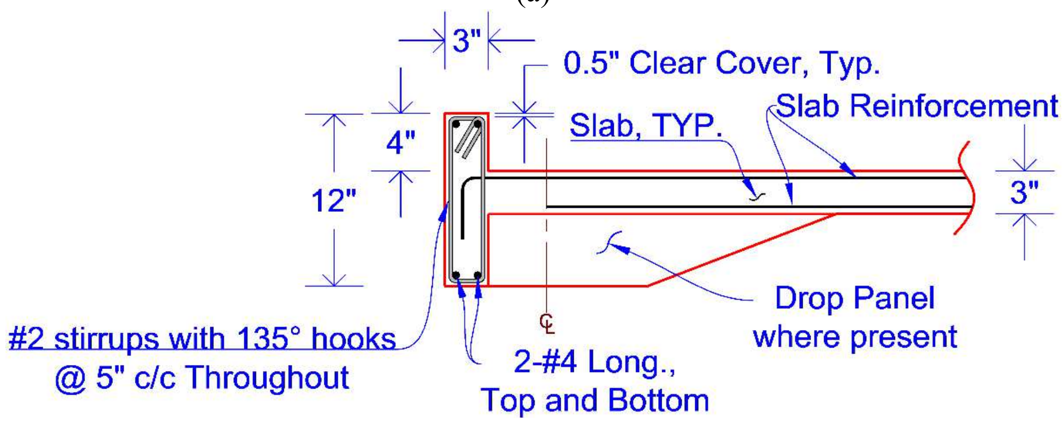

(b)

Figure 3.4: Beam reinforcement, (a) elevation view, (b) cross section view.

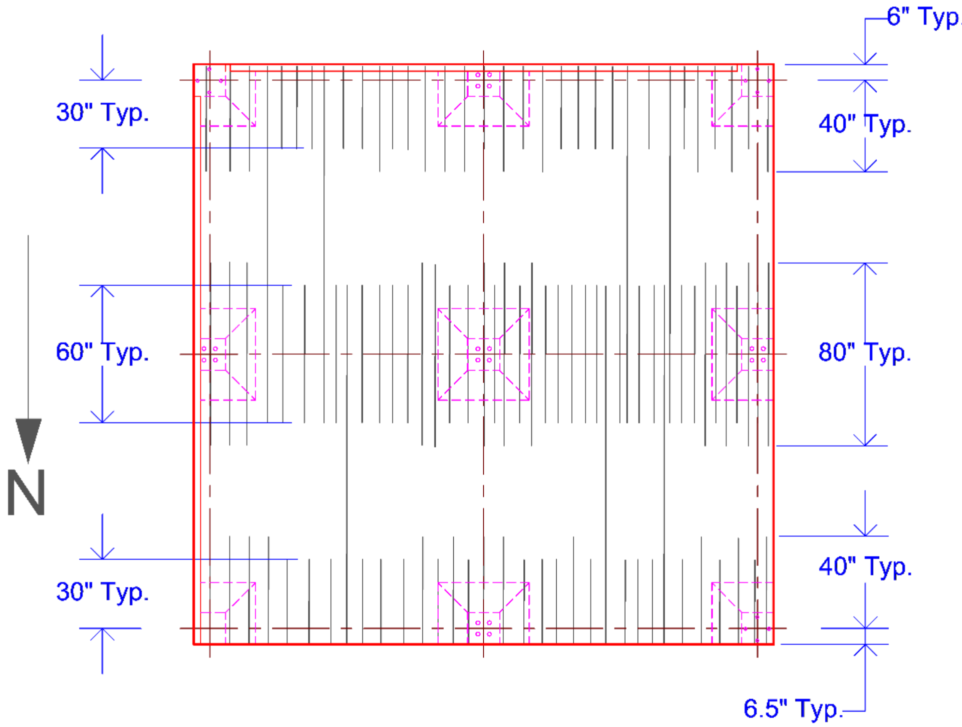

Figure 3.5: Top slab reinforcement in N-S direction using Grade 40 - #3 bars.

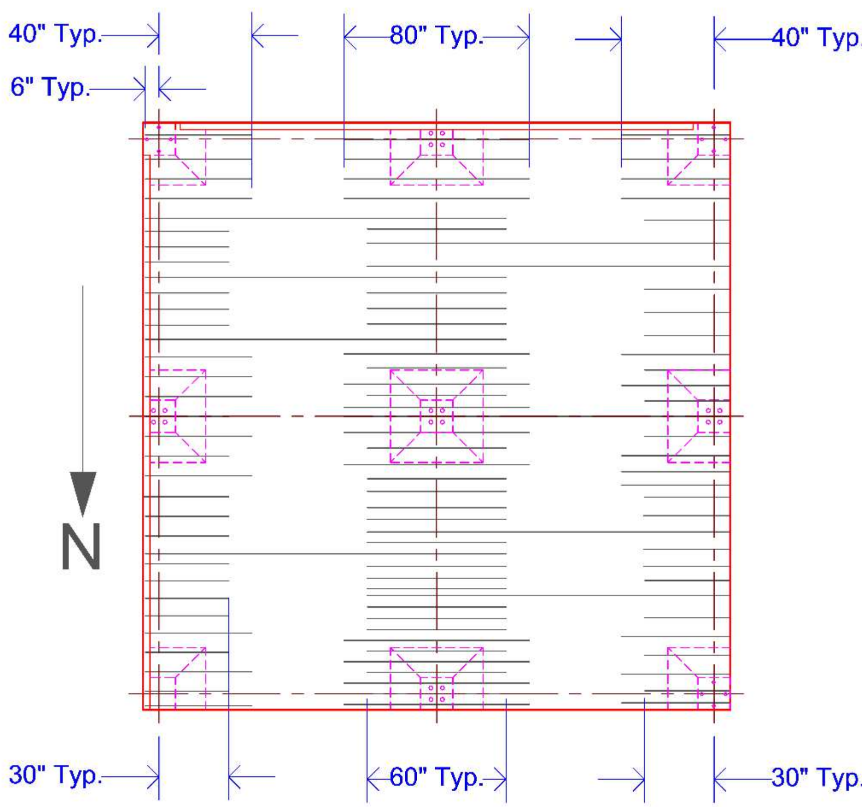

Figure 3.6: Slab top reinforcement in E-W direction using Grade 40 - #3 bars.

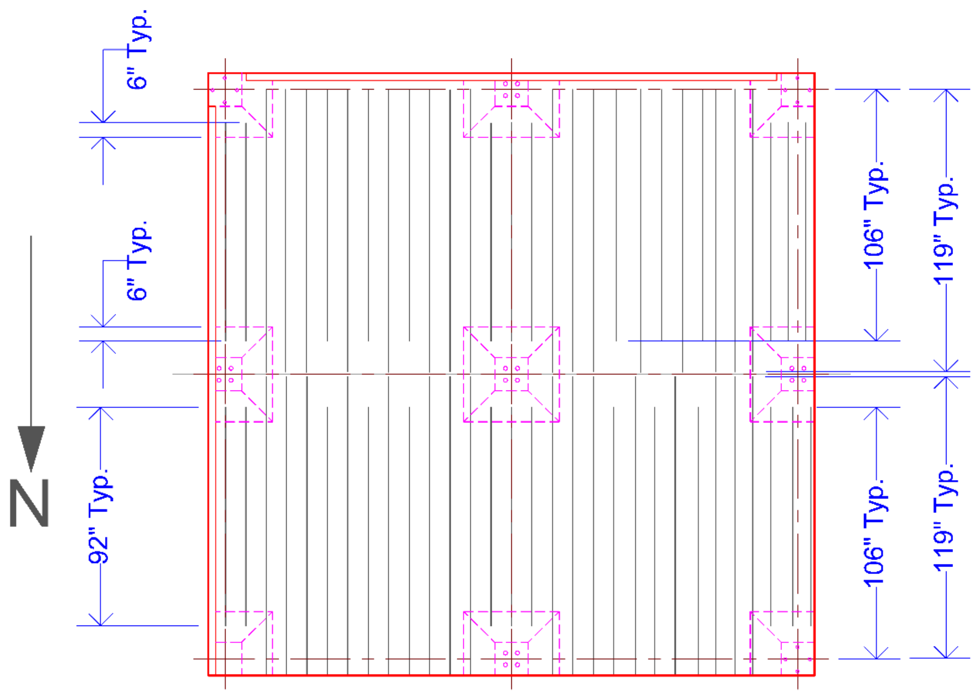

Figure 3.7: Slab bottom reinforcement in N-S direction using Grade 40 - #3 bars.

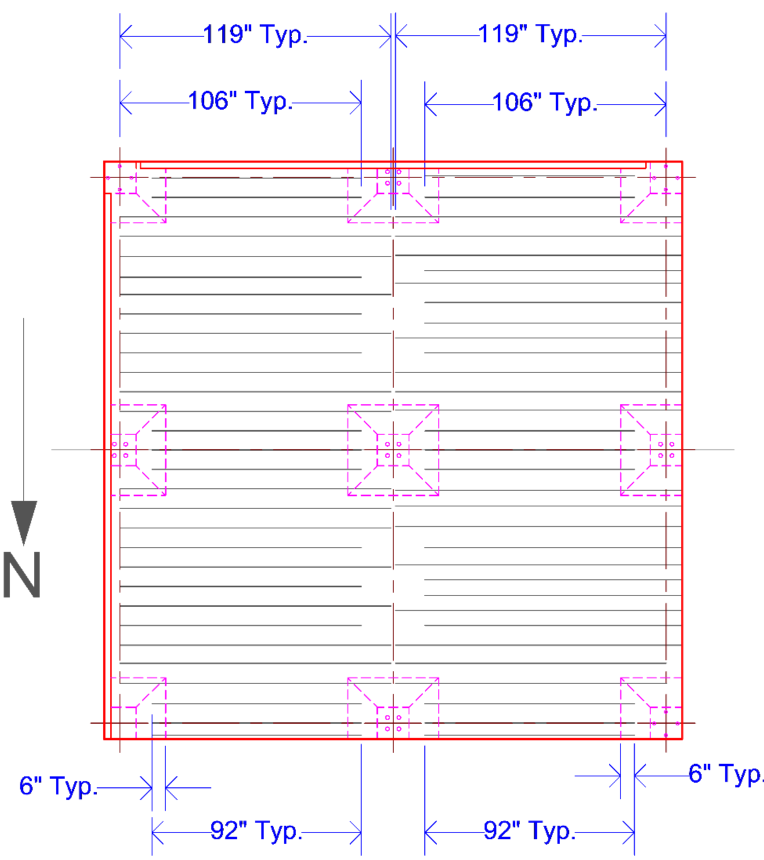

Figure 3.8: Slab bottom reinforcement in E-W direction using Grade 40 - #3 bars.

ACI -318 (1956) does not provide any special reinforcement in the drop panel zone except for the continuous vertical column rebar, which in this case does not exist as the columns were not constructed and the specimen was supported on load cells. Therefore, a cage of #3 rebar was provided to prevent local drop panel failure during the push tests. Figure 3.9 shows a schematic of the extra rebar cage provided at the drop panel locations. At the three push locations, extra bond is provided between the slab and the drop panels using two or three #3 deformed bars running 15” into the slab from the edge of the drop panels to avoid failure at support locations.

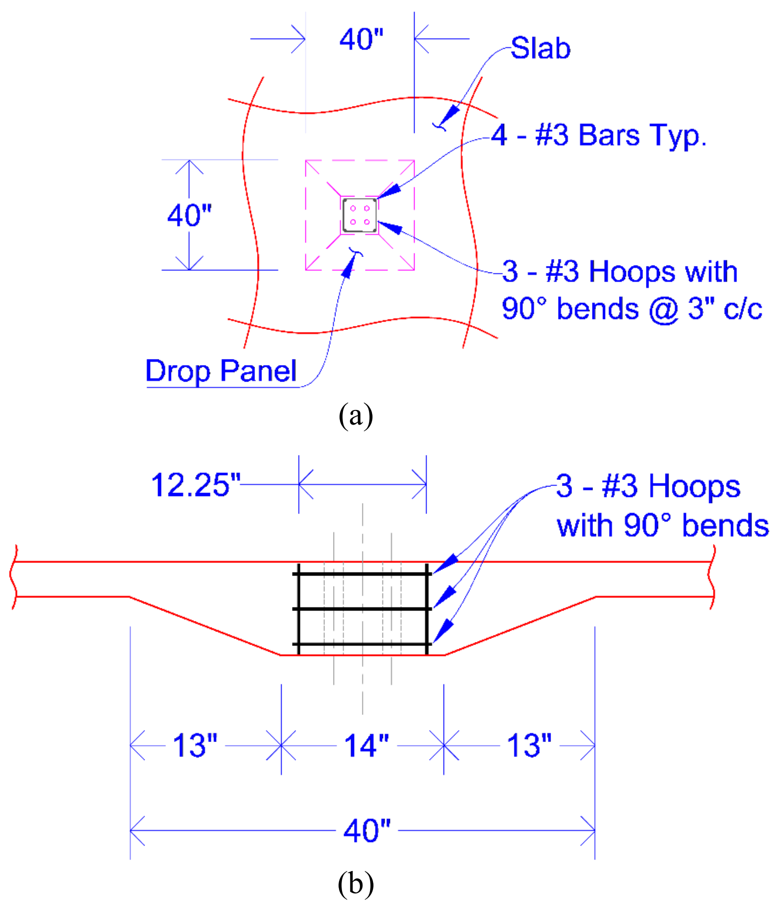

Figure 3.9: Drop panel reinforcement at support locations, (a) plan view, (b) profile view.

3.2.2 Material Properties

Materials used for construction of the specimen were tested in the Powell Laboratories at UCSD. The results from concrete and steel material tests are summarized in the following sections.

3.2.2.1 Concrete Material Properties

The final specimen was cast in place with a single concrete pour of Type II cement with 28 concrete compressive strength of 4.4 ksi. This particular concrete mix design was selected from the available mix provided by the supplier because of several characteristics. This particular mix design had the maximum aggregate size of 3/8 in., which is important due to the small cover provided in the slab and beam due to 1/3rd scale of the specimen. The water content ratio of 0.4-0.6 also assured the mix was workable and readily placed during construction. Unconfined uni-axial compression tests were performed on 6 in.×12 in. concrete cylinders to monitor the concrete strength gain and its strength on the actual day of test. Table 3.1 provides a summary of the concrete strength as obtained from uni-axial compression tests. On the day of the testing, the strength was higher at 6.3 to 6.6 ksi. It is noted that such a strength gain may be realistic over several decades (ACI-209, 1982) and may also be attributed to higher mean strength than specified at the time of construction (ACI-214, 1977).

Table 3.1: Concrete unconfined compression test results

Days from Pour	No. of Specimens	Average Strength	Target Strength
28 Days	3	4400 psi	4000 psi
Push 1 (203 Days)	3	6300 psi	N/A
Push 2 and 3 (223 Days)	2	6600 psi	N/A

3.2.2.2 Steel Material Properties

Grade 40 and Grade 60 rebar were used to provide longitudinal reinforcement in the slab and spandrel beams, respectively. Rebar tension tests were performed on three sample of each type. Figure 3.10 (a) and (b) presents the stress vs. strain response of these samples.

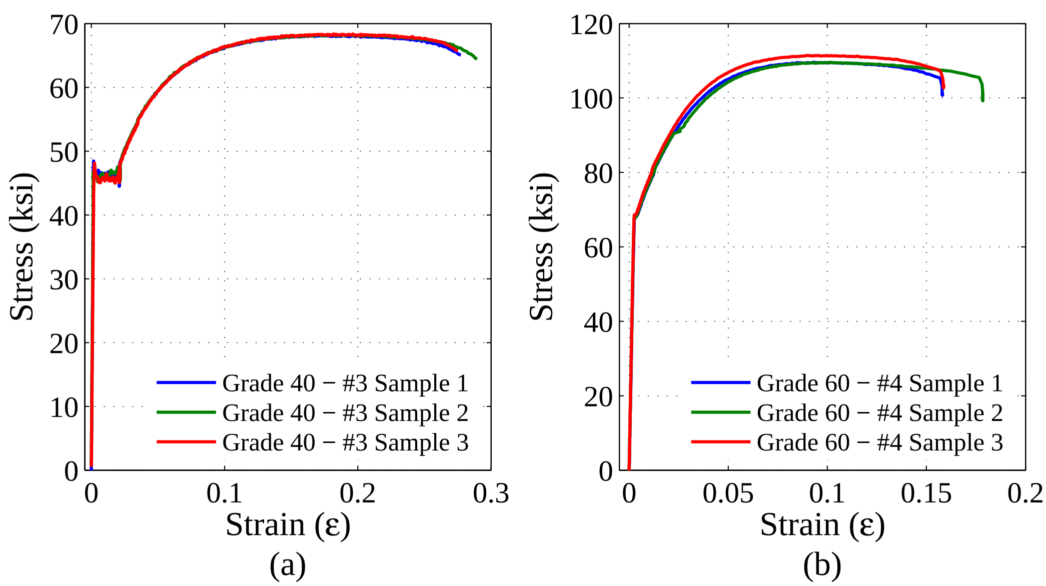

Figure 3.10: Stress-strain response of the reinforcement provided, (a) Grade 40 - #3 slab reinforcement, and (b) Grade 60 - #4 beam longitudinal reinforcement.

Based on the tensile tests, the average engineering yield stress for Grade 40 and Grade 60 steel was found to be 45.9 ksi and 68.9 ksi, respectively, using the 0.2% offset method. A well-defined yield plateau was observed in the Grade 40 rebar, followed by strain hardening and eventual failure at 280000με. The Grade 40 rebar had an ultimate strength of 68.3 ksi at approximately 150000με. Grade 60 steel did not exhibit a well-defined yield plateau, but instead experienced strain hardening immediately after initial yield. Grade 60 rebar achieved its ultimate strength of 110.2 ksi at approximately 100000με. Grade 60 steel also had lower elastic modulus, approximately 26850 ksi, compared to 28200 ksi for Grade 40 steel.

3.2.3 Loading Protocol and Test Setup

3.2.3.1 Loading Protocol

The total uniform gravity load, in additional to its self-weight, applied on the specimen was 90 psf. As the specimen was a scaled model of the prototype structure, this load consisted of 70 psf of simulated scaled mass and 20 psf of reduced live load. The simulated scaled mass was calculated based on the scaling laws which require that $\rho_m = \rho_p \times E_r / L_r$, where ρ_m and ρ_p are the material mass density in model and prototype scale, respectively, E_r is the model to prototype modulus scale factor and L_r is the model to prototype geometric scaling factor. If both the material density and modulus are maintained, i.e $\rho_m = \rho_p$ and $E_r = 1$, extra weight needs to be added to simulate the increase in effective mass density of the structural material. For a one-third scale model, an additional weight of two times the weight of the model structure is required, which for a 3 in. thick slab corresponds to approximately 70 psf. The total gravity load of 90 psf was applied using two layers of concrete blocks, consisting of 38 psf from layer 1 and 52 psf from layer 2.

Three pattern loads were applied on the slab by re-arranging or removing the second layer of concrete blocks as shown in Figure 3.11. The first two pattern loads were arranged to induce maximum moments at fixed support locations by loading alternate panels in each direction as shown in Figure 3.11(a) and (b). Figure 3.11(c) shows another pattern load which was imposed on the specimen simulating possible corridor loading around the center column. The primary objective for applying the pattern loads before the actual simulated column removal test was to induce further cracking in the specimen to mimic the damage that could have occurred in the prototype structure over decades of use.

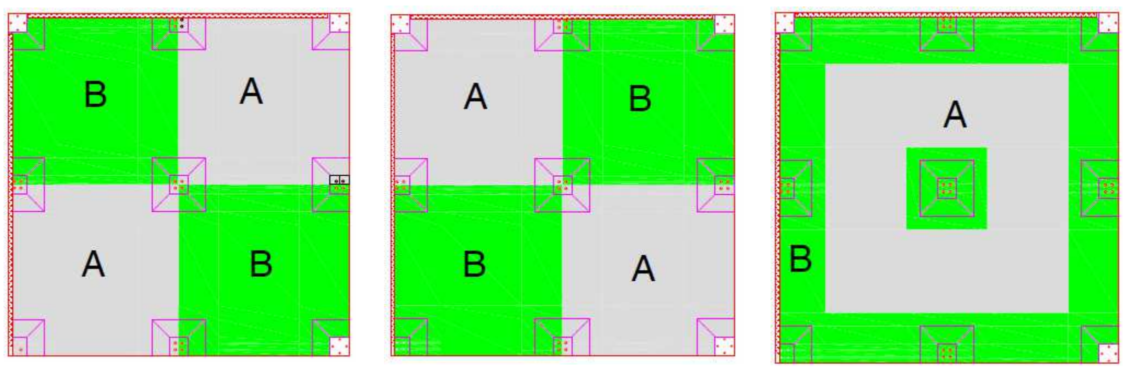

(a) (b) (c)

Figure 3.11: Different loading patterns imposed on the slab; A= 90 psf and B=38 psf.

The specimen was tested under slow push, in displacement control, at the three simulated column failure locations using a 50 kip actuator. Each location was tested one at a time with load cells in place at the other push locations. After removal of the respective test location load cell and attachment of the actuator to the test location, the specimen was pushed to approximately 9 in. vertical displacement. Once the maximum displacement was attained, the actuator was retracted to zero load and detached from the specimen before moving it to the next test location. It is to be noted that once the test was completed at a given location, the respective load cell was unable to be moved back in place due to the large plastic deformation that developed. Therefore at the end of each test, after the actuator was removed, the support at the push location was shored using wooden blocks to prevent any accidental displacements during tests at subsequent push location(s).

3.2.3.1 Test Setup

Figure 3.12 presents a schematic of the test setup including the naming convention for all support locations and the three test locations denoted by Push #1 (beam-beam corner), Push #2 (slab-slab corner) and Push #3 (beam-slab corner). The specimen was supported at nine locations, of which five were multi-axis load cells (LC1 through LC5) at center and center-edge supports, and four 200 kip commercially available axial load cells at the corner supports (LC6 through LC9) seated on concrete pedestals. For push tests at the beam-beam and beam-slab corner (supports LC8 and LC9), the actuator was mounted on steel frames on the strong wall. For the test at the slab-slab corner (support LC6), the actuator was attached to a rectangular steel reaction frame, which was bolted to the strong floor below as shown in Figure 3.12 (b).

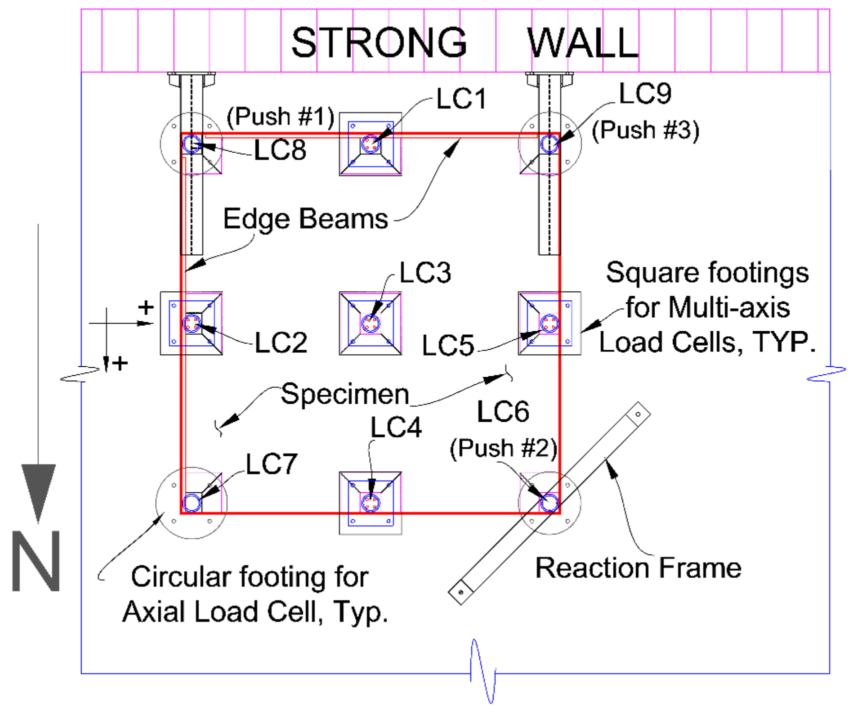

(a)

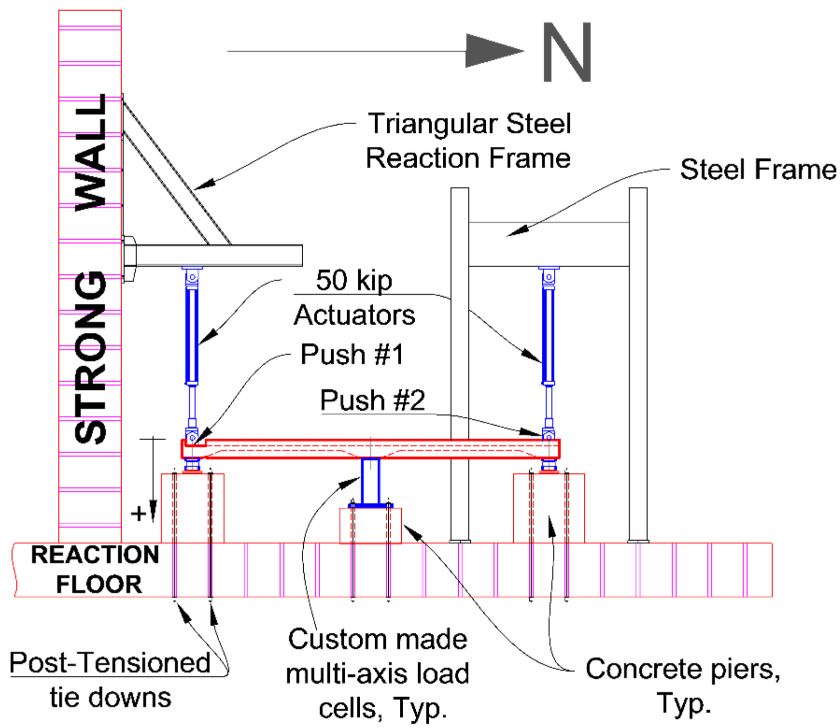

(b)

Figure 3.12: Schematic of the test setup specimen 1: (a) Plan view of the experimental setup, and (b) NS view of the test setup. Note: LC1 through LC5 are multi-axis load cells and LC6 through LC9 are axial only load cells. Direction of positive forces in NS and EW directions are also shown in part (a).

3.3 Specimen 1 - Test Results

Global results from the tests conducted on the first specimen are presented in this section. For the gravity load tests, load distribution, and physical observations are presented. For the push tests at three corner locations, results including global load-deflection curve, load redistribution at supports, deflection profile and observed damage are presented.

3.3.1 Uniform Gravity Load

3.3.1.1 Load Distribution at Support Locations

The following section presents the response of the slab under uniform gravity loads. Figure 3.13 presents the change in force at support locations due to the applied gravity load of 38 psf and 90 psf on the slab surface using concrete blocks. The axial force is shown as positive acting downwards and shear and moment resultants are positive in West and North direction, respectively, as shown in Figure 3.13a.

Figure 3.13(b) and (c) presents the recorded change in axial load at the support location. Center edge supports LC1, LC2, LC4 and LC5 experienced an increase of approximately 3 kips and 7 kips due to 38 psf and 90 psf uniform gravity loads. LC3 experienced greater increase of 4 kips and 10 kips at 38 psf and 90 psf, respectively, due to the larger tributary area supported by the center support. Corner supports LC6 through LC9 experienced the smallest increase, between 0.6 kips and 1.0 kips due to 38 psf and 90 psf uniform loads, respectively. Figure 3.13(d) and (e) show the recorded change in shear at the multi-axis load cell locations. All the center edge supports (i.e.

supports LC1, LC2, LC4 and LC5) experienced outward shear forces perpendicular to the free edge, of approximately 2.5 kips and 5.7 kips at 38 psf and 90 psf uniform load, respectively, while little to no shear force was introduced parallel to the edge at these support locations due to system symmetry. Also due to symmetry of the structure and loading, support LC3 experienced minor increase in resultant shear, in the order of 0.4 to 0.6 kips at 38 psf and 90 psf uniform load, respectively.

Recorded change in moments, shown in Figure 3.13(f) and (g), were also found to be consistent showing unbalanced hogging moments at the edge support locations, with supports LC1 and LC2 experiencing the largest increase of 1.9 kip-ft. and 6.7 kip-ft. at 38 psf and 90 psf uniform load, respectively. Supports LC4 and LC5 experienced a slightly lower change in resultant moments in the order of 1.3 to 5 kip-ft. at 38 psf and 90 psf, respectively. Although, LC1/LC2 and LC4/LC5 were all placed at the center-edge location of the specimen, LC1 and LC2 experienced higher moment demands under uniform gravity loads due to the presence of stiffer spandrel beam along the edge on South and East edge of the specimen.

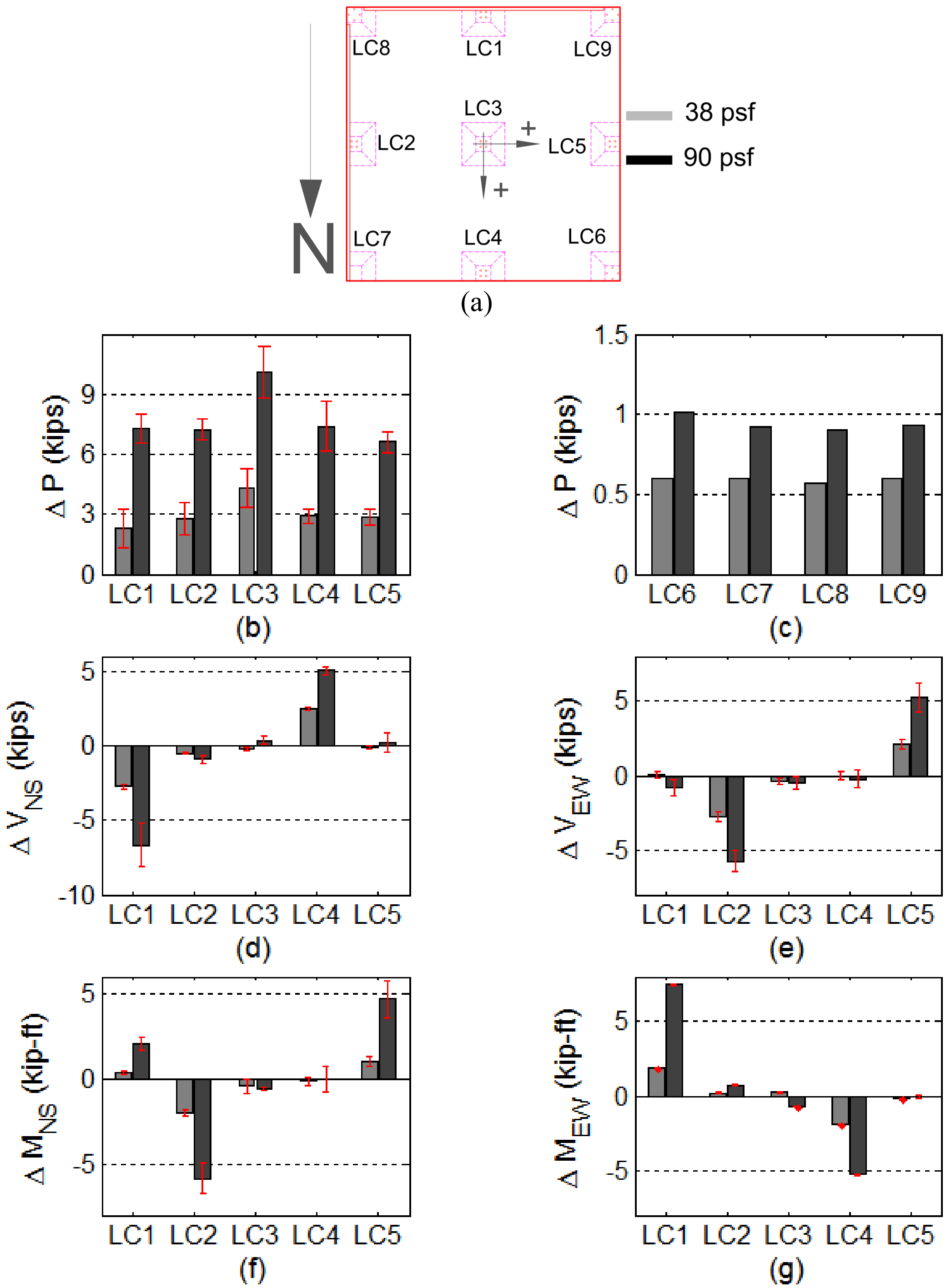

Figure 3.13: Resolved forces at the support locations due to applied uniform gravity loads: (a) location and name of support locations, (b) change in axial load at multi-axis load cell locations, (c) change in axial loads at corner axial only load cells, (d) change in NS shear force, (e) change in EW shear force, (f) change in NS moment, and, (g) change in EW moment. Note: The values presented are average values obtained from the multi-axis load cells. The error bars show the deviation in the resolved values.

3.3.1.2 Physical Observations

Digital photographs were taken to monitor the crack formation in the slab after each load case. Using the photographs taken at the end of gravity load application, a schematic of the observed cracks on the specimen is presented in Figure 3.14.

Under uniform gravity loads, the maximum positive and negative moments are expected to occur near mid-span of each panel and support locations, respectively. At the end of 38 psf uniform load on the specimen only minor cracking was observed on top and bottom surface of the specimen due to the presence of thickened drop panel at each support locations. Nonetheless, some flexure cracks were observed on the spandrel beams at the center-edge support locations, LC1 and LC2, as shown in Figure 3.15.

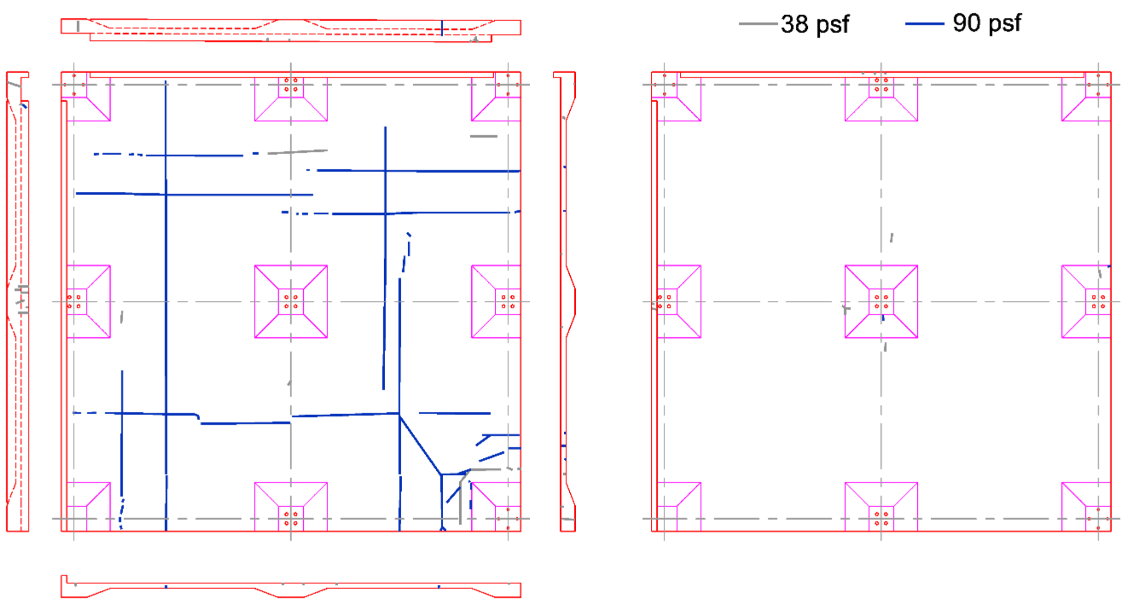

(a) (b)

Figure 3.14: Schematic of cracking on specimen 1 after uniform gravity load application, (a) bottom and sides of the specimen, (b) top of the specimen. Black - cracks after 38 psf and blue- cracks after 90 psf.

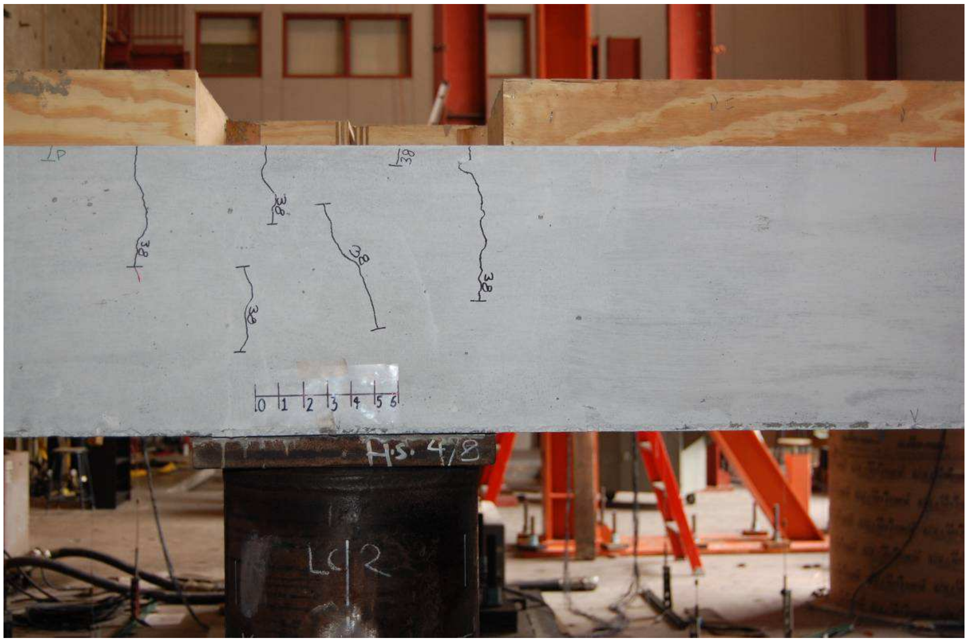

Figure 3.15: Negative moment cracks at support LC2 at 38 psf uniform load.

When the load was increased to 90 psf, increased cracking was observed on the bottom surface of the specimen due to the increased moment demand along the panel mid-span. As expected, these cracks on the bottom surface formed near the mid-span of each panel, in both EW and NS direction, as shown in Figure 3.14 (a). Some additional cracking was observed around support LC6 due to the absence of stiff spandrel beam on either edge at this support location. No significant cracks were observed on the top surface even with 90 psf uniform load on the top of the specimen.

3.3.2 Pattern Loads

Following the uniform gravity load tests, three pattern loads were applied on the specimen. The first two pattern loads applied had 38 psf uniform load on two alternate panels and 90 psf on the rest of the specimen. The third pattern load on the specimen was a possible corridor loading around the center column. It is noted that due to an error in data acquisition the data (load cells, displacements etc.) for pattern load 2 and pattern load 3 were not recorded. Therefore, this section presents the load distribution and deflection profiles for pattern load case 1, and the observed damage at the end of all of the pattern load cases.

3.3.2.1 Load Distribution at Supports

Figure 3.16 present the change in loads at support locations due to application of pattern load 1 on the specimen. The values presented in Figure 3.16 are the changes observed between the previous load case of 90 psf uniform load. As the pattern load was applied by removing 52 psf load from two of the panels, all load cells experienced small decrease in the axial load as shown in Figure 3.16(b) and (c). Center-edge supports, LC1, LC2, LC4 and LC5, experienced a decrease of 1.3 kips while center support LC3 experienced the greatest decrease of approximately 2.2 kips. Axial load cells installed at the corner of the specimen also recorded small decrease in axial load due to the removed loads. Supports LC7 and LC9 did not experience a significant decrease in the axial load compared to the other support locations as the applied pattern load did not remove any load from the panels at these supports. These changes in axial loads at all the support locations are in good agreement with the simplified tributary area method, which suggests a change in axial load of 1.3 and 2.6 kips at center-edge and center support locations.

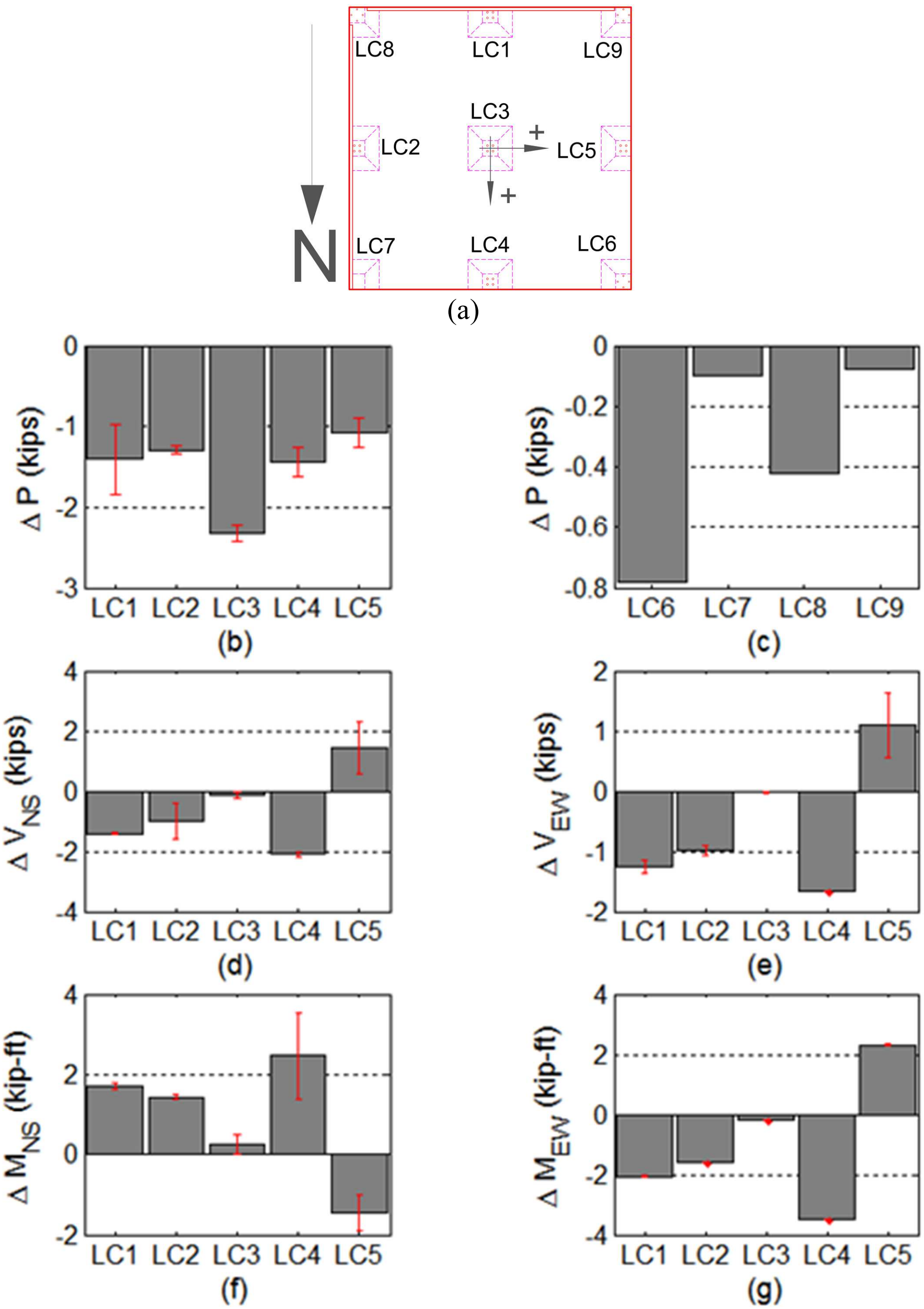

Figure 3.16: Resolved forces at the support locations due to pattern load case 1: (a) location and name of support locations, (b) change in axial load at multi-axis load cell locations, (c) change in axial loads at corner axial only load cells, (d) change in NS shear force, (e) change in EW shear force, (f) change in NS moment, and, (g) change in EW moment. Note: The values reported are the changes observed since the application of previous load case, i.e. uniform load of 90 psf.

Figure 3.16(d) and (e) show the change in shear loads at multi-axis load cell locations. All the supports experienced a change in resultant shear force in the order of 2 kips with maximum change recorded at supports LC4 and LC5. Small changes in moments were also observed at the multi-axis supports as shown in Figure 3.16(f) and (g). Among all multi-axis load cells, LC4 and LC5 experienced the largest change in resultant moments in the order of 3.5 kip-ft., while LC1 and LC2 experienced a change of 2.5 kip-ft. in resultant moment.

3.3.2.2 Physical Observations

Figure 3.17 presents a schematic of the cracks observed on the specimen at the end of all gravity tests. Before the application of pattern loads, some shrinkage cracks were observed in the slab.

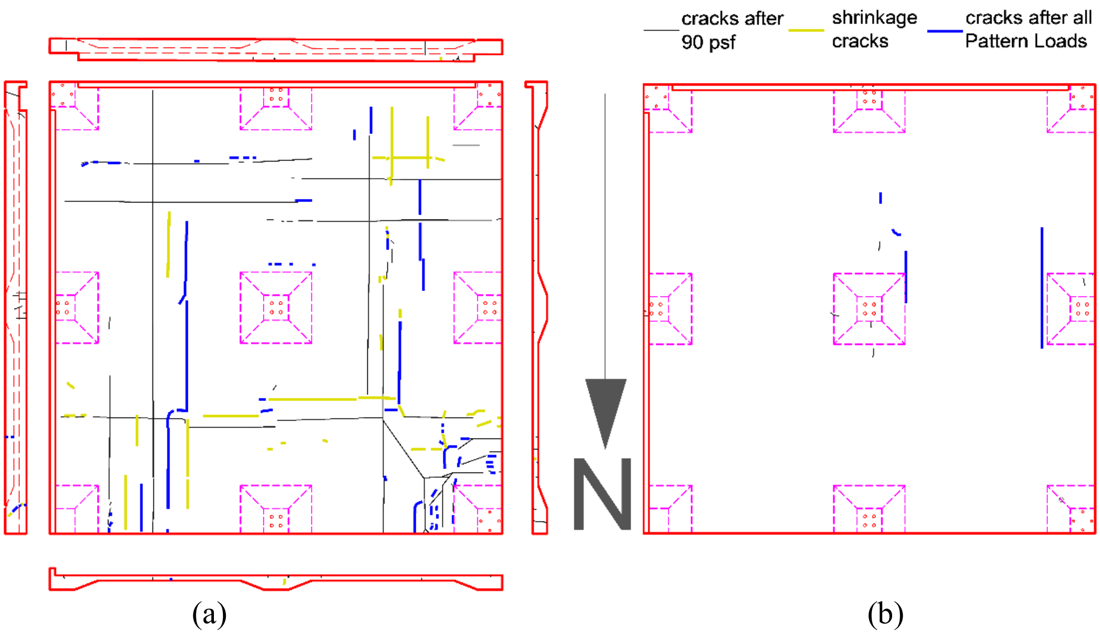

Figure 3.17: Observed cracks on the specimen at the end of pattern load tests, (a) bottom surface, and (b) top surface of specimen.

Few cracks were also observed around support LC6 due to the reduced section stiffness at this support location. At the end of the pattern load tests additional cracks were observed on the bottom surface of the specimen. Most of these cracks occurred close to the mid-span between column supports as expected. The specimen corner with no beam (support LC6) showed further crack formations after the application of the pattern loads. The least number of new cracks occurred in the beam-beam panel as the beam was able to take most of the load without cracking. On the top surface, only a few minor cracks were observed, developing near the support LC3 and LC5 due to higher negative moment demands at the supports during pattern load application.

By end of the gravity load tests on the specimen, most of the observed cracking on the bottom surface was localized near the mid-span of each panel. Orthogonal cracks formed in each panel from one end to other. These cracks were more localized in the slab-slab edge, due to the reduced stiffness as compared to the other three panels where the spandrel beam provided additional stiffness to the cross-section. Only a few cracks were observed on the top surface, mostly localized near the end of the drop panel near supports LC3 and LC5, with no cracks observed on the top surface elsewhere on the specimen. Few cracks were also observed along the edge of the specimen, with most of these cracks localized near the fixed supports, due to the negative moment demands at the center-edge support locations.

3.3.3 Column Removal Scenario

Following the end of the gravity load tests, the specimen was subjected to column removal tests at three corner locations as discussed. The load cell was removed at these test location(s) and the specimen corner was pushed down using a 50 kip actuator under displacement control. At the end of each push, the load was reduced to zero before the next location was tested. In the following section, downward external load from the actuator and slab displacement are considered positive.

3.3.3.1 Load-Deflection Relation

Figure 3.18 presents the vertical load versus the corner displacement at the three test locations. It is noted that the initial negative load at zero displacement (denoted by SW) is the initial reaction at the push location due to the specimen self-weight and applied gravity load (90 psf).

During the test at the beam-beam corner location, the specimen started to deform with an initial tangent stiffness of 9.6 kips/in until a deflection of approximately 1.5 in. was achieved. Beyond this, the stiffness decreased to 2 kips/in. due to cracks on the top surface of the edge beams near the fixed supports LC1 and LC2. When pushed further, the system continued to deform until a peak load of 9.3 kips was attained at 4.5 in. vertical displacement. Beyond this the system deformed plastically with no significant change in load capacity until a deflection of 6 in. At this point, the actuator inadvertently retracted to zero displacement due to an error in actuator control resulting in an upward force of 6.6 kips being applied on the specimen at zero vertical deflection at the beam-beam corner location. Nonetheless, the specimen was able to attain the maximum load of 9.1 kips at 7.2 in. displacement during the second cycle. A small strength degradation was observed during the second cycle when pushed beyond 7.4 inches, with the final load of 8.3 kips at maximum displacement of 9.5 in. Loading was terminated at this point as further displacement was hindered by the presence of the footing under the test location. When returned to zero load, the beam-beam corner exhibited unloading stiffness of approximately 2.8 kips/in (~33% of the initial stiffness) and retained a permanent deformation of 7 in.

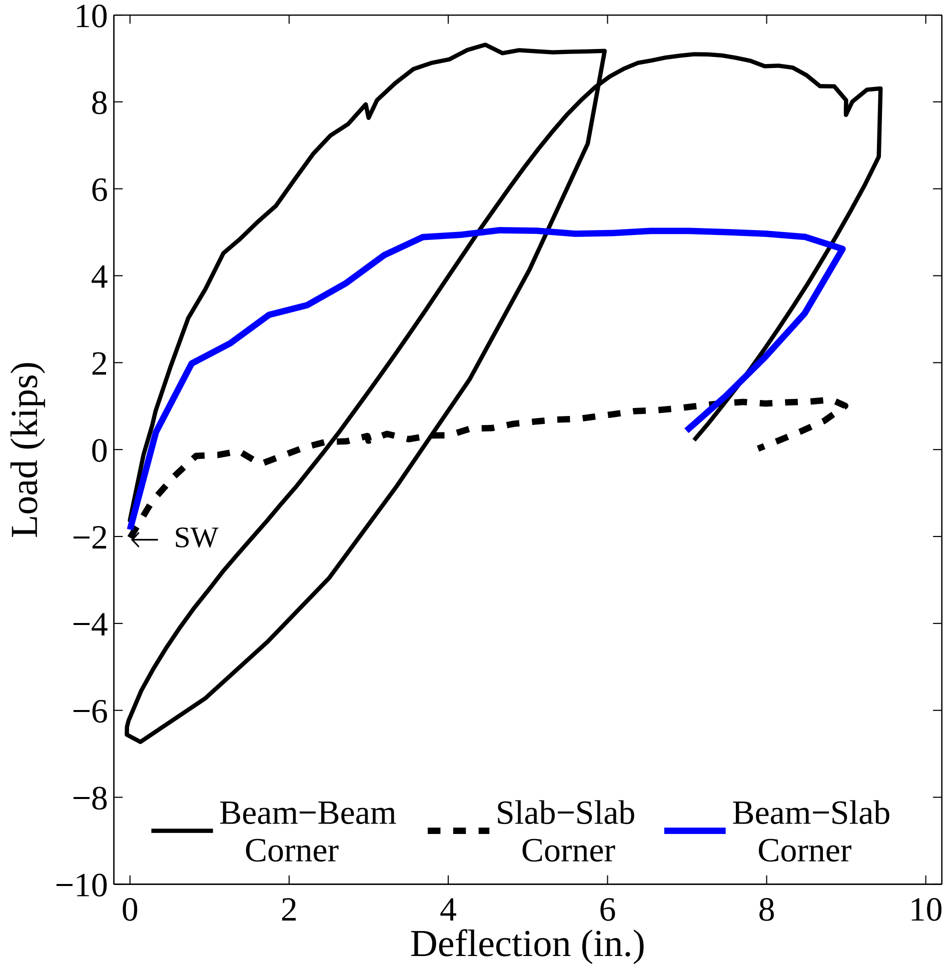

Figure 3.18: Load vs. displacement relation during the test at three corner locations on specimen 1 (SW = self-weight).

During the test at the slab-slab corner, the specimen began to deform with an initial tangent stiffness of 3.6 kips/in. As the deformation increased, the system softened, with the specimen deformation of 1 in. at zero load (i.e. no external load applied by the actuator). Beyond this, the specimen continued to deform with the stiffness of 0.14 kips/in. until it reached the maximum deformation of 9.0 in, with actuator load of 1.2 kips. At this point the specimen was unloaded as it was deemed unsafe due to formation of a through crack near support LC5. When returned to zero load, the specimen exhibited an unloading stiffness of approximately 1.1 kips/in., approximately 35% of the initial stiffness, and retained a permanent deformation of 7.9 in.

During the test at the beam-slab corner (spandrel beam on one edge only), the specimen began to deform with an initial stiffness of 6.5 kips/in until a displacement of 0.6 in. was achieved at the push location. Beyond this, the stiffness dropped to 1 kips/in. due to cracking of the spandrel beam along the EW direction. When pushed further, the specimen continued to deform until a peak load of 5.1 kips was attained at 4.6 inch vertical displacement. Beyond this point the specimen deformed plastically, with no significant change in vertical load capacity, and achieved a final load capacity of 4.84 kips at 8.75 in. vertical displacement at the corner push location. Loading was terminated at this point as further displacement was hindered by the presence of the footing under the test location. When returned to zero load, the specimen exhibited an unloading stiffness of approximately 1.85 kips/in, approximately 34% of the initial stiffness, and retained a permanent deformation of 6.7 in.

Compared to the Yield Line Theory estimates, the system was able to attain significantly higher load capacity at all the three corner push locations. Table 3.2 presents the YLT estimates for each test and the enhancement observed, when compared with the achieved capacities during each test. It is noted that the location of the yield lines were assumed to coincide with the observed damage at the end of each test as shown in Appendix B. The ultimate capacity of the slab and beam section along the yield lines were calculated based on the actual rebar layout and the material properties as used for the construction of the specimen. For the two tests performed at locations where the spandrel beam was present on at least one edge, the average load enhancement was about 1.7, while the slab-slab corner experienced a load enhancement of 2.4. Although the enhancement at the slab-slab corner might suggest presence of large in-plane membrane forces resulting in significant load enhancement, however, it has to be noted that the actual difference between the YLT estimate and the achieved load was only 700 lbf or 0.7 kips.

Table 3.2: Comparison between experimental and YLT load capacities for the tests performed at three corner support locations on specimen 1.

	P_{YLT}	$P_{EXPERIMENT}$	$P_{EXPERIMENT}/P_{YLT}$
Beam-Beam Corner, kips	5.4	9.3	1.7
Slab-Slab Corner, kips	0.5	1.2	2.4
Beam-Slab Corner, kips	2.9	5.1	1.8

3.3.3.2 Load Redistribution

Figures 3.19 through 3.22 shows the change in loads at different support locations during the tests performed at the three corner support locations. It is noted that the results are presented at the maximum achieved loads during each push test.

Figure 3.19(a) shows a schematic of the specimen with the locations of the load cells, and the push location. It is noted that NS force resultants are positive in the North direction, while the EW force resultants are positive in the West direction. Figure 3.19(b) and (c) show the calculated change in axial loads at each support location during the test at the beam-beam corner location. At maximum load condition, supports LC1 and LC2 experienced an increase of 9.5 kips and 8.7 kips in axial compression, respectively, while support LC3 experienced a decrease in axial load of about 1.8 kips in compression. Other supports (LC4 through LC9), away from the push location, experienced small change in additional axial force demand due to the applied load at the push location. More uplift was observed at supports LC7 and LC9, in the order of 1.6 kips, due to the presence of spandrel beam along the East and South edge of the specimen. The total increase in axial loads at the support locations (13.6$\pm$2.5 kips) shows a good agreement with the total change in load as recorded by the actuator (11.0 kips).

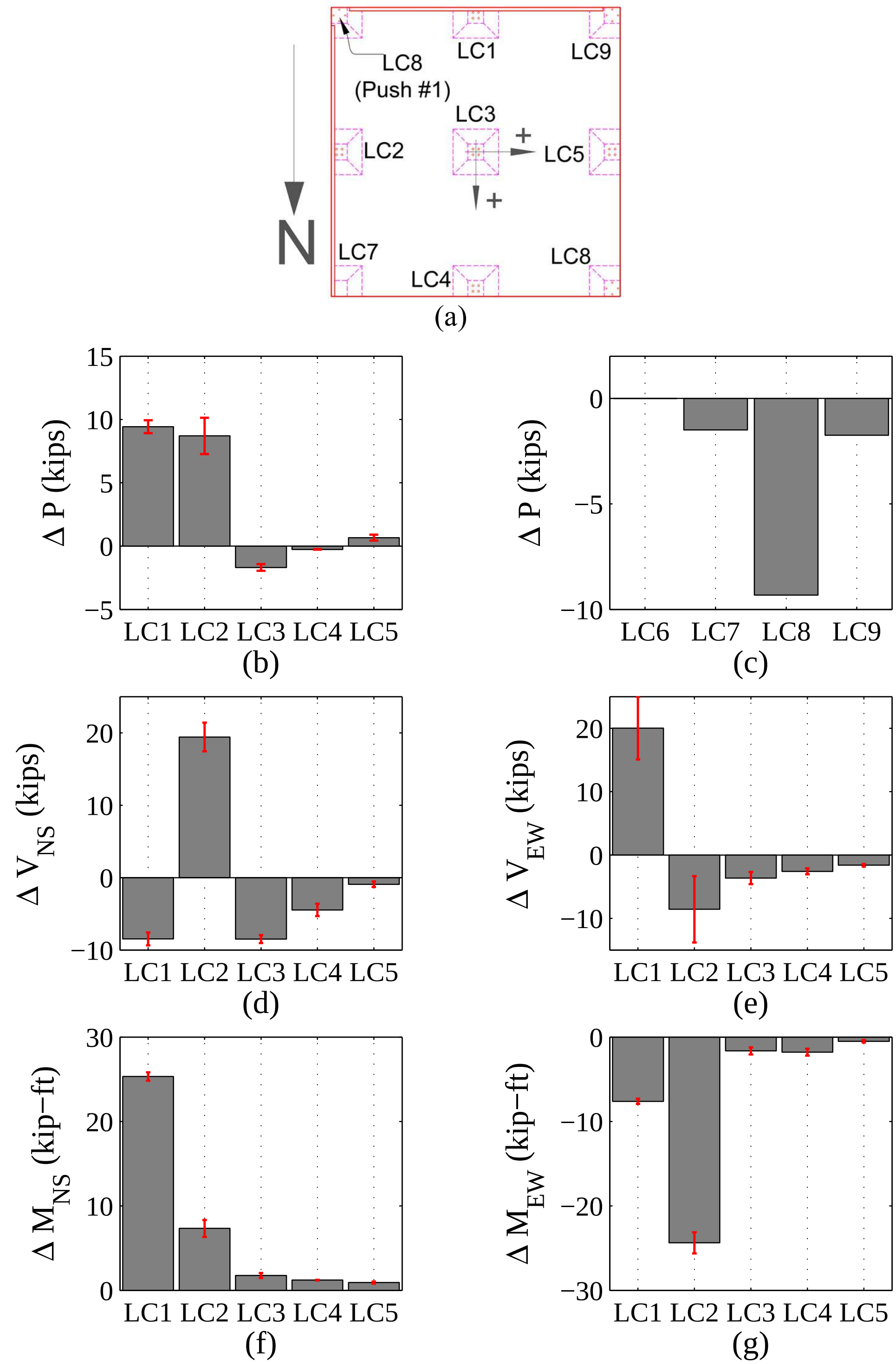

Figure 3.19: Load distribution at supports at maximum load during test at beam-beam corner on specimen 1: (a) location and name of support locations, (b) change in axial load at multi-axis load cell locations, (c) change in axial loads at corner axial only load cells, (d) change in NS shear force (e) change in EW moment, (f) change in NS moment, and, (g) change in EW shear force.

A similar distribution of change in shear loads at multi-axis support locations in the NS and EW directions are presented in Figure 3.19(d) and (e), respectively. Supports LC1 and LC2, closest to the test location experienced an increase of 21.5 kips in resultant shear each, with most of the induced shear along the respective spandrel beam longitudinal direction. The direction of the shear forces at support LC1 and LC2 suggest the presence of in-plane forces, resulting in an outward shear force, pushing the supports away from the test location. Shear induced at other support locations was small compared to LC1 and LC2, with resultant shear of approximately 9 kips at LC3, 1.5 kips at LC4 and 4.5 kips at LC5.

A similar distribution was observed in the additional moments induced at the supports as shown in Figure 3.19(f) and (g). Supports LC1 and LC2 experienced an overall increase of 26.7 kip-ft. of resultant moment at maximum load condition. At both locations the larger moment, approximately 25 kip-ft., was induced along the spandrel beam transverse axis. At maximum load of the other supports, LC3 through LC5, experienced a very small increase in resultant moment, on the order of 2 to 2.5 kips-ft.

Figure 3.20 presents the change in load distribution at maximum load during the test at the slab-slab corner location. Observations made during this test were similar to the previous test at beam-beam corner, with most of the loads transferred to the adjacent supports LC4 and LC5. At maximum load during the test at slab-slab corner, an increase in axial load of 2.6 kips and 2.5 kips was recorded at supports LC4 and LC5, respectively. Compared to the additional axial load at LC4 and LC5, only small changes in axial loads were observed at other support locations, with supports LC3 experiencing a small uplift force of approximately 0.5 kips as shown in Figure 3.20(b) and (c).

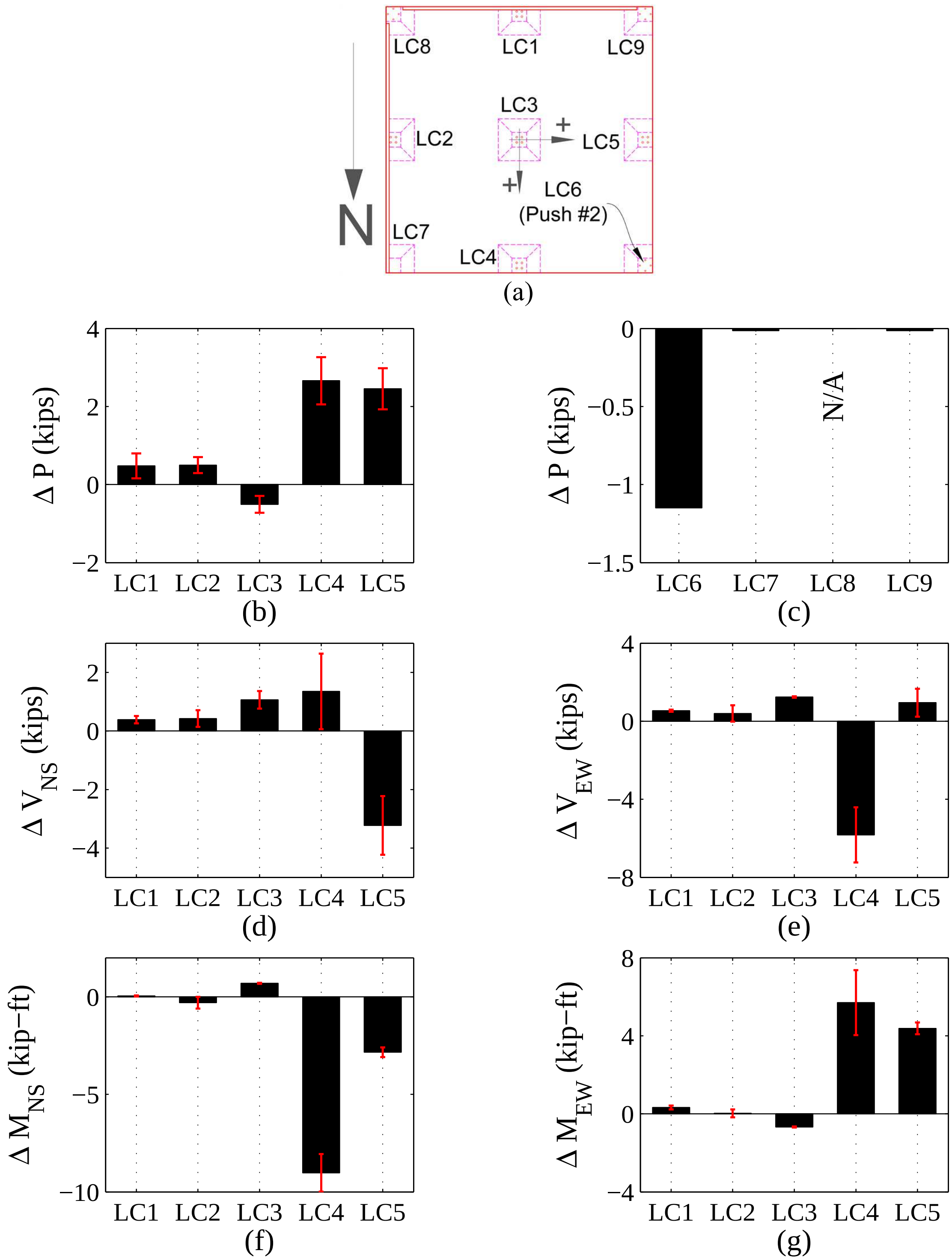

Figure 3.20: Load distribution at supports at maximum load during test at slab-slab corner of specimen 1: (a) location and name of support locations, (b) change in axial loads at corner axial only load cells, (c) change in EW shear force, (d) change in NS shear force, (e) change in axial load at multi-axis load cell locations, (f) change in NS moment, and, (g) change in EW moment.

At maximum load, adjacent supports also experienced the maximum change in resultant shear, an increase of 6.0 kips and 3.4 kips at LC4 and LC5, respectively, followed by LC3 which experienced an increase of 1.6 kips of resultant shear. Due to their remoteness from the test location, LC1 and LC2 only experienced an increase of 0.6-0.7 kips in resultant shear as shown in Figure 3.20(d) and (e).

The push also caused an additional resultant moment of 10.7 kip-ft. and 5.2 kip-ft. at LC4 and LC5, respectively as shown in Figure 3.20(f) and (g). This disproportionate distribution in shear and moments between LC4 and LC5 is likely due to the through crack that formed near support LC5 during the test (Figure 3.21) , resulting in lower shear and moment demands at support LC5 with that to support LC4. Due to the their remoteness from the test location and failure surface LC1 through LC3 only experienced comparatively small moment increase, between 0.3 to 1.0 kip-ft., at maximum load condition.

Figure 3.21: Localized failure near LC5 during test at slab-slab corner of specimen 1.

Figure 3.22 present the change in forces on the load cells at maximum load during test at the beam-slab corner. Axial force distribution at maximum load are shown in Figure 3.22(b) and (c). Supports LC1 and LC5 experienced the largest increase in axial compression of 6 kips and 2.8 kips, respectively. Other supports, especially LC2 and LC3 experienced uplift of approximately 1 and 2.2 kips, respectively, at maximum load condition. Uplift at LC2 was caused due to presence of stiff section (spandrel beam) connecting LC9-LC1-LC8-LC2, while the uplift at LC3 was caused due to the hogging moment generated along the yield line connecting LC1 and LC5. The total increase in axial loads at the support locations (5.9 $\pm$ 2.3 kips) shows acceptable agreement with the total change in vertical load as recorded by the actuator (7.0 kips) at maximum load.

A similar load distribution for the recorded shear loads at support locations are presented in Figure 3.22(d) and (e). Compared to support LC5, LC1 experienced a larger change in transferred loads due to the presence of stiffer spandrel beam along LC1 and LC9 at maximum load. At this instance, LC1 experienced a resultant shear force increase of 18 kips while LC5 experienced an increase of 12 kips in resultant shear. At both these supports, the majority of the induced shear was directed along the edge connecting the failure location with the column. Compared to the increase in loads at LC1 and LC5, other supports only experienced small increase in resultant shear with supports LC3 and LC2 experiencing and increase of 5 and 6 kips, respectively, at maximum load condition. Support LC2 also experienced an increase in shear due to the presence of stiff spandrel beam along the NS and EW direction resulting in more forces to be transferred to the support LC2.

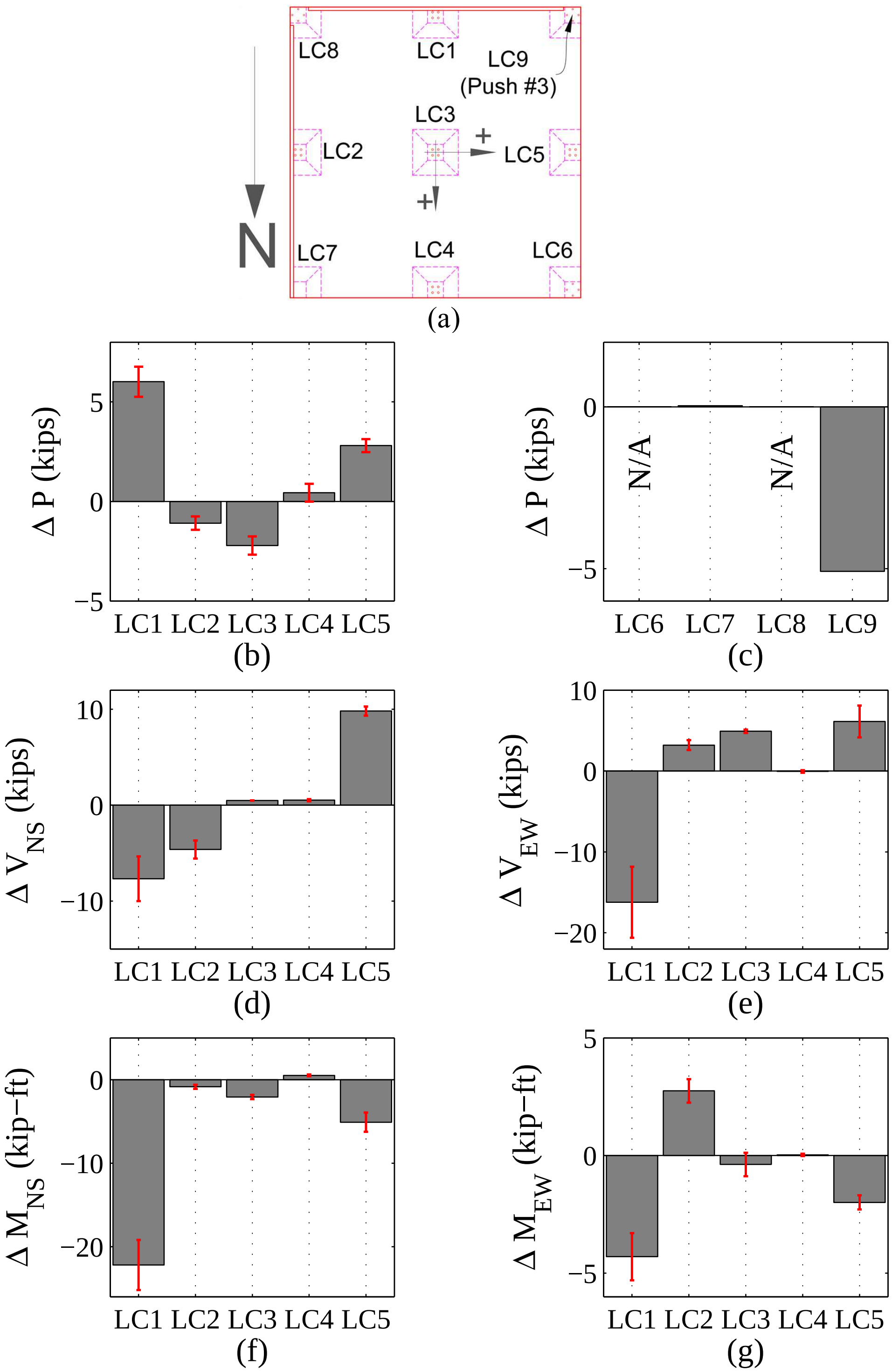

Figure 3.22: Load distribution at supports at maximum load during test at beam-slab corner.: (a) location and name of support locations, (b) change in axial loads at corner axial only load cells, (c) change in EW shear force, (d) change in NS shear force, (e) change in axial load at multi-axis load cell locations, (f) change in NS moment, and, (g) change in EW moment.

A similar profile was observed for the additional moment transferred to the supports at maximum load condition. Support LC1 experienced an increase of 22.6 kip-ft. in resultant moment followed by LC5 which showed an increase of approximately 5.5 kip-ft as shown in Figure 3.22 (f) and (g). Compared with the previous two tests where both the adjacent supports experienced similar increase in moments, during the test at beam-slab corner, one of the adjacent support experienced a larger change in moment due to the presence of stiff spandrel beam between LC1 and the simulated failure location, LC9.

3.3.3.3 Physical Observations

Figure 3.23 presents a schematic of the crack pattern after completion of each push test (cracks caused during the gravity tests are omitted). As expected, cracks were observed on the top surface along yield lines, generally connecting adjacent support location. The region of cracking was broad, spreading over a width of approximately 30-55 in. with average crack spacing of 4 to 7 in. The cracks on the top surface at the end of the test at the slab-slab corner location were more tightly spaced when compared to the other two test locations due to smaller stiffness provided by the slab. Cracks observed on the bottom surface suggest the presence of torsion and two-way slab action, as diagonal cracks radiating away from the push location towards the interior of the specimen were observed (Figure 3.23b). These cracks were constrained between the push location and the yield line on the specimen, with only minor cracking observed beyond the yield line during each test.

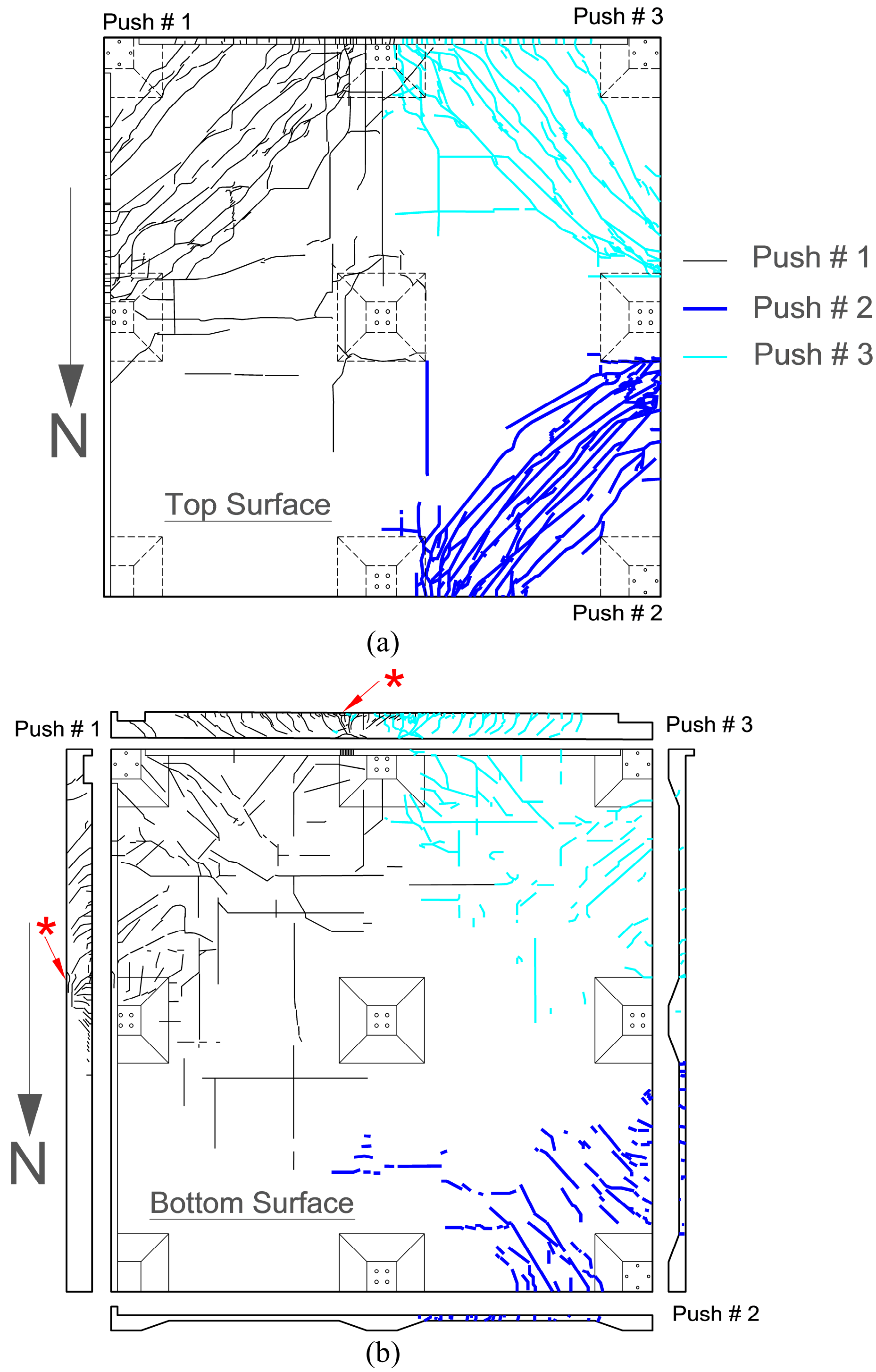

Figure 3.23: Cracking on the specimen at the end of tests on specimen 1, (a) cracks on the top surface, and (b) cracks on the bottom surface and edges. *are the location of compressive failure shown in Figure 3.24.

At the end of the push test at the beam-beam corner and the beam-slab corner, a significant number of flexural and shear cracks were observed on the spandrel beams between the test location and the corresponding adjacent support location. Shear cracks were observed between the push locations and the mid-span to the adjacent support, while flexure cracks were observed closer to the adjacent supports, suggesting beam failure dominated by flexure. In addition to the cracks on the top and sides of the edge beams, compressive failure was observed at the bottom of the beams during the test at the beam-beam corner and beam-slab corner test location as shown in Figure 3.24 and 3.25.

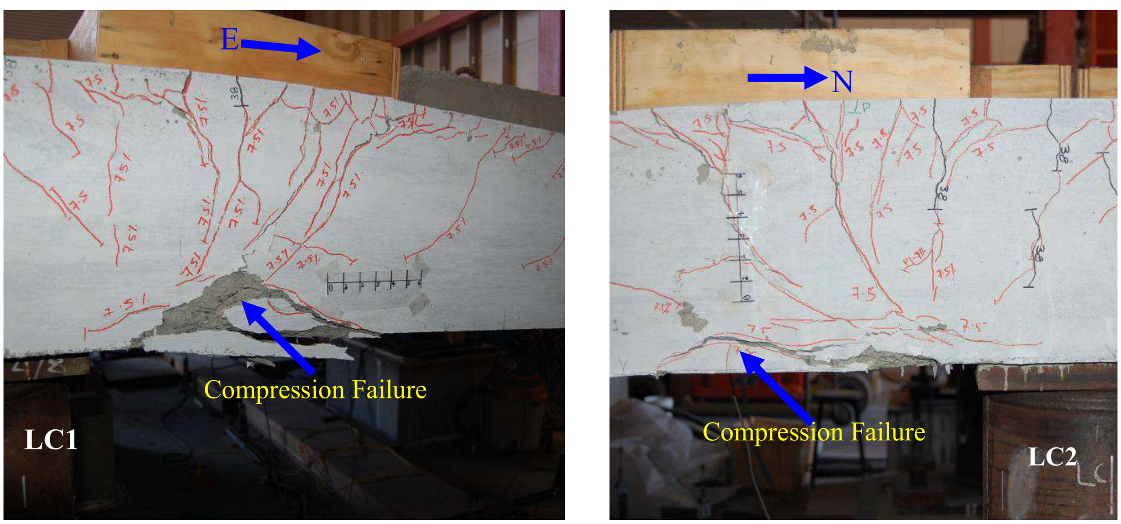

(a) (b)

Figure 3.24: Local failure and concrete spalling at beam support locations: (a) E-W beam at support LC1, (b) N-S beam at support location LC2.

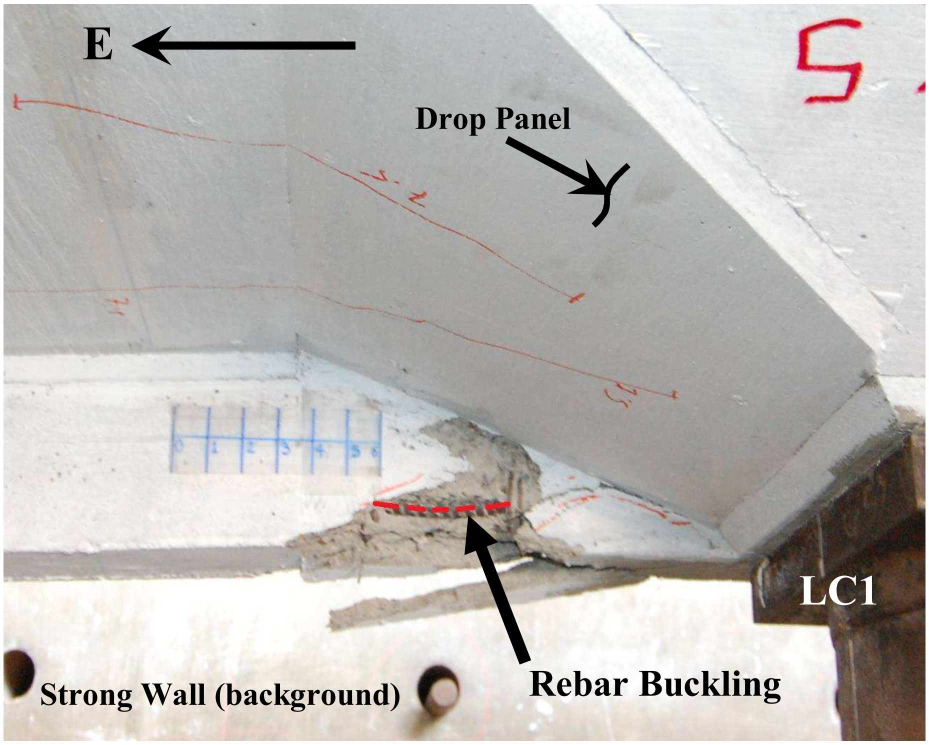

Figure 3.25: Rebar buckling and concrete spalling in EW-beam at support LC1 at the end of the test at the beam-beam corner on specimen 1.

3.3.3.4 Deflection Profiles

Figure 3.26a presents the location of the linear-potentiometers on the specimen for column failure test at the beam-beam corner. A similar naming convention is used when presenting the deflection profiles during the test at the slab-slab and the beam-slab corner. Figure 3.26b shows the history of the deflection profile during the push at the beam-beam corner location. Measurements L3 and L4, installed close to the mid-span of the spandrel beams show the largest deflection away from the push location, followed by the deflection at L5. A large difference in deflection profiles is observed between the two linear potentiometers placed at L5 and L6, as the yield line formed between these two sensor locations. A similar deflection profiles during the test at the slab-slab and beam-slab test locations is shown in Figure 3.27. It is interesting to note that for the slab-slab corner push location, L3 and L4 show significantly different deflection profiles, caused due to the localized failure near support LC5 during the test at slab-slab corner location (Figure 3.21).

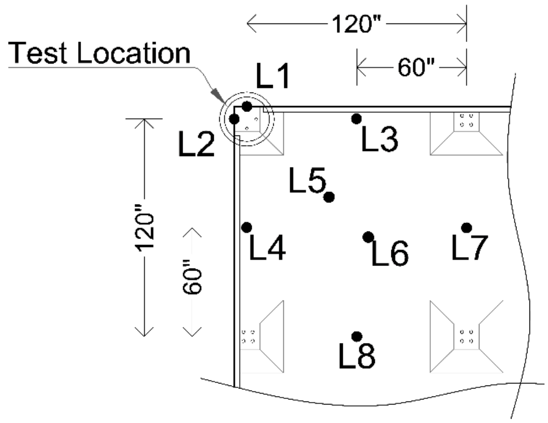

(a)

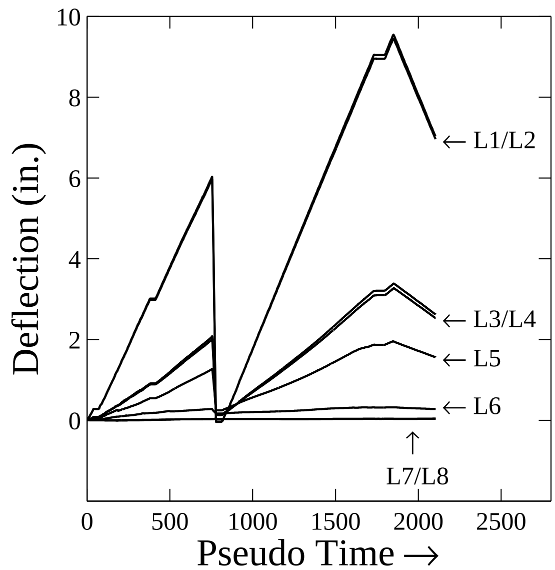

(b)

Figure 3.26: Deflection profile during test at beam-beam corner on specimen 1: (a) location of linear potentiometers, (b) deflection profile at sensor locations.

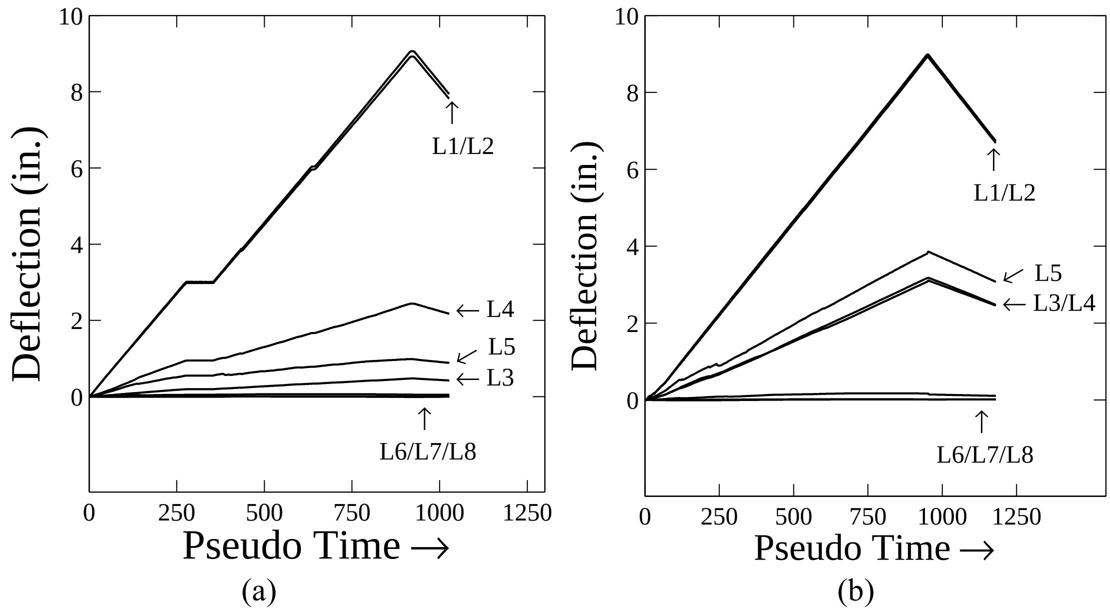

Figure 3.27: Change in deflection recorded by linear potentiometers during test at slab-slab corner and beam-slab corner on specimen 1, (a) linear potentiometers in the test panels during the test at slab-slab corner, and (b) linear potentiometers in the test panels during the test at beam-slab corner.

3.4 Specimen 2 Details

The second specimen depicts a portion of a floor plan, extending two panels from a building edge as shown in Figure 3.28. The geometric and reinforcing details for the second specimen were similar to the previous tests, with minor changes made to suit the objectives of this test program.

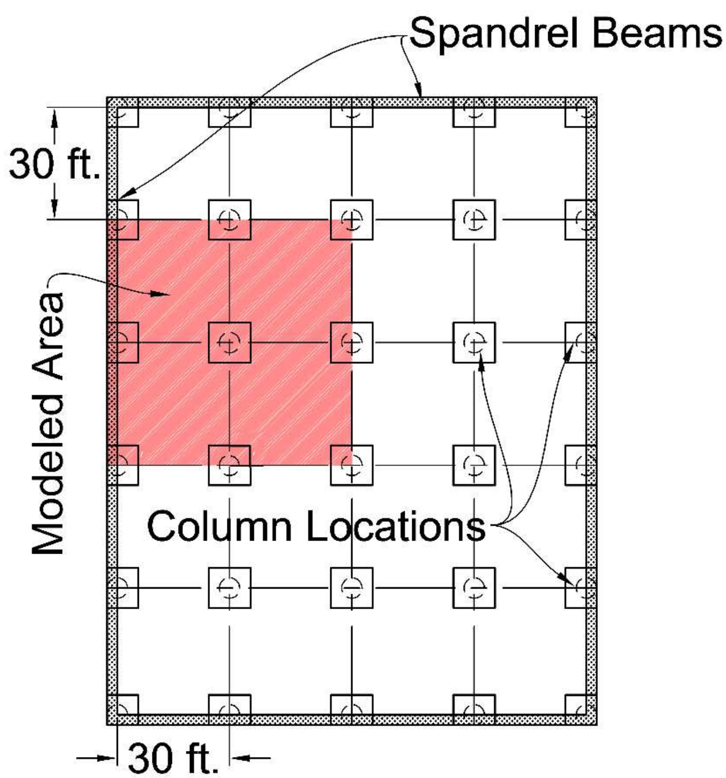

Figure 3.28: Region of building modeled for specimen 2.

The symmetric 2×2 panel beam-slab test specimen was one-third scale with a plan dimension of 21ft.-2in. in both direction with 3 in. thick slab. Supports were provided at every 10 ft. as shown in Figure 3.29.

The specimen had 3 in. × 12 in. (width × height) spandrel beams along one of the exterior edges which was commonly found in structures from that era. Lightly reinforced sloped drop panels, commonly observed in structures were also incorporated at each support location. The specimen was supported on four 200-kip axial only load cells at center edge locations, while the other five supports were provided by custom built multi-axis load cells. Two support failure locations at the edge of the specimen are namely: (i) push 1 - slab edge, and (ii) push 2 - beam edge; identified in Figure 3.29 as

"Push 1" and "Push 2". It is noted that no restraints were provided along the slab edge of the specimen, therefore the specimen does not account for the presence of additional panels in a multi-panel system.

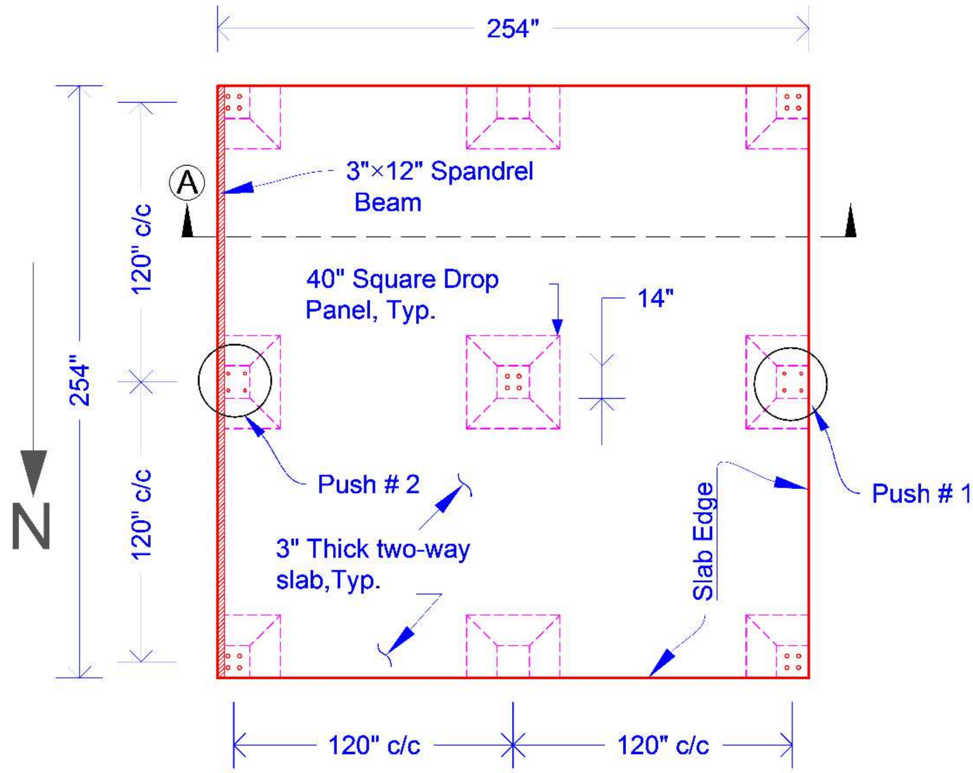

(a)

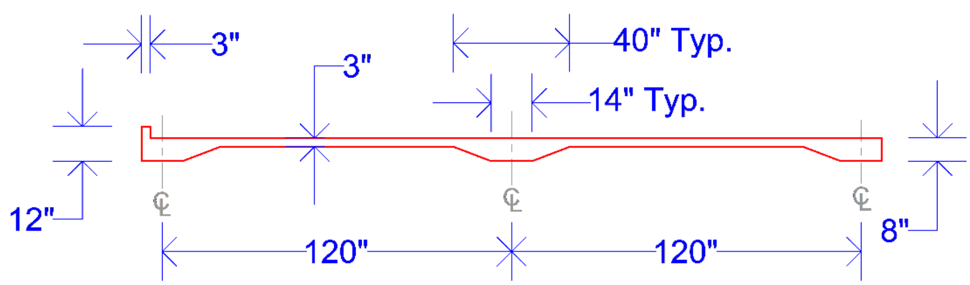

(b)

Figure 3.29: Schematic of the second specimen, (a) plan view, and (b) section A-A.

3.4.1 Reinforcement Details

As the specimen was similar to the first specimen, where the failure of corner supports was investigated, the reinforcing details were largely identical to the previous test specimen. A schematic of the slab and beam reinforcement in the specimen are shown in Figures 3.30 through 3.34. Other reinforcing details including, minimum spacing; embedment length; concrete cover in slab and beam, were selected based on ACI 318 (1956).

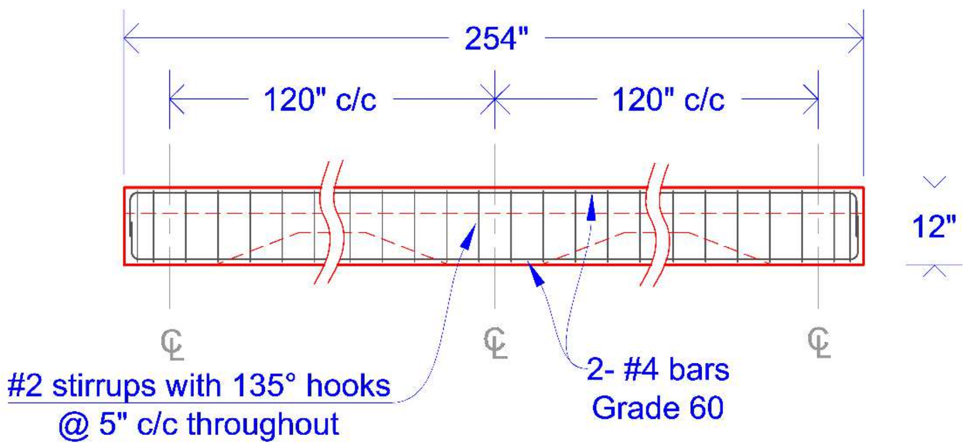

(a)

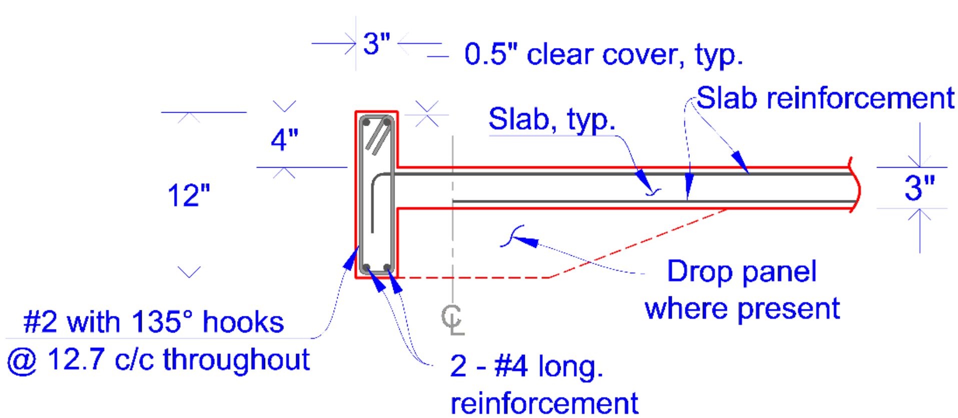

(b)

Figure 3.30: Schematic of beam reinforcement of specimen 2, (a) profile view of the beam reinforcement, and (b) cross-section view of the spandrel beam showing detailing along the length of the beam.

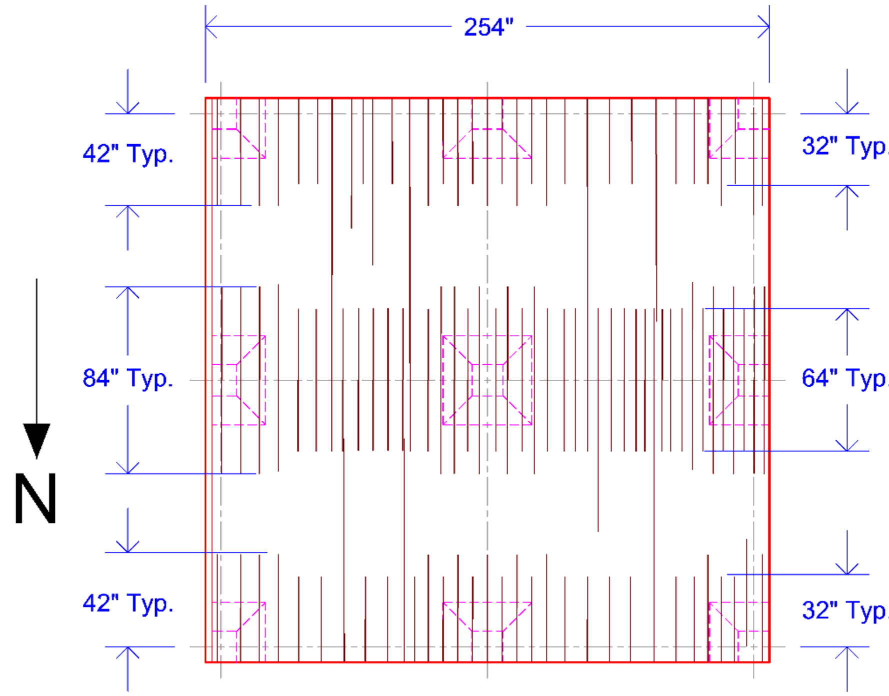

Figure 3.31: Top slab reinforcement in the NS direction.

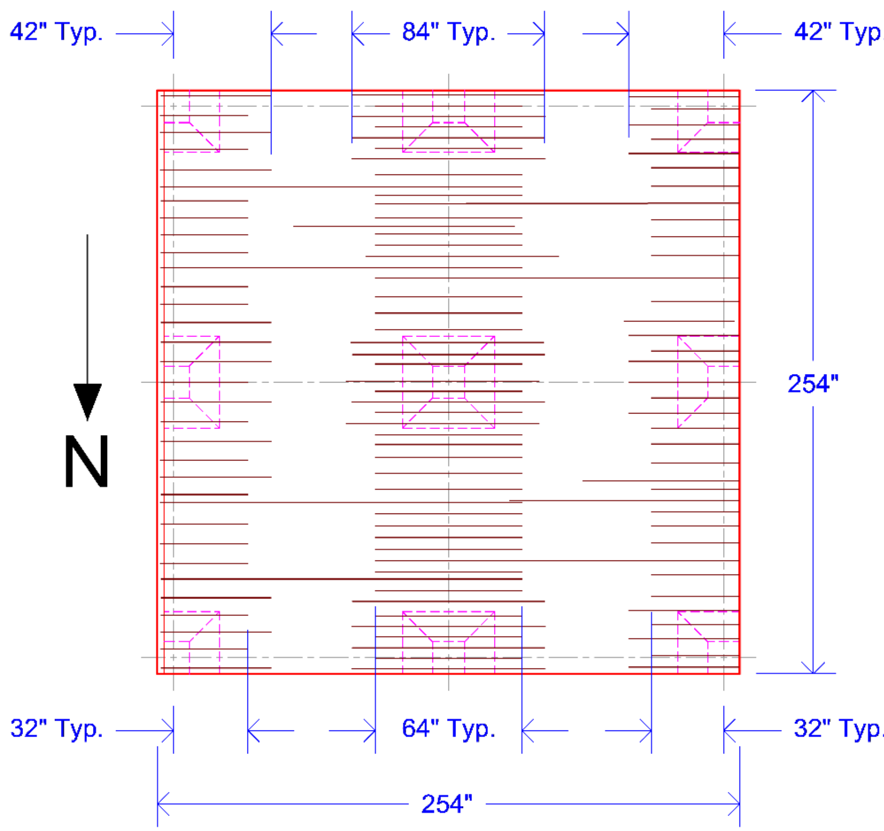

Figure 3.32: Top slab reinforcement in the EW direction.

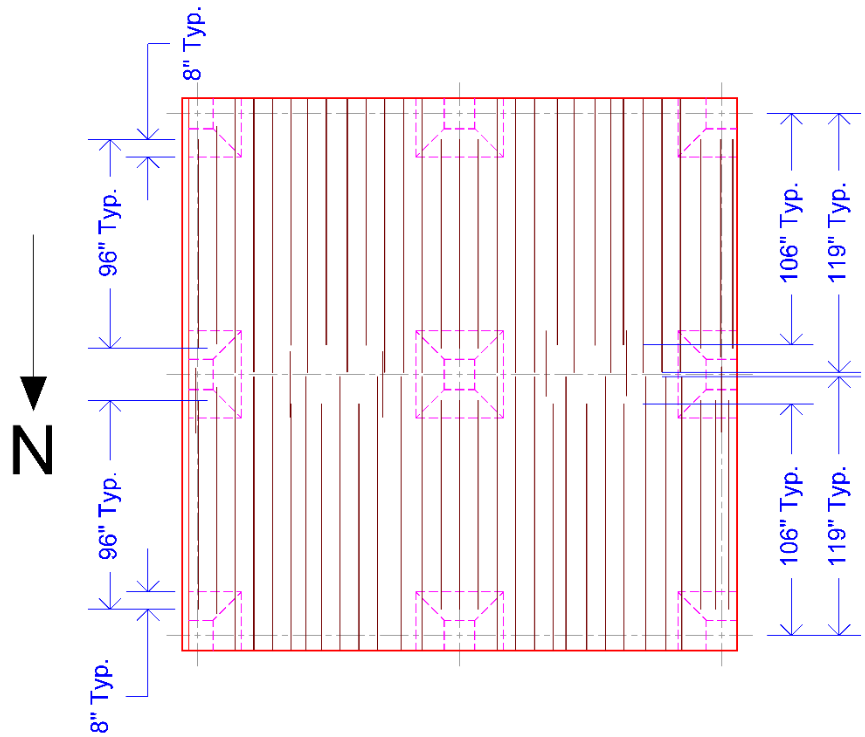

Figure 3.33: Bottom slab reinforcement in the NS direction.

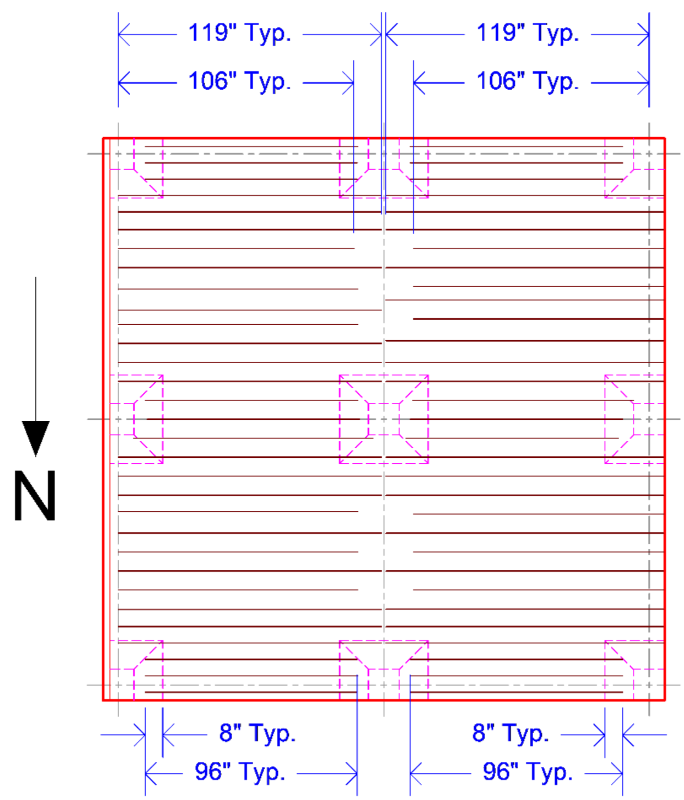

Figure 3.34: Bottom slab reinforcement in the EW direction.

The ACI-318 (1956) does not provide any special reinforcement in the drop panel zone, except for the continuous vertical column rebar. As no concrete columns were constructed at the support locations, a rebar cage made of #3 rebar was provided at each support location to prevent any localized failure at the supports. Figure 3.35 shows a schematic of the extra rebar cage provided at the drop panel locations. At the two push locations, extra bond was provided between the slab and the drop panels using two to three #3 deformed bars running 15 in. into the slab from the edge of the drop panels to avoid local failure at support locations during the push tests.

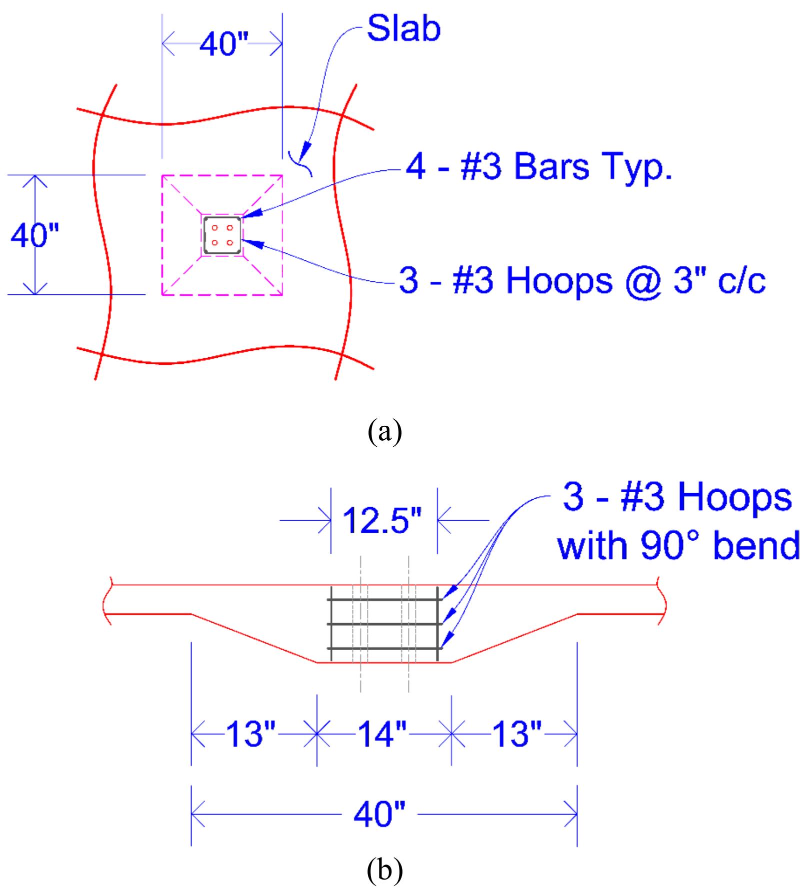

Figure 3.35: Schematic of the extra reinforcement provided at drop panel locations, (a) plan view, and (b) cross section view.

3.4.2 Material Properties

Material used for construction of the second test specimen were tested in the Powell Laboratories at UC San Diego. The results from concrete and steel material tests are summarized in the following sections.

3.4.2.1 Concrete Material Properties

The specimen was cast in place with a single pour of Type II concrete provided by Vulcan, of Mission Valley. Unconfined uni-axial compression tests were performed on three 6"×12" concrete cylinders to monitor the concrete strength gain and its strength on the actual day of test. The results from the compression tests are summarized in Table 3.3.

Table 3.3: Concrete cylinder compressive strength

Days from Pour	No. of Specimens	Average Strength	Target Strength
28 Days	3	5172 psi	5000 psi
43 Days (Slab Edge)	3	5382 psi	N/A
49 Days (Beam Edge)	3	5517 psi	N/A

3.4.2.2 Steel Material Properties

Grade 40 and Grade 60 rebar were used to provide longitudinal reinforcement in the slab and the spandrel beam, respectively. Rebar tension tests were performed on three sample of each rebar type. Figure 3.36(a) and (b) presents the stress vs. strain plot for Grade 40 and Grade 60 rebar, respectively.

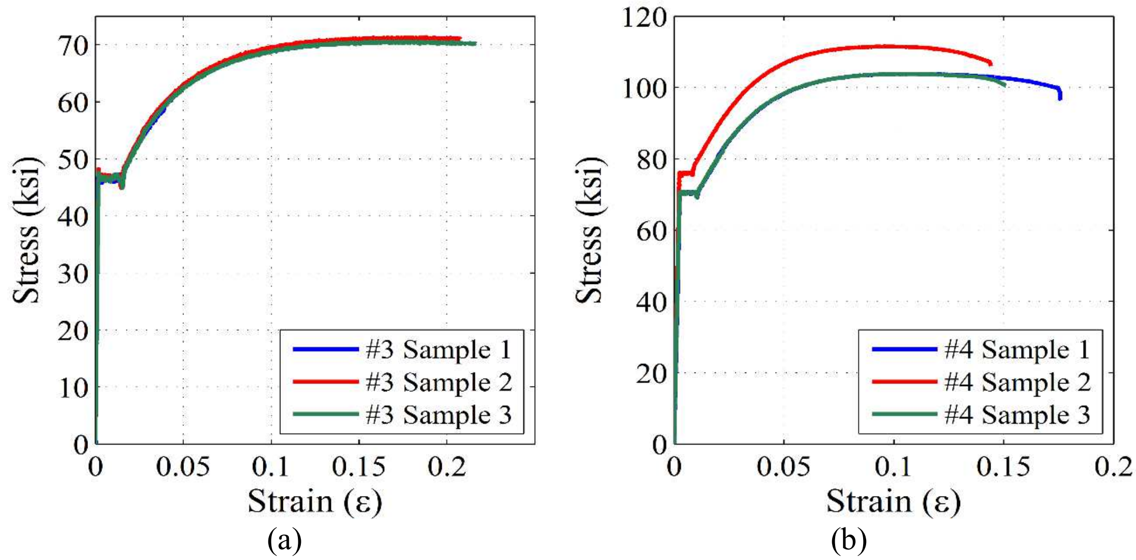

Figure 3.36: Stress-strain curve of the steel reinforcement, (a) Grade 40 - #3 slab reinforcement, and (b) Grade 60 - #4 beam longitudinal reinforcement.

Based on the rebar tensile tests, an average yield stress for the Grade 40 and Grade 60 steel was found to be 46.5 ksi and 70.4 ksi, respectively. Well defined yield plateaus were observed in both steel, followed by strain hardening and eventual failure at 0.15 to 0.2 in/in strain. Both rebar showed similar initial elastic modulus of approximately 28500 and 28350 ksi for Grade 40 and Grade 60 rebar, respectively.

3.4.3 Loading Protocol and Test Setup

3.4.3.1 Loading Protocol

Before the column removal tests were performed on the specimen, uniform load was applied on the specimen to depict the scaled mass and reduced live load on the specimen. Using the concrete blocks used during the test of the first specimen, a total uniform load of 90 psf was applied on the second specimen, consisting of 70 psf of simulated scaled mass (corresponding to $1/3^{rd}$ scale) and 20 psf of reduced live load.

Following the end of the gravity test, the specimen was tested under slow push, in displacement control at the two simulated column failure locations using a 50 kip actuator. Each location was tested one at a time with load cells in place at other push location. A linear potentiometers was mounted using metal brackets near the test location to monitor the vertical displacement and control the actuator. After removal of the respective test location load cell and attachment of the actuator, the specimen was pushed to 10.5 inch and 14.5 inch vertical displacement at the slab edge and the beam edge test location, respectively. Once the maximum displacement was attained, the actuator was retracted to zero load and detached from the specimen before moving it to the next test location. It is noted that once the test was complete at a given location, the specimen was shored using wooden blocks as the respective load cell was unable to be moved back in place due to large plastic deformation.

3.4.3.2 Test Setup

The specimen was supported at nine support locations, of which five were multi-axis load cells (LC1 through LC5) at center and corner support locations, and four 200 kip axial only load cells at the center-edge supports (LC6 through LC9) as shown in Figure 3.37. The five multi-axis load cells, LC1 through LC5 were seated on 42" x 42" x 24" concrete pedestal and tied to strong floor using tie-down rods to provide fixed end condition at the bottom of each support. The axial load cells, at the center edge locations, were seated on Φ42"x48" circular pedestal, held in place by two post tension rods.

Figures 3.38 and 3.39 show a schematic of the profile view of the test setup. The load frames were attached to the strong wall and a 50 kip actuators was attached near the end of the load frame arm. As the two locations were tested separately, the same load frame-actuator assembly was used by moving it at the end of the first push test at the slab edge location. It is to be noted that the pedestals under the test locations (supports LC6 and LC8, respectively) were not anchored to the strong floor below to help expedite the removal of the load cells at these locations and also move the pedestals to provide room for vertical displacement beyond 12 in. (Push #2 at beam edge).

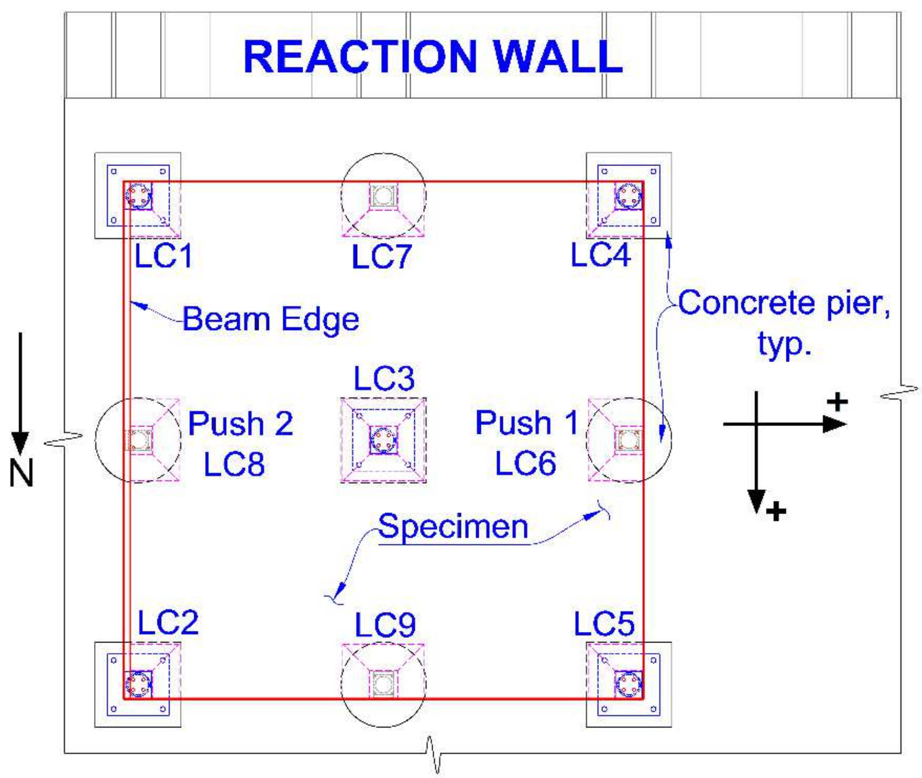

Figure 3.37: Plan view of the experimental setup showing load cell and test locations. Direction of positive NS and EW force resultants is shown.

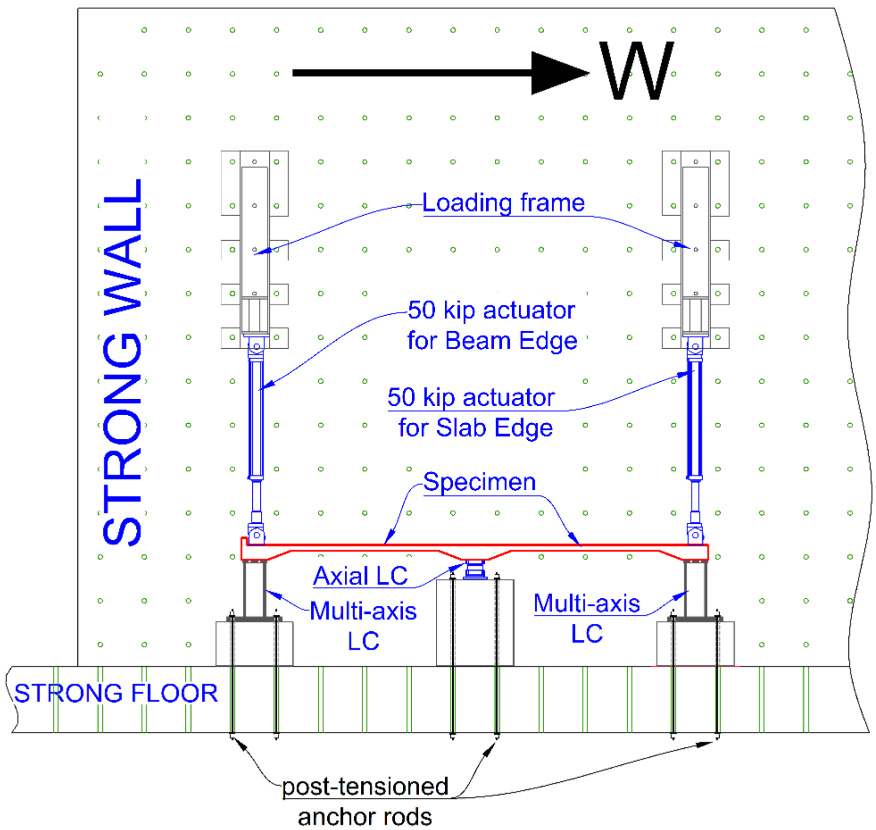

Figure 3.38: E-W view showing setup for push down location 1 and 2.

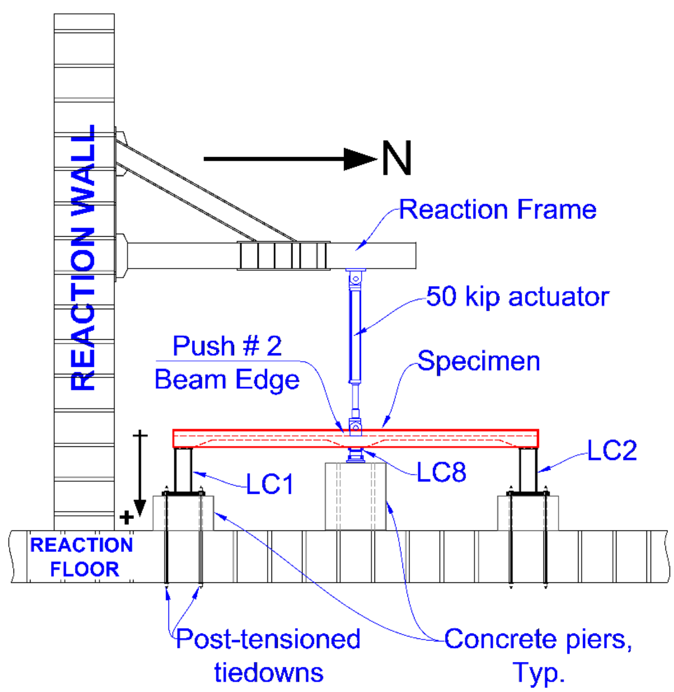

Figure 3.39: N-S view showing setup for push down location 1. Direction of positive vertical load is shown.

3.5 Specimen 2-Test Results

Global results from the gravity load tests and column removal tests from specimen 2 are presented in this section. Global results include force versus displacement (for push tests only), load distribution among various load cells at support locations during the test, the observed damage to the specimen at the end of each tests, and the deformation of the slab as recorded by the linear potentiometers.

3.5.1 Uniform Gravity Load

3.5.1.1 Load Distribution at Support Locations

Figure 3.40 presents the *change* in force at support locations due to the applied gravity load of 90 psf. As the data acquisition started after removal of the formwork, the forces shown in Figure 3.40 are the changes caused by the additional 90 psf gravity load only. Figure 3.40(a) shows the location and names of the load cells with the direction of positive forces in the NS and EW direction. Vertical forces acting downwards on the supports are represented to be positive, while horizontal forces and moments are positive towards North and West in the North-South and East-West direction, respectively.

Recorded changes in axial loads at each support are presented in Figure 3.40(b) and (c). Corner supports LC1, LC2 experienced an increase of 3.3 and 3.5 kips respectively, whereas LC4 and LC5 experienced an increase of 3.7 and 4.9 kips increase in axial load due to the 90 psf uniform gravity loads. Load cell at support LC3 recorded a greater increase in axial load (12.5 kips) due to the larger tributary area (~4 times the corner locations) supported by the center support location. The center edge axial load cells (LC6 through LC9) experienced an average increase of 3.25 kips. Total increase in axial loads at support (40.8±3 kips) is in good agreement with the total vertical load applied on the system due to the 90 psf uniform load (38 kips).

Figure 3.40(d) and (e) show the recorded change in shear at the multi-axis load cell locations. The four corner supports, supported on multi-axis load cells, experienced an outward shear force due to the applied uniform load on the specimen. LC1 and LC2, along the beam edge, experienced an increase in resultant shear of approximately 3.6 kips while supports LC4 and LC5 experienced an increase of 4.6 and 5.9 kips in resultant shear, respectively. This difference in resultant shear at LC4 and LC5 was due to the different shear force along the EW direction between the two support locations, likely caused due to slightly different local responses at LC4 and LC5.

Recorded change in moments, shown in Figure 3.40(f) and (g), were also found to be consistent showing unbalanced hogging moments at the corner support locations. Supports LC1 and LC2 experienced slightly higher change in resultant moments of 4.0 and 5.2 kip-ft., respectively, compared to resultant moments of 3.0 and 3.2 kip-ft. at supports LC4 and LC5, respectively, due to the presence of stiffer spandrel beams along the NS edge between LC1↔LC8↔LC2. The center support location, LC3, showed small change in shear and moment due to the symmetry of the structure and loading about this support location in both the NS and the EW direction.

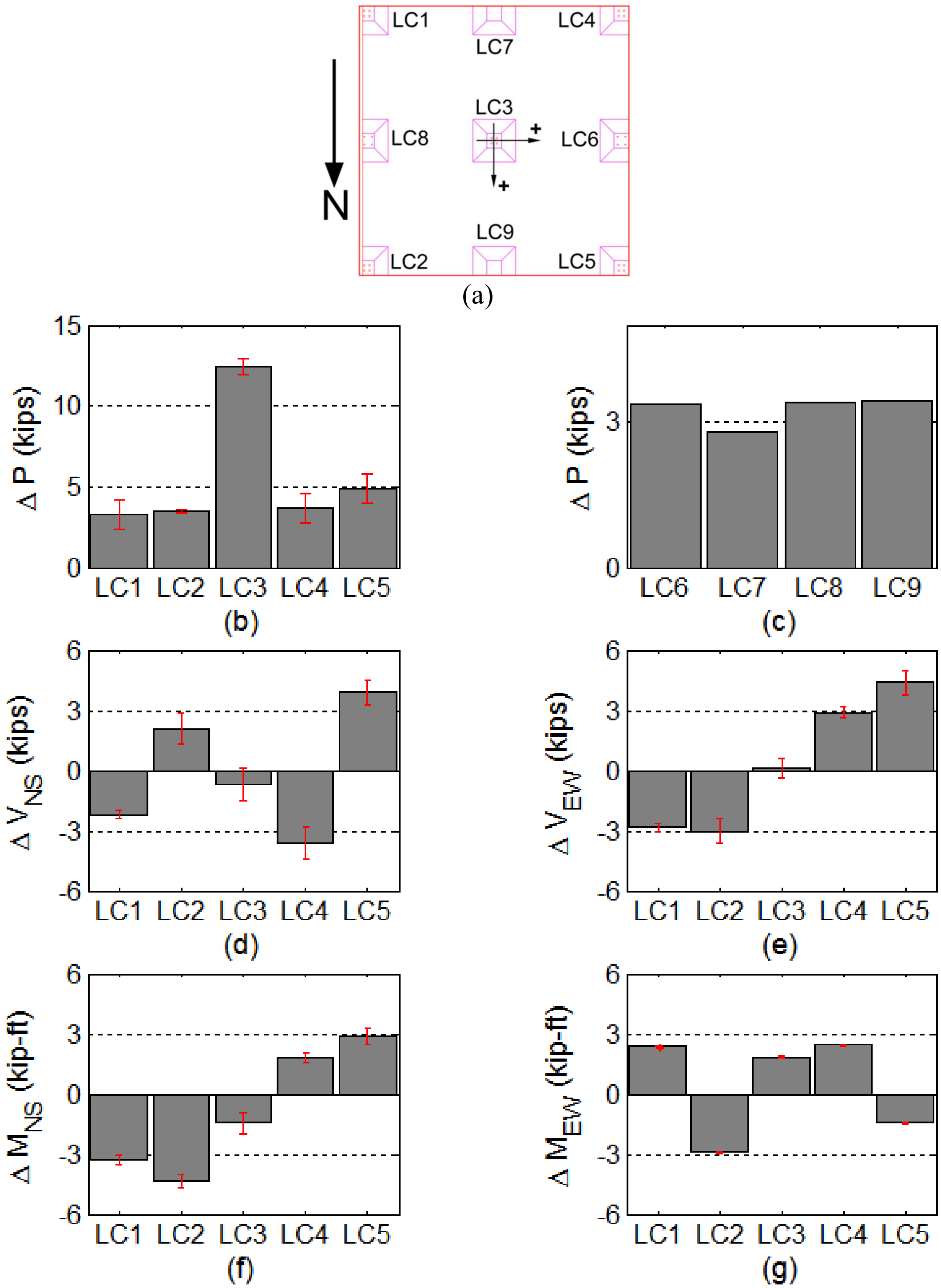

Figure 3.40: Resolved forces at the support locations due to applied uniform gravity loads on specimen 2: (a) location of the load cells and the positive direction in EW and NS direction, (b) change in NS shear, (c) change in EW shear, (d) change in NS moment, (e) change in EW moment, (f) change in axial load at multi-axis load cells, and, (g) change in axial loads at axial only load cells.

3.5.1.2 Physical Observations

After the gravity load was applied on the specimen, the concrete blocks were removed to mark cracks on the top and bottom surface of the specimen caused due to the uniform load. Using the digital photographs taken at the end of gravity load test, a schematic of the observed cracks is shown in Figure 3.41.

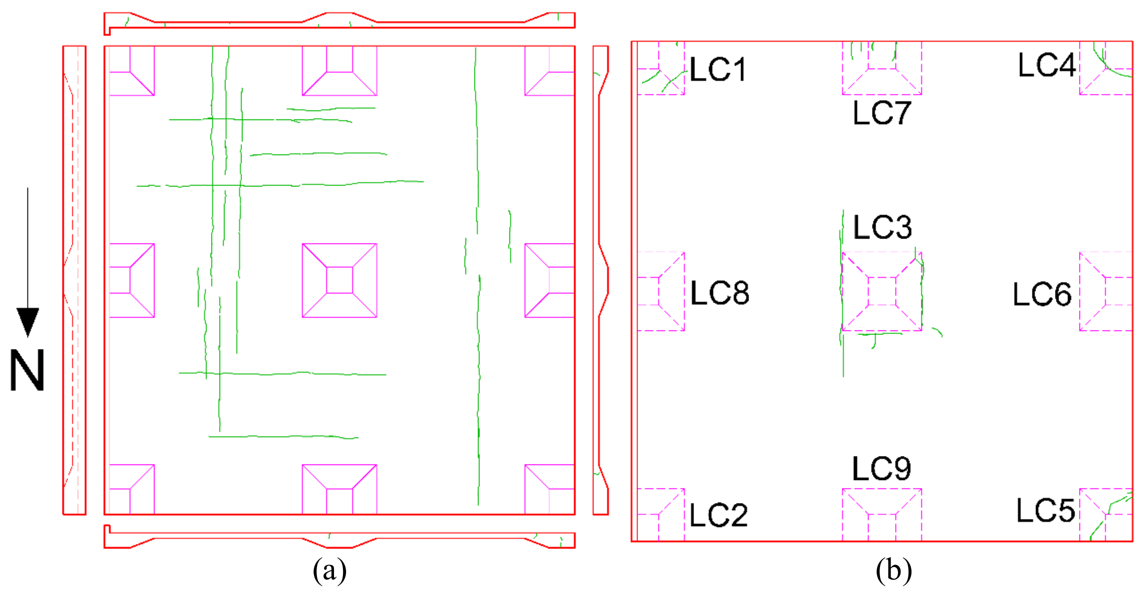

Figure 3.41: Cracking in the specimen 2 after uniform gravity load of 90 psf, (a) Bottom and sides of the specimen, (b) Top of the specimen.

Under uniform gravity loads, the maximum positive and negative moments are expected to occur near panel mid-span and support locations respectively. Cracks were observed near the mid-span of each panel as expected due to the presence of large positive moments at these locations. As the concrete block were placed on the specimen one at a time (East edge loaded first), more cracks were observed on the East end of the specimen (panels next to the spandrel beam) compared to the other two panels on the west end of the specimen. Only minor cracking was observed on the top surface of the specimen due to thick drop panel section and greater amount of top reinforcement at support locations. Few cracks were also visible near the corner supports due to the rotational fixity provided by the multi-axis load cells as shown in Figure 3.41(b). These cracks were more prominent near supports LC4 and LC5 compared to the other two corner supports (LC1 and LC2) due to the reduced stiffness at these supports in the absence of the edge beam.

3.5.2 Column Removal Scenario

The specimen was subjected to column removal tests at two center edge locations. The load cell was removed at the test location and the specimen was pushed down using a 50 kip actuator under displacement control. At the end of each push, the load was reduced back to zero and a similar protocol was used to conduct the test at the next location. This sections presents the global results from the two column failure tests conducted at the slab edge and the beam edge locations. Results include load-deflection behavior, load redistribution at support locations, observed damage at the end of each test, and deflection profiles as recorded by the linear potentiometers.

3.5.2.1 Load-Deflection Relation

Figure 3.42 presents the vertical load versus the displacement relation during the push test at the slab edge and beam edge column location. Vertical deflection and actuator load in downward direction are shown as positive values. The initial load at zero displacement (SW) is the initial support reaction due to the specimen self-weight and the applied uniform gravity load of 90 psf at the test location.

During the test at the slab edge, the specimen began to deform with an initial tangent stiffness of 14.5 kips/in. until a deflection of 0.3 in. As the deflection increased, cracking caused the stiffness to drop by 50% (≈7 kips/in.). When pushed further, at approximately 1 in. vertical deflection the stiffness decreased significantly to 14% of the initial stiffness or 1.8 kips/in. Beyond this, the specimen continued to deform until it achieved a load of 9.2 kips at 10.7 inch vertical deflection. Further vertical movement was precluded by the presence of the concrete pedestal below the test location, therefore the actuator load was retracted to zero load. When returned to zero load, the specimen exhibited an unloading stiffness of approximately 4.7 kips/in. (33% of the initial stiffness) and retained a permanent deformation of 9 in.

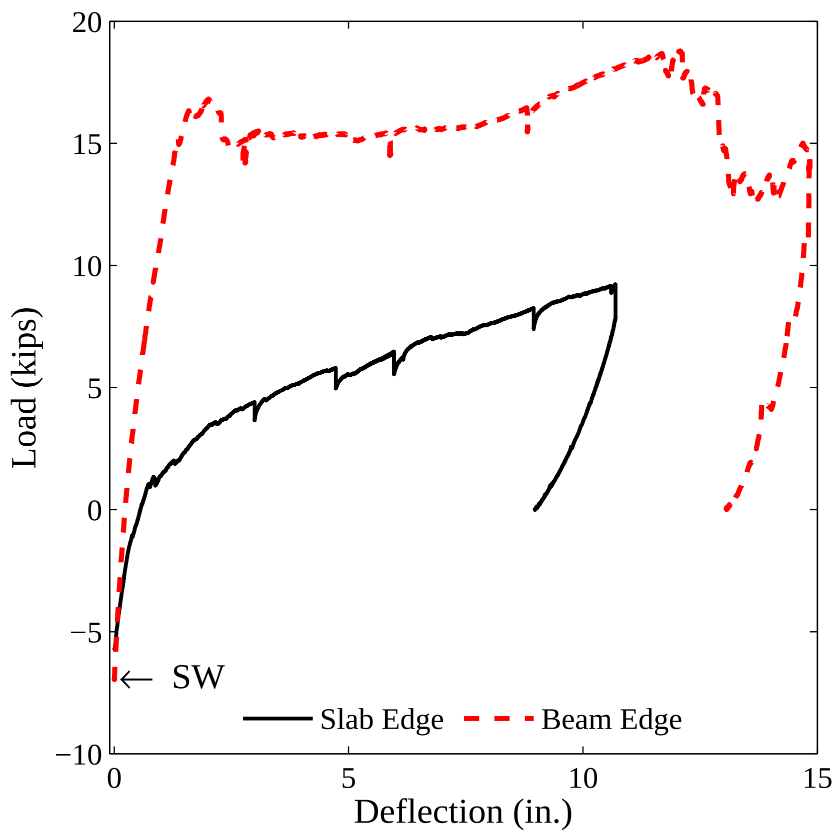

Figure 3.42: Load vs. displacement relation during the test at two edge locations on specimen 2.

During the test at the beam-edge, the specimen began to deform with an initial stiffness of 35 kips/in., or about 2.5 times that of the slab edge initial stiffness until no external load was applied by the actuator at 0.22 in. vertical deflection. When pushed further, the system attaining its peak capacity of 16.8 kips at 2 in. deflection. At this point during the test, load dropped suddenly to 15.4 kips due to the loss of bond near the beam ends near supports LC1 and LC2 (see section on *Physical Observations*). Beyond this point the system deformed plastically, with no significant change in applied load, until vertical displacement of 7.5 in. following which the stiffness increased to 0.7 kips/in until maximum load of 18.8 kips was attained at a vertical deflection 12.1 in. At this point, due to the large stresses induced at the push location, the column section of the drop panel failed in a punching failure mode, creating large torsional demands on the spandrel beam (Figure 3.43). After failure at the column section of the drop panel, additional displacement of the actuator resulted in continued rotation of the failed region without imposing additional displacement on the rest of the specimen. At this point the actuator was retracted back to zero load with final residual displacement of 13.1 in.

Compared to the Yield Line Theory estimates, the system was able to attain significantly higher load capacity at the two edge push locations. Table 3.4 presents the YLT estimates for each test and the enhancement observed, when compared with the achieved capacities during each test. It is noted that the location of the yield lines were assumed to coincide with the observed damage at the end of each test as shown in Appendix B. The ultimate capacity of the slab and beam section along the yield lines were calculated based on the actual rebar layout and the material properties as used for the construction of the specimen. For the test at the slab edge location, the specimen was able to achieve double the capacity estimated by YLT, due to formation of tensile catenary in the NS direction. However, the beam edge achieved only 20% higher strength compared to its YLT estimate. This is due to the premature failure of the edge beam due to initial damage that occurred near the ends of the beam at support LC1 and LC2 (see discussion on Physical Observations).

Figure 3.43: Local failure at beam edge push location creating large torsion in the beam.

Table 3.4: Comparison between experimental and YLT load capacities for the tests conducted at two edge support locations on specimen 2.

	P_{YLT}	$P_{EXPERIMENT}$	$P_{EXPERIMENT}/P_{YLT}$
Slab Edge, kips	4.4	9.2	2.1
Beam Edge, kips	15.5	18.8	1.2

3.5.2.2 Load Distribution at Supports

Figure 3.44 presents the load distribution at the support locations at maximum achieved load during the test at the slab edge. Figure 3.44(a) presents the location and name of all the supports and the direction of positive NS and EW force resultants. Vertical forces acting down on the supports are shown as positive.

Figure 3.44(b) and (c) presents the change in axial loads at the support location at maximum load during the test at slab edge location. As expected most of the axial load was transferred to the adjacent support locations, LC3, LC4 and LC5. Supports LC4 and LC5 experienced an increase of 6.9 kips in axial load each (78 % of the total load change), followed by LC3 which experienced an axial load increase of 3.8 kips (21% of the total load change). Due to their remoteness from the test location, supports LC1, LC2 and LC8 experienced very small changes in axial load, while supports LC7 and LC9 experienced an uplift of approximately 0.8 kips each due to large negative moments along the yield line and their proximity to the failure surface. Total change in axial load of 16$\pm$4 kips, as resolved at supports LC1 through LC9, is in good agreement with the total change in vertical load applied by the actuator (15 kips).

Figure 3.44(d) and (e) present the change in shear force at the support locations LC1 through LC5 (LC6 through LC9 did not provide any shear or moment resistance). Due to their proximity to the test location, supports LC4 and LC5 experienced the maximum change in shear load followed by support LC3. Supports LC4 and LC5 experienced an increase of 34 and 38 kips in resultant shear, respectively. The direction of the shear forces at these supports was outward, pushing these supports away from the specimen center, i.e. compression along LC3↔LC4 and LC3↔LC5. Support LC3 also experienced an increase of 18.5 kips, directed in the EW direction away from push location. At maximum load, supports LC1 and LC2 also experienced a small increase in resultant shear, in the order of 7-10 kip, mostly directed in EW direction due to slab continuity.

A similar distribution observed for the additional moments induced at the supports are shown in Figure 3.44(f) and (g). Supports LC4 and LC5 experienced an increase of 8.0 and 11.1 kip-ft. of resultant moment, respectively, caused due to the negative moments generated along the yield lines at these supports. Support LC3 experienced the maximum increase in resultant moment of approximately 19.5 kip-ft., most of it caused due to negative moment in the NS direction due to push at support LC6. The small change in moment recorded at support LC3 in the NS direction was likely due to some asymmetry in the system.

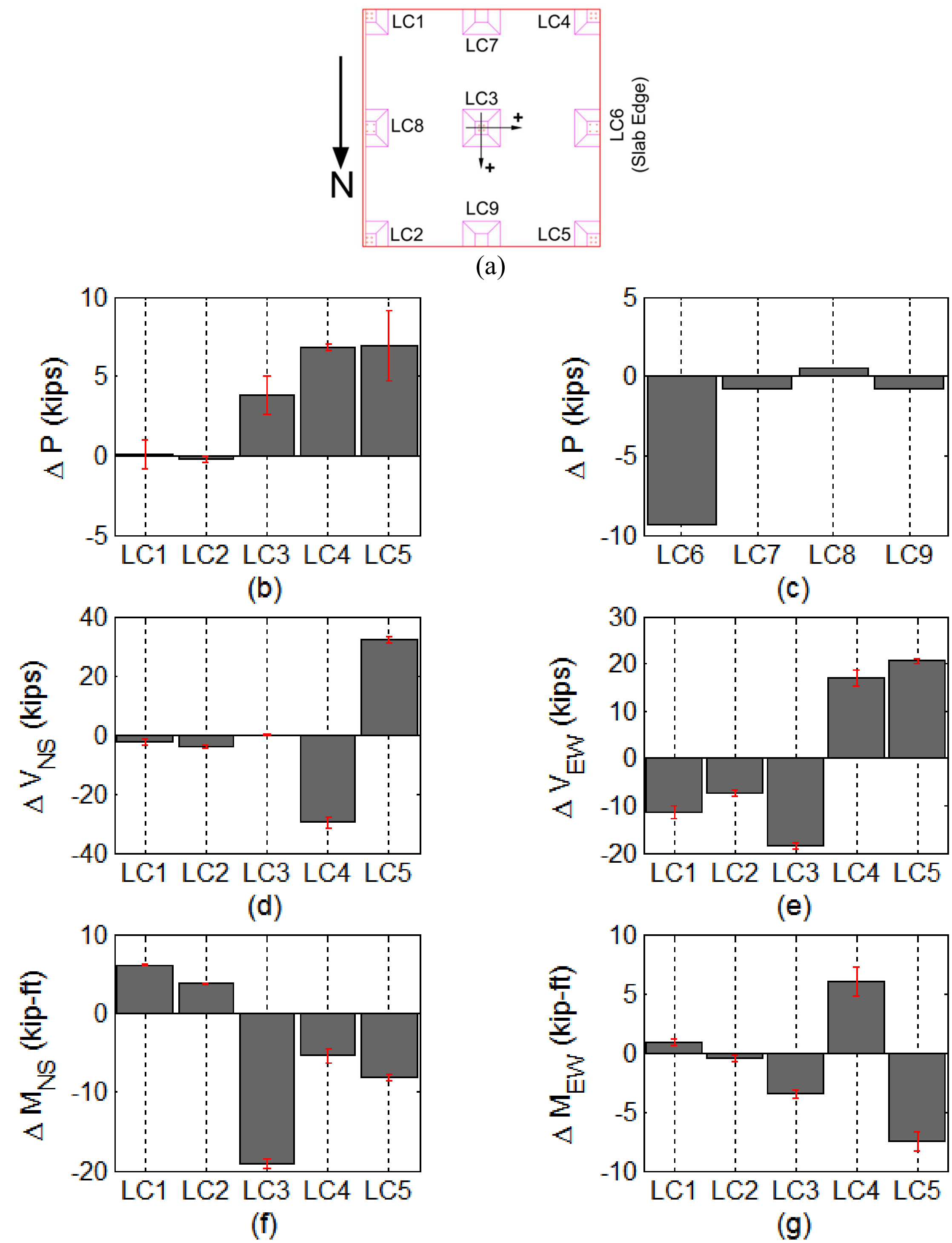

Figure 3.44: Load distribution at supports at maximum load during the test at the slab edge on specimen 2: (a) location and naming convention for the load cells, (b) change in axial load at multi-axis load cells, (c) change in axial loads at axial only load cells, (d) change in NS shear, (e) change in EW shear, (f) change in NS moment, and, (g) change in EW moment.

Figure 3.45 presents the load distribution at the support locations during the test at the beam edge location at maximum load (deflection of 12.1 in). Figure 3.45 (a) presents the location and name of all the supports (LC1 through LC9) and the direction of positive NS and EW force resultants. The vertical forces, i.e. the axial force at the supports, are positive acting downwards on the supports.

Figure 3.45(b) and (c) presents the change in axial loads at the support location at maximum load during the test at the beam edge. At maximum load most of the axial load was transferred to the adjacent support locations, LC1 through LC3. Support LC1 experienced an increase of 14.8 kips while support LC2 experienced an increase of only 8.7 kips. This discrepancy between the load cells LC1 and LC2 was likely due to initial damage that occurred at the beam ends resulting in an uneven force distribution. Support LC3 also experienced an increase of 3.7 kips in axial load due to its proximity to the failure surface during the test at maximum load condition. Due to their remoteness from the test location, supports LC4 through LC9 experienced very small changes in axial load, with supports LC7 and LC9 experiencing small uplift.

Figure 3.45(d) and (e) presents the change in shear force at the support locations LC1 through LC5. Due to their proximity to the test location, supports LC1 and LC2 experienced the maximum change in shear load followed by LC3. Supports LC1 and LC2 experienced an increase of 47 and 44 kips in resultant shear, while support LC3 experienced an increase of 35 kips at maximum load condition. The direction of the resultant shear force at LC1 and LC2 was outward pushing the supports away from the center of the specimen. LC4 and LC5 also experienced a small increase in shear, in the order of 11-13 kips, mostly directed in EW direction due to slab continuity.

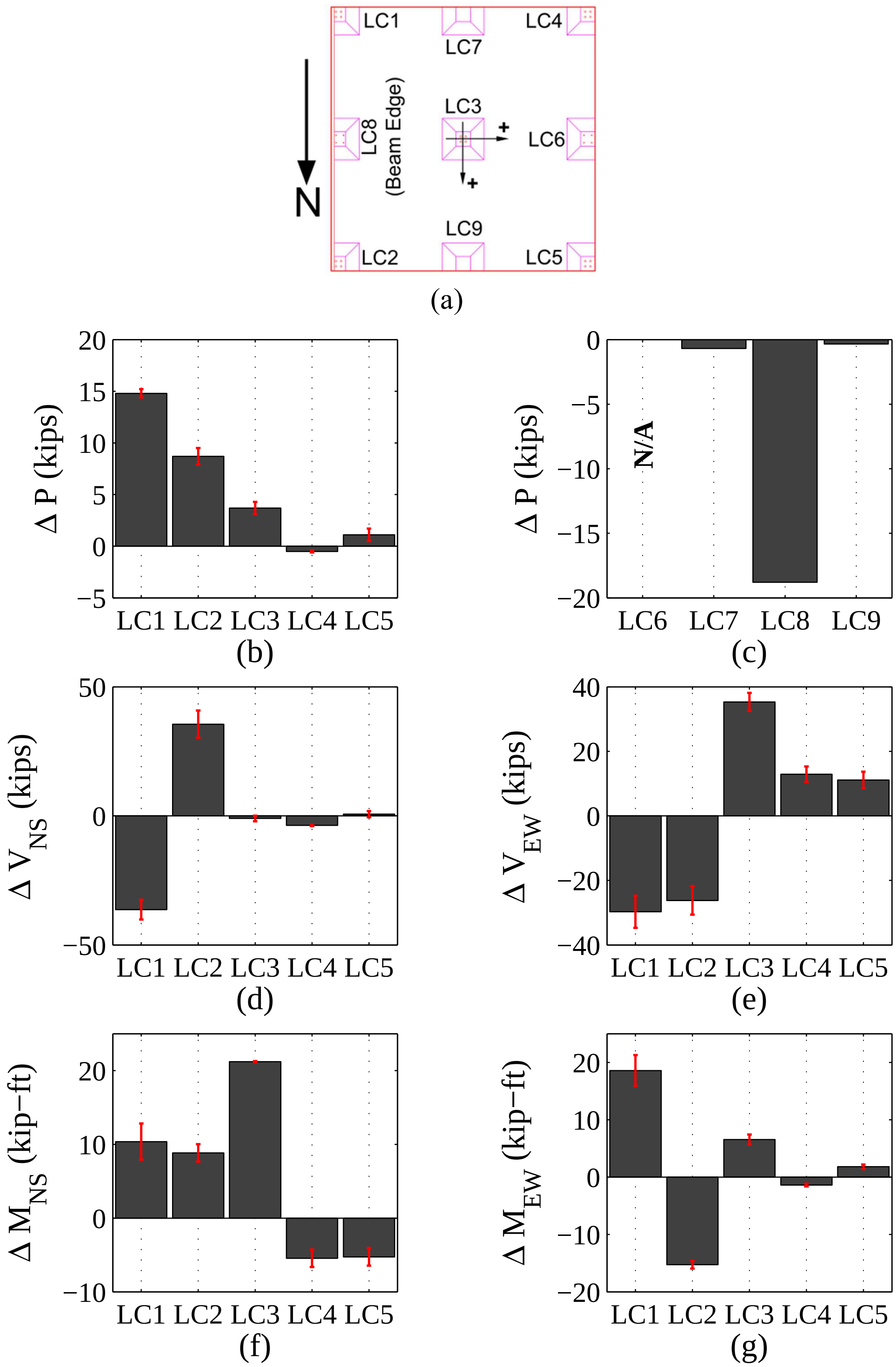

Figure 3.45: Load distribution at supports at maximum load during the test at the beam edge on specimen 2: (a) location and naming convention for the load cells, (b) change in axial load at multi-axis load cells, (c) change in axial loads at axial only load cells, (d) change in NS shear, (e) change in EW shear, (f) change in NS moment, and, (g) change in EW moment.

A similar distribution is observed for moments at supports LC1 through LC5, as shown in Figure 3.45(f) and (g). At maximum load, supports LC1, LC2 and LC3 experienced an increase of 21 kip-ft., 18 kip-ft., and 22 kip-ft. of resultant moment, respectively. At support LC1 and LC2 the supports experienced moment increase of 15-20 kip-ft. along the spandrel beam transverse axis (EW direction), caused due to the yielding of the spandrel beam in flexure at the supports. Support LC3 experienced the maximum increase in moment in the NS direction (21 kip-ft.), caused due to the large moment demand imposed due to the push at support LC8. Supports LC4 and LC5 also experienced a small increase in resultant moment demand of approximately 6 kip-ft. each.

3.5.2.3 Physical Observations

Figure 3.46 presents a schematic of the observed damage on the specimen at the end of the column removal tests conducted at the slab edge and beam edge. Only the cracks formed during the push tests are shown in the schematic, i.e. cracks formed due to gravity loads are omitted.

During the test at both the edge locations, cracks formed on the top surface along the expected yield lines, connecting LC3-LC4-LC5 and LC1-LC3-LC2 for the slab edge and beam edge, respectively. These cracks on the top surface were spread over a broad region with a width of 30-45 in., with an average crack spacing of 5-6 in. Cracking was also observed near the middle of the specimen in the NS direction between supports LC7-LC3-LC9, caused by the presence of large in-plane forces.

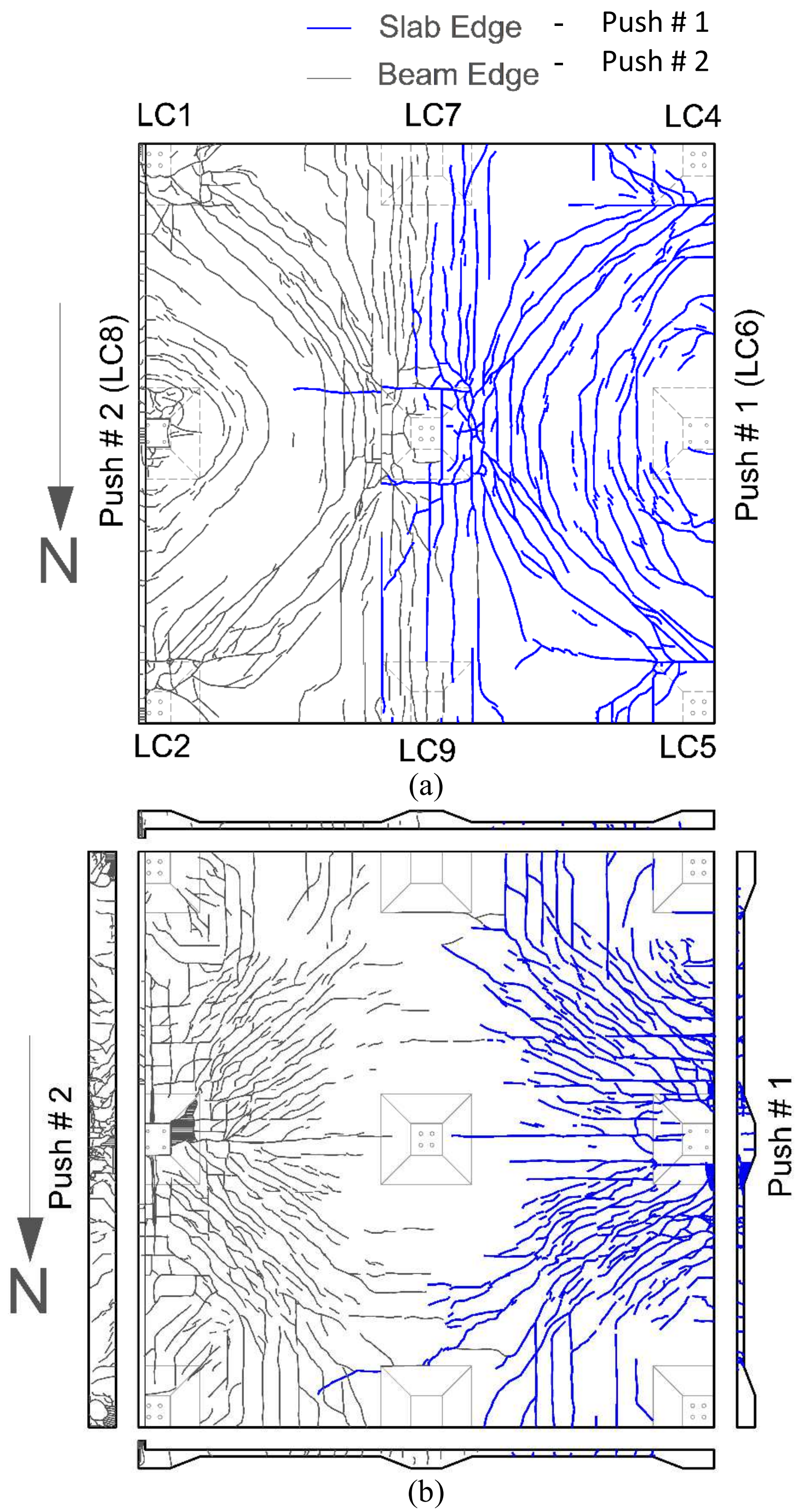

Figure 3.46: Schematic of the observed damage on the specimen at the end of push tests on specimen 2, (a) cracks on top surface of the specimen at the end of the test, and (b) cracks observed on bottom surface and sides of the specimen at end of the test.

Figure 3.46(b) presents a schematic of the cracks that formed on the bottom surface of the specimen. At the end of each test, tensile cracks were observed originating from the push locations extending towards LC3 due to the imposed positive moment along LC3-LC6 and LC3-LC8 during the test at the slab edge and beam edge, respectively. More severe form of cracking was observed in the form of cracks radiating away from the push location. These cracks were spread over a width of 55-75 in. with an average crack spacing of 4-5 in. For both tests, these cracks were bounded by the yield line on the top surface, with very few cracks outside of the failure zone.

During the test at the beam edge, severe damage was observed along the length of the beam. Cracks that formed on the spandrel beams were localized near the two adjacent supports (LC1 and LC2) and the push location (LC8). At the two ends of the spandrel beams (supports LC1 and LC2), concrete breakout was observed caused by bond failure of beam longitudinal rebar (Figure 3.47). This resulted in large cracks to form on the side of the spandrel beam, which caused the initial drop in load at 2 in. vertical displacement during the test at the beam edge. By end of the test at the beam edge location, punching failure of the column section of the drop panel resulted in large cracks, concrete spalling, and longitudinal rebar bucking near the push location (Figure 3.48).

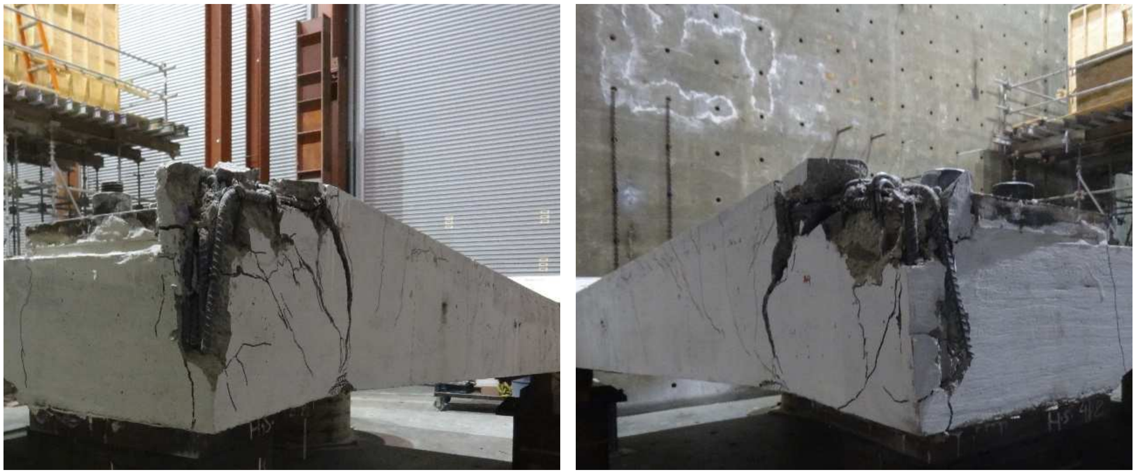

(a) (b)

Figure 3.47: Photograph of concrete breakout at two ends of the spandrel beam during the test at beam edge on specimen 2, (a) at support LC1, and (b) at support LC2.

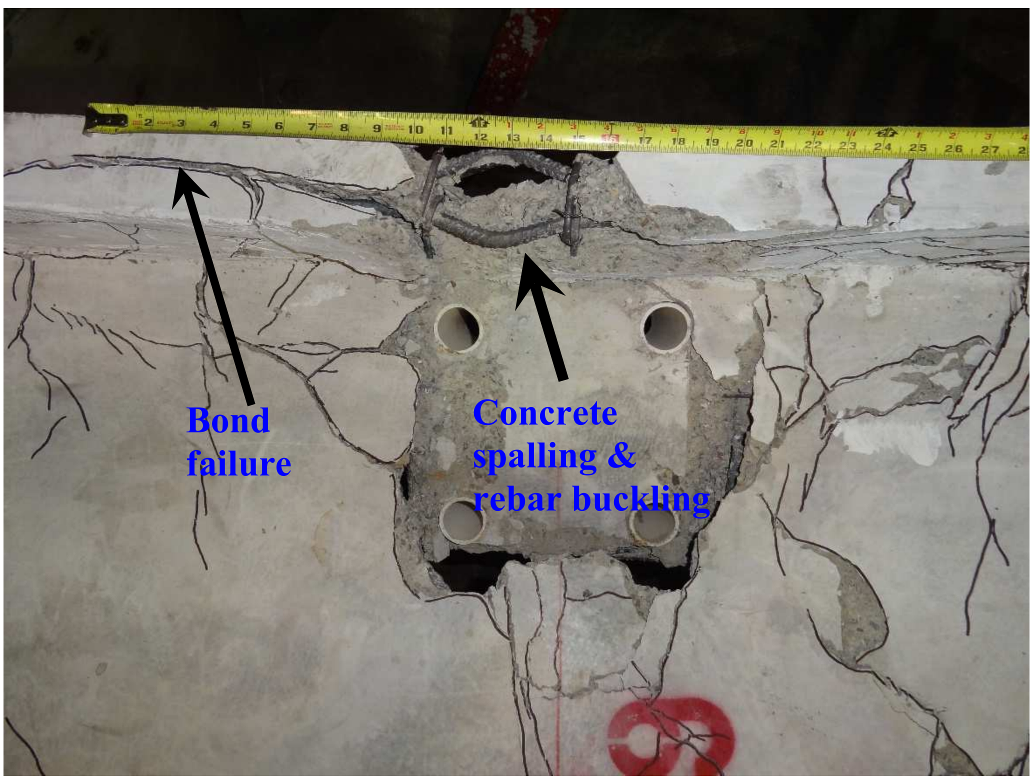

Figure 3.48: Concrete spalling and rebar bond failure at push location during test at beam edge on specimen 2.

3.5.2.4 Deflection Profiles

Out of plane deflections were recorded at discrete points using linear potentiometers installed under the slab. The profiles of the recorded deflection at individual linear-potentiometers during the test at the slab edge and the beam edge locations are shown in Figures 3.49 and 3.50.

Figure 3.49 (a) shows a schematic of the location and numbering of the linear potentiometers in the panels adjacent to the test location during the column removal test at the slab edge. Figure 3.49(b) shows the deflection at these linear potentiometer vs. the displacement at the edge of the slab at push location. As expected, large displacements are observed closer to the push location while smaller deflections are recorded away from the slab edge and near supports LC3, LC4 and LC5. At the maximum tip displacement of 10.7 in. at test location, locations L11 and L12 experienced a maximum deflection of 8.3 and 8.8 in., respectively. L06 experienced a comparatively smaller deflection of 6.3 in. as deflection along LC3↔LC6 varied proportionally with the distance from support LC3.

The displacement imposed on the slab decreased as the distance increased from the push location. Linear potentiometers L03 and L08 show very similar deflection profiles, maximum deflection of 1.7 in., as they are equidistant from the push location (83.5 in.). Similar to the measurements at L03 and L08, L04 (83.75 in.), L10 (84.0 in.) and L13 (85 in.) show small deflections in the order of 1.5 in. at the maximum deflection condition at the slab edge push location. Linear potentiometers L02, L05 and L09 show considerably lower deflections compared to other linear potentiometers in their vicinity as they are located close to the failure zone. Sensor L01 only shows minor deflection due to its remoteness from the test location and the failure surface on the specimen, with maximum deformation of only 0.15 in. at maximum deflection at the slab edge push location.

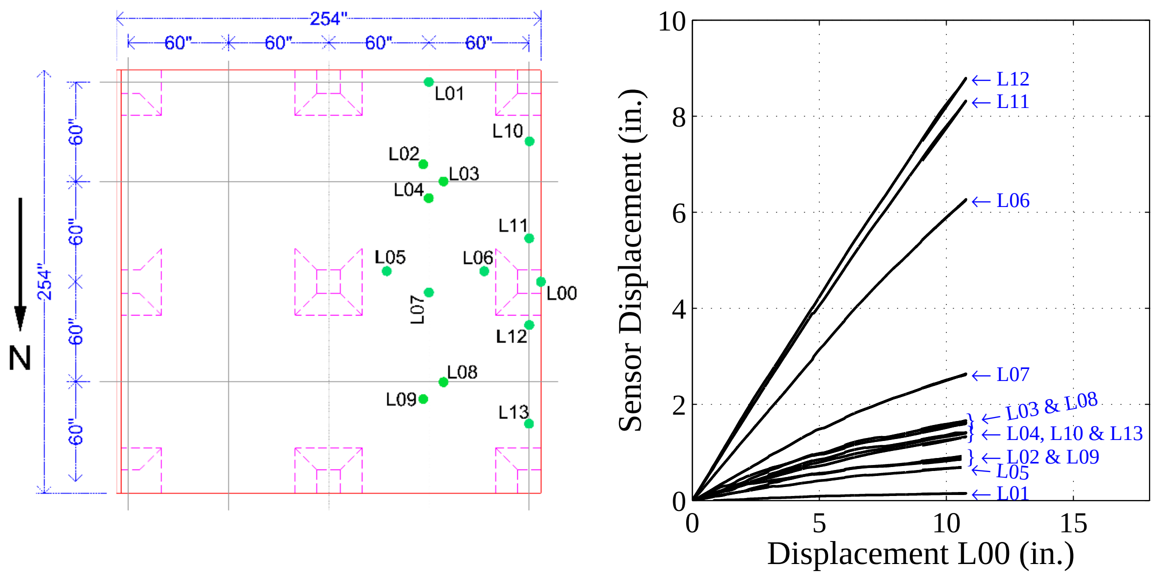

(a) (b)

Figure 3.49: Displacement profile at linear-potentiometers during test at slab edge, (a) location and naming of linear potentiometers in test panels, and (b) deflection at the linear potentiometers vs. displacement at the push location. Note: downward deflections are shown as positive values.

Figure 3.50(a) shows a schematic of the location and numbering of the linear potentiometers in the panels adjacent to the beam edge test location. Figure 3.50 (b) shows the deflection at these linear potentiometer vs. the displacement at the edge of the beam at push location. All the linear potentiometers show linear relation with the deflection at the push location until the deflection of 12.2 in. Beyond this, once the drop panel failed, none of the linear potentiometer show any significant deflection as the subsequent motion of the actuator caused torsion on the failed block and did not impose any additional deflection to the rest of the specimen. The deflection at L07 shows a sudden drop at the end of the test as it was connected to the concrete which spalled near the drop panel at support LC8. As expected large displacements were observed closer to the push location while smaller deflections were recorded away from the beam edge and near supports LC1, LC2 and LC3.

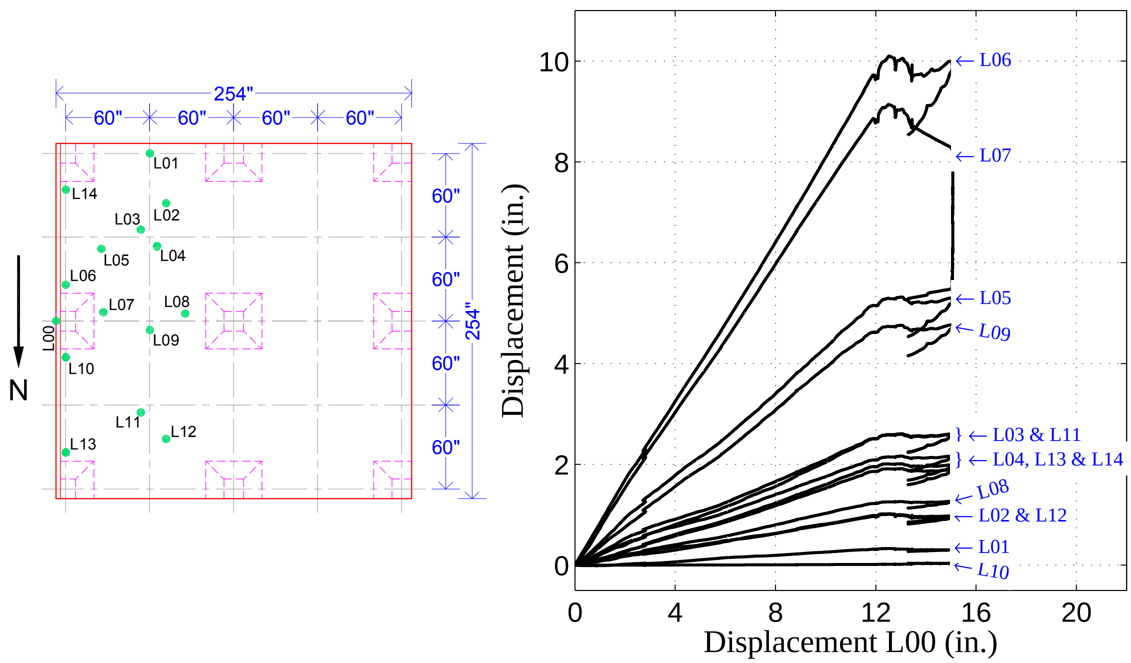

(a) (b)

Figure 3.50: Displacement profile at linear-potentiometers during test at beam edge, (a) location and naming of linear potentiometers in test panels, and (b) deflection at the linear potentiometers vs. displacement at the push location.

At maximum tip displacement of 12.2 inch at test location, L06 and L07, closest to the test location experienced maximum deflection of 10.0 and 9.1 in., respectively. It is to be noted that linear-potentiometer L10 did not record data during the course of the test and hence does not show any significant deflections. Sensors L03, L04, L11, L13 and L14 experienced a maximum deflection between 2.0 in. to 2.6 in. Sensors L02, L08 and L12 only experienced maximum displacement of about 1.2 in. due to their proximity to the yield surface resulting in smaller displacement demands at these locations. Sensor L01 only shows a small displacement of 0.3 in. due to its remoteness from the test and failure location. Sensor pairs L02/L12 and L03/L11 which were placed at symmetric locations about the test location shows very similar displacement profiles suggesting a symmetric failure of the specimen. Sensors L05 and L09 also show similar displacement profiles as their distance from the test location was similar resulting in similar displacements recorded at these locations.

3.6 Conclusions

3.6.1 Overview

This chapter summarizes the results of tests performed on two 1/3rd scale beam-slab specimens under gravity loads and simulated column failure at the corner and edge support locations. The specimen were detailed according to ACI-318 design guidelines from 1956, and as envisioned to be observed in non-ductile buildings.

Both specimen represent a portion of a typical floor slab, in this case with supports at nine locations (3×3 support or 2×2 panel configuration). Supports adjacent to simulated column failure locations were supported on multi-axis load cells, while 200-kips axial only load cells were used to provide support at other locations, to monitor the load at each column location during the tests.

3.6.2 Findings

Specimen 1 – Corner Support Failure: For all column removal scenarios, specimen 1 performed extremely well, attaining large displacements, on the order of 3 times the slab thickness (or 0.075 times the span length), with little to no loss in its load carrying capacity. The maximum vertical load attained at the three test locations was: 9.2 kips for the beam-beam corner, 1.2 kips at the slab-slab corner and 5.1 kips at the beam-slab corner. The maximum load capacities achieved during each test were 1.7 to 2 times higher than corresponding YLT estimates.

Using the multi-axis and axial only load cells, forces imposed on adjacent supports due to the corner column removal were recorded. For all tests, most of the load was transferred to the two adjacent supports, with remaining supports experiencing little to no change in force and moment demand. For the un-symmetric case, the beam-slab corner, the support connected by the stiffer connection experienced a larger force demand compared with other adjacent supports.

Physical damage observed during the tests were in agreement with that which would be suggested by yield line theory, where the cracks on the top surface formed between the adjacent supports, forming a triangular region of the slab which is expected to rotate upon yield. The observed damage to the specimen was primarily concentrated between the test location and yield line, with the remainder of the slab experiencing little to no damage. For the two tests where spandrel beams were present (beam-beam and beam-slab corner), shear and flexural cracks were observed on the beam between the test location and the adjacent supports.

Specimen 2 – Edge Support Failure: For the two column removal scenarios, the specimen performed well, attaining large displacements, on the order of 3 to 4 times the slab thickness, with little to no loss in its load carrying capacity. The maximum vertical loads attained at two test locations were: 9.2 kips for the slab edge and 18.8 kips at the beam edge test location, 2.2 and 1.2 times higher than YLT estimates. A lower enhancement was observed during the test performed at the beam-edge location due to the initial failure that occurred at the end of the beams.

During the test at both locations most of the load was transferred to the adjacent support locations. Sixty to seventy percent of the additional axial load applied was transferred to the two corner supports, while the center support carried another 15-20% of the axial load. The plasticity in the slab was spread over a width of approximately 20 to 40 inches. This plasticity occurred along the expected yield lines connecting the adjacent supports. This spread of plasticity was more prominent at the slab edge test location, where all the load was resisted by the slab. During the test at the beam edge, localized failure was observed due to several weak zones along the spandrel beam, which formed during the concrete pour.

******

Portions of following publications, for which author was the principal researcher and author, are contained in this chapter:

- Prasad, S. and Hutchinson, T. C. (201X), “Evaluation of Older Reinforced Concrete Floor Slabs under Edge Support Failure", ACI Structural Journal, (In review).

- Prasad, S. and Hutchinson, T. C. (2014), “Evaluation of Older Reinforced Concrete Floor Slabs under Corner Support Failure", ACI Structural Journal, Vol. 111, No. 4, pp 839-850.
- Prasad, S. and Hutchinson, T., (2014). "Experimental Evaluation of a 1/3rd scale Lightly Reinforced Concrete Slab under Uniform and Pull Down Load: Edge Conditions (Version B)." Structural Systems Research Project (SSRP) Report No. 14/02, Department of Structural Engineering University of California, San Diego, 100 pp.
- Prasad, S. and Hutchinson, T., (2014). "Experimental Evaluation of a 1/3rd scale Lightly Reinforced Concrete Slab under Uniform and Pull Down Load: Edge Conditions (Version A)." Structural Systems Research Project (SSRP) Report No. 14/01, Department of Structural Engineering University of California, San Diego, 85 pp.
- Prasad, S. and Hutchinson, T. C. (2013) “Behavior of Reinforced Concrete Flat Slab Systems under Corner and Center Support Failure Scenarios”, Proceedings of 10th International Conference on Urban Earthquake Engineering (CUEE), Tokyo, Japan, March.
- Prasad, S. and Hutchinson, T., (2012). "Experimental Evaluation of a 1/3rd scale Lightly Reinforced Concrete Slab under Uniform, Pattern and Concentrated Pull Down Load: Corner Conditions." Structural Systems Research Project (SSRP) Report No. 12/11, Department of Structural Engineering University of California, San Diego, 120 pp.

Chapter 4: Numerical Modeling and Validation

4.1 Introduction

To better understand the behavior of a beam-slab system under column failure scenarios, it is necessary to conduct experimental and/or numerical studies considering various design parameters and systematically evaluating the behavior and capacity of the system. However, it is not always feasible to conduct extensive number of experiments due to cost and time limitations. Therefore, in the present work a parametric analysis is conducted considering a broad range of important design parameters. However, prior to the parametric study which is presented in Chapter 5, the analysis tools to be used are evaluated against the available experimental results to access their accuracy. In this regard, this chapter presents the model selection protocol and results of the validation study. For this purpose, the results from the three push tests conducted at the corner locations of specimen 1 are compared against the results obtained from a detailed finite element model.

The 3-dimensional finite element model was created in the commercially available finite element software LS-DYNA (LSTC, 2013a, b). For this study version 7.0.0 version of the LS-DYNA solver was used. Although LS-DYNA is primarily used for high strain rate analyses (e.g. blast, impact, automobile crash) using explicit time integration, recent developments have introduced robust implicit analysis support, which are needed to analyze quasi-static loaded systems, similar to that presented in Chapter 3.

This chapter is organized into three sections:

- **Section 4.2: Description of LS DYNA Model**

  Details of the models, including their mesh strategy, material models, and element formulations implemented in LS-DYNA are presented. A summary is also provided to describe the contact definition at the interface between the multi-axis load cells and the specimen.

- **Section 4.3: Results Comparison**

  The results from the numerical models are compared with the results obtained from the tests performed at the three corner locations (Chapter 3). Of particular interest in these comparisons are the following: force-deflection relation for push tests, load distribution at supports, deflection profiles, and observed damage at the end of each push test.

- **Section 4.4: Summary Remarks**

  Conclusions regarding the performance of the LS-DYNA model are provided.

4.2 Description of LS DYNA Model

LS-DYNA is a multi-purpose finite element software developed by LSTC, Livermore, CA (LSTC, 2013a, b). Over the past few years, researchers have used LS DYNA to model and study behavior of reinforced concrete and steel structures (e.g. Liu et al. 2005; McConnell and Brown, 2011; Sadek et al., 2011; Shetye, 2013; Bao et al., 2014).

LS DYNA provides several element and material models for modeling reinforced concrete, either using eight node solid elements or four node shell elements. When modeling concrete using solid elements, rebar can be modeled using either a smeared approach (for some available material models only), or explicitly using two node beam elements. For this study, the concrete was modeled using eight node solid elements, and the rebar was explicitly modeled using two node beam elements. The multi-axis load cells were also modeled using four node shell elements. Details of the model, including geometry, boundary conditions and loading protocol are presented in the following sections.

4.2.1 Geometric Model

The meshing of all the parts were conducted using the pre and post processor LS Prepost. The model was divided into several '*PARTS'*, depending on the type of material, element formulation and the cross-sectional properties. This section provides an overview of the entire model including the physical model, the rebar-concrete interface, and boundary conditions applied to the model.

4.2.1.1 Concrete Model

To accurately capture the bending stresses along the failure zones, a finer mesh near locations of high non-linearity is needed. As three separate tests were performed on a specimen 1 (Chapter 3), three different models were created to maintain a reasonable model size for each push test. With each, the finer mesh was defined near the zones of highest non-linearity, while a coarser mesh was used to define remainder of the specimen. In the panel under consideration, four solid elements were used to define the thickness of the slab (i.e. solid element size in the thickness direction was $\frac{3}{4}$ in. = 0.75 in.), while the other three panels were modeled using two solid elements through the thickness (i.e. solid element size in the thickness direction was $\frac{3}{2}$ in. = 1.5 in.) with element aspect ratio between 1 and 2. The mesh size on the spandrel beams were selected to match the mesh size on the slab adjacent to the beams in each model.

Total number of solid elements in the model ranged between 90,000 to 110,000 depending on the corner under consideration. Figures 4.1 to 4.4 show the model of the concrete and the element mesh size provided for the models simulating the push at three corner locations. Drop panels were modeled at each support location by extruding the slab mesh in the vertical direction, and the slope to the drop panel was provided by approximating it by a *staircase* model (Figure 4.5). This was only done at locations where high non-linearity was expected, such as supports adjacent to the push location. It is noted that a skewed mesh in the drop panels could affect the convergence during the solution phase.

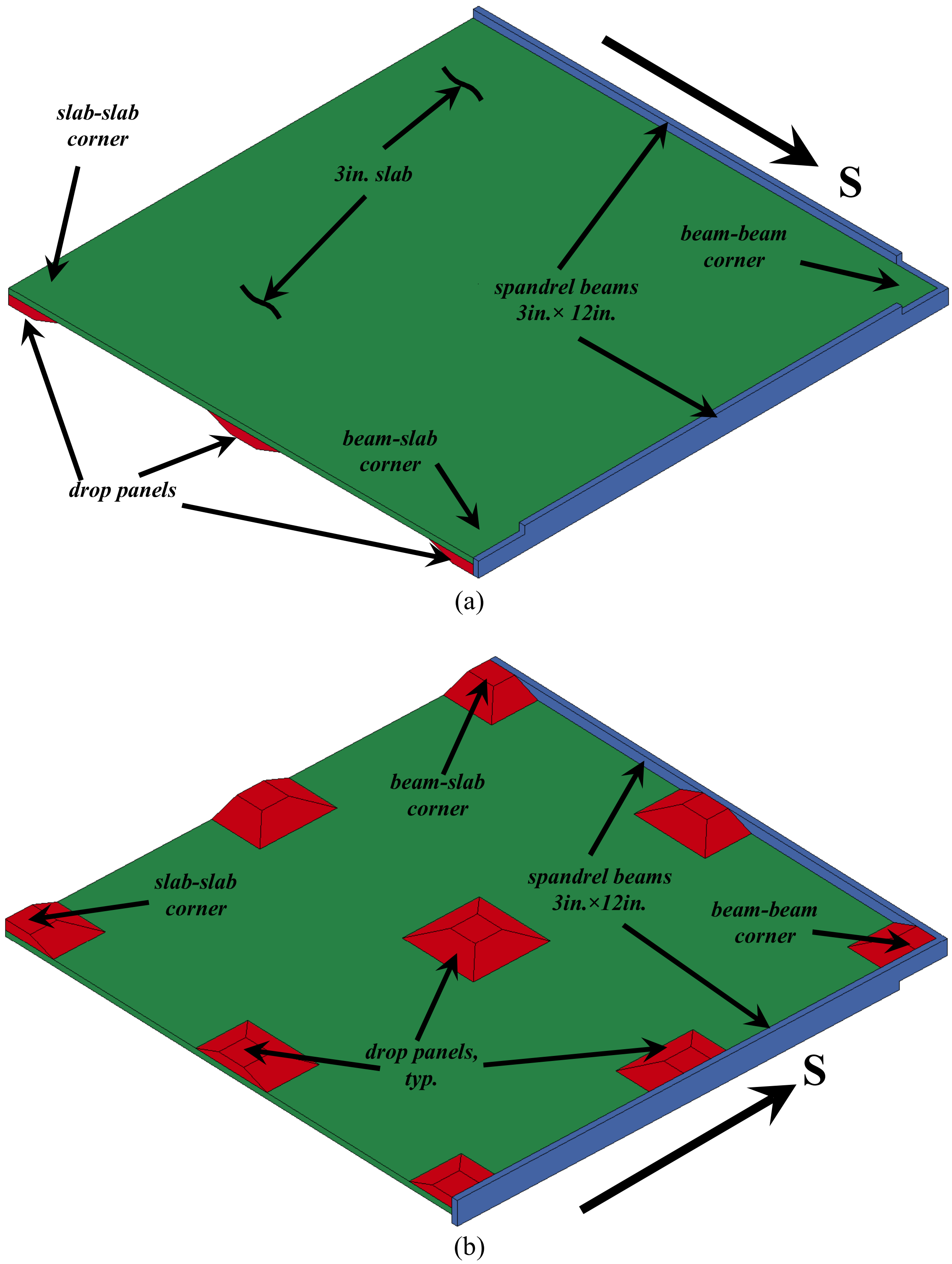

Figure 4.1: Isometric views of the concrete model implemented in LS DYNA. (a) top surface, and (b) bottom surface. Different concrete components are shown in different color, red-drop panels, green-slab deck, and blue-spandrel beams.

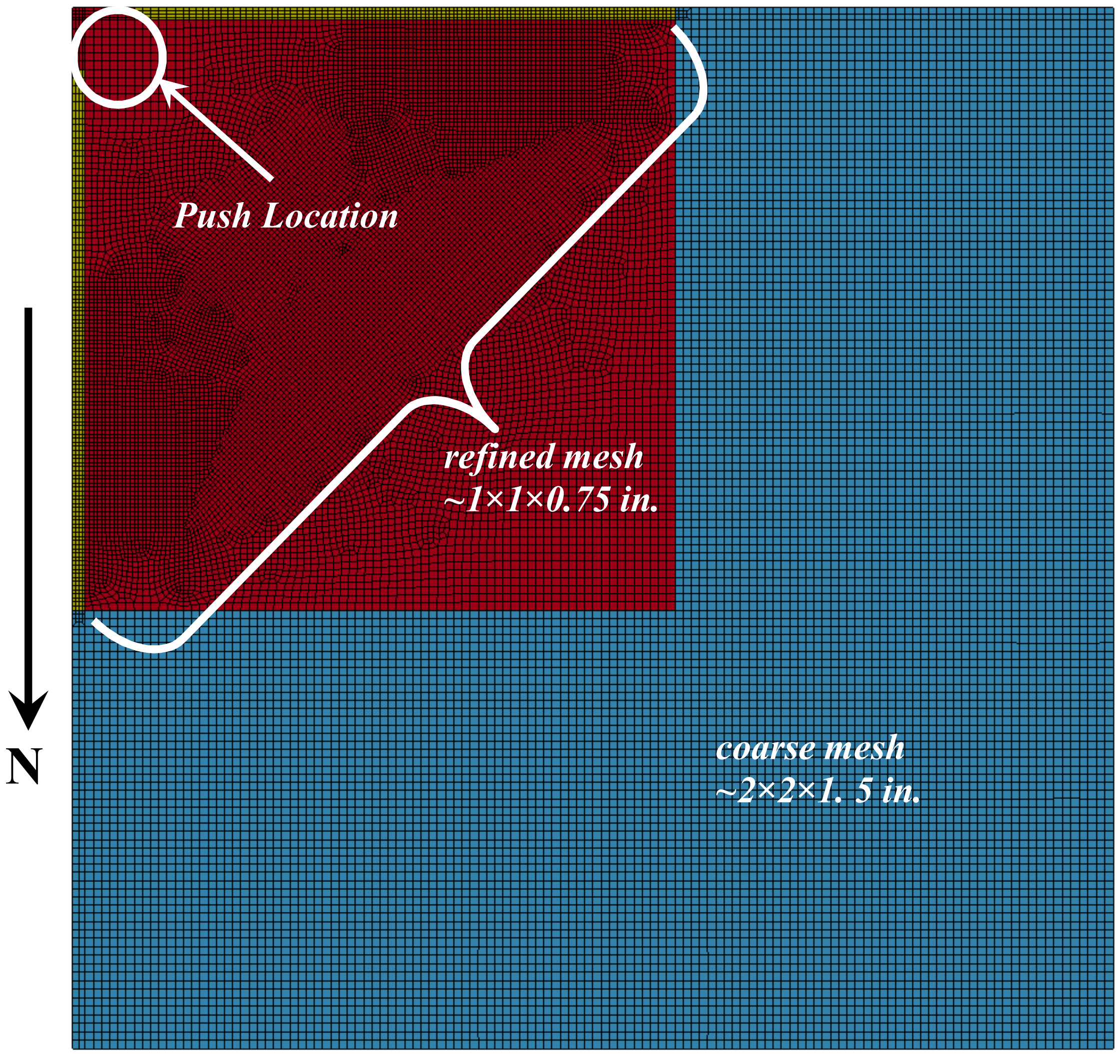

Figure 4.2: Top view of the concrete model implemented in LS DYNA for modeling push at the beam-beam corner. Total of 112,058 solid elements.

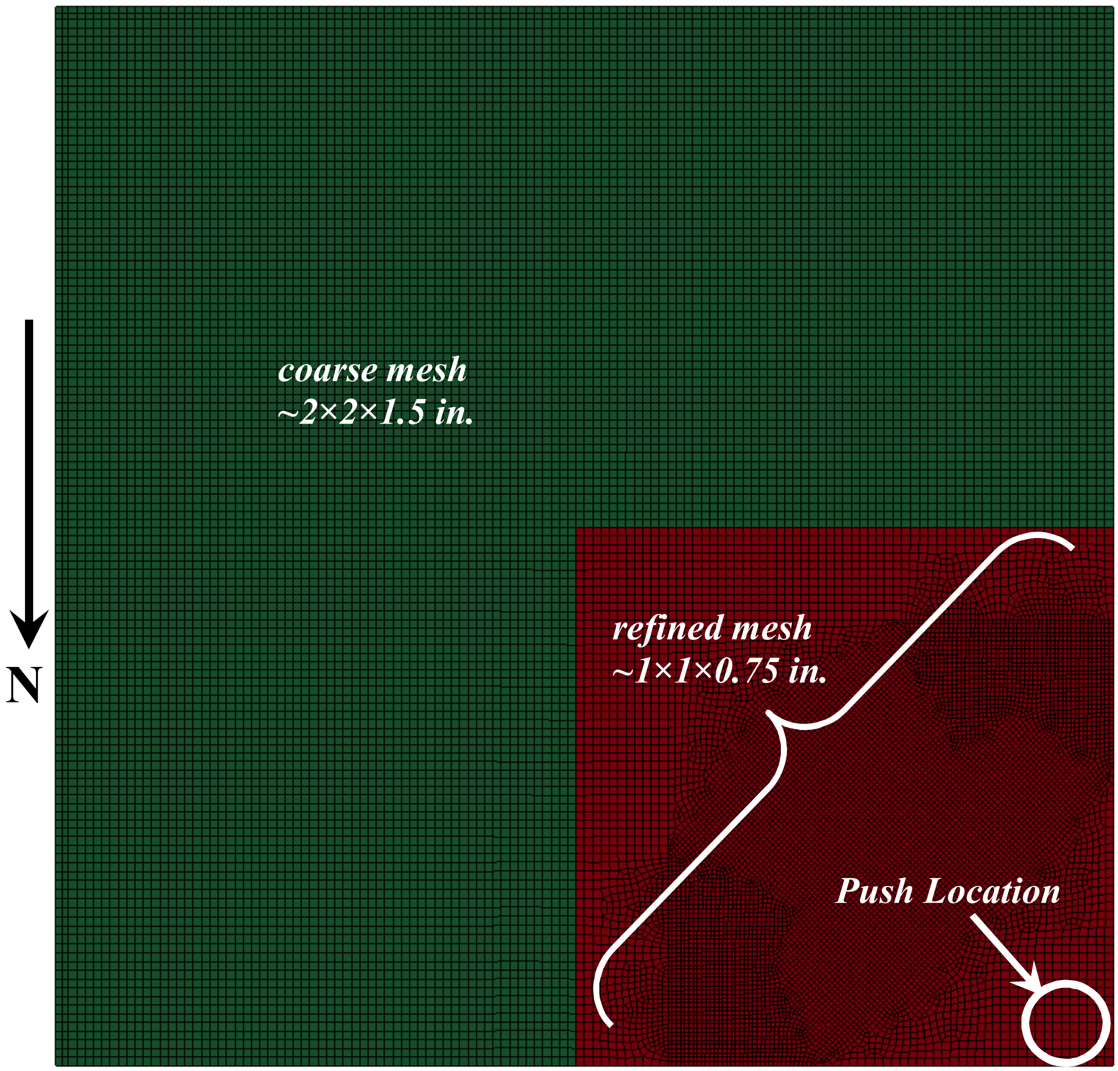

Figure 4.3: Top view of the concrete model implemented in LS DYNA for modeling push at the slab-slab corner. Total of 93,531 solid elements.

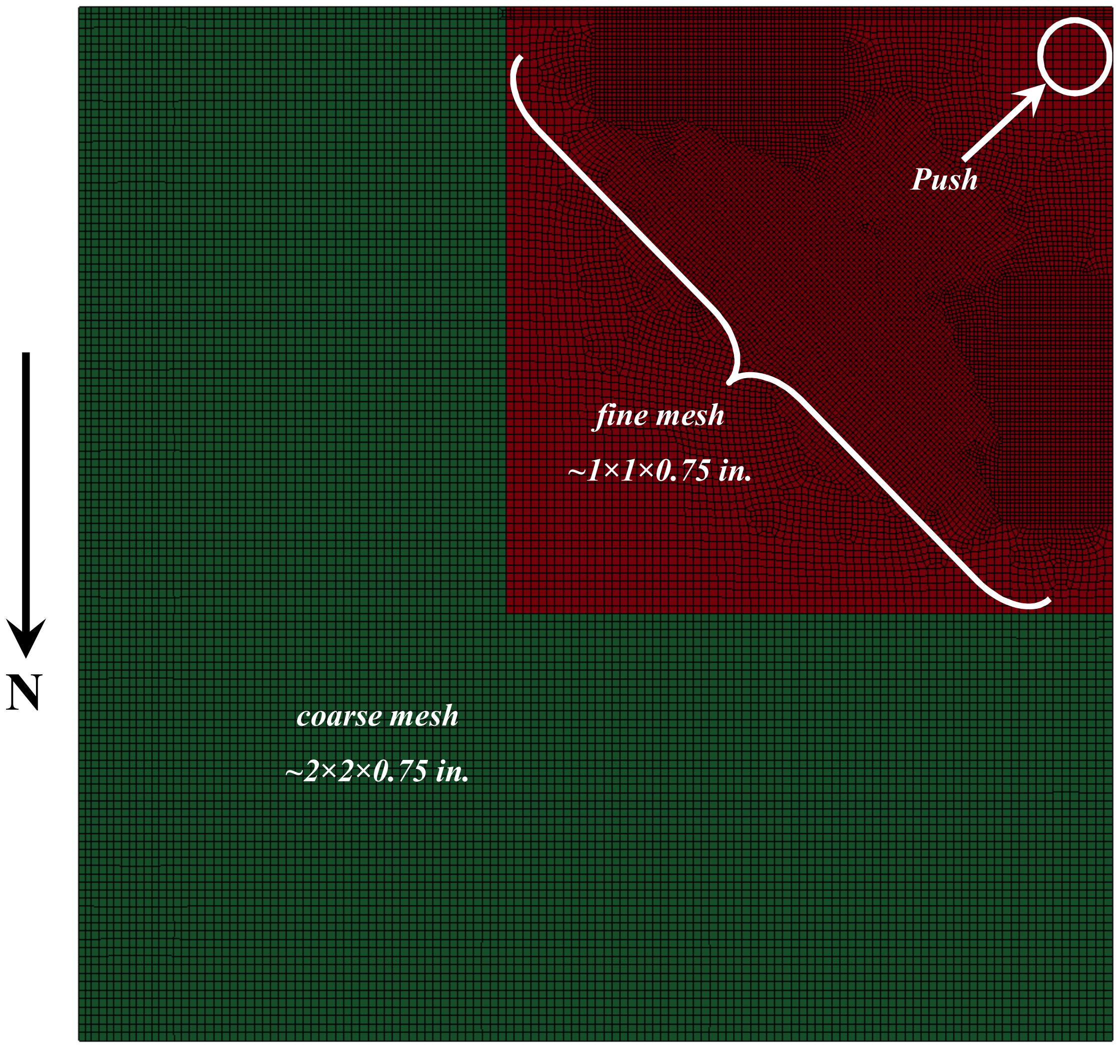

Figure 4.4: Top view of the concrete model implemented in LS DYNA for modeling push at the beam-slab corner. Total of 96,957 solid elements.

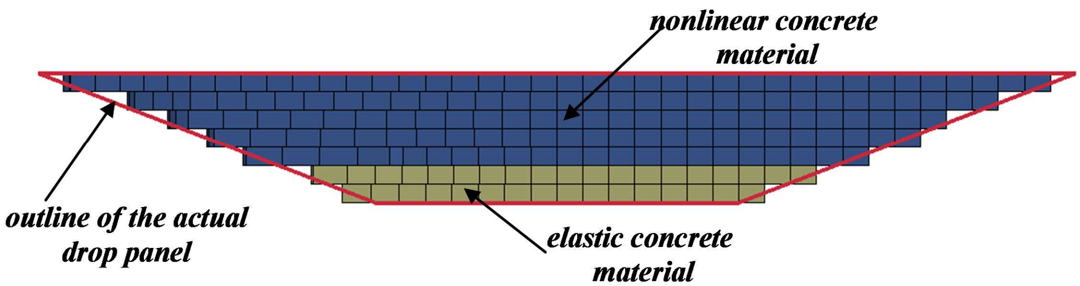

(a)

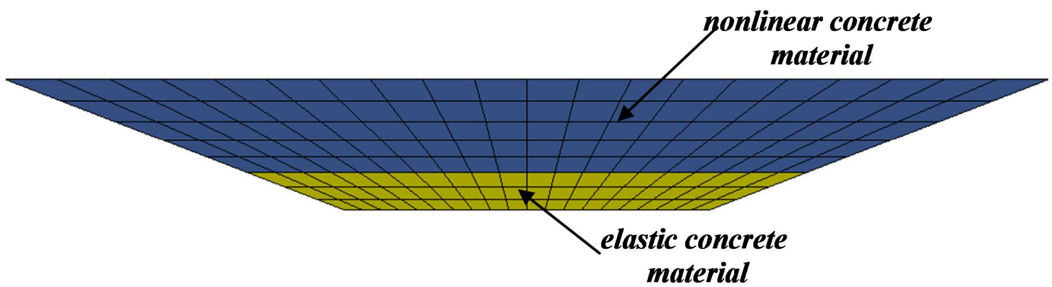

(b)

Figure 4.5: Side view of the drop panels, (a) staircase mesh provided at locations with non-linear behavior, and (b) drop panel mesh provided at other support locations. The figure also shows the elastic material used to define the bottom 2 to 3 layers of the drop panel to avoid numerical convergence issues due to contact with multi-axis load cell locations.

4.2.1.2 Rebar Model

The rebar was modeled using two node beam elements and were placed according to the construction drawings. In total eight parts were used to define all rebar:

i) beam longitudinal rebar (No. 4 rebar, Φ0.5 in., Grade 60),

ii) beam shear stirrups (No. 2 rebar, Φ0.25 in., Grade 40),

iii) and ***iv)*** slab bottom mat in the EW and NS direction (No. 3 rebar, Φ0.375 in., Grade 40),

v) and ***vi)*** slab top mat in the EW and NS direction (No. 3 rebar, Φ0.375 in., Grade 40),

vi) Extra rebar cage provided at the support drop panels (No. 3 rebar, Φ0.375 in., Grade 40), and

viii) extra rebar provided at the push locations (No. 3 rebar, Φ0.375 in.)

The length of the two node beam elements were defined such that the ratio of size of the beam elements and solid elements ranged between 1 and 2. This resulted in a beam element length of approximately 1.5 in. near the push location for each model, and 3 in. farther way in the other three panels. In total approximately 25000-35000 beam elements were defined for each model. Figures 4.6 to 4.9 provide a schematic of the rebar mesh used in the model.

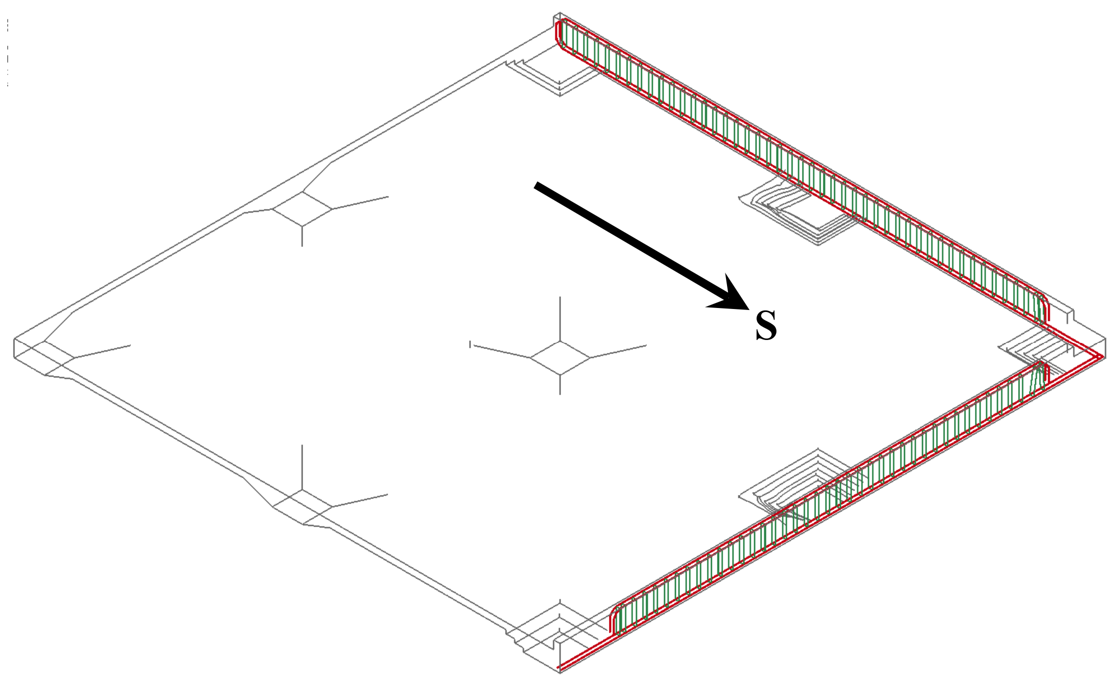

Figure 4.6: Isometric view of the beam rebar, red-#4 longitudinal rebar, and green-#2 shear stirrups. An outline of the concrete model is shown in grey.

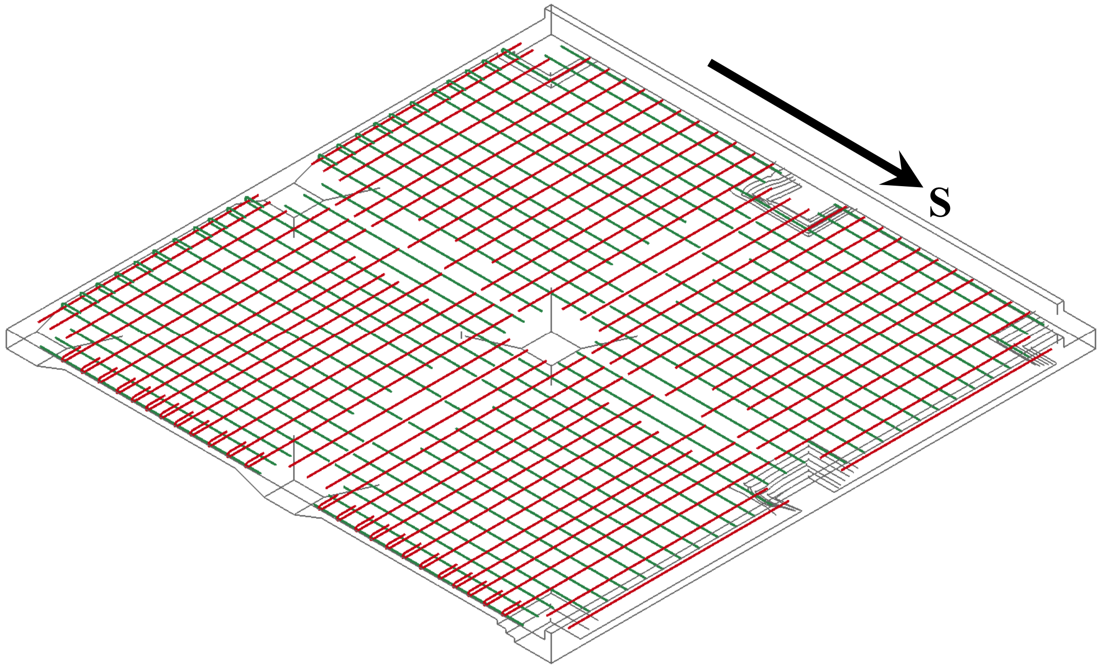

Figure 4.7: Isometric view of the slab bottom mat, red - EW #3 rebar, and green - NS #3 rebar. An outline of the concrete model is shown in grey.

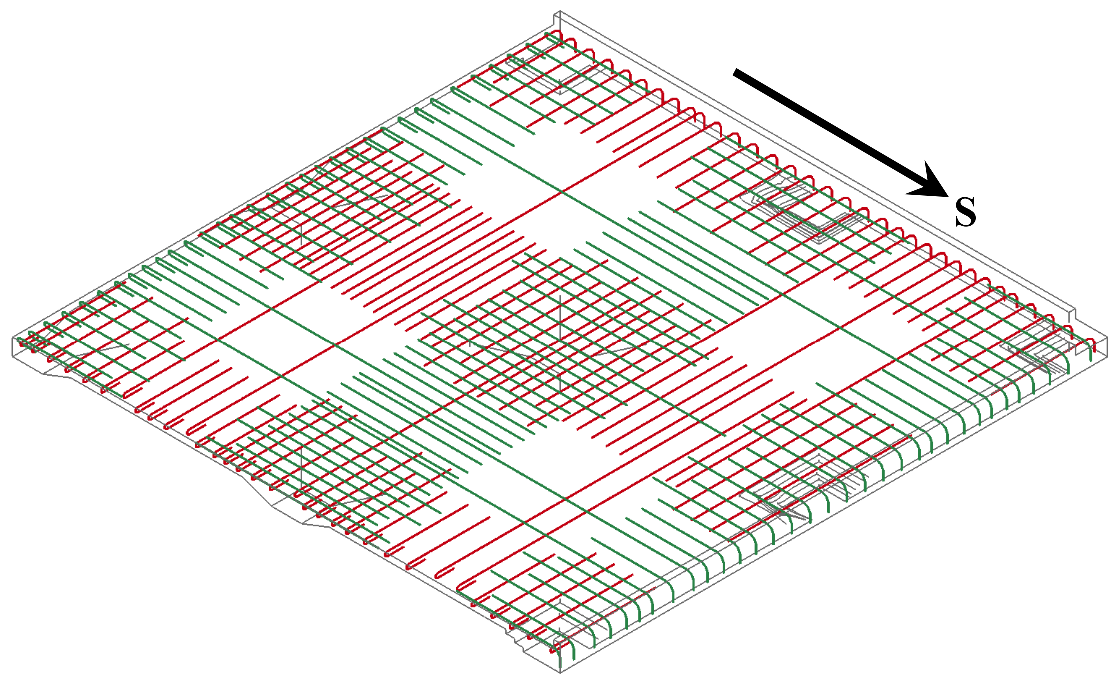

Figure 4.8: Isometric view of the slab top mat, red - EW #3 rebar, and green - NS #3 rebar. An outline of the concrete model is shown in grey.

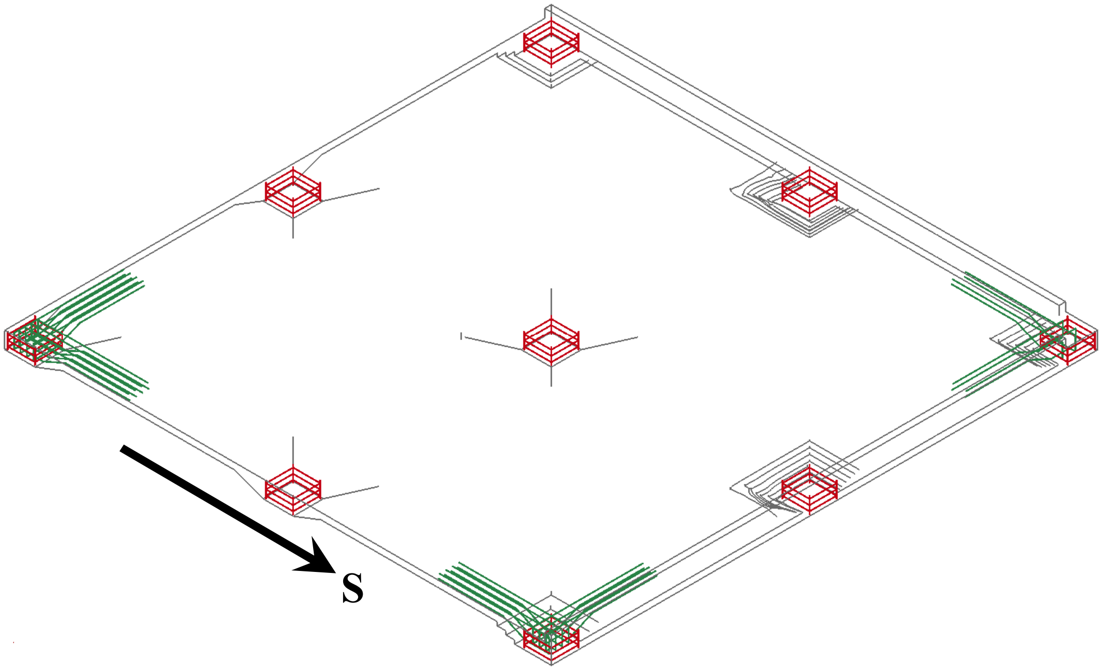

Figure 4.9: Isometric view of the extra reinforcement provided in the slab, red - #3 cage at support locations, and green - extra #3 rebar at push locations. An outline of the concrete model is shown in grey.

4.2.1.3 Beam and Solid Element Interface

For the rebar (modeled using two node beam elements) and the concrete (modeled using eight node solid elements) to interact with each other, an interface needs to be defined to ensure that the two meshes deform as a composite material. To achieve this, three methods are available in LS DYNA:

i) the beam nodes used to model the rebar share the same node with the solid element, thus providing a perfect bond between the two. This requires that care must be taken while meshing to ensure that the beam elements and solid elements share the same nodes.

ii) a bond slip behavior can be defined using **CONTACT_1D*. This method also requires that the beam nodes and solid element nodes are aligned along the same line.

During analysis, the beam nodes can slide parallel to the curve defined using the solid element nodes, but not in the transverse direction. Although this method is suitable for regular meshes, this option is currently not available for implicit analysis.

iii) to define a perfect bond between the beam nodes and the solid nodes using **CONSTRAINED_LAGRANGE_IN_SOLID* (*CLIS*) formulation. This removes the burden of aligning the beam and solid element nodes and they can be modeled independently. For this study, this option was used for its simplicity in modeling the structure. It is noted that this assumes the absence of any bond slip behavior during the test at the three corner push locations. When a coupling between beam and solid elements are defined using CLIS, only the end nodes of the beam elements are coupled to the solid elements.

To define this constraint, two **SET_PART* are defined: 1) master set which consists of all the parts consisting of solid elements (concrete), and 2) slave set, which consists of all the parts used to model the beam elements (rebar). During the simulation, the movement of the beam nodes and the solid nodes are tracked at the coupling points (*NQUAD*) and depending on the relative motion between the two elements, coupling forces are applied to the beam and solid element nodes. Currently, in implicit analysis only the end nodes of the beam elements are coupled with the solid element.

4.2.1.4 Load Cell and Actuator Model

Shell elements were used to define the multi-axis load cells, while the axial only load cells at four corner locations were defined using two node beam elements. The multi-axis load cells were divided into four parts:

i) top plate with thickness of 1.5 in.,

ii) cylindrical load cell with thickness of 1 in,

iii) bottom plate with thickness of 2.25 in., and

iv) Φ1.5 in. beam elements used to define the bolts connecting the multi-axis load cells to the specimen. These bolts were also constrained to the solid elements using **CONSTRAINED_LAGRANGE_IN_SOLIDS* as described in the previous section.

Due to the circular shape of the connection between the plates and the cylinder, it was not economical to maintain a square mesh in the shell elements. Care was provided to ensure that the cylinder had a refined mesh to accurately capture the behavior of the load cells. On average the element size in the multi-axis load cells varied between 0.8 to 2.0 in., with smaller elements on the top plate and larger element size on the bottom plate. In total, approximately 9000 elements were used to define all of the five multi-axis load cells in each model. Figure 4.10 shows the mesh used to define the three parts for each multi-axis load cells. Figure 4.11 shows the overall model with multi-axis load cells and the connecting bolts.

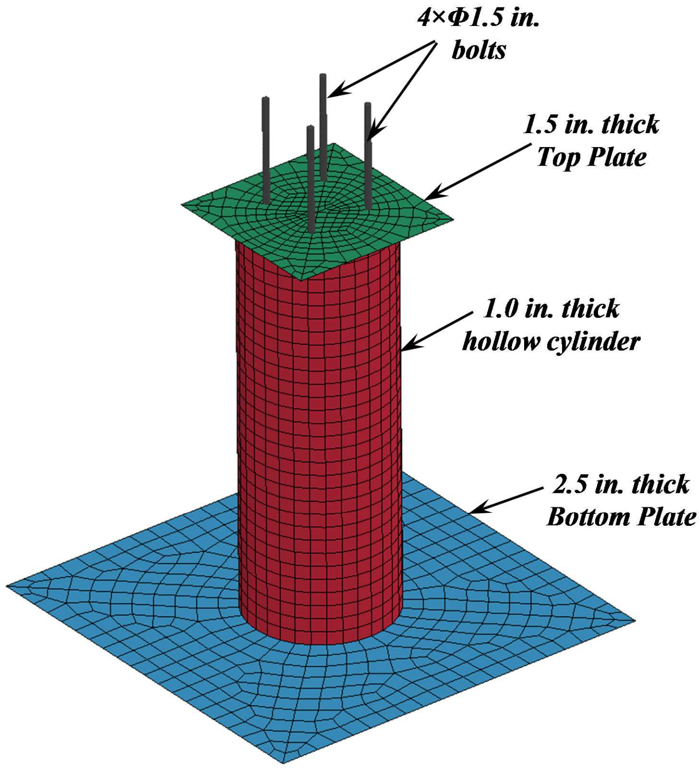

Figure 4.10: Mesh provided in an individual load cell. Four parts of the load cell are shown, green-top plate, red-steel pipe, blue-bottom plate, and black-connecting bolts.

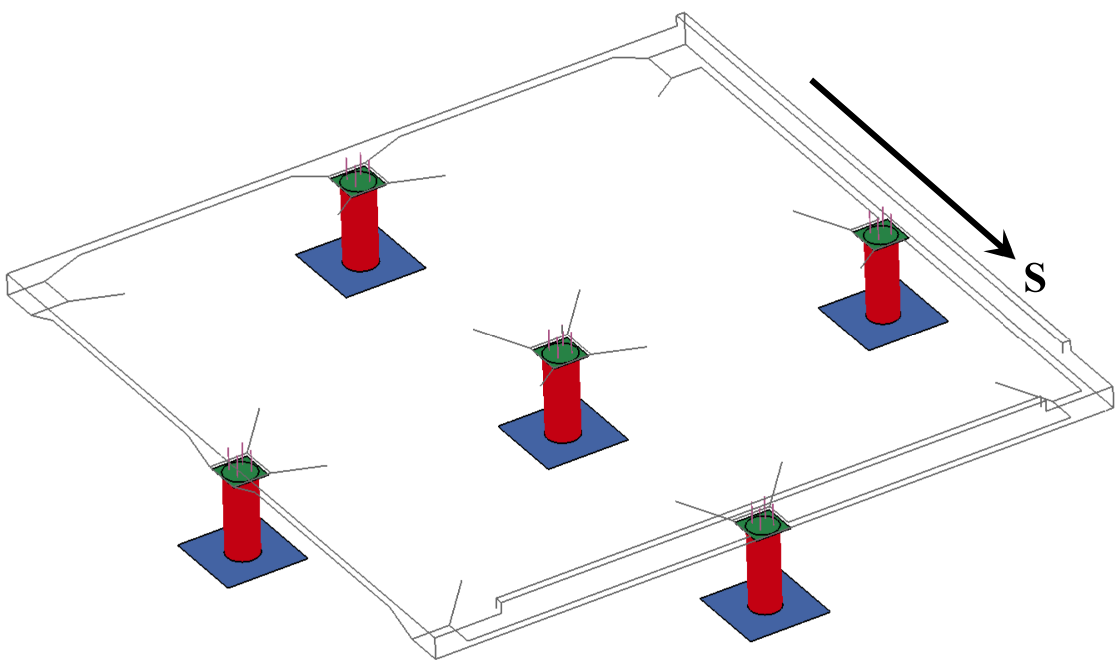

Figure 4.11: Isometric view of the specimen showing the multi-axis load cells with the connecting bolts. An outline of the concrete specimen is shown in grey.

The axial only load cells and the actuator at the push location were modeled using two node beam elements with a circular cross section of Φ10 in. As the single integration point solid elements used to define concrete do not have rotational freedom, the beam elements were constrained to the nodes on the bottom surface of the corner drop panels using **CONSTRAINED_NODAL_RIGID_BODY*. The *nodal rigid body* was defined by specifying a set of nodes using **NODE_SET*, where the first node in the set is the master node and has six-degrees of freedom (beam element node). The rest of the nodes in the set (nodes used to define the concrete elements) are constrained to the master node and behave as a rigid body, thus allowing transfer of both rotations and translation between the beam and solid elements. Figure 4.12 shows the nodal rigid body defined at one of the axial only load cells. It is noted that the actual diameter of the beam cross-section is not shown in the figure.

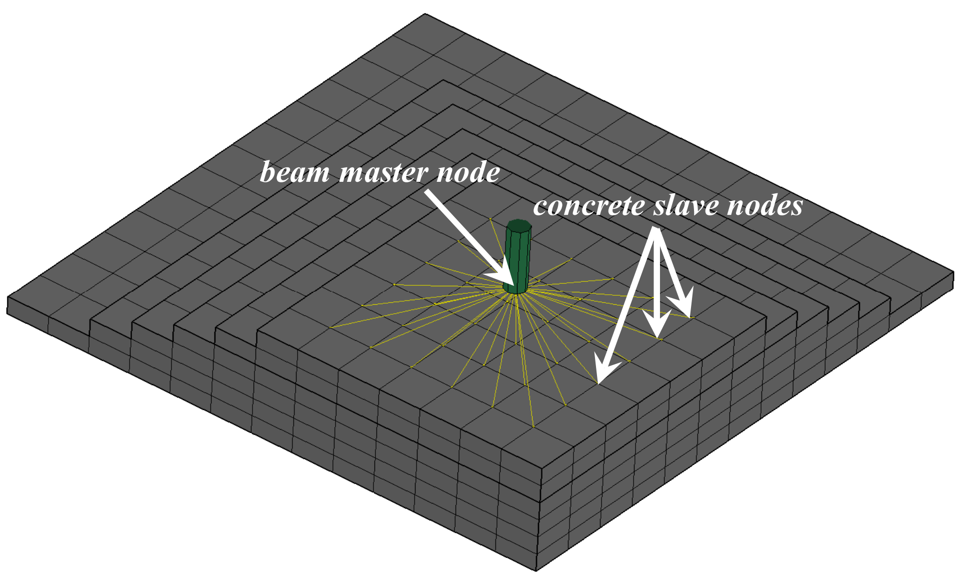

Figure 4.12: Nodal rigid body definition at one of the axial load cell locations. All the nodes behave as a part of rigid body, thus transferring rotation and translation.

4.2.1.5 Concrete and Load Cell Interface Definition

Figure 4.13 shows the connection details provided at each multi-axis load cell location (Prasad and Hutchinson, 2012). During the test, the load transfer between the concrete specimen and the multi-axis load cells occurred through tension in the four Φ1.5 in. bolts and compression through the concrete and top plate interface. To accurately capture the force transfer between the concrete specimen and the load cells, the interface contact between the concrete and the top plate of the load cells must be defined.

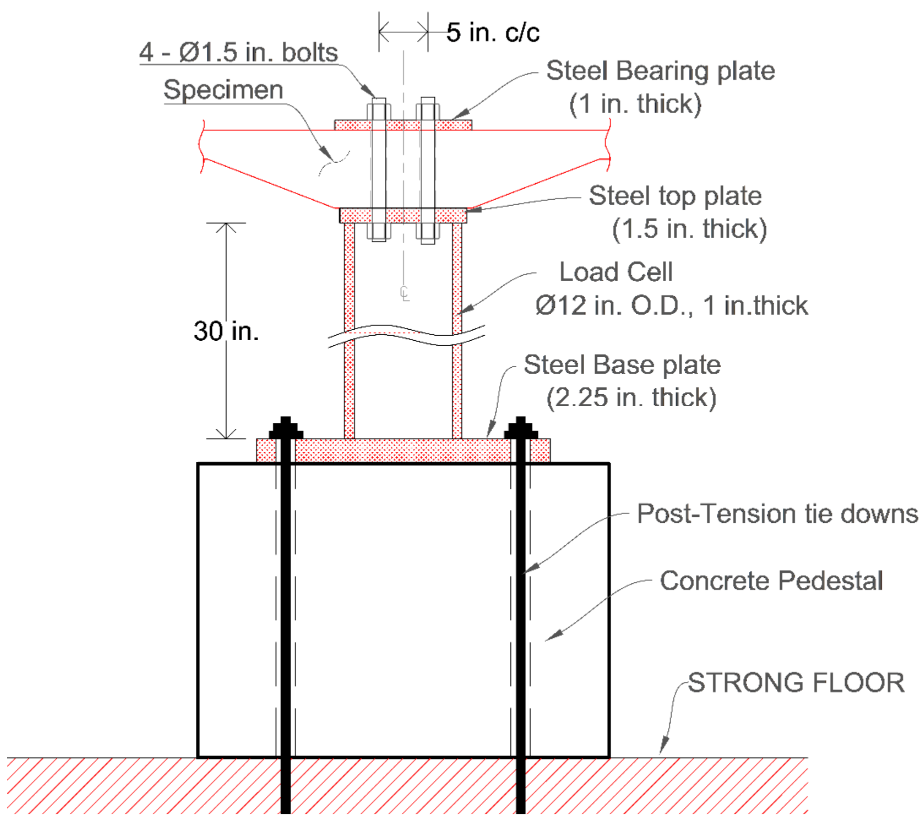

Figure 4.13: Connection detail between the multi-axis load cell and test specimen.

LS DYNA provides several methods to capture the force transfer between two interfaces undergoing contact using **CONTACT_OPTION*. Of the several available contact methods, for this study, **CONTACT_AUTOMATIC_SURFACE_TO_SURFACE* was used to define the interface between the two surfaces. During the iterative process, the solver internally calculates the penetration between the slave and the master surfaces defined using **SET_SEGMENT* and applies normal force on the surfaces to overcome penetration, and the friction force parallel to the surface based on the coefficient of friction. Apart from defining the surfaces using **SET_SEGMENT*, in each contact definition, all other input parameters were taken as their default values.

4.2.2 Elements used in LS DYNA

LS DYNA provides a suite of element formulations for two node beam elements, four node shell elements and eight node solid elements used to model rebar, concrete and multi-axis load cells, respectively. This section provides a brief discussion on the element formulations used in this numerical study.

4.2.2.1 Eight Node Solid Elements

LS DYNA provides different solid element formulations which are defined using **SECTION_SOLID*. Different solid element formulations can be selected under the **SECTION_SOLID ELFORM* option. *ELFORM* = 1, which corresponds to the constant stress formulation (one integration point at the center of the element) is used for modeling the concrete in this study. This solid element formulation has three translational degree of freedom at each node (total of $8\times3 = 24$ degrees of freedom per element), and is the default solid element formulation in LS DYNA.

Although a single point integration formulation is effective for modeling non-linear material behavior and capturing large deformations, it does suffer from "hourglassing" or zero-energy modes. Figure 4.14 shows two of the twelve hourglass modes possible in eight node under-integrated solid element. To avoid zero energy deformations, or hourglassing, an artificial stiffness is added to the eight node solid elements to resist these zero-energy deformation modes using the keyword **HOURGLASS* or **CONTROL_HOURGLASS* in LS DYNA. The choice of hourglass control is dependent on the type of simulation, and stiffness based hourglass control is suggested for implicit simulations (viscous based hourglass control being the other option used in high strain rate analysis). For implicit analysis, stiffness based hourglass control was provided. The amount of hourglass stiffness was defined by the parameter *QM*, which is usually set in range of 0.01 to 0.1 for non-linear analyses to avoid overly stiff response at large deformations. As a large value of hourglass coefficient would cause stiff response at large deformation, while a small value would be inefficient in preventing the hourglass modes, for this study the hourglass coefficient (QM) was set to a value of 0.05.

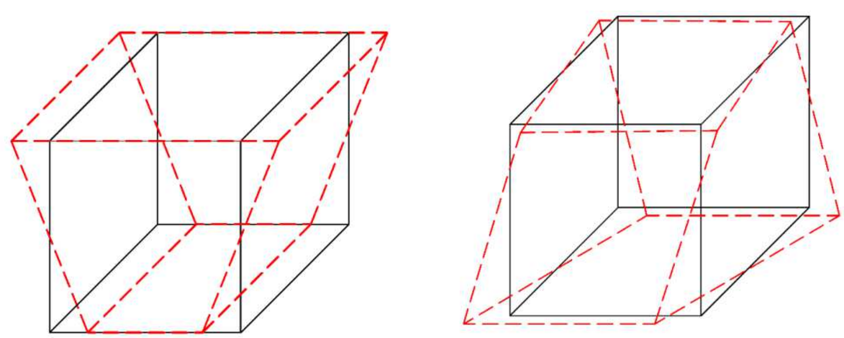

Figure 4.14: Two of the twelve hourglass modes in 8 node solid elements with one integration point. Black solid lines are the un-deformed shapes of the solid elements, and red dashed lines are the possible zero energy hourglass modes.

4.2.2.2 Two Node Beam Elements

Rebar was explicitly modeled using two-node beam element formulations available in LS DYNA. Different beam formulations can be used by changing the parameter *ELFORM* under the keyword **SECTION_BEAM*. For this simulation, the default formulation based on Hughes-Liu beam (*ELFORM* = 1) formulation is used for modeling the beam elements. Cross section of the beam is defined by specifying the cross section type as 1 under parameter *CST*, corresponding to tubular or circular sections, and then defining the outside diameter of the rebar to be equal to the nominal rebar diameter for #2, #3 and #4 rebar. Table 4.1 provides a summary of the different parameters used for defining the No. 2, No. 3, and No. 4 rebar.

Table 4.1: Beam section parameter for rebar defined using *SECTION_BEAM

Parameter	**Description**	**Rebar Size**		
		No. 2	**No. 3**	**No. 4**
ELFORM	Hughes-Liu formulation	1	1	1
SHRF	shear factor	0.83	0.83	0.83
CST	cross-section type	1	1	1
TS1 (TS2)	outer diameter at node 1 and 2	0.25 (in.)	0.375 (in.)	0.5 (in.)
TT1 (TT2)	inner diameter at node 1 and 2	0.0 (in.)	0.0 (in.)	0.0 (in.)

The bolts used to tie the multi-axis load cells to the specimen are also explicitly modeled using beam elements to capture the force transfer mechanism between the concrete specimen and the multi-axis load cells. These bolts were defined using a circular cross-section with beam element diameter of 1.5 in. The axial only load cells at the corner locations and the actuator head are also modeled using circular beam sections with diameter of 10 in. Table 4.2 provides a summary of the different parameters used for the axial load cell and actuator, respectively.

Table 4.2: Beam section parameter for axial load cells and actuator defined using *SECTION_BEAM

Parameter	Description	Value
ELFORM	Hughes-Liu formulation	1
SHRF	shear factor	0.83
CST	cross-section type	1
TS1 and TS2	outer diameter at node 1 and 2	10.0 (in.)
TT1 and TT2	inner diameter at node 1 and 2	0.0 (in.)

4.2.2.3 Four Node Shell Elements

The multi-axis load cells were modeled using four node, fully integrated shell elements (*ELFORM 16*) with 4 in-plane integration points using **SECTION_SHELL*. Three different shell sections were defined with different thickness, for top plate, steel cylinder and bottom plate of the load cell. Apart from the parameters *ELFORM* and the shell thickness at four nodes (*T1* through *T4*), all other parameters were taken as their default values. Table 4.3 provides a summary of the input parameters used to define the three shell sections.

Table 4.3: Shell section parameter for multi-axis load cell using *SECTION_*SHELL*

Parameter	Description	Top Plate	Load Cell	Bottom Plate
ELFORM	fully integrated	16	16	16
SHRF	shear factor	0.83	0.83	0.83
T1–T4	shell thickness	1.5 (in.)	1.0 (in.)	2.5 (in.)

4.2.3 Material Models in LS DYNA

This section presents details of the material models assigned to the various elements of the model. Five different materials are defined, namely; two nonlinear materials for each of the Grade 40 and Grade 60 rebar, one nonlinear concrete material, and two elastic materials used to model the load cells and concrete at base of the drop panels (Figure 4.5, to avoid convergence issues during implicit solution).

4.2.3.1 Steel Material Model

Several material models are available in LS DYNA for capturing the behavior of steel in both elastic and inelastic domain. One such material model is **MAT_024* (**MAT_PIECEWISE_LINEAR_PLASTICITY*). This material model provides the user the flexibility to define either a bilinear elastic-plastic behavior, or an arbitrary post-yield stress-strain using a curve. A curve is defined using **DEFINE_CURVE* function in LS DYNA where the X-axis or abscissa of the curve represents the effective plastic strain and the Y-axis or the ordinate of the curve represents the true stress. The effective plastic strain and true stress are given by:

$$\left.\begin{aligned}
\varepsilon_{True} &= \ln\left(1+\varepsilon_{Engg}\right) \\
\sigma_{True} &= \sigma_{Engg}\left(1+\varepsilon_{Engg}\right) \\
\varepsilon_{Eff} &= \varepsilon_{True} - \frac{\sigma_{True}}{E_{Elastic}} \approx \varepsilon_{True} - \varepsilon_{Yield}
\end{aligned}\right\} \quad \text{Equation 4.1}$$

where $\varepsilon_{\mathrm{Engg}}$ is the engineering strain, σ_{Engg} is the engineering stress, $\varepsilon_{\mathrm{Yield}}$ is the yield strain, and E_{Elastic} is the initial elastic modulus of the material. It is noted that the 1D element (i.e. two node beam element) used to model the rebar does not account for "necking" and hence the Y-axis of the curve was defined as σ_{Engg} instead of σ_{True}. This material model also has the option of element erosion to model rupture when the effective plastic strain is larger than a certain limit using the user input parameter *FAIL* in the material model. The eroding strain is defined for the Grade 40 and Grade 60 steel based on coupon tests that were performed before the beam-slab specimen test. It is however noted that, rebar, when modeled using two-node beam element only captures failure or erosion due to axial strains, and any shear failure of the rebar is not modeled.

Using the stress-strain curve obtained from the rebar tension tests on No. 3 (Grade 40) and No. 4 (Grade 60) rebar, the behavior of the Grade 40 and Grade 60 is defined to best fit to the LS-DYNA steel model. As no tests were performed on the #2 smooth rebar used for providing shear stirrups in the spandrel beams, its stress-strain behavior was assumed to be similar to Grade 40 rebar. Table 4.4 provides a summary of the input parameters used to define the two rebar materials using

**MAT_PIECEWISE_LINEAR_PLASTICITY*. Appendix C provides the input curves used to define the post-yield behavior of the two steel material.

Figure 4.15 shows a comparison between the actual stress-strain curve of the rebar and the corresponding stress-strain curve from the two LS-DYNA material models for Grade 40 and Grade 60 rebar in tension. It is observed that the material models are able to capture the stress-strain behavior of the rebar in both the elastic and plastic regions. It is noted that for either rebar material, stress reduction just before bar fracture (fracture shown by ***X*** in Figure 4.15) cannot be captured as the strength reduction in this material model results in model instability in implicit time integration.

Table 4.4: Values for the parameters as input to the LS DYNA steel model

Parameter	**Definition**	**Grade 40 (Grade 60)**	**Units**
RO	mass density	7.5E-04 (7.5E-04)	lbf-s^2/in
E	elastic modulus	2.825E+07 (2.685E+07)	psi
PR	Poisson’s ratio	0.3 (0.3)	--
SIGY	yield stress	4.61e+04 (6.8e+04)	psi
FAIL	failure strain	0.20 (0.16)	in./in.
LCID	curve ID to define post yield behavior (see appendix C)	1 (2)	--

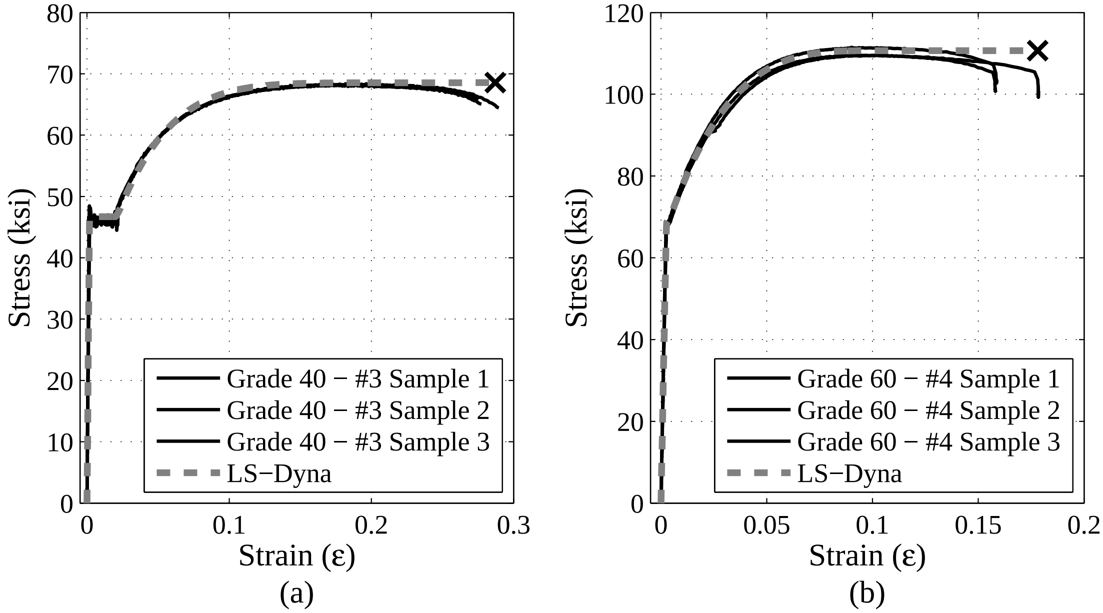

Figure 4.15: Comparison between stress-strain response from the rebar tension tests and the LS DYNA model: (a) Grade 40 slab rebar, and (b) Grade 60 beam rebar. X at the end of the LS DYNA material model identifies rebar fracture.

4.2.3.2 Concrete Material Model

LS-DYNA provides several concrete models where the behavior of the material is calculated using the basic strength data (e.g. f'c from concrete cylinder test), thus removing the burden of comprehensive tests (triaxial compression, triaxial tension etc.) to characterize complete concrete material behavior. Concrete material models available for modeling concrete using eight node solid elements in LS DYNA are **MAT_PSEDO_TENSOR (MAT_16), *MAT_WINFRITH_CONCRETE (MAT_84/85), *MAT_CONCRETE_DAMAGE_REL3 (MAT_072R3)* and **MAT_CSCM* _CONCRETE *(MAT_159)*. For this study **MAT_**CSCM**_CONCRETE* (**C**ontinuous **S**urface **C**ap **M**odel) is selected for modeling concrete as **MAT_84/85* does not account for damage in compression, i.e. it behaves in an elastic perfectly plastic manner under compression and does not account for shear dilation. In addition, **MAT_72R3* showed convergence issues during the initial testing of the model when using implicit time integration.

MAT_CSCM* (*C**ontinuous **S**urface **C**ap **M**odel*) is a concrete model based on work of Murray et al. (2007) and Murray (2007) which was developed for the Federal Highway Administration to study road side safety structures. This material model uses a smeared crack approach to model the reduction in concrete strength at large strains. The softening behavior of concrete in tension and compression is associated with the fracture energy of concrete in tension and compression, which in turn is related to concrete compressive strength and maximum aggregate size, based on CEB-FIP 1990. For this study, the concrete compressive strength was defined based on the cylinder tests that were performed on the day of the push tests and the maximum aggregate size was based on the concrete mix design obtained from the concrete supplier. A concrete material was defined based on the average strength of concrete between the three push tests ($f'_c = 6500$ *psi*). Table 4.5 provides a summary of the input parameters used to define the concrete material in LS-DYNA. It is noted that the initial elastic modulus and the tensile strength are based on CEB-FIP 1990 recommendations.

Figure 4.16 shows the stress-strain curve of the 6500 psi concrete materials defined in LS DYNA under uniaxial tension and compression. This material also has the option of eroding elements when the maximum principal strain is greater than a certain value defined using the parameter *ERODE* in the material definition. The element is eroded or removed from the numerical simulation if the maximum principal strain exceeds 1-ERODE. Although erosion of solid elements is non-physical and might result in convergence issues if significant number of elements are removed during implicit integration, a value of 1.2 was selected to remove elements which become highly distorted during the simulation while ensuring that no elements were removed during normal run. This ensures that the numerical analysis does not become unstable due to large distortion in few elements.

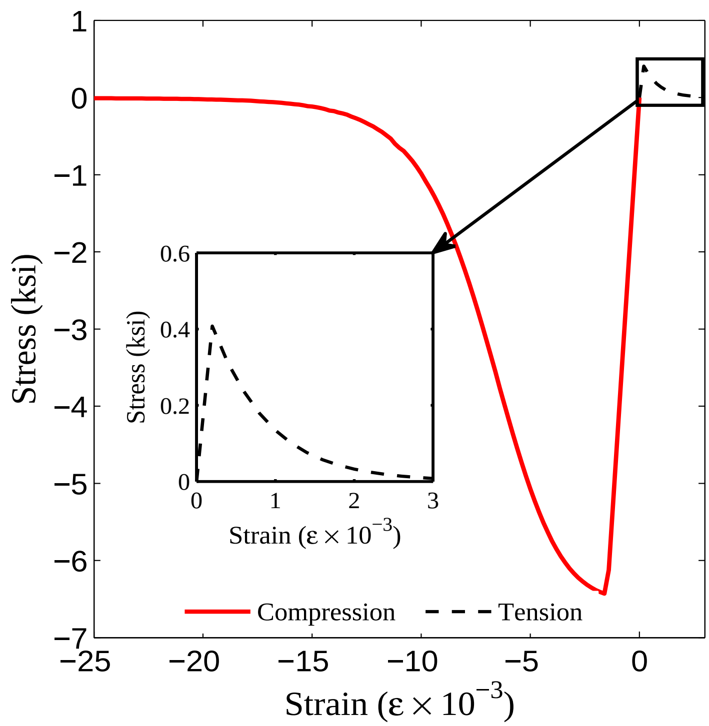

Figure 4.16: Concrete stress strain curve for 6500 psi concrete implemented in LS-DYNA. Compressive stress and strains are shown as negative value.

Table 4.5: Concrete material parameters for **MAT_CSCM_*CONCRETE

Parameter	Comments	Value	Units
RO	mass density	2.2E-04	lbf-s^2/in.
FPC	compressive strength	6.5E+03	psi
DAGG	maximum aggregate size	0.375	in.
ERODE	--	1.2	--

4.2.3.3 Elastic Material Model

All load cells, including the multi-axis and axial only load cells, were modeled using elastic materials. Elastic materials in LS DYNA were defined using **MAT_*ELASTIC, with elastic modulus of 29000ksi (2.90 E+7 psi as model units are in psi) for the steel material. Another elastic material was defined with an initial elastic modulus of $57000\sqrt{f'c}$ (in psi) to model solid elements at the interface of the concrete and the top plate of the multi-axis load cells. Table 4.6 provides a summary of the parameters (mass density, elastic modulus and Poisson's ratio) for the two elastic materials.

Table 4.6: Elastic material parameters for **MAT_ELASTIC*

Parameter Name	Description	Steel	Concrete Interface	Units
RO	mass density	7.50E-4	2.20E-4	lbf-s^2/in.
E	elastic modulus	2.90E+7	4.50E+6	psi
PR	poisson's ratio	0.25	0.15	--

4.2.4 Boundary Condition and Loading Protocol

Boundary constraints in the model were modeled using **BOUNDARY_SPC_NODE*. To model the correct boundary conditions, fixed constraints were provided at four node locations on the bottom plate of the multi-axis load cells to simulate the fixity provided by the four pre-tensioned anchor rods. As the axial load cells only provide vertical constraints, the axial load cell nodes were only constrained in the vertical direction, and were therefore free to translate or rotate to simulate an axial only load cells at three of the four corner locations. At the push location in each model, the constraint was provided by defining zero vertical deflection, while the gravity load was applied, thus applying an axial only constraint at the push location, as would be provided by the axial only load cell at the push location in each test specimen. Figure 4.17 shows nodes where the boundary conditions were applied.

Similar to the actual sequence of loading during the test, the self-weight, uniform gravity load, pattern loads and the push test were simulated sequentially on each model. Self-weight and additional gravity loads were simulated by applying a surface load on the model using **LOAD_SEGMENT_SET_NONUNIFORM*. Five different surfaces were defined, namely: beam surface to apply self-weight of beam, slab surface to apply slab self-weight and total uniform load of 90 psf, and three surfaces for application of pattern loads. Following the end of the gravity load application, the push test is simulated by applying a vertical deflection at the push location in each model. A deflection curve was defined using **DEFINE_CURVE*, where the vertical deflection was defined as zero during the gravity loading (thus acting as an axial only load cell) and then increased to the maximum achieved deflection during the test. The simulation was stopped when the deflection at the push location reached the deflection achieved during each test.

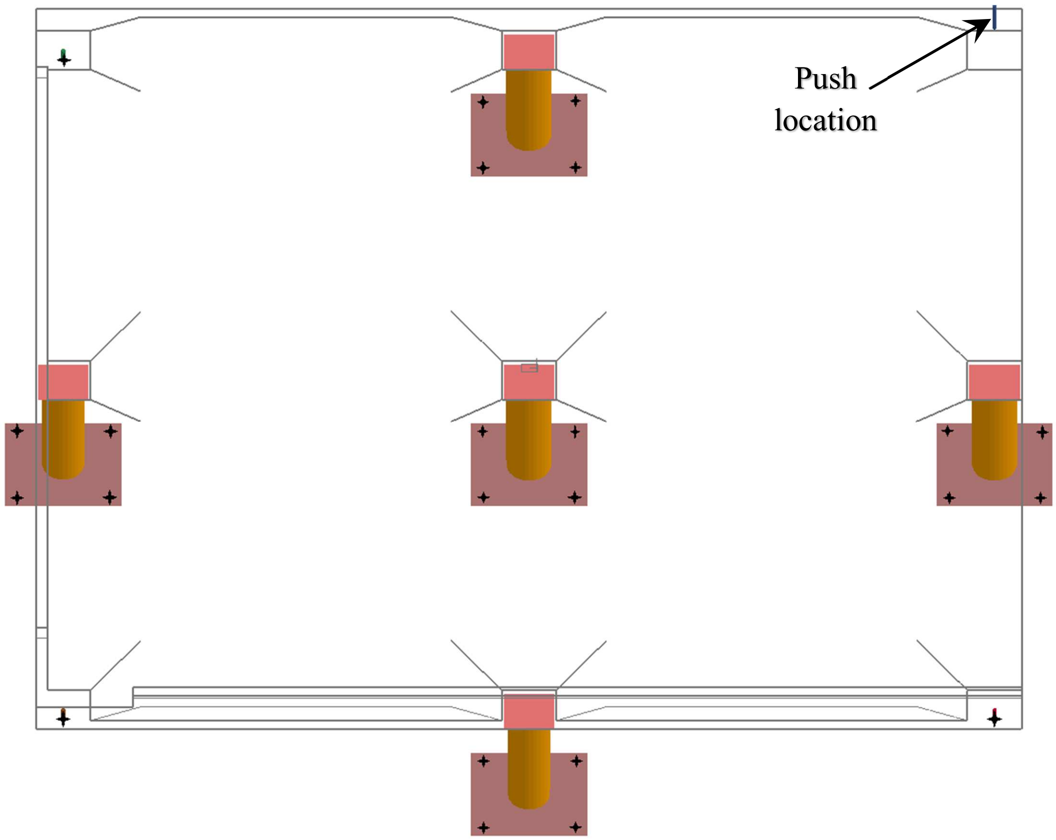

Figure 4.17: Location of single point constraints on the load cells. Three of the axial only load cells have only vertical constraint and can move freely in other degrees of freedom. *SPC* nodes are shown by a cross at the base of the load cells. One of the actuator modeled using two-node beam element is also shown.

4.3 Results Comparison

This section presents a comparison of global results from the numerical model implemented in LS DYNA with the recorded responses during the test at the three corner locations of specimen 1. Gravity load data comparison include support reaction and recorded deflections at the end of 90 psf uniform load application (in addition to specimen self-weight). For the push tests performed at the three corner locations, the load-deflection relation, support reactions at maximum achieved load during the test, deflection profiles and observed cracking or damage patterns on the surface of the specimen are compared.

4.3.1 Gravity Test: 90 psf Uniform load

Support Reactions: Figure 4.18 presents the comparison between the support reactions from the test and the LS DYNA model at the end of the gravity load application (total uniform load of 90 psf). The values presented are the change in support reactions, i.e. the load induced due to the self-weight of the specimen is assumed to be zero as the data acquisition during the test was started after removal of the formwork during the experiment as described in Chapter 3.

Figure 4.18(a) shows the location and naming convention of the load cells. It is noted that the EW and NS force resultants are positive in the West and North direction, respectively, while the axial loads acting down on the load cells are shown as negative. Figure 4.18(b) and (c) show the comparison between the recorded axial loads and the axial loads computed from the numerical model in LS-DYNA. On average it is observed that the LS-DYNA model slightly underestimates the axial loads transferred to the four multi-axis load cell support locations (LC1, LC2, LC4 and LC5) by 1.5 kips, while overestimates the loads transferred to the axial only load cells, LC6 through LC9 i.e. the corner load cells, by ~0.3 kips.

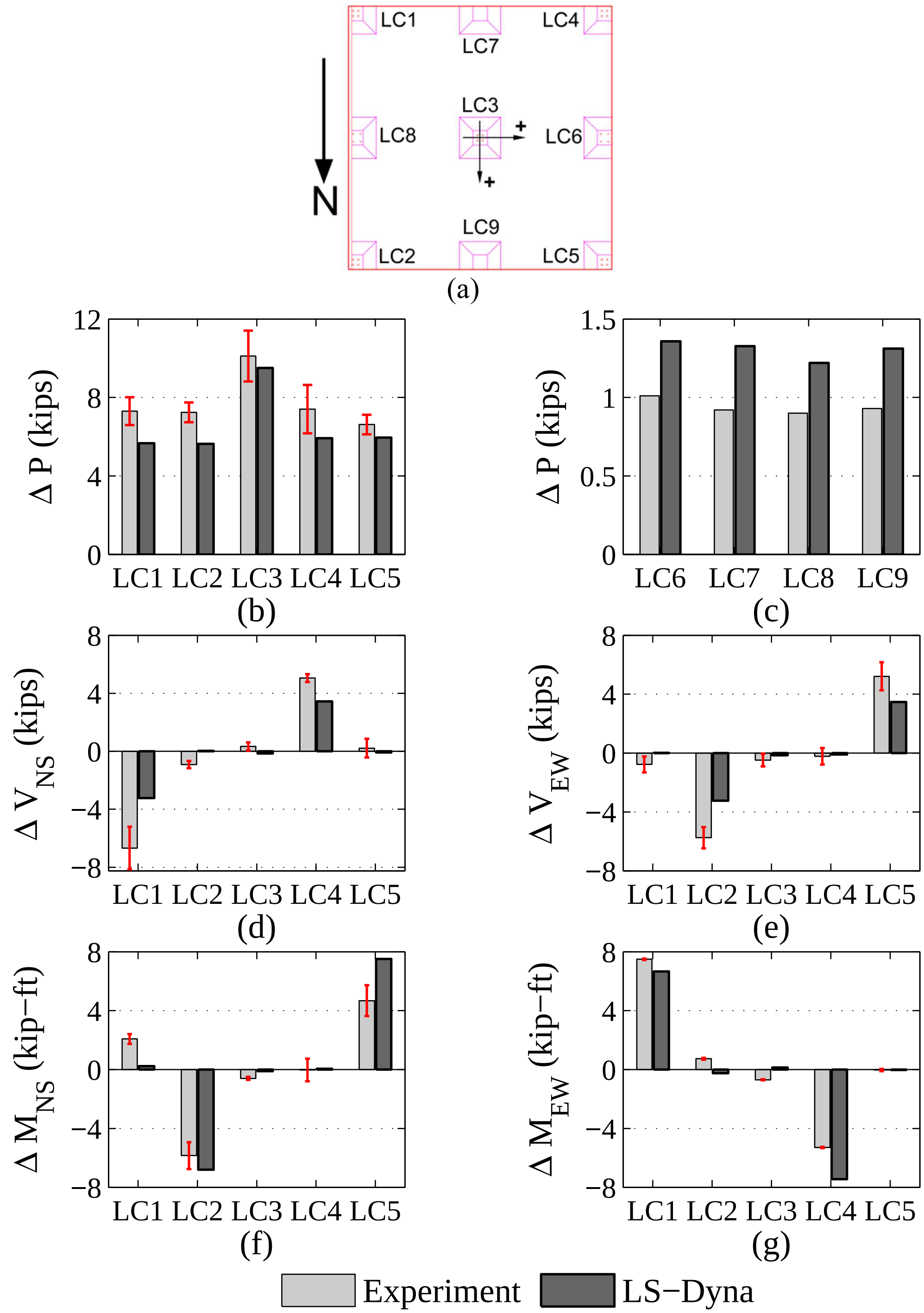

Figure 4.18: Comparison of change in support loads at the end of 90 psf uniform load on specimen 1, (a) location and naming convention of the load cells and direction of positive NS and EW force resultant, (b) and (c) change in axial loads at multi-axis and axial only load cell locations, (d) and (e) change in NS and EW shear force at multi-axis load cell locations, and (f) and (g) change in NS and EW moment at multi-axis load cell locations.

Figure 4.18(d) and (e) shows the comparison of the NS and the EW shear forces induced at the five multi-axis support locations due to the application of 90 psf uniform load on the specimen. When compared to the test results, the numerical model was able to accurately predict the direction of the shear force in both the EW and the NS direction. While the predictions of the directions were correct, the magnitude of resultant shear force from the numerical models were between 50-75% of the recorded values from the load cells (difference of 1.5 to 3 kips in resultant shear). This observed difference could be due to the following reasons:

- The magnitudes of loads are small hence a small difference is more prominent.
- Some error is expected in the experimentally recorded forces (shown by error bars on each resolved force).

Figure 4.18(f) and (g) presents a similar distribution of the moments induced at the multi-axis load cells in the NS and the EW direction, respectively. The LS DYNA model shows an acceptable prediction of the moments imposed at the multi-axis load cells when compared with the resolved loads from the experiment. The numerical model was able to predict both the direction and the magnitude of the imposed moments at the multi-axis load cell locations within +25% of the recorded resultant moment even for small changes observed during the experiment.

Deflection Comparison: This section presents a comparison between the changes in recorded deflections at the installed linear-potentiometer locations due to the 90 psf uniform load application. The deflections from the LS-DYNA model are the values recorded at the *node* closest to the linear-potentiometer location installed on the specimen. It is noted that the values presented are the change in deflections at the sensor locations and does not account for the deflection that occurred due to the specimen self-weight.

Figure 4.19(a) presents the location and naming convention of the linear potentiometers installed on the bottom of the slab. It is noted that for clarity the linear potentiometers are divided into four groups, one group for each panel, shown by different color in Figure 4.19(a). Figure 4.19(b) through (e) presents the comparison of the change in deflection in all the panels. When compared with deflections recorded during the test, the LS DYNA model was able to predict the deflections with good accuracy. On an average, the LS DYNA predictions are within $\pm$15% of the deformations recorded during the test at all locations. It is noted that although the variation in the relative deflection between the experiment and finite element model seems high, the actual recorded deflections were on the order of -0.08 to -0.006 in, hence the absolute difference observed between the experiment and the model are very small.

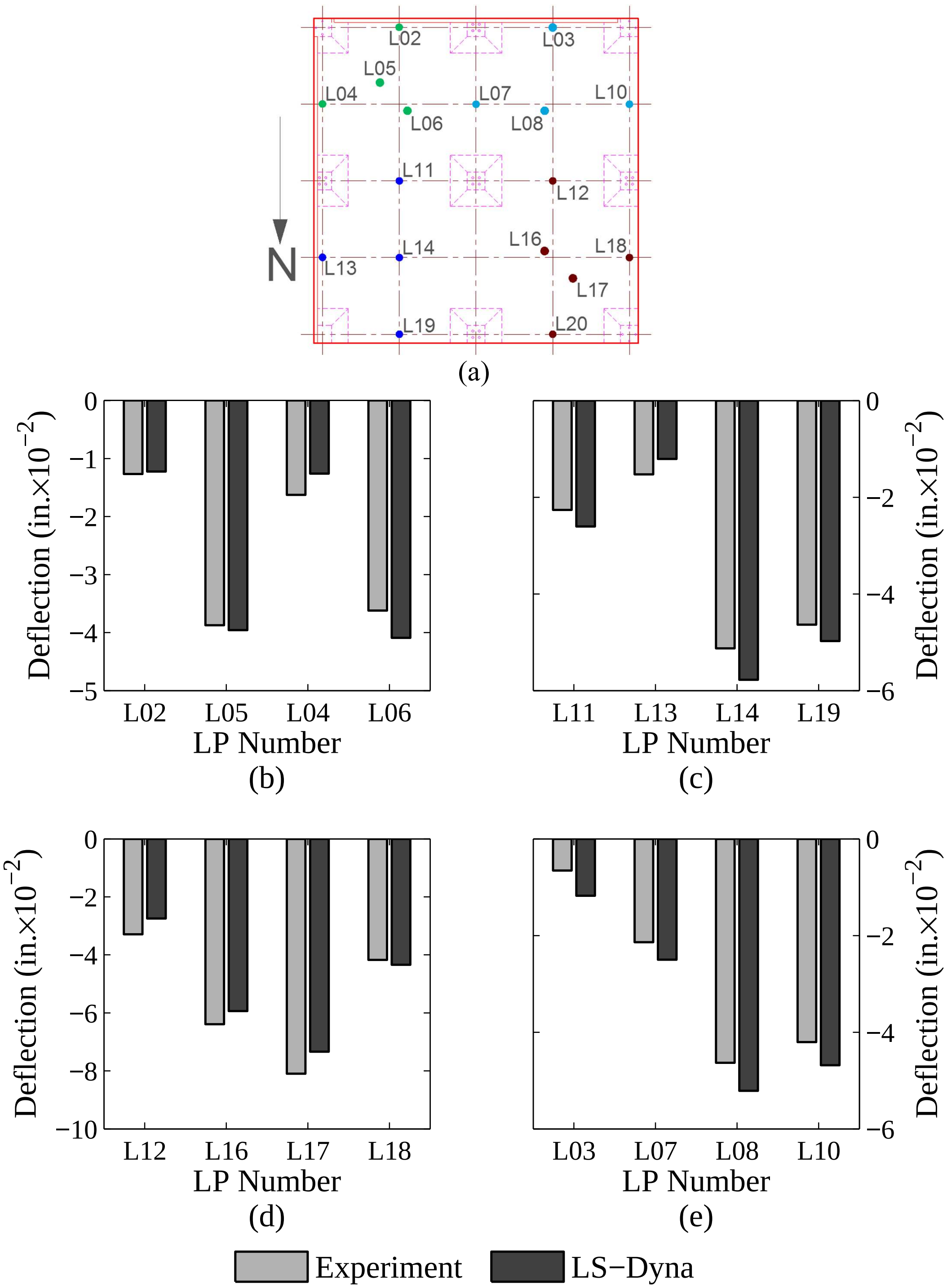

Figure 4.19: Deflection comparison between the test and the numerical model in LS DYNA, (a) location and naming of the linear potentiometers, (b) recorded deflections in panel 1, (c) recorded deflections in panel 2, (d) recorded deflections in panel 3, and (e) recorded deflections in panel 4. It is noted that downward deflections are shown as negative values.

4.3.2 Column Removal at Corner Support Locations

This section presents the results comparison between the column removal tests performed at the three corner locations and the numerical results of the same from the numerical model implemented in LS DYNA. Results include load-deflection relation, distribution of support reactions at maximum load conditions, deflection profiles at linear-potentiometer locations in the test panel, and observed damage on the surface at the end of the test.

4.3.2.1 Push Test 1 (beam-beam corner)

Load Deflection Response: Figure 4.20 presents a comparison of the load deflection curve from the test and the LS DYNA model at the beam-beam corner location. The initial negative loads at zero deflection are the initial load applied at the column failure location due to the specimen self-weight and the applied uniform load of 90 psf on the specimen.

At the beginning of the push test at the beam-beam corner location, LS DYNA model recorded an initial tangent stiffness of approximately 10.8 kips/in., compared to the actual recorded initial tangent stiffness of 8.5 kips/in. during the test (defined as the secant stiffness between initial load and zero vertical load at the push location). As the deflection was increased, the numerical model shows continuous softening due to damage that occurred in the concrete. The LS-DYNA model reached its peak load at vertical deflection of 3 in. with a vertical load of 10.4 kips. Beyond this numerical model shows hardening as the deflection was further increased. Pushed further, LS-

DYNA model achieved a load of 10.9 kips at a vertical deflection of 4.5 in. (deflection at which the peak load recorded during the test), compared to 9.3 kips recorded during the test. During the unloading of the model, the LS-DYNA model attained a much higher capacity of -12.3 kips at zero in. deflection compared to -6.7 kips achieved during the test. However, during the second loading, the LS-DYNA model achieved a load capacity of 9.2 kips at 9.5 in. vertical deflection compared to 8.3 kips achieved during the test at the beam-beam corner location at the same deflection amplitude.

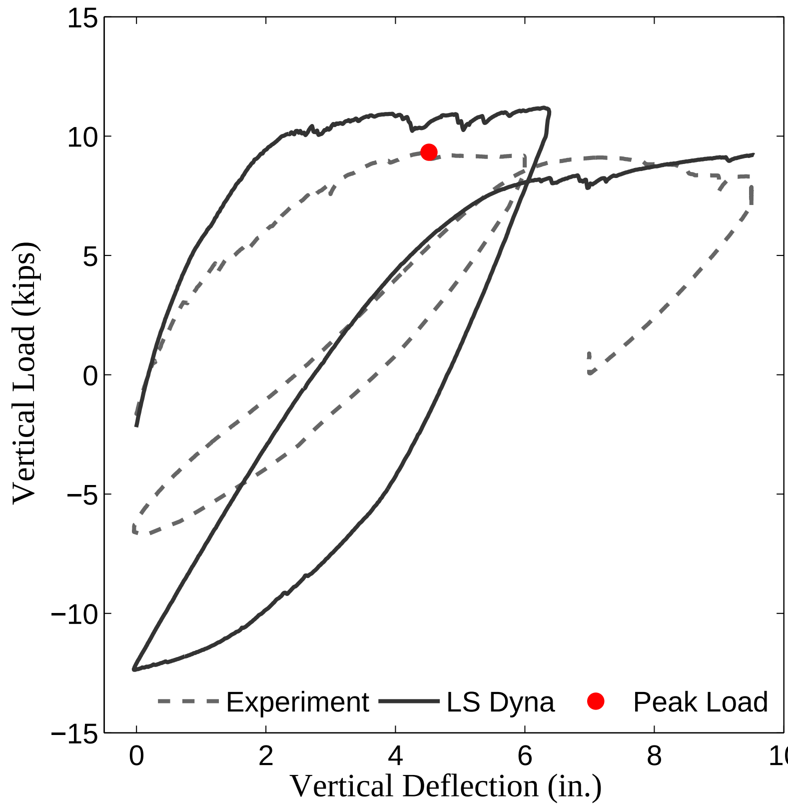

Figure 4.20: Comparison of the load deflection relation during the test at beam-beam corner location.

Although LS-DYNA model was detailed according to the actual specimen specifications, the load-deflection curve was not able to capture the deflection at peak load and post yield behavior exactly due primarily to some drawbacks in the concrete material. The smeared crack modeling technique used to model the concrete material results in a very ductile behavior of concrete in both tension and compression. This results in its inability to capture sudden change in stiffness due to cracking and also in residual concrete strength in compression even at large strains, resulting in post-peak hardening as observed beyond the initial peak load at 3 in. vertical deflection. Nonetheless, the resulting difference of about 10% in peak strength is not unreasonable given the complexity of the system.

Support Reactions: Figure 4.21 shows the additional loads imposed at the support locations at a deflection of 4.5 in. The loads are compared at this deflection as the test specimen achieved its maximum load capacity at a deflection of 4.5 in. Figure 4.21 (a) shows the location and naming convention of all the load cells. It is noted that the EW and NS force resultants are positive in the West and North direction, respectively, while the axial loads acting down on the load cells are shown as negative value.

Figure 4.21 (b) and (c) present the additional axial loads transferred to the load cells at a deflection of 4.5 in. As expected, supports LC1 and LC2 show the greatest increase in axial load due to the support removal at LC8. On average, the LS DYNA model was able to generate acceptable prediction of the axial load transferred to the two adjacent supports LC1 and LC2 (85% of the recorded increase). Although the models showed good agreement in axial load prediction at the supports LC1 and LC2, show some differences in the support locations far from the two supports were observed. Notably, LS DYNA model showed an axial load increase of 0.4 kips at support LC3, while a decrease in axial load (i.e. upward force at the support location) of -1.5 kips was recorded during the test. This disagreement in axial load at support LC3 was likely due to the additional concrete strength along the slab failure surface and connection stiffness at the multi-axis support location, resulting in greater force transferred to the support LC3.

Figure 4.21 (d) and (e) presents a comparison of the horizontal shear forces imposed at the multi-axis load cell locations at 4.5 in. vertical deflection. The LS DYNA model was able to predict the resultant shear force at supports LC1 and LC2 load within 95% of the recorded values during the tests. The finite element model was also able to predict the induced shear at support LC3 with acceptable accuracy (85% of the recorded value during the test). Some discrepancy was observed in the shear force distribution at supports LC5, likely due the fact that the numerical model does not account for any localized affects that might occur due to the variation in the material or section properties and exhibits a behavior expected of an ideal model and the use of a coarse mesh away from the test location.

A similar comparison for the additional moments is presented in Figure 4.21 (f) and (g). Although the LS DYNA model was able to predict the directions of the moments at each support accurately, the magnitudes of the resultant moments at supports LC1 and LC2 were overestimated by 45%. This overestimation of moment capacity at support locations may partially be due to the difference in rotational connection stiffness between the specimen and the multi-axis load cells. If the connection in the LS DYNA model were stiffer compared to the actual connection at the support locations, for example a higher moment demand will be realized on the multi-axis load cells.

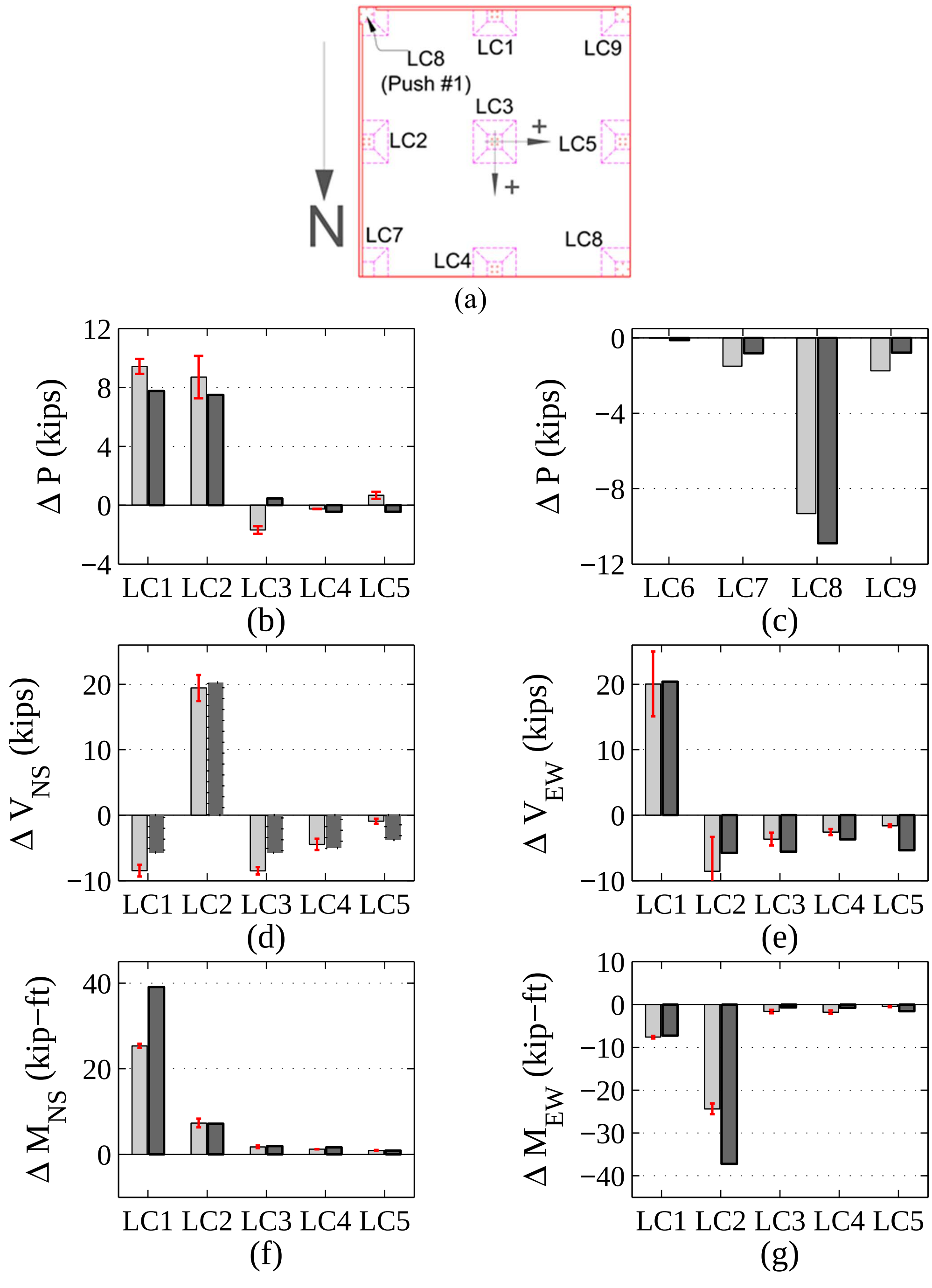

Figure 4.21: Comparison of change in support loads at 4.5 in. vertical deflection during the test at the beam-beam corner location on specimen 1, (a) location and naming convention of the load cells, (b) and (c) change in axial loads at multi-axis and axial only load cell locations, (d) and (e) change in NS and EW shear force at multi-axis load cell locations, and (f) and (g) change in NS and EW moment at multi-axis load cell locations.

Deflections: This section compares the profiles of the deflections recorded in the test panel. It is noted that the x-axis of the figures are the deflection at the push location as averaged by the linear potentiometers at L00 and L01, while the y-axis presents the deflection at the selected sensor location.

Figure 4.22(a) presents the location and naming convention of the linear-potentiometers installed on the test panel. Figure 4.22 (b) and (c) present the deflection profiles as recorded at mid-span between supports LC8 and the two adjacent supports LC1 and LC2 (sensor locations L02 and L03). The LS DYNA model was able to accurately predict the deflection profile over the entire range, with a maximum deflection of 3.5 in. at the end of the simulation compared to the recorded value of 3.3 in. during the test. A similar profile for the sensors installed closer to the mid-span of the panel near the failure surface (sensor location L04 and L05) is shown in part (d) and (e). Although LS DYNA model was able to accurately predict the deflection profiles at L04 within 10% of the recorded values, and underestimates the deflection at L05 by 0.06 in. (20% error).

Figure 4.22(f) and (g) compare the profiles recorded away from the failure zone at sensor locations L06 and L07. Even though these sensor locations were placed closer to the coarse mesh, and experienced very small deflection, both of them show good agreement with the experimental results (within 0.04 in. of the deflections recorded during the test).

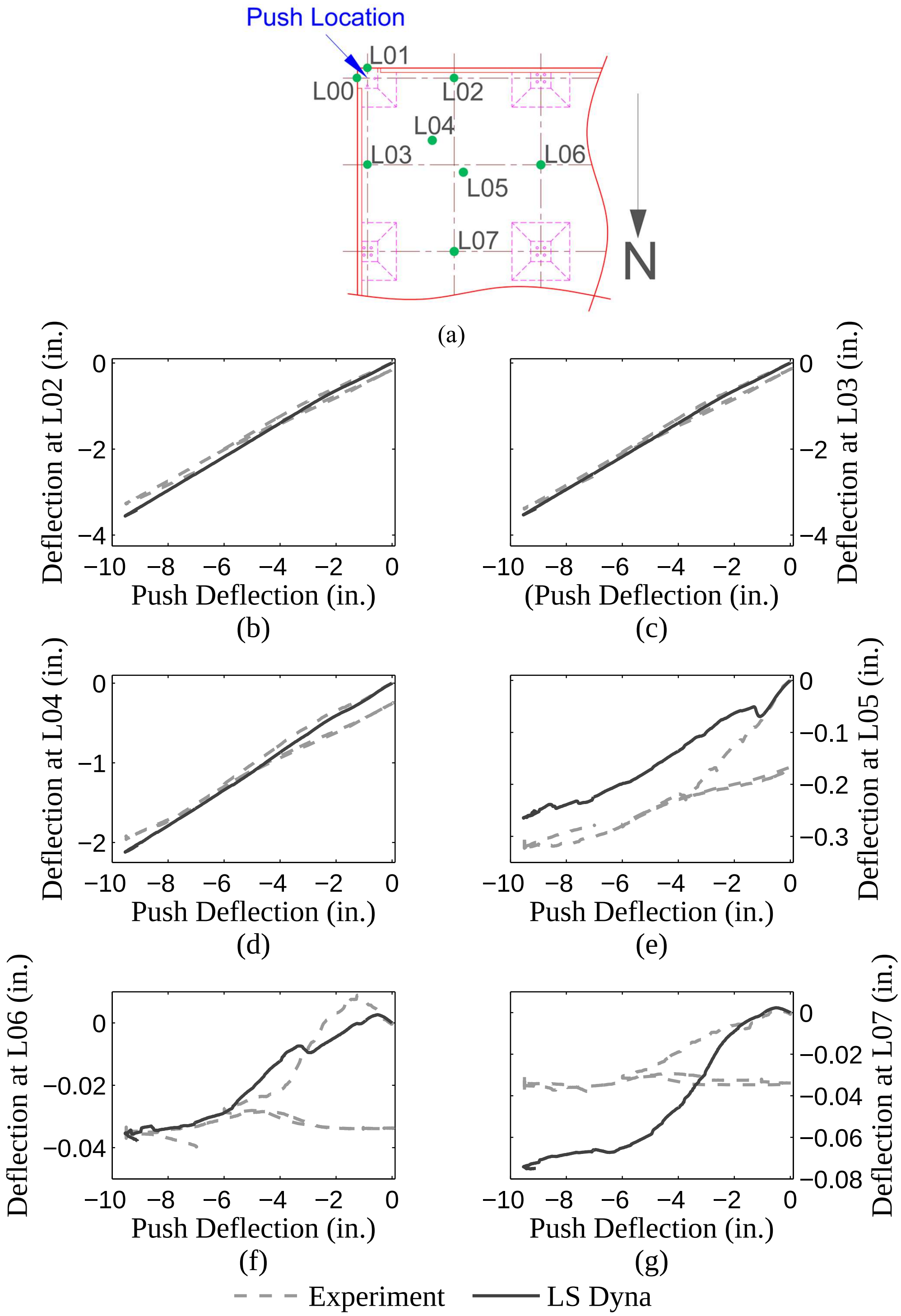

Figure 4.22: Comparison of deflection profiles at linear-potentiometer locations vs the tip deflection at the beam-beam corner push location, (a) location and naming convention of the locations where the deflections are compared, (b) to (g) deflection profiles at linear potentiometer locations L02 through L07. The X-axis of the plots are the deflections as averaged by L00 and L01.

Observed Damage: This section presents a comparison between the observed damage at the end of the test and the peak tensile strain concentrations from the LS DYNA model. Although the LS DYNA concrete material model does not explicitly show the cracks that form on the surface, a reasonable approximation of crack location can be obtained by plotting the maximum principal strain at the solid element integration points used to model the concrete material (eight node solid elements for this study).

Figures 4.23 and 4.24 present the comparison between the observed cracking on the top and bottom surface of the specimen, respectively. It is observed that the plot of the *maximum principal strain* (tensile strain) was able to accurately capture the damage profile on both the top and the bottom surface of the specimen. On the top surface, higher tensile strains were recorded between the two adjacent supports LC1 and LC2, suggesting severe cracking as observed during the experiment. The model also captured the possible cracking on the top surface, away from the failure zone, i.e. cracks near push location and between supports LC1 and LC3 and between supports LC2 and LC3.

A similar comparison of the tensile strains on the bottom surface is presented in Figure 4.24. In like fashion, the LS DYNA model was able to very reasonably predict the damage pattern on the bottom surface. Similar to the cracking observed during the tests, tensile strains were predicted by the model radiating away from the push location due to the presence of torsion and two-way slab action. It is noted that the fringe plot of the maximum tensile strain on the concrete only gives a qualitative idea of the crack pattern.

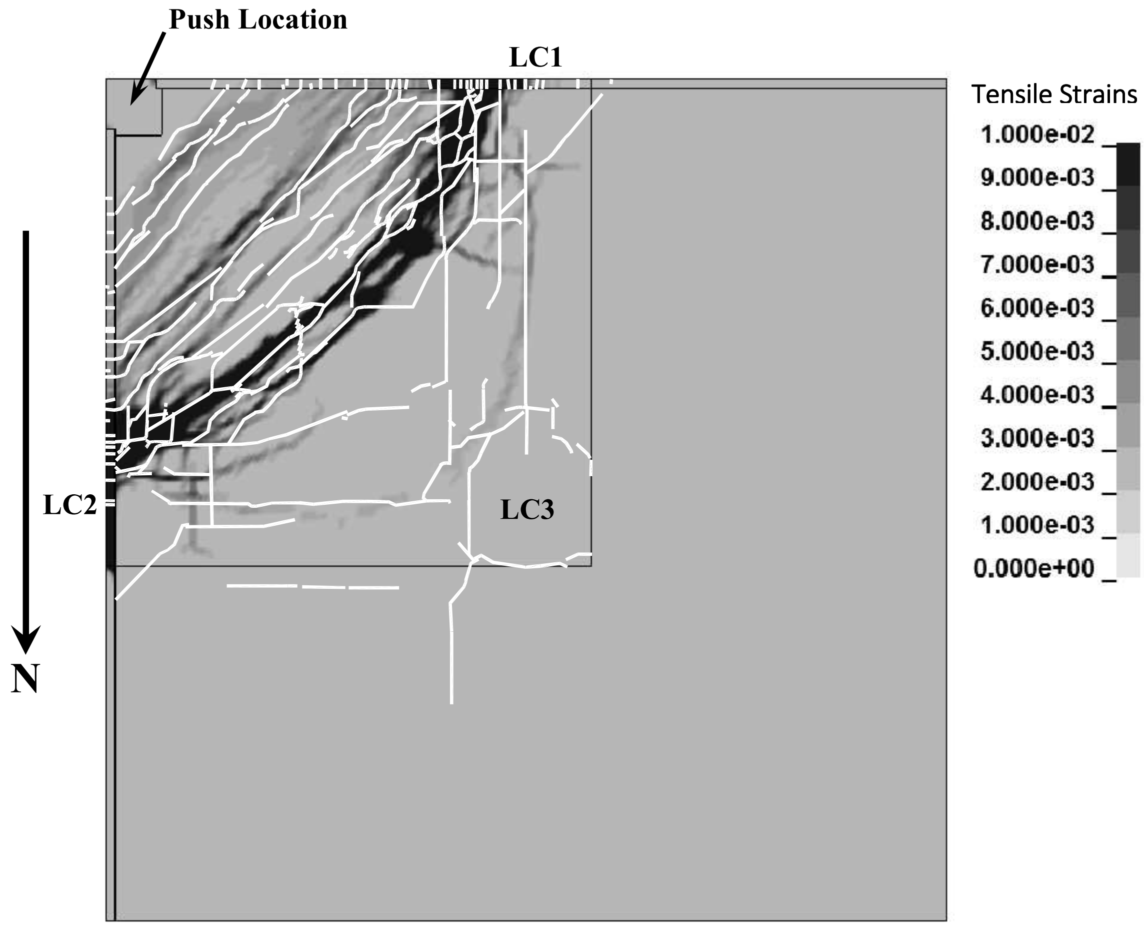

Figure 4.23: Comparison of the observed damage on the top surface of the specimen during the test at beam-beam corner. The cracks observed during the tests (white lines) are overlaid on the plot of maximum principal strain (tensile strains) from LS-DYNA model. Thin black lines on the LS-DYNA models show an outline of the different concrete parts defined in the model.

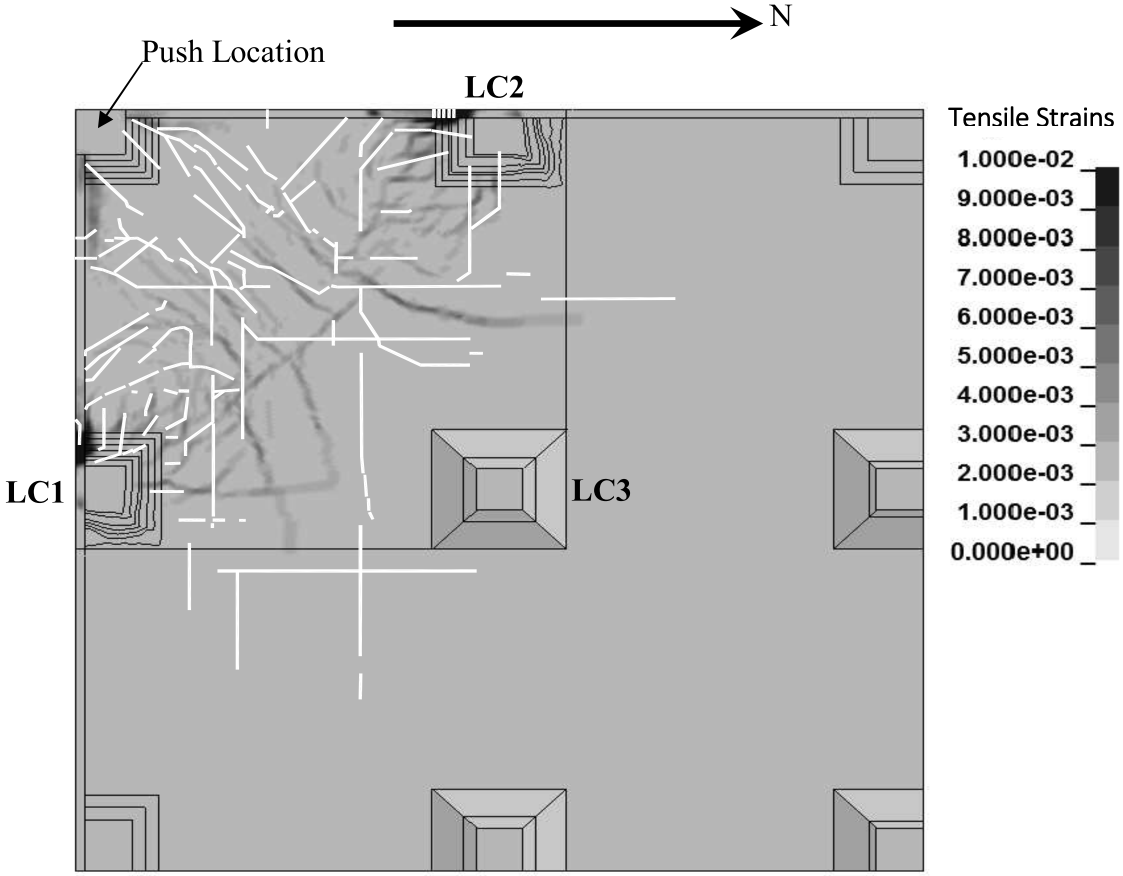

Figure 4.24: Comparison of the observed damage on the bottom surface of the specimen during the test at beam-beam corner. The cracks observed during the tests (white lines) are overlaid with the plot of maximum principal strain (tensile strains) from LS-DYNA model. Thin black lines on the LS-DYNA models show an outline of the different concrete parts defined in the model.

4.3.2.2 Push Test 2 (slab-slab corner)

Load Deflection Response: Figure 4.25 presents the comparison of the load deflection curve from the test at the slab-slab corner location and the LS DYNA finite element model. The initial negative loads at zero deflection are the initial load applied at the column failure location due to the specimen self-weight and the applied uniform load of 90 psf on the specimen.

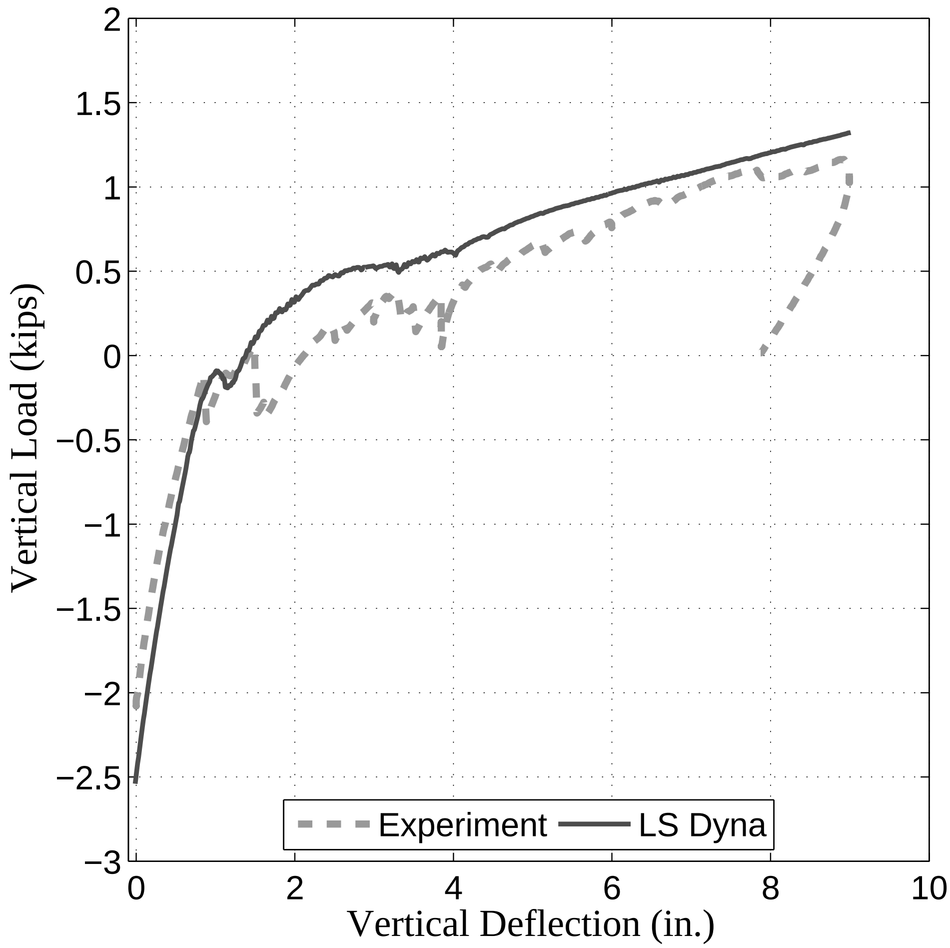

Figure 4.25: Comparison of the load deflection relation during the test at slab-slab corner location.

At the beginning of the push test at the slab-slab corner location, the LS-DYNA model predicted an initial tangent stiffness of approximately 3.1 kips/in., which was in good agreement with the recorded initial stiffness of 3.3 kips/in. during the test. As the deflection was increased, the LS-DYNA model was able to capture the onset of nonlinearity in the system at a deflection of approximately 1 in. Beyond this, the LS-DYNA model deforms with a post yield stiffness (secant stiffness between 1 in. and 9 in. deflection) of approximately 0.18 kips/in., which was in good agreement with the recorded post-yield stiffness of 0.2 kips/in from the experiment. As the deflection was increased to its maximum value of 9 in. at the slab-slab push location, the LS-DYNA models predicted vertical load capacity of 1.3 kips, compared to the recorded maximum strength of 1.1 kips at a vertical deflection of 9 in. This comparison is viewed as very reasonable.

Support Reactions: Figure 4.26 shows the additional loads imposed at the support locations at a deflection of 9 in. during the test at the slab-slab corner location. Figure 4.26(a) shows the location and naming convention of all the load cells. It is noted that the EW and NS force resultants are positive in the West and North direction, respectively, while the axial loads acting down on the load cells are shown as negative.

Figure 4.26(b) and (c) presents the comparison of the additional axial loads transferred to the load cells at a deflection of 9 in. As expected, supports LC4 and LC5 experienced the greatest increase in axial load due to the support removal at LC6. On average, the LS DYNA model reports a reasonable prediction of the axial load transferred to the two adjacent supports LC4 and LC5 (within $\pm$10% of the recorded axial load increase during the test).

Figure 4.26(d) and (e) presents a comparison of the horizontal shear forces imposed at the multi-axis load cell locations at 9 in. vertical deflection. The LS-DYNA model was able to predict the resultant shear force at supports LC4 and LC5 load within $\pm$25% of the recorded values during the tests (difference of 1 to 1.5 kips between the test results and LS DYNA predictions). The LS DYNA model also provides a fairly accurate results for the induced resultant shear for support LC3 (difference of 0.4 kips).

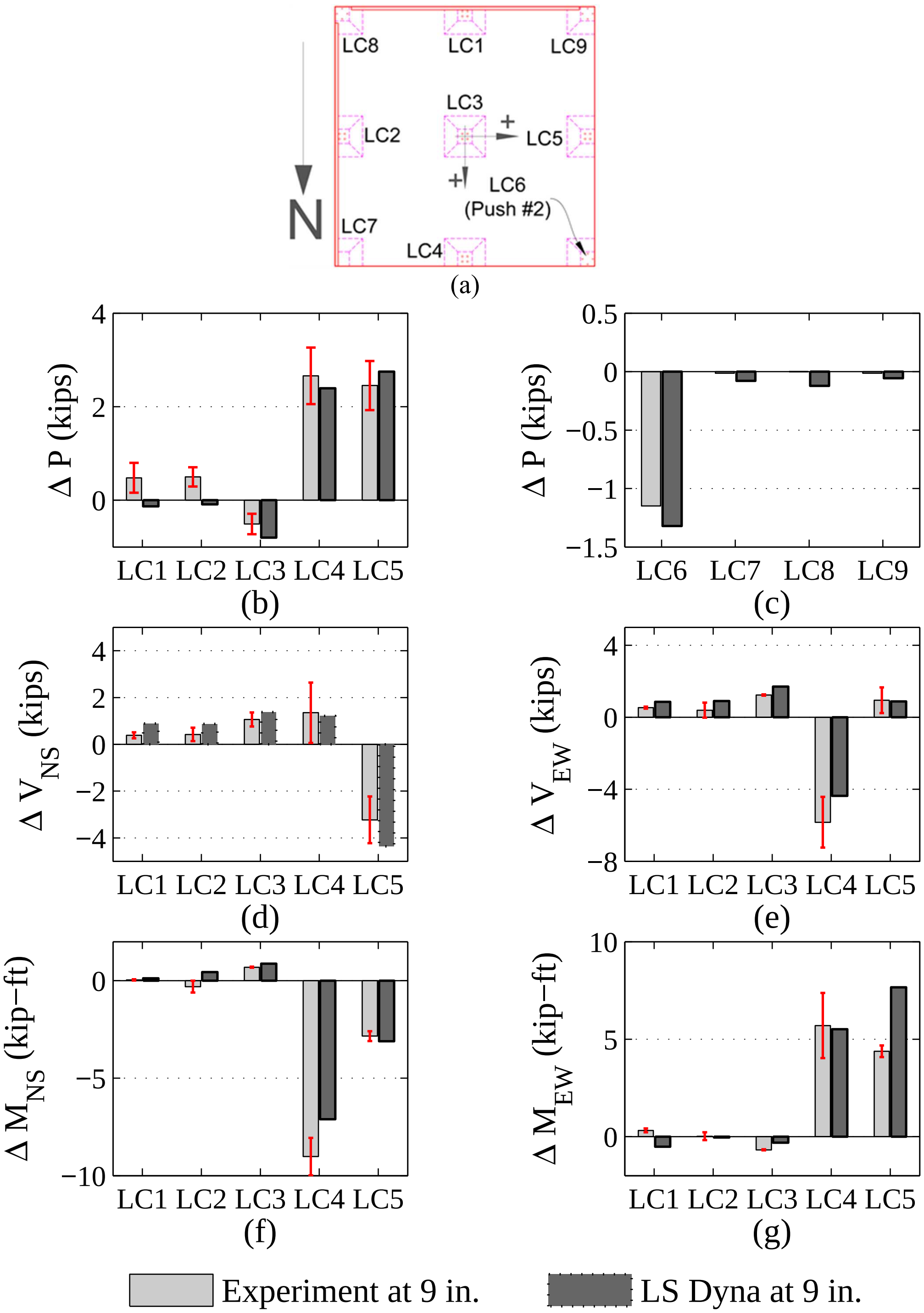

Figure 4.26: Comparison of change in support loads at 9 in. vertical deflection during the test at slab-slab corner location, (a) location and naming convention of the load cells, (b) and (c) change in axial loads at multi-axis and axial only load cell locations, (d) and (e) change in NS and EW shear force at multi-axis load cell locations, and (f) and (g) change in NS and EW moment at multi-axis load cell locations.

A similar comparison for the additional moment demand at the multi-axis load cell locations is presented in Figure 4.26(f) and (g). Although the LS DYNA model was able to predict the direction and magnitude of the moments at supports LC3 and LC4 within 85 to 95% of recorded values from the test, some discrepancy was observed for the moment transferred to support LC5. This was due to the fact that the LS DYNA model did not capture the localized failure that occurred near support LC5 during the test (Figure 4.27), which resulted in a lower demand this support location.

Figure 4.27: Localized failure near LC5 during test at slab-slab corner.

Deflections: This section presents the deflection profiles vs. the tip deflection at the push location during the test at the slab-slab corner location. Figure 4.28(a) presents the location and naming convention of the linear-potentiometers installed in the test panel. It is noted that the x-axis of the figures are the deflection at the push location as averaged by the linear potentiometers at L00 and L01.

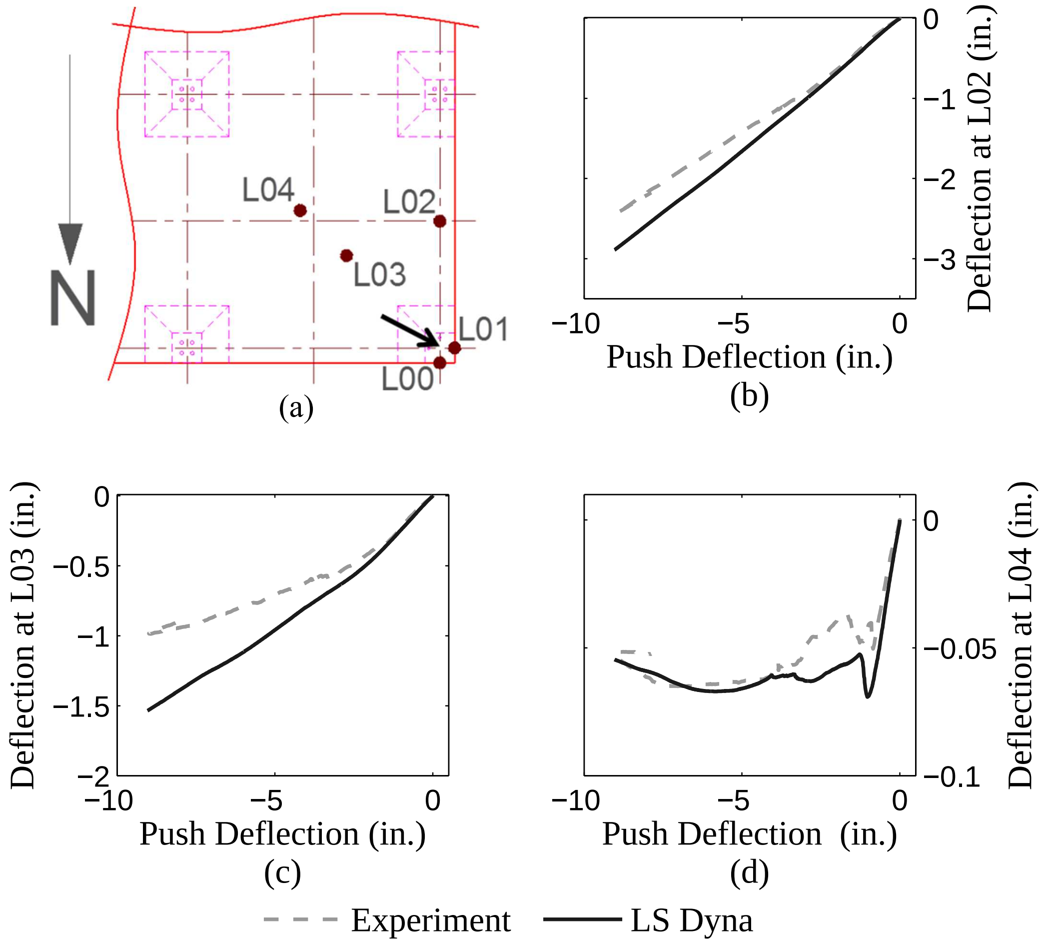

Figure 4.28: Comparison of deflection profiles at linear-potentiometer locations vs the tip deflection at the slab-slab push location, (a) location and naming convention of the locations where the deflections are compared, (b) deflection profile at L02, (c) deflection profile at L03, (d) deflection profile at L04, and (e) deflection profile at L05. Note that the push location is shown by an arrow in (a).

Figure 4.28(b) presents the deflection at mid-span between the push location and the adjacent support LC5 (location L02). At maximum tip deflection of 9 in. at the push location, the LS DYNA model approximates a deflection of -2.8 in. at L02, which is in good agreement with the recorded deflection of -2.45 in. during the test at the slab-slab corner location. Figure 4.28(c) and (d) presents a similar profile for two linear-potentiometers installed closer to the yield line near the center of the panel (location

L03 and L04). The LS DYNA model predicts a 50% greater deflection at L03 (-1.5 in.) compared to the measured deflection during the test (-1.0 in.) at the slab-slab corner location, however it reports a good prediction of the deflection at L04, which was placed away from the yield line that formed on the top surface. The discrepancy at L03 was likely due to some local affects that occurred during the experiment (including the localized failure near support LC5) which resulted in a lower deflection at L03. It is noted that the deflection history tracks that of the experiment with high accuracy until approximate system yield at 1 to 1.5 in. corner deflection.

Observed Damage: This section compares the observed cracking on the specimen surface at the end of the test at the slab-slab corner with the distribution of the maximum principal strains on the concrete from the LS-DYNA model. Figures 4.29 and 4.30 and present the comparison between the observed cracking from the experiment and the tensile strain from the LS-DYNA model, on the top and bottom surface of the specimen, respectively. It is observed that the plot of the *maximum principal strain* (tensile strain) was able to predict the damage profile on both the top and the bottom surface of the specimen. On the top surface, large tensile cracks were observed between the two adjacent supports, LC4 and LC5, suggesting severe cracking as observed during the experiment. The LS-DYNA model was able to accurately predict the damage on the bottom surface as shown in Figure 4.30. Similar to the cracking observed during the test at the slab-slab corner location, tensile strain plots from the LS DYNA model suggests damage radiating away from the push location due to the presence of torsion and two-way slab action.

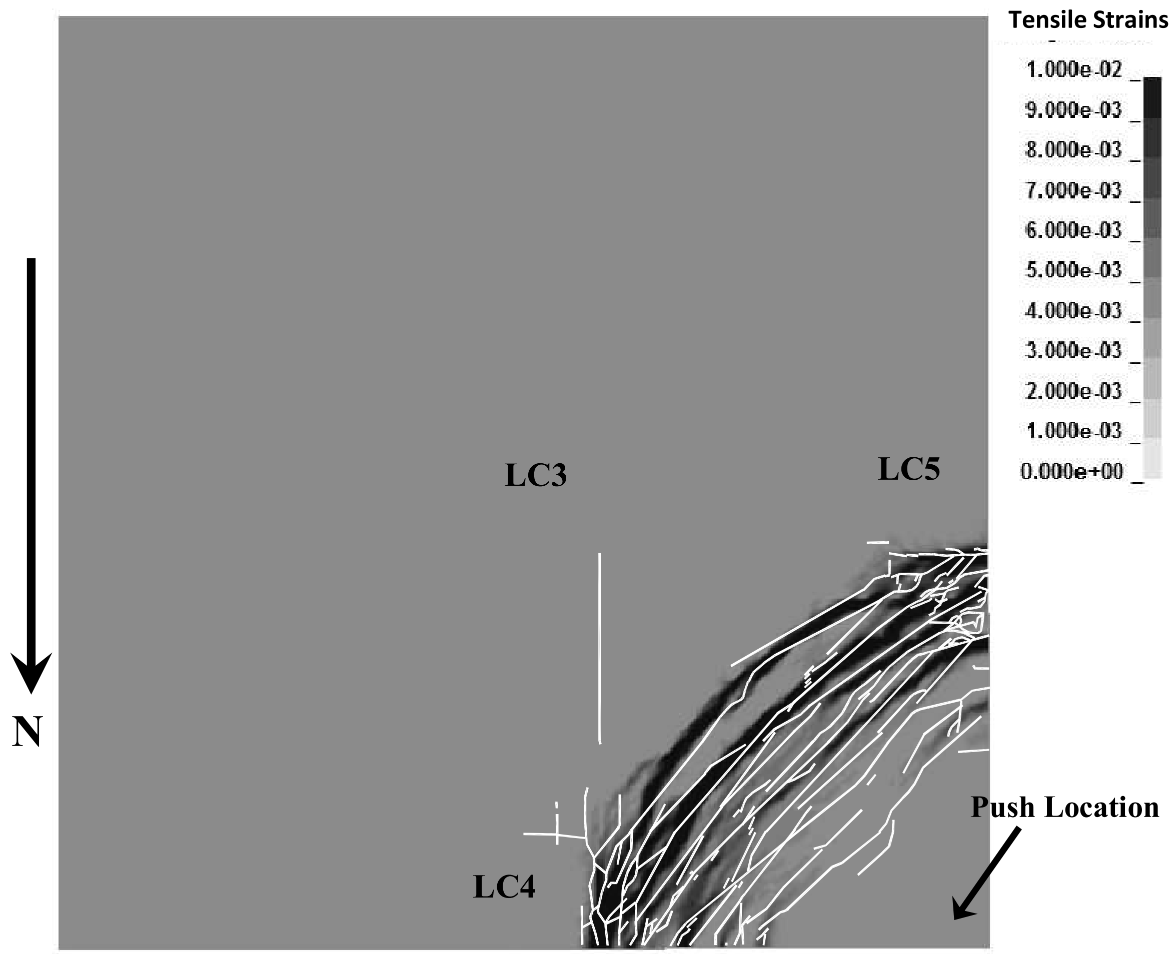

Figure 4.29: Comparison of the observed damage on the bottom surface of the specimen during the test at the slab-slab corner. The cracks observed during the tests (white lines) are overlaid on the fringe of maximum principal strain from LS DYNA model.

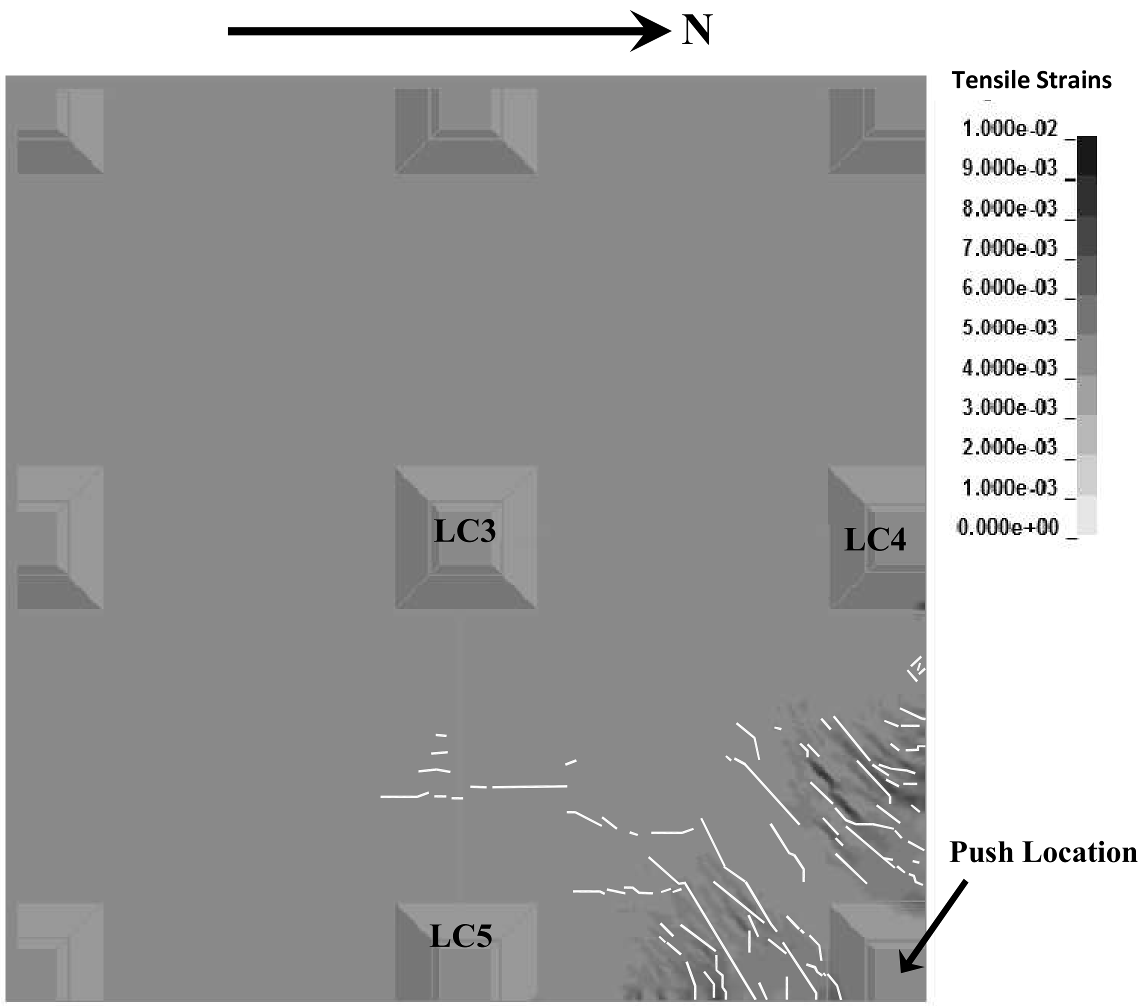

Figure 4.30: Comparison of the observed damage on the bottom surface of the specimen during the test at the slab-slab corner. The cracks observed during the tests (white lines) are overlaid on the fringe of maximum principal strain from LS DYNA model.

4.3.2.3 Push Test 3 (beam-slab corner)

Load Deflection Response: Figure 4.31 presents the comparison of the load deflection relation from the test at the beam-slab corner. The initial negative loads at zero deflection are the initial load applied at the column failure location due to the specimen self-weight and the applied uniform load of 90 psf on the specimen.

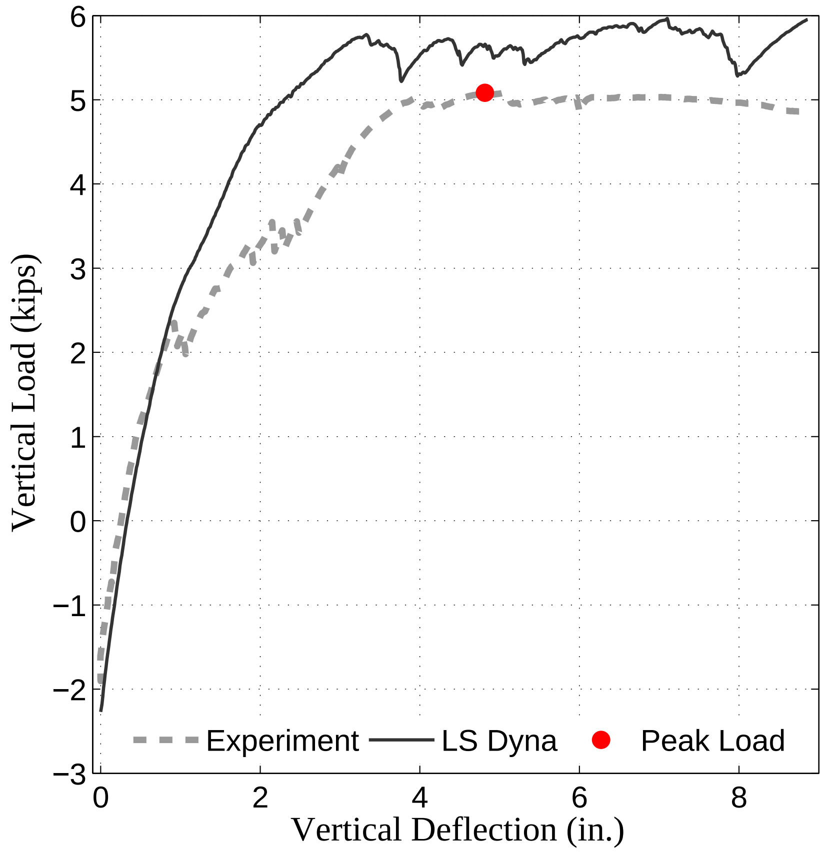

Figure 4.31: Comparison of the load deflection relation during the test at the beam-slab corner location.

At the beginning of the push test at the beam-slab corner location, the LS DYNA model deformed with an initial tangent stiffness of approximately 7.2 kips/in., compared to the recorded initial tangent stiffness of 6.7 kips/in. during the test. As the deflection increased, the LS DYNA model showed continuous softening until it reached its peak load of 5.8 kips at 3.3 in. vertical deflection. Compared to the tests results, the peak load predicted by the model was higher by 15%. When pushed beyond the initial peak, the LS-DYNA model showed a slight increase in load, reaching a load capacity of 5.9 kips at a vertical deflection of 9 in., compared to a capacity of 4.8 kips from the experiment.

Support Reactions: Figure 4.32 presents the additional loads imposed at the support locations at a deflection of 4.6 in. during the test at the beam-slab corner location. The loads are compared at this deflection as the test specimen achieved its maximum load capacity at a deflection of 4.6 in.

Figure 4.32(b) and (c) presents the additional axial loads transferred to the load cells at a deflection of 4.6 in. The LS-DYNA model gives a good prediction of the axial load transferred to the two adjacent supports LC1 and LC5 (difference of 0.5 kips at both locations from their respective values recorded during the test). Although the LS-DYNA model shows a good agreement in axial load prediction at supports LC1 and LC5, it shows some differences in axial load at supports far from the failure zone.

Figure 4.32(d) and (e) presents a comparison of the horizontal shear forces imposed at the multi-axis load cell locations at a deflection of 4.6 in. vertical deflection. The LS DYNA model was able to predict the resultant shear force at supports LC1 and LC5 within 70 to 80% of the recorded values during the tests. The finite element models also provides a good estimate of the induced resultant shear for support LC3 (95% of the recorded value during the test). A similar comparison of the additional moments is presented in Figure 4.32(e) and (f). Although the LS-DYNA model was able to predict the directions of the moments at each support accurately, the magnitudes of the resultant moments were overestimated by 10% and 30% and at the two adjacent supports LC1 and LC5, respectively, partly due to the difference in connection stiffness at multi-axis load cells at these supports. It is noted that although the percent difference was relatively higher at support LC5, the difference in resultant moment magnitude is only 1.8 kip-ft. between the LS DYNA model and the test results.

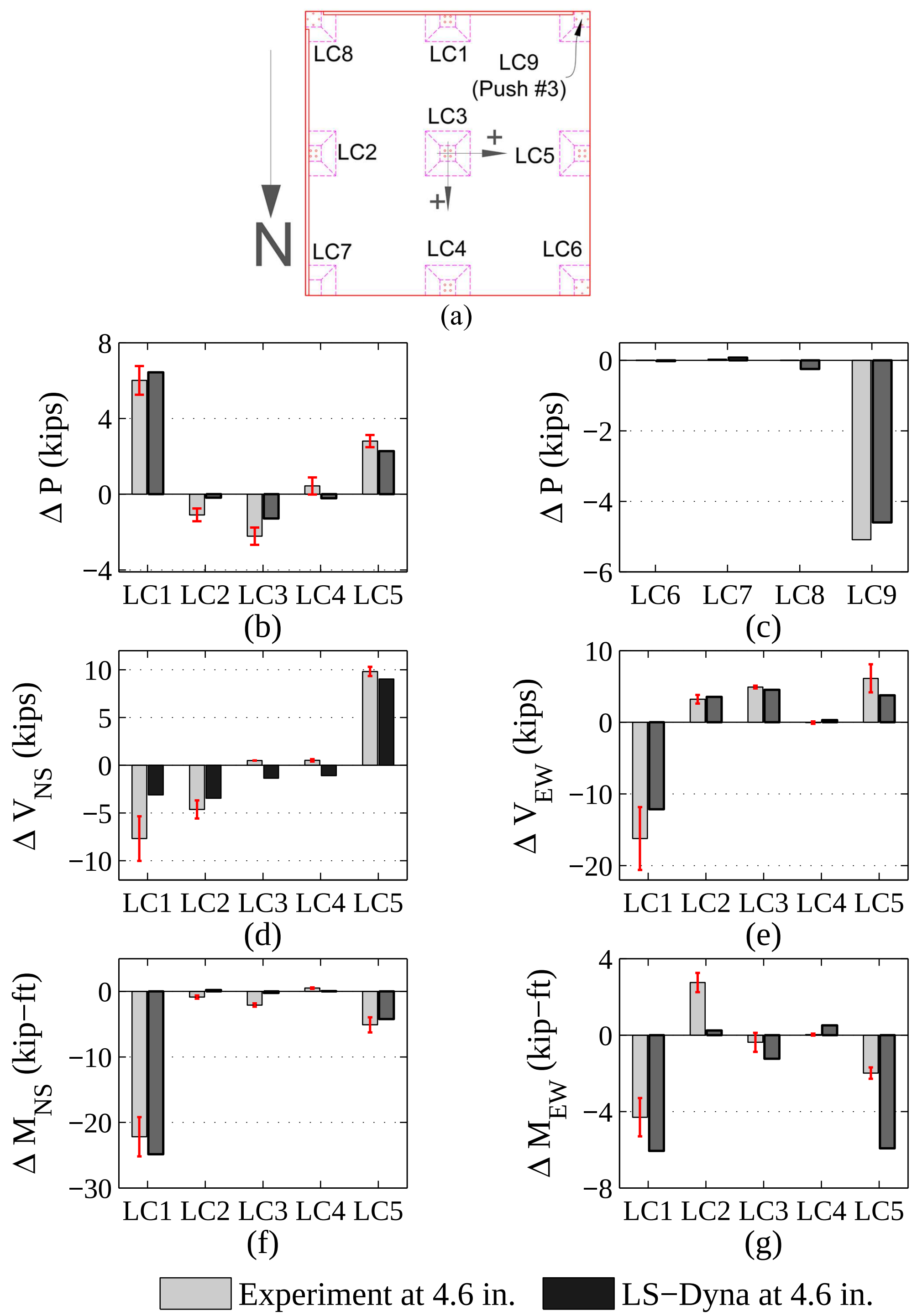

Figure 4.32: Comparison of change in support loads at 9 in. vertical deflection during the test at the beam-slab corner location. (a) location and naming convention of the load cells, (b) and (c) change in axial loads at multi-axis and axial only load cell locations, (d) and (e) change in NS and EW shear force at multi-axis load cell locations, and (f) and (g) change in NS and EW moment at multi-axis load cell locations.

Deflections: This section compares the profiles of the deflections recorded in the test panel during the test at the beam-slab corner location. The deflection at linear potentiometer locations are plotted against the tip deflection at the push location. Figure 4.33(a) presents the location and naming convention of the linear-potentiometers installed in the test panel.

Figure 4.33(b) and (c) presents the deflection profiles as recorded at sensor locations between the push location and the two adjacent supports LC1 and LC5, respectively. At sensor locations L02 and L03, the LS-DYNA model was able to accurately predict the deflection profile over the entire range of test, with a maximum deflection of -3.2 in. and -3.4 in. at L02 and L03, respectively at maximum tip deflection.

A similar profile is shown for the sensors installed closer to the mid-span, near the failure surface that formed between the supports LC1 and LC5 in Figure 4.33 (d) and (e). At sensor L04, the LS-DYNA predicts a slightly lower deflection of -2.7 in., compared to the recorded deflection of -3.7 in. during the test. At sensor location L05, the LS-DYNA model is able to accurately capture the deflection behavior, recording a maximum deflection of -0.14 in. compared to the recorded value of -0.17 in. during the test. Figure 4.33(f) and (g) show the deflection comparison away from the failure surface that formed during the test at the beam-slab corner location. At both the sensor locations, L06 and L07, the LS-DYNA was able to predict the deflection profile and magnitude of deflection with acceptable accuracy.

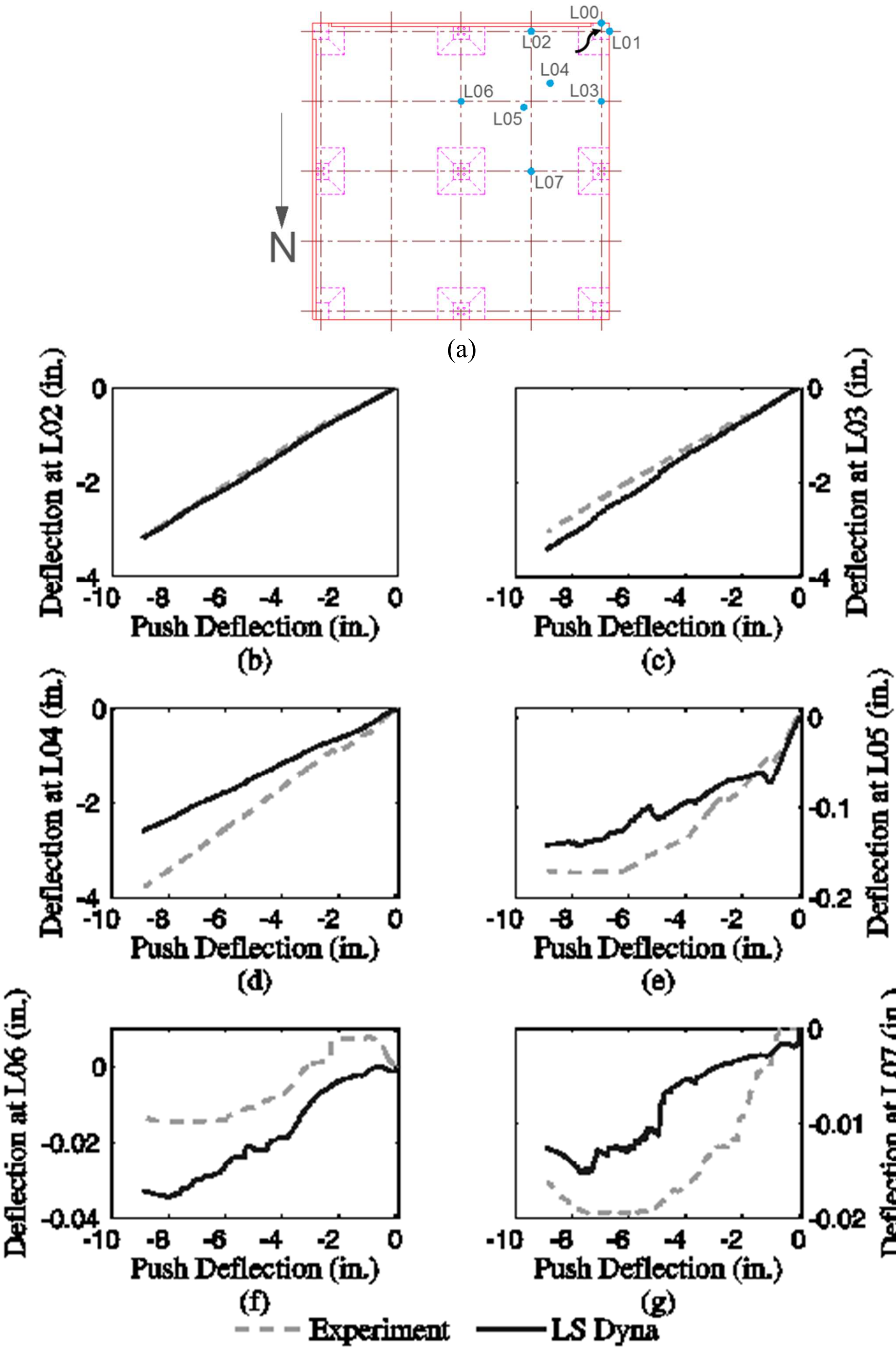

Figure 4.33: Comparison of deflection profiles at linear-potentiometer locations vs the tip deflection at the beam-slab push location.(a) location and naming convention of the locations where the deflections are compared, (b) deflection profile at L02, (c) deflection profile at L03, (d) deflection profile at L04, and (e) deflection profile at L05.

Observed Damage: This section presents a comparison between the observed damage at the end of the test and damage predictions from the LS-DYNA model due to column removal at the beam-slab corner location. Figures 4.34 and 4.35 present the comparison between the observed cracking and the plot of maximum principal strains (tensile strain) from the LS-DYNA model on the top and bottom surface of the specimen, respectively. It is observed that the plot of the tensile strain was able to accurately capture the damage profile on both the top and the bottom surface of the specimen. On the top surface, higher tensile strains were observed between the two adjacent supports LC1 and LC5, suggesting severe cracking as observed during the experiment. The LS-DYNA model was able to predict the damage on the bottom surface, but showed considerably high tensile strains near support LC5 as shown in Figure 4.35. This localization of cracks near support LC5 is caused by the numerical instability during the analysis process, which also resulted in a drop in load capacity after the initial peak and near the end of the analysis. It is noted that the plot of the maximum tensile strain on the concrete only gives a qualitative idea of the crack pattern.

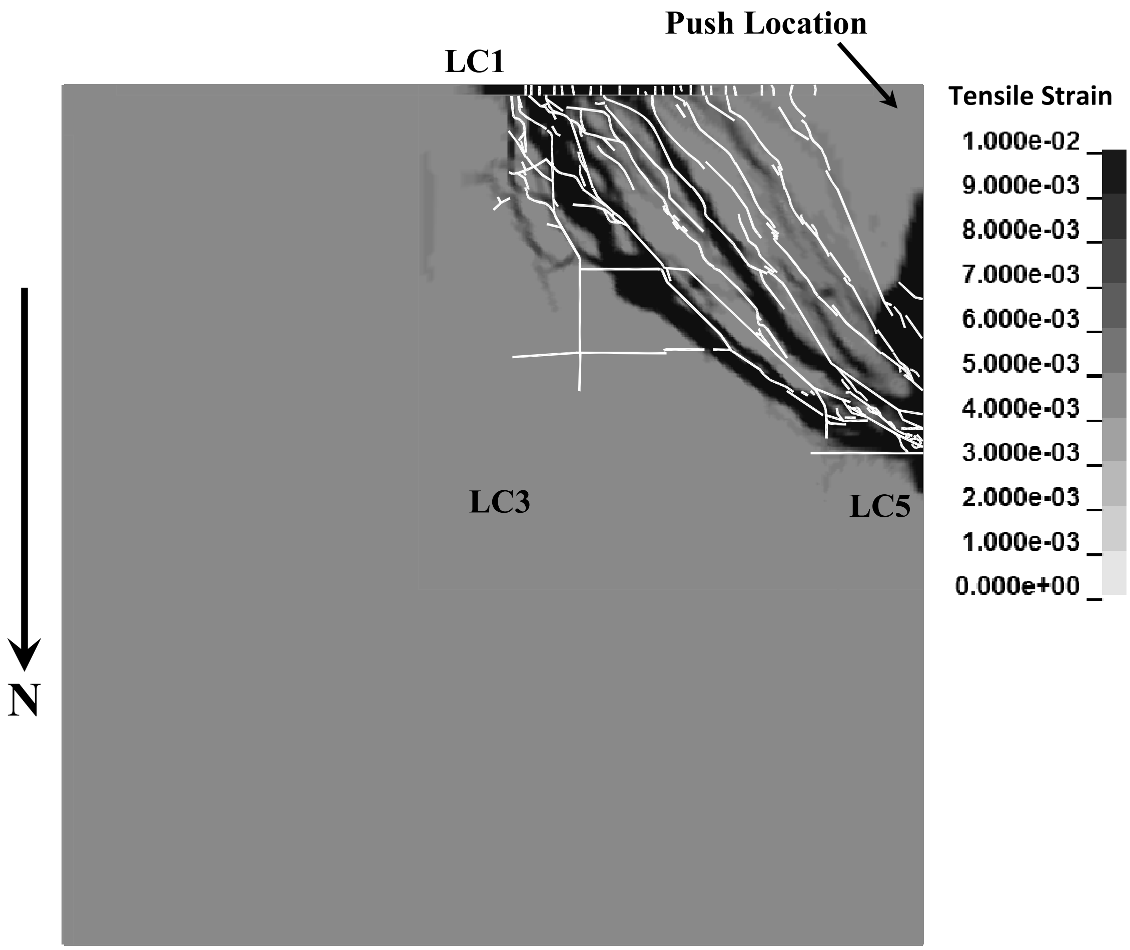

Figure 4.34: Comparison of the observed damage on the top surface of the specimen during the test at the beam-slab corner. The cracks observed during the tests (white lines) are overlaid on the plot of maximum principal strain from the LS DYNA model.

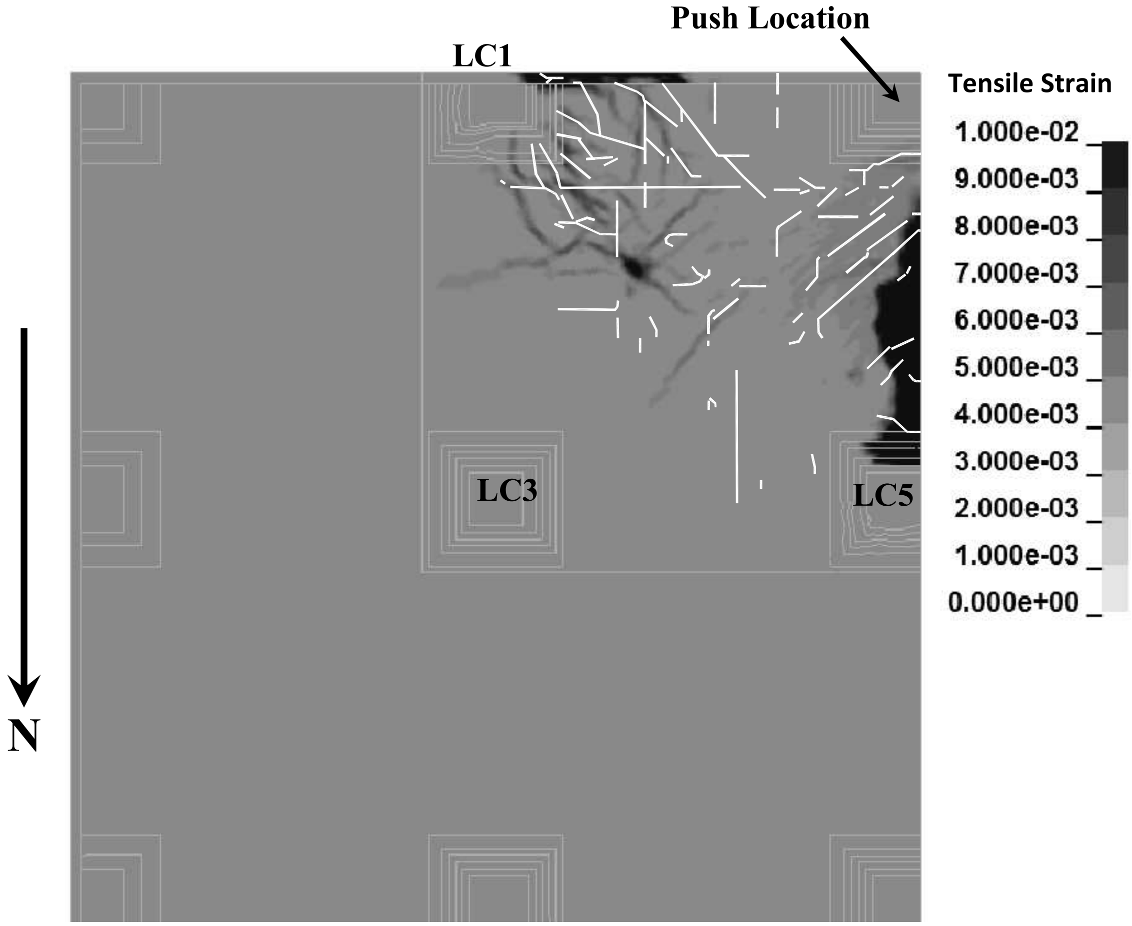

Figure 4.35: Comparison of the observed damage on the bottom surface of the specimen during the test at the beam-slab corner. The cracks observed during the tests (white lines) are overlaid on the plot of maximum principal strain from the LS DYNA model.

4.4 Summary Remarks

Finite element modeling has been widely used by researchers to predict the response of components and systems in the absence of experiments. Although finite element analysis does provide a relatively quick and cost effective method to assess different scenarios; it is necessary to validate the models against available test results. This in turn not only helps in ensuring that the results from the numerical models are in agreement with the available test results and can be used to expand the analyses for similar cases, it also provides insight into the shortcomings of the numerical models employed. In this chapter, numerical models for the three tests performed at the corner location of the test specimen 1 were implemented in finite element software LS-DYNA (LSTC, 2013a, b). The results from these models were systematically compared to the results obtained during the test program.

In each of these models, the concrete was modeled using eight node solid elements, rebar was modeled using two node beam elements, and the multi-axis load cells were modeled using four node shell elements. Each model was then subjected to loads experienced by the specimen (self-weight, uniform gravity load of 90 psf, and three pattern loads), before the push test was simulated. The results obtained from the LS-DYNA model were then compared with the experimental results to validate their accuracy for the gravity load case (90 psf uniform load on the surface) and the three push tests. For the gravity load, the support loads and deflections at linear potentiometer locations were compared, while for the three push tests, load deflection curve and damage observed in the model at maximum deflections were also compared.

For the gravity loads, the model was able to capture the force distribution at all support locations with acceptable accuracy. The model did show some discrepancies within the shear force distribution, especially at the four center edge multi-axis load cell locations LC1, LC2, LC4 and LC5. This was likely due to limitations in accurately capturing the connection stiffness between the concrete specimen and the multi-axis load cells. The LS-DYNA model was also able to capture the additional deflections due to the additional gravity load of 90 psf within 15% of the recorded values during the tests. When compared with the three push tests at the corner locations, the finite element model is able to capture the initial tangent stiffness, and strength with acceptable accuracy. For the two models with either one or two beams on the edges, the finite element model overestimates the strength by 10 to 15%. This is likely due to the material model definition, where the concrete material behaves in a fairly ductile manner in compression, resulting in residual strength at large strains. For the three push down locations, the model was able to capture the load redistribution, deflection profile and the observed damage with good accuracy.

Invariably the numerical model adopted in the present work presents with a number of practical limitations. The following are some of the most important aspects to take note of:

- The concrete material behaves in an elastic manner until it reaches its capacity of *f'c*. This may result in an overestimation of stiffness of the system during the analysis particularly for elements that carry a stress less than *f'c*.
- The concrete material model (**MAT_CSCM_CONCRETE*) performs in a fairly ductile manner in compression as shown by Wu et al. (2012). It has also been shown by Khoe and Weerheijm (2012) that this material would predict higher system strength due to its smeared crack damage formulation based on fracture energy.
- The current modeling technique does not account for bond-slip behavior between the rebar and the concrete, i.e. it is assumed that the concrete is perfectly bonded to the rebar. Prior studies have shown that for reinforced

concrete modeling, this may result in over prediction of stiffness (e.g. Kwak and Fillippou, 1992; Spacone and Limkatanyu, 2000; Kwak and Kim, 2001; Limkatanyu and Spacone, 2003), and possibly strength if failure occurs near the ends of rebar, as rebar will not be able to develop large stresses due to bond-slip behavior.

- The steel material model assumes symmetric stress-strain behavior, i.e. similar response in both tension and compression.
- Each analysis requires a significant run time. This is attributed to not only the large model size, but also large distortions that cumulate towards the later stages of severe damage to the specimen. At this point the implicit time integration may experience numerical instability, and solver then requires a smaller time step and more iterations to converge.

******

Portions of the following publication in preparation, for which author is the principal researcher and author, are contained in this chapter:

- Prasad, S. and Hutchinson, T. C., “Behavior of older reinforced concrete beam-slab systems considering a corner support failure scenario: model validation and parametric study”.
- Prasad, S. and Hutchinson, T. C. (2014), “Evaluation of Older Reinforced Concrete Floor Slabs under Corner Support Failure", ACI Structural Journal, Vol. 111, No. 4, pp 839-850.

- Prasad, S. and Hutchinson, T. (2013), “Behavior of Reinforced Concrete Flat Slab Systems under Corner and Center Support Failure Scenarios”, Proceedings of 10th International Conference on Urban Earthquake Engineering (CUEE), Tokyo, Japan, March.
- Prasad, S. and Hutchinson, T. (2012), "Experimental Evaluation of a 1/3rd scale Lightly Reinforced Concrete Slab under Uniform, Pattern and Concentrated Pull Down Load: Corner Conditions." Structural Systems Research Project (SSRP) Report No. 12/11, Department of Structural Engineering University of California, San Diego, 120 pp.

Chapter 5: Parametric Study

5.1 Overview

During an earthquake, corner columns are expected to experience cyclic axial load demands due to the presence of lateral movement of the structure, which in addition to the lateral load demands increases the likelihood of a corner column failure. Furthermore, failure of a corner column might be more detrimental to structures stability due to the absence of multiple panels to redistribute the loads. To assess the impact of this, in prior chapters a detailed experimental program and numerical model validation are conducted. In the present chapter, these models are extended to consider the broader range of design parameters likely to be encountered in practice. This chapter presents the results obtained from these parametric study and is divided into four sections:

- **Section 5.2:** This section provides a description of the baseline model used in the non-linear finite element analysis. A description of the different parameters which were changed during this study are described.
- **Section 5.3:** This section discusses the results obtained from the parametric models and the observed behavior. Results include load-deflection behavior, ultimate load capacity, and the demands on the adjacent columns due to corner support failure. The ultimate load capacities obtained from the analyses are also compared with the yield line theory estimates for each parametric case.

- **Section 5.4:** This section describes a simple model to calculate the initial stiffness for a flat slab structure under corner column failure scenario. A description of the failure mechanism is provided and is used to calculate the ultimate capacity of the beam-slab system to account for the observed load enhancement. These results are then compared with the recorded values from the numerical model and the 1/3rd scale test at beam-beam corner location on specimen 1.
- **Section 5.5:** A numerical study is conducted to examine the impact of loss of bond and possible slip between concrete and rebar. The results are compared with their respective perfect bond model, with particular focus on the change in strength and ductility of the system.
- **Section 5.6:** A summary of the finding from the nonlinear parametric analysis is provided in this section.

5.2 Model Description

This section provides a description of the baseline model structure and the finite element model(s) implemented in LS-DYNA. The baseline structure is based on the full scale model of the specimen 1 with some changes made to better represent the structural drawings provided by Nabih Youssef and Associates, which were used for detailing the two test specimens presented in Chapter 3. Subsequently finite element models, where the design parameters are changed from the baseline model, are also discussed.

5.2.1 Baseline Structure and LS-DYNA Model

5.2.1.1 Description of the baseline structure

The model floor represents a typical two-way flat slab structure with a regular floor plan. Similar to the two experiments, where only a portion of the floor plan was constructed, only four panels near the corner support locations are modeled for the non-linear parametric study in an effort to maintain a reasonable model size, while accounting for any restraint provided by the adjacent panels (Figure 5.1). The member sizes used for the models are based on drawings provided by Nabih Youssef and Associates to represent a typical older reinforced concrete construction. The overall baseline model is 65ft. in both directions, with supports spaced at 30ft. apart (center to center), supported on 30in. square columns. The finite element model also incorporates sloped drop panels at each support location, which is common in flat slab construction. The baseline structure has 9in.×64in. (width×height) spandrel beams along two exterior edges, a characteristic found to be common in structures from that era. The slab itself is 9 in. thick (L_{Span}/40), based on the minimum required thickness according to ACI 318-1956. A story height of 14 ft. is selected to represent a typical structure where the story height could range between 12 to 16 ft. Figures 5.2 and 5.3 provide a schematic of the model. The push location at the corner location is identified in Figure 5.2 as *"Push Location"*.

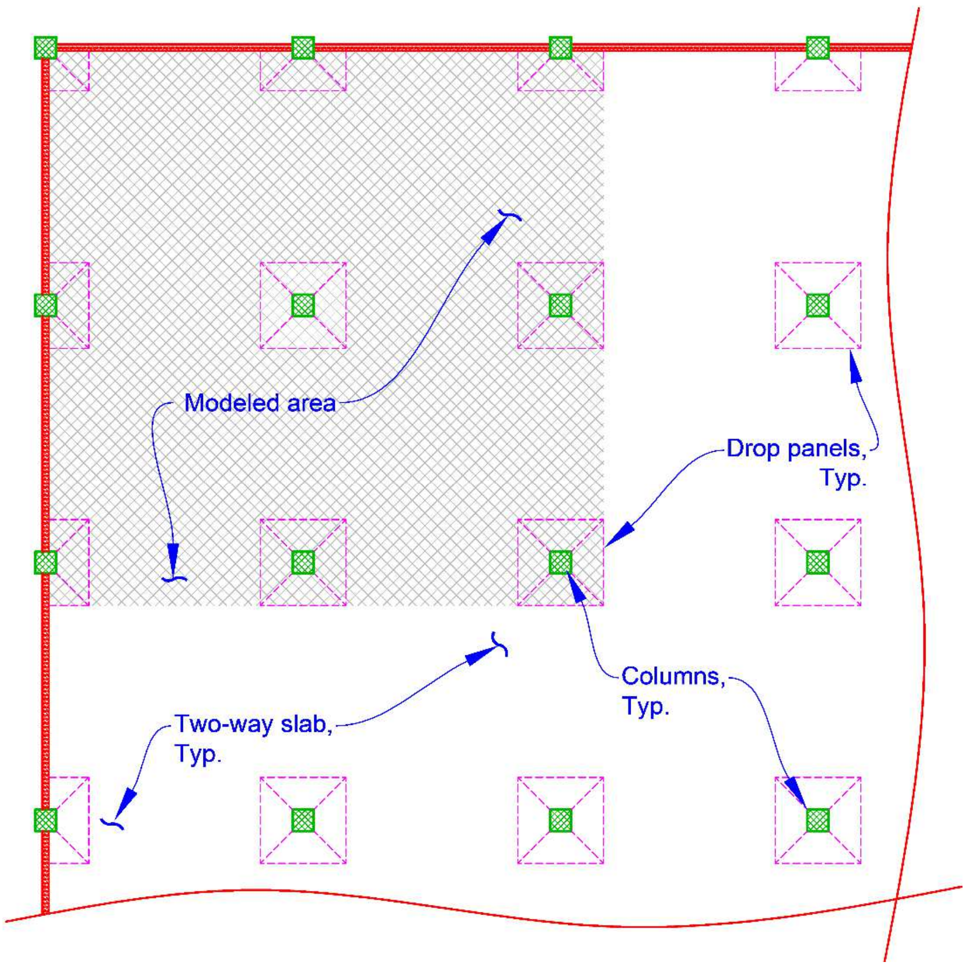

Figure 5.1: Schematic of the overall structure with the modeled region shown by shaded area.

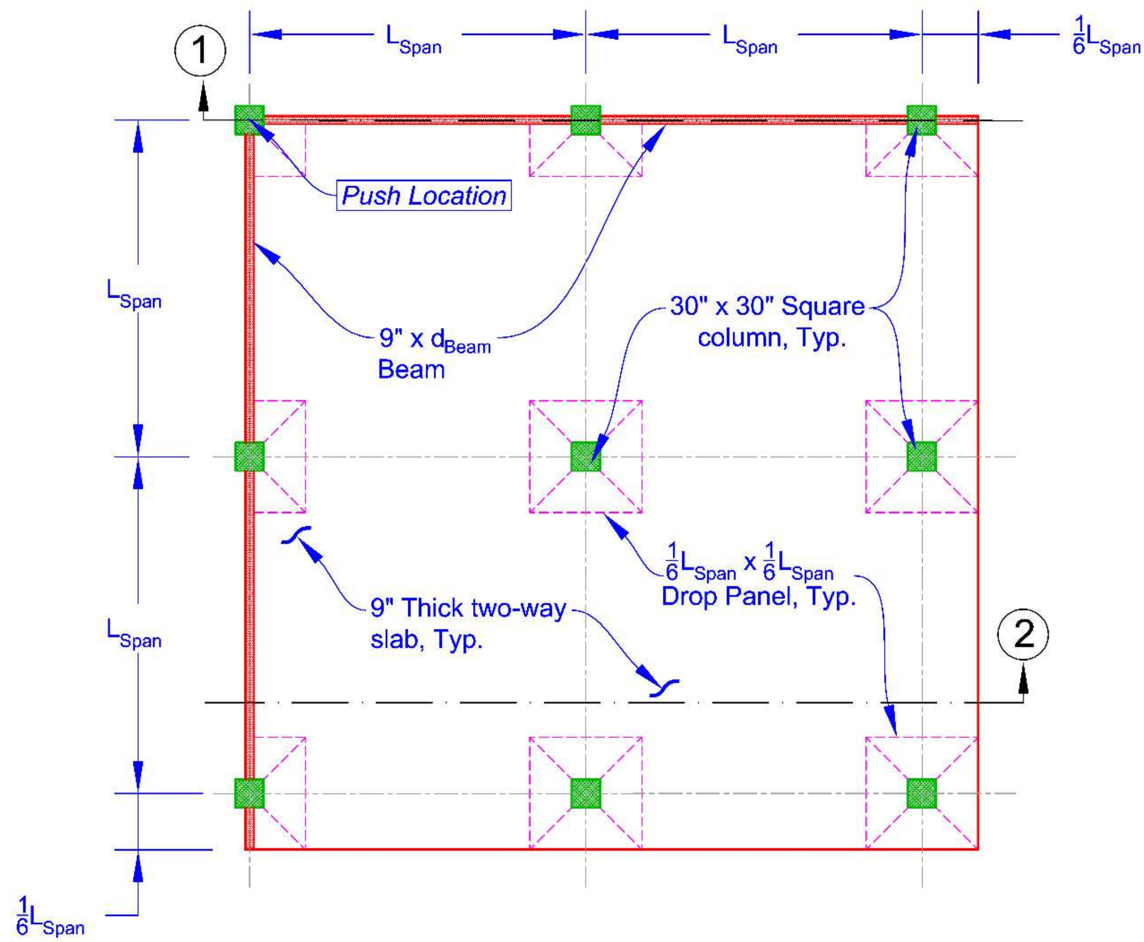

Figure 5.2: Plan view of the LS-DYNA model. Push location on the top left corner is identified as *"Push Location"*. For the baseline model: L_{Span} = 30ft. and d_{Beam}=64in.

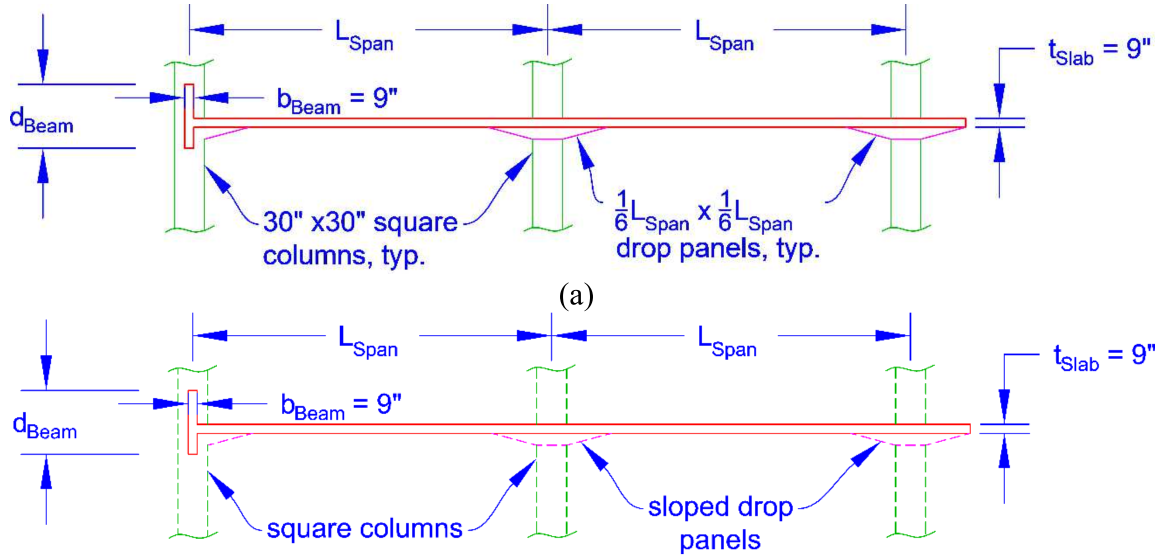

Figure 5.3: Cross-section view of the baseline structure, (a) section 1-1, and (b) section 2-2. For the baseline model: L_{Span} = 30ft. and d_{Beam}=64in.

Although the reinforcing in the actual structure could vary widely for the beam and slab reinforcement, depending on the demands, for the baseline model, an average value of the longitudinal reinforcing is selected to be 0.5% and 1.0% for the slab and beams longitudinal reinforcement, respectively. Based on the spacing requirements (less than two times the slab thickness), #7 Grade 40 rebar at 13.25 in. c/c spacing were used to provide reinforcement in the slab and achieve these ratios, while beam longitudinal reinforcement consists of 3-#10 Grade 60 and 2-#9 Grade 60 rebar. Shear stirrups in the beams are provided using #5 Grade 60 rebar with 12in. c/c spacing. Minimal reinforcement (2%) is assumed within the column to avoid any localized failure during the finite element analysis. Figures 5.4 through 5.7 show schematics of the reinforcing details in the baseline model for the slab, the spandrel beam(s) and the columns. Other reinforcing details including, minimum rebar spacing; embedment length; concrete cover, were provided based on ACI 318-1956.

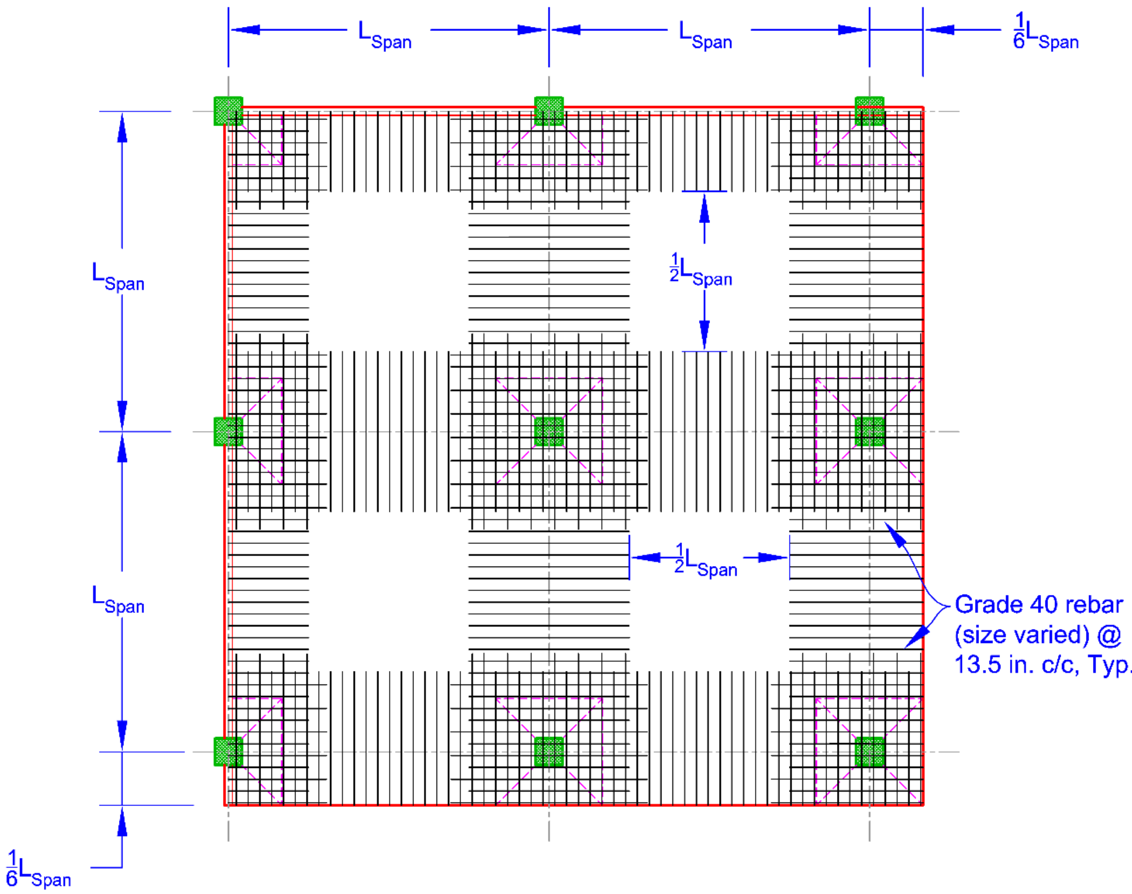

Figure 5.4: Schematic of the top rebar mat provided in the baseline model. L_{Span} = 30ft. for the baseline model.

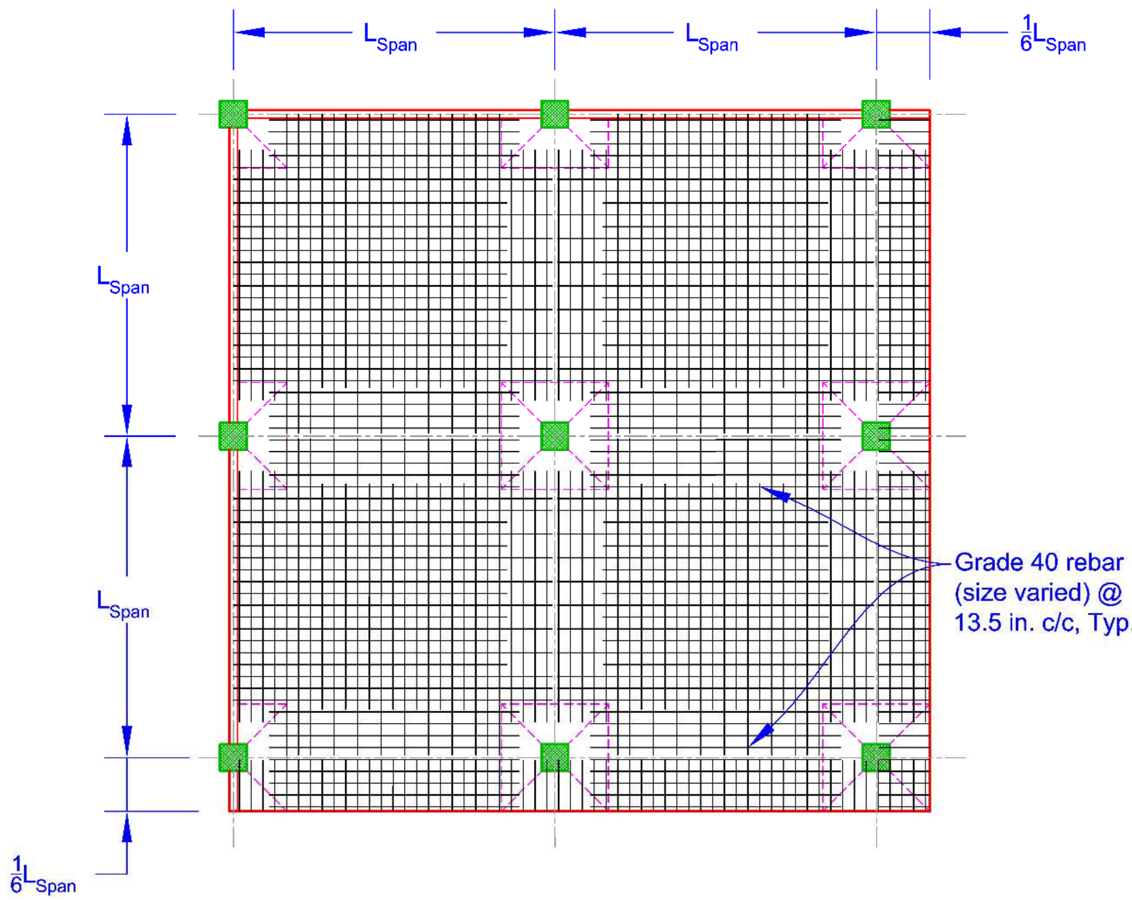

Figure 5.5: Schematic of the bottom rebar mat provided in the baseline model. L_{Span} = 30ft. for the baseline model.

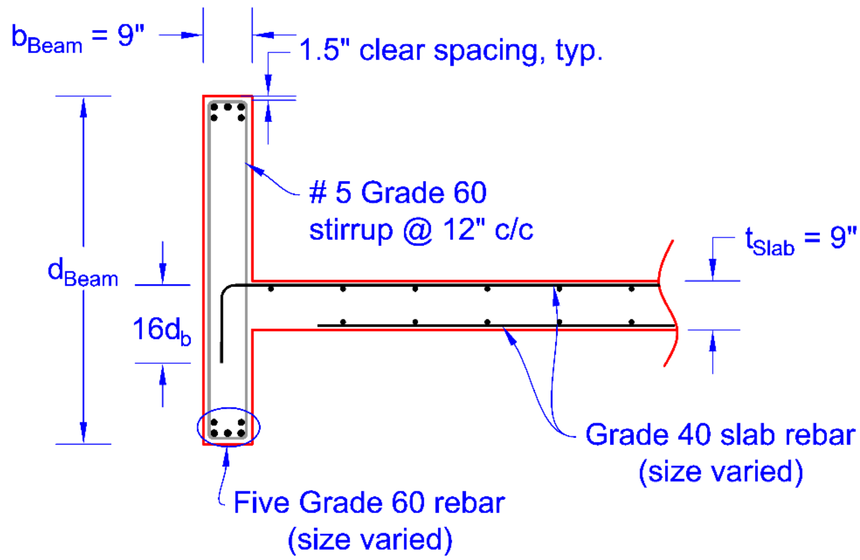

Figure 5.6: Cross section of the beam showing the beam longitudinal and shear reinforcement. d_{Beam} = 64in. for the baseline model.

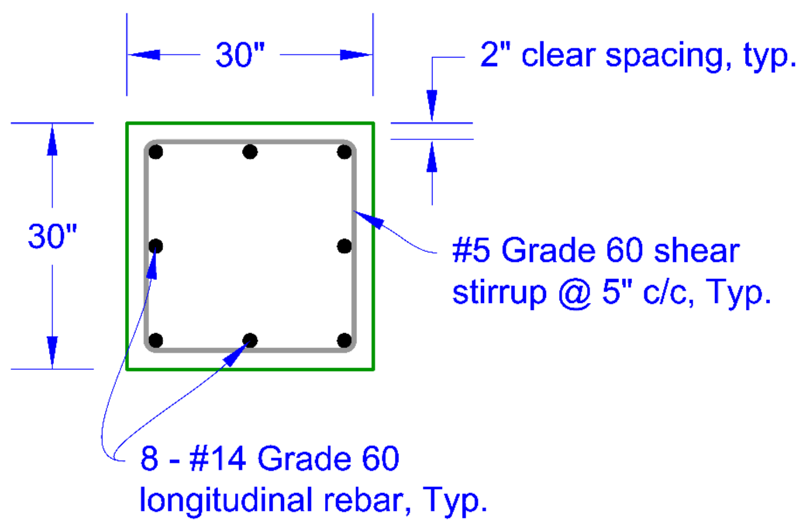

Figure 5.7: Cross section view of the columns showing the rebar arrangement in the columns.

5.2.1.2 LS-DYNA Model of the Baseline Structure

The LS-DYNA model is implemented using a similar approach adopted during the validation process presented in Chapter 4. Namely, the concrete is modeled using eight node solid elements while the rebar is modeled using two node beam elements. As this study focuses on the behavior of the beam-slab system, it is undesirable to have any failure in the supports, therefore, for this study columns are assumed to be elastic, with reduced cross-section stiffness to account for cracking. For the columns, two node beam elements with square cross-section are utilized.

5.2.1.2.1 Geometric Model

Similar to the validation model, two different mesh sizes are provided in the model, with a fine mesh discretization near the push location, and a coarser mesh in the other three panels. As the mesh size near the push location is defined based on four elements through the thickness of the slab, the mesh size near the push location was approximately 3×3×2.25 in. compared to 6×6×4.5in. in the other three panels, away from the corner push location. The mesh size provided for the beam elements, which represent rebar, is based on the nearby solid element mesh size and varied between 3 and 8 in. Figures 5.8 through 5.12 show the concrete model and different rebar models implemented using solid elements and beam elements, respectively. Similar to the validation model, the drop panels in the LS-DYNA model were idealized by a stair case model to avoid convergence issues during the analysis. In total, the numerical model for the baseline structure had approximately 125,000 solid elements and 45,000 beam elements.

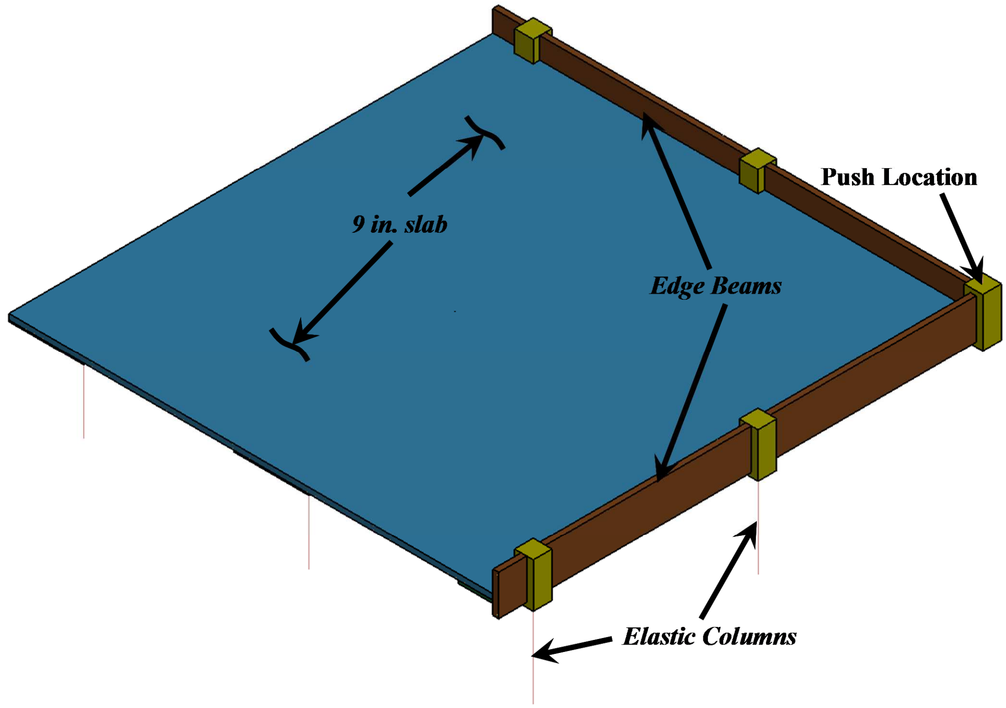

(a)

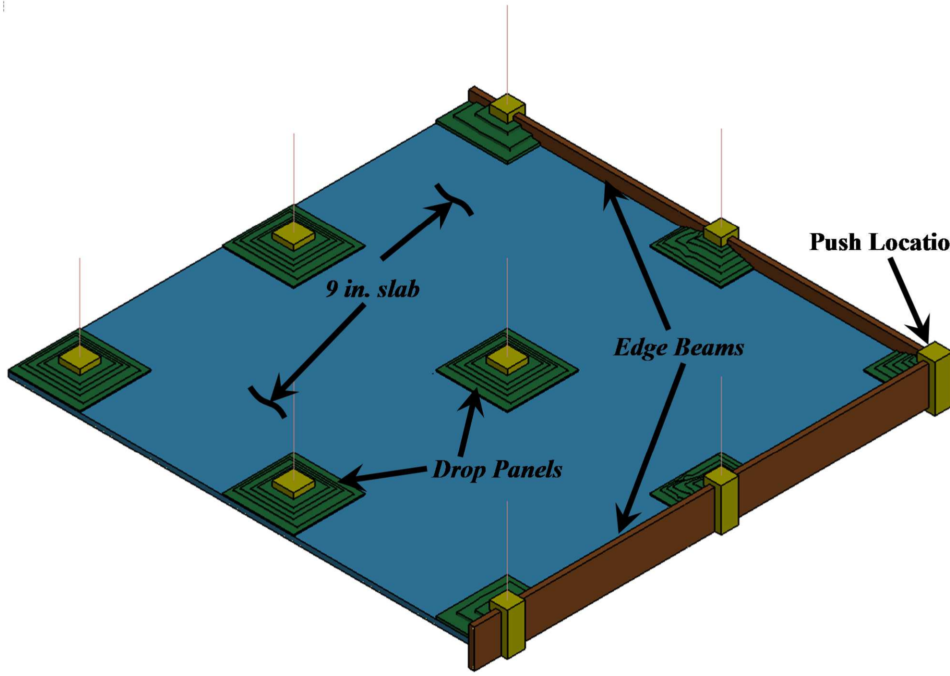

(b)

Figure 5.8: Isometric views of the model implemented in LS DYNA. (a) top surface, and (b) bottom surface. Different concrete components are shown in different color, green-drop panels, blue-slab deck, brown-spandrel beams, and yellow-columns.

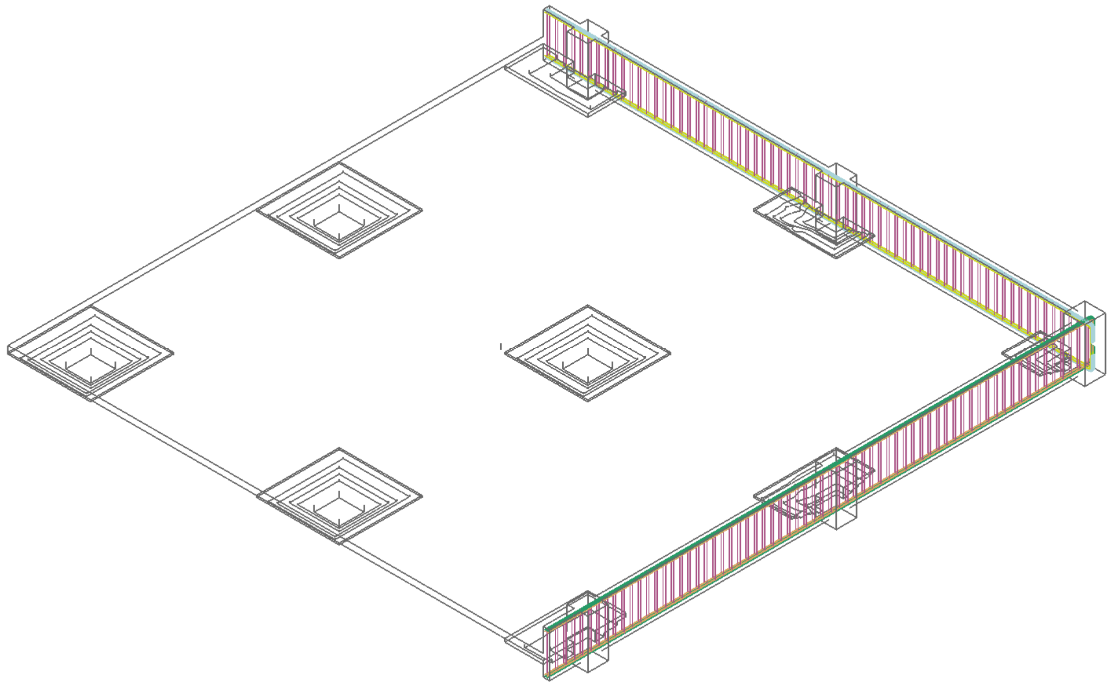

Figure 5.9: Isometric view of the beam rebar along the spandrel beams. Note: an outline of the concrete model is shown in grey. Elastic columns are not shown.

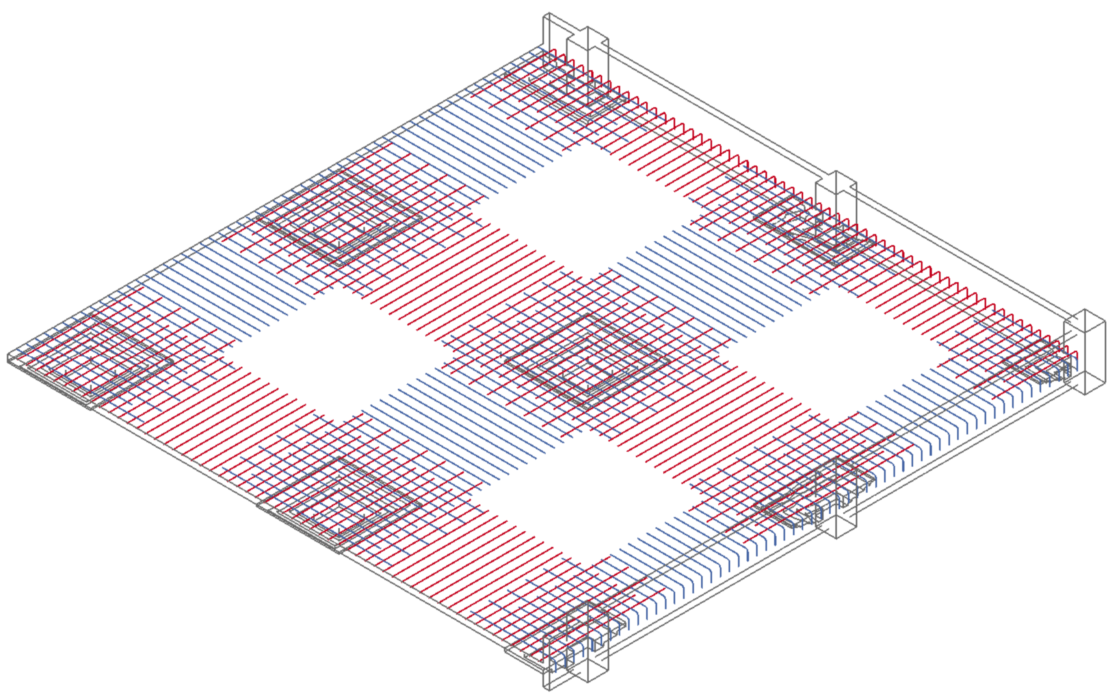

Figure 5.10: Isometric view of the slab top rebar top mat in two directions. Note: an outline of the concrete model is shown in grey. Elastic columns are not shown.

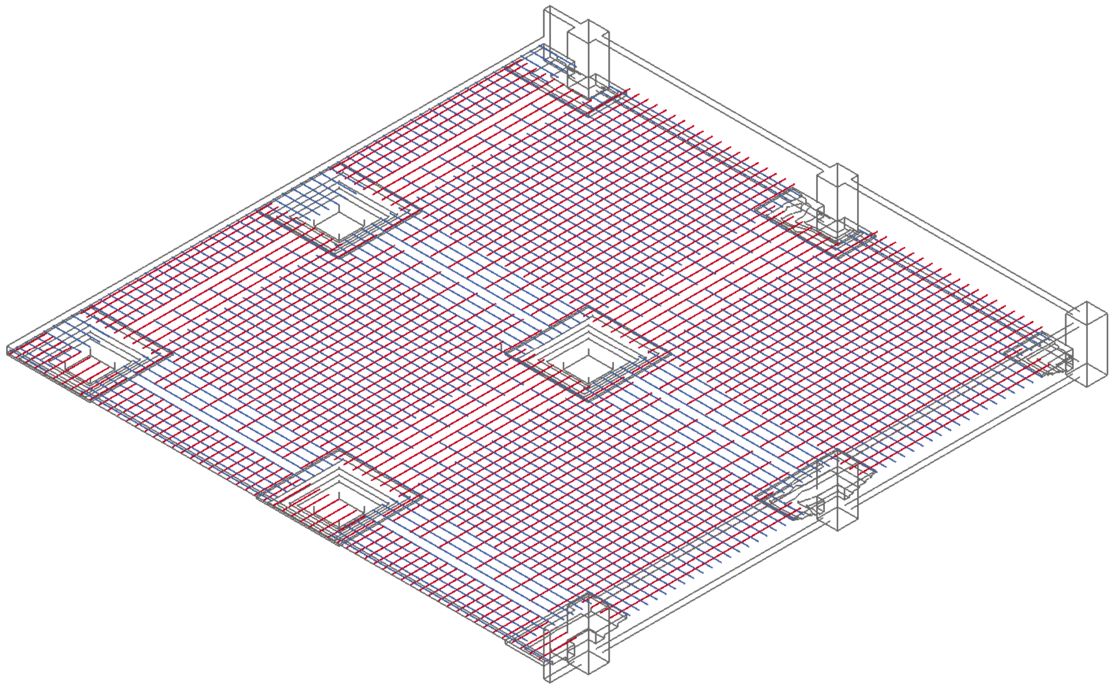

Figure 5.11: Isometric view of the slab bottom rebar mat in two directions. Note: an outline of the concrete model is shown in grey. Elastic columns are not shown.

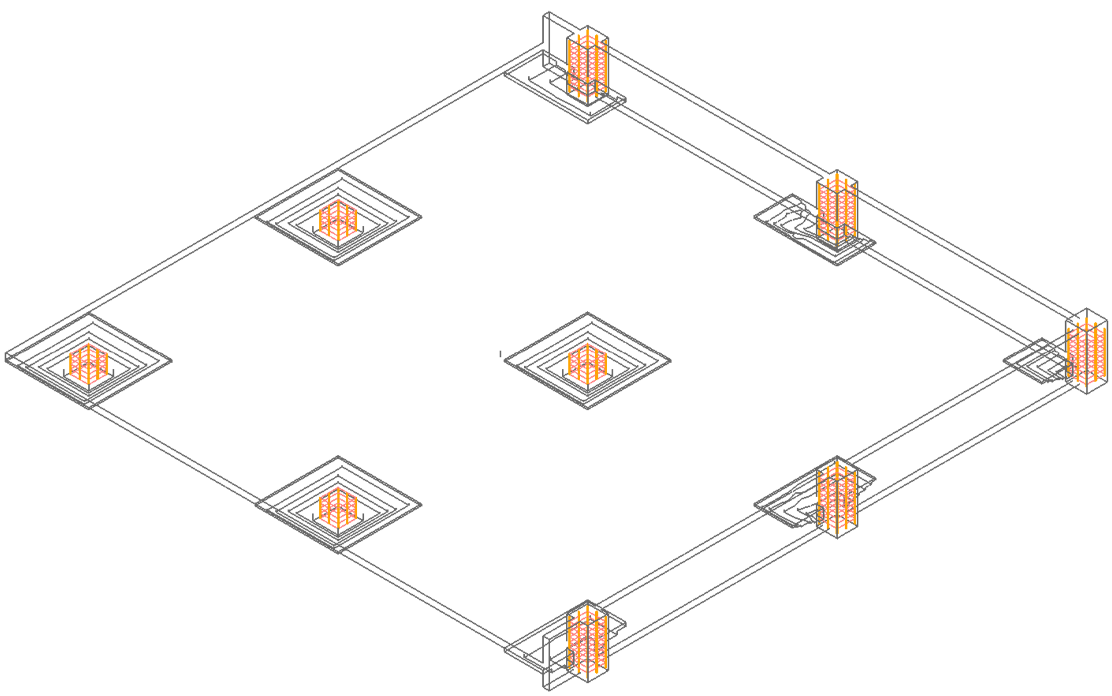

Figure 5.12: Isometric view of the support rebar provided at each support location. Note: an outline of the concrete model is shown in grey. Elastic columns are not shown.

5.2.1.2.2 Support column model

As mentioned earlier, the supports are modeled as elastic beam elements to avoid premature failure in the columns. Although it is desirable for this study to consider the columns to be elastic, it is also necessary to include any stiffness reduction due to cracking in the concrete section. Therefore, for the baseline case the effective lateral and rotational stiffness of the concrete column is assumed to be 50% of the gross uncracked 30in.×30in. section provided for the column. As the cracking only affects the lateral and rotational stiffness of the column, while the axial stiffness remains more or less the same, it is necessary to define the column section and material to allow for the change in lateral and rotational stiffness, while maintaining the same axial stiffness as the gross uncracked section. This can be achieved either by defining a beam element with resultant formulation, where area and section modulus are explicitly defined, or the size of the column and elastic material properties could be modified to achieve the same effect. For example, consider two square cross-sections with initial width of b_1 and b_2 and elastic modulus E_1 and E_2, respectively. For both the cross sections the axial stiffness K_A and lateral and rotational stiffness K_{LF} can be determined by Equation 5.1:

$$\begin{aligned} \left(K_A\right)_i &\propto E_i \times A_i = E_i \times b_i^2 \\ \left(K_{LF}\right)_i &\propto E_i \times I_i = E_i \times \frac{b_i^4}{12} \end{aligned} \qquad \text{Equation 5.1}$$

Considering that the axial stiffness of the two columns is the same, while the lateral and flexural stiffness of the second column is *'n'* times the first column,

$$\frac{(K_A)_2}{(K_A)_1} = \frac{E_2 b_2^2}{E_1 b_1^2} = 1$$
$$\frac{(K_{LF})_2}{(K_{LF})_1} = \frac{E_2 b_2^4}{E_1 b_1^4} = n$$

Equation 5.2

Solving the two equations simultaneously gives: $b_2 = b_1 \times \sqrt{n}$ and $E_2 = E_1/n$.

This transformation allows modelling a cross-section with reduced lateral stiffness due to cracking while maintaining the same axial stiffness as the uncracked section. For the base case the effective lateral stiffness was assumed to be 50% of the gross uncracked stiffness (i.e. n = 0.50) resulting in an elastic column with Young's modulus of 8800 ksi and an effective column size of 21 in. x 21 in. (for initial concrete strength of 6000 psi and column dimension of 30in.x30in.). These beam elements, used to model elastic column section, are constrained to the base of each drop panel using **CONSTR-AINED_NODAL_RIGID_BODY*, which allows transfer of moment between solid element and beam elements representing the beam-slab system and elastic columns, respectively. Figure 5.13 provides a view of the nodal rigid body provided at one of the column locations. It is noted that the elastic columns are only provided below the floor level under consideration, and the columns on the floors above are not considered. Length of each column was provided in such a way that the total distance between the bottom surface of the slab and the end of the elastic column is the same as the assumed story height (= 168 in. = 14 ft.).

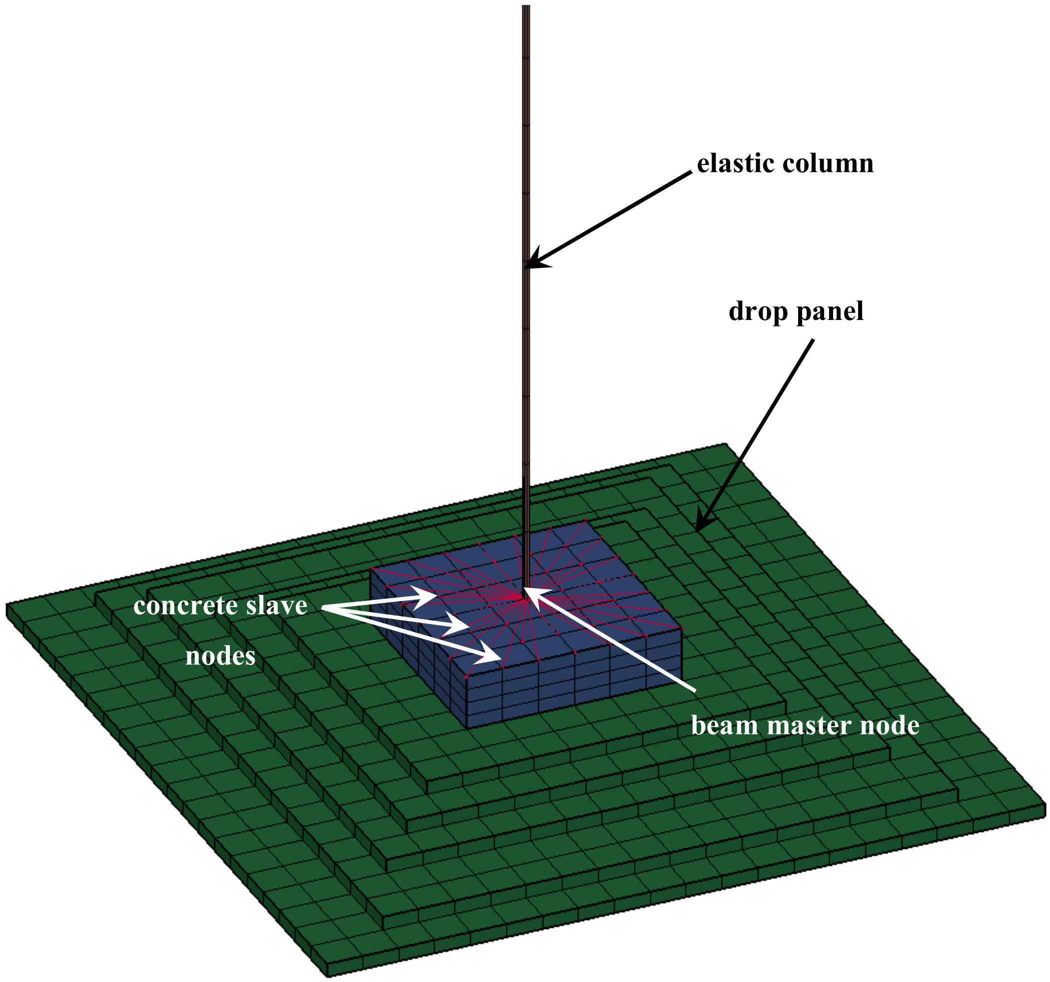

Figure 5.13: Nodal rigid body definition at one of the support locations. All the nodes behave as a part of rigid body, thus transferring rotation and translation. Drop panels are shown in green, and portion of the concrete column is shown in blue.

5.2.1.2.3 Loading Protocol and Boundary Conditions

The model is subjected to self-weight, uniform dead and live load followed by a column removal test at the corner location. The self-weight of the specimen is applied on the model using **LOAD_SEGMENT_SET_NONUNIFORM*, where the intensity of load on the spandrel beam, slab and the drop panels are based on an assumed concrete density of 150 pcf. Following the application of self-weight, additional dead and live load are applied on the structure. Additional gravity loads on the structure are assumed to be 70 psf (consisting of dead and live load). Following the end of the gravity load application, the corner column is subjected to downward vertical movement, simulating support failure. The deflections at the corner is increased until the vertical deflection of approximately $0.1 \times L_{Span}$ (=36 in.) is achieved at the corner push location. It is however noted that all the analyses stopped at a slightly lower deflection of 34.5 in. as some of the initial simulation time is used to apply the gravity loads.

Since only one floor of a multi-level structure are modeled, fixity is provided at the base of each column using **BOUNDARY_SPC_NODE*. The base of the columns, represented by two node beam elements, is constrained in all six degrees of freedom (three rotation and three translation) to mimic a fixed support condition. At the corner support location, where column failure is modeled, the constraint is provided by imposing zero deflection until the gravity load is applied. Following the application of gravity loads, the deflection at the corner support is increased to mimic corner support failure. Apart from the global constraints provided at the base of the supports, and the deflection boundary at the corner support location, no additional constraints are imposed on the model, i.e. no additional restraints are provided along the two slab edges.

5.2.1.2.4 Material Properties and Models in LS-DYNA

In total, four material models are defined, one nonlinear concrete material model, two steel models for Grade 40 and Grade 60 rebar, respectively, and one elastic material to account for reduced column stiffness. The nonlinear concrete model is defined using *MAT_CSCM_CONCRETE* where the concrete compressive strength was defined to be 6000 psi with 1 in. maximum aggregate size. Although most of the older construction was done using 4000 psi concrete, it is noted that such strength gain may be realistic over several decades (ACI 209R-82) and/or could also be attributed to higher mean strength than specified at time of construction (ACI 214-77). Figure 5.14 provides a stress strain curve of the 6000 psi concrete model implemented in LS-DYNA.

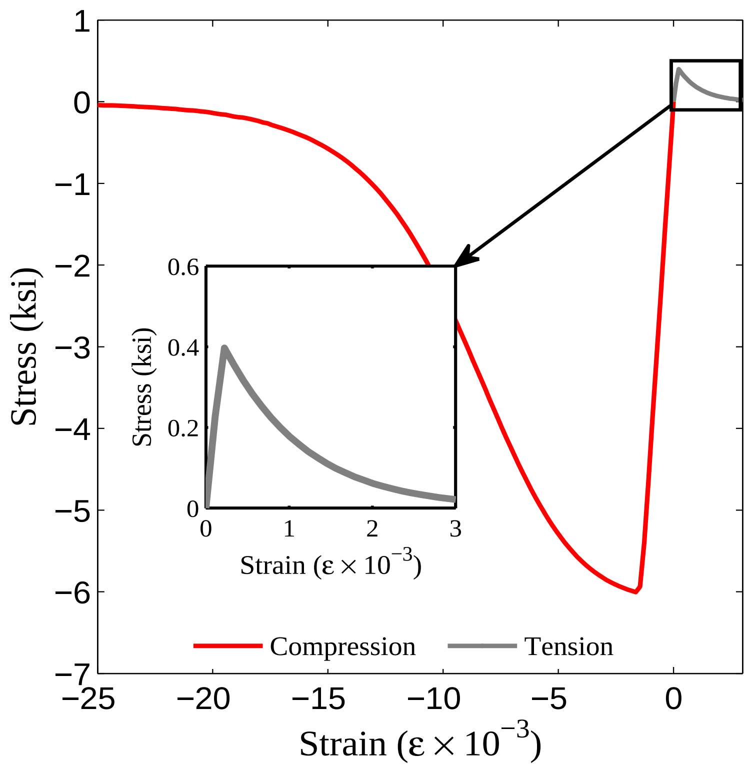

Figure 5.14: Stress-strain plot of the 6000 psi concrete material model implemented in LS-DYNA for the base line model.

Two steel material models were defined in LS-DYNA for the Grade 40 and Grade 60 steel using *MAT_PIECEWISE_LINEAR_PLASTICITY*. For both the material models the initial elastic tangent stiffness is assumed to be 29000 ksi (or 2.9E+07 psi) with no post-yield hardening, i.e. elastic perfectly plastic behavior. Rebar fracture was also modeled in both the steel material models by defining an assumed failure strain of 0.20 in./in. for both steel materials, an average failure strain from the observed coupon tests conducted during the experimental phase of the study.

An elastic material model was defined to model the beam elements representing the columns with reduced lateral and rotational stiffness. As the columns are assumed to have 50% of the lateral stiffness of the uncracked column, the elastic modulus of this material is defined to be $57000\sqrt{f_c^{'}}/0.5$ (in psi).

5.2.2 Description of the Parameters Varied

To better understand the failure mechanism of beam-slab systems under corner support failure, a set of design parameters are varied from the baseline structure. In addition, two additional finite element models are implemented, first where lateral restraint is provided along the interior edge of the structure (Figure 5.15) to simulate an in-plane restraint that might be present due to additional panels. The second model assumes a column removal on only the edge beams as shown in Figure 5.16. Comparing the results from the baseline case with the '*no-slab*' model, the contribution of the slab to the overall behavior can be easily quantified.

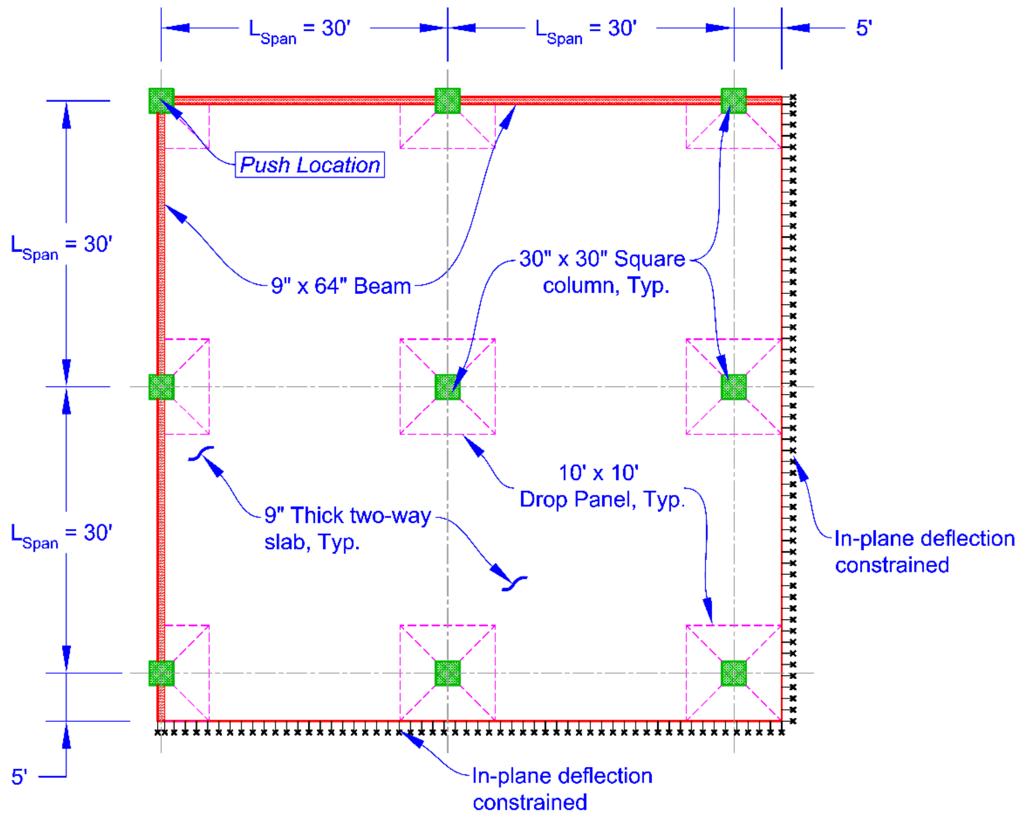

Figure 5.15: Schematic of additional restraints provided for the special case to model the presence of in-plane restraint provided by additional panels.

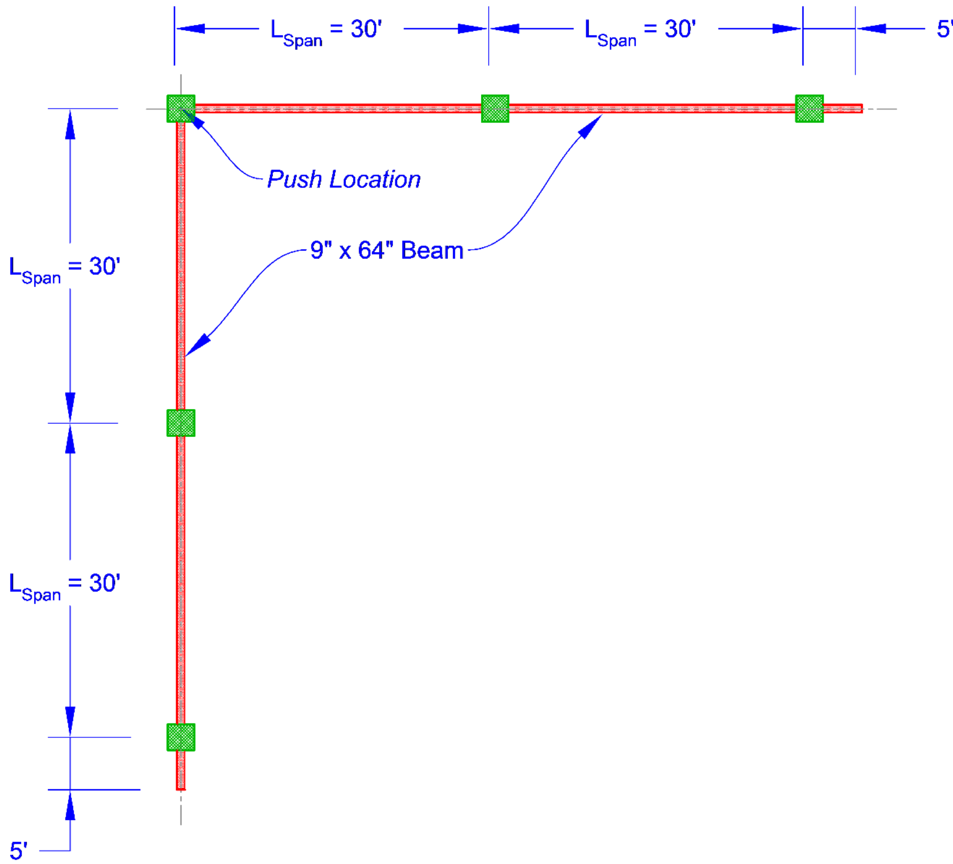

Figure 5.16: Schematic of the special case model where only the edge beams are modeled. The slab is not incorporated in this model.

Apart from the two models described above, six different parameters are studied by changing one parameter at a time in the baseline model. Table 5.1 provides a list of all of the parameters, which are systematically modified and the values considered for each case. For each of these models, a similar modeling technique to that of the baseline model is used.

Table 5.1: List of different design parameters considered for the parametric study. The values changes are highlighted

Model Short Name	d_{Beam} (in.)	ρ_{Beam} (%)	t_{Slab} (in.)	ρ_{Slab} (%)	L_{Span} (ft.)	$f'c$ (ksi)	Support Stiffness (% of $E_c \times (I_g)_{Col}$)
BL (Baseline)	64	~1.1	9.0	0.5	30	6.0	50
d_{Beam}_56*	56	~1.25	9.0	0.5	30	6.0	50
d_{Beam}_72*	72	~1.0	9.0	0.5	30	6.0	50
ρ_{Beam}_0.5	64	~0.5	9.0	0.5	30	6.0	50
ρ_{Beam}_2.0	64	~2.0	9.0	0.5	30	6.0	50
ρ_{Slab}_0.25	64	~1.1	9.0	0.25	30	6.0	50
ρ_{Slab}_1.0	64	~1.1	9.0	1.0	30	6.0	50
L_{Span}_20	64	~1.1	9.0	0.5	20	6.0	50
L_{Span}_40**	64	~1.1	12.0	0.5	40	6.0	50
***fc*_4000**	64	~1.1	9.0	0.5	30	4.0	50
***fc* _5000**	64	~1.1	9.0	0.5	30	5.0	50
$(EI)_{col}$_25	64	~1.1	9.0	0.5	30	6.0	25
$(EI)_{col}$_100	64	~1.1	9.0	0.5	30	6.0	100

* To investigate the influence of d_{Beam}, the total longitudinal rebar area is held constant, therefore the steel ratio does change slightly

** For the L_{Span}_40ft. case, minimum slab thickness is 12 in. (L_{Span}/40) based on ACI-318 (1956)

5.3 Results from the Parametric Study

This section presents the results obtained from the parametric case study. First, the results from the baseline case are presented, where focus is given to the load-deflection behavior, tensile strain concentration and the loads transferred to the adjacent support locations due to the removal of a corner support. This is followed by a comparison of the results from the parametric study.

5.3.1 Results from the Baseline Model

5.3.1.1 Load-Deflection Behavior

Figure 5.17 presents the load deflection behavior of the baseline model. The vertical loads and deflection at the corner support location are defined as positive values. The initial negative load at zero deflection is demand at the corner column location due to gravity load (self-weight + dead load + live load). The model began to deform with an initial stiffness of approximately 90 kips/in. (defined as the secant stiffness between initial point and zero load), followed by some softening at small deflections. As the model is pushed beyond a deflection of approximately 1 in., the stiffness reduced to 40 kips/in. (45% of the initial stiffness), until it reached a vertical deflection of 4 in. (load of 126 kips) at the push location. When pushed further beyond this point, the specimen stiffness decreases significantly, and the model attains a peak load of 142 kips at a deflection of 8.75 in. Beyond the peak, the vertical load capacity decreased consistently reaching a load of 129 kips at 34.5 in. vertical deflection (i.e. 10% strength degradation from peak).

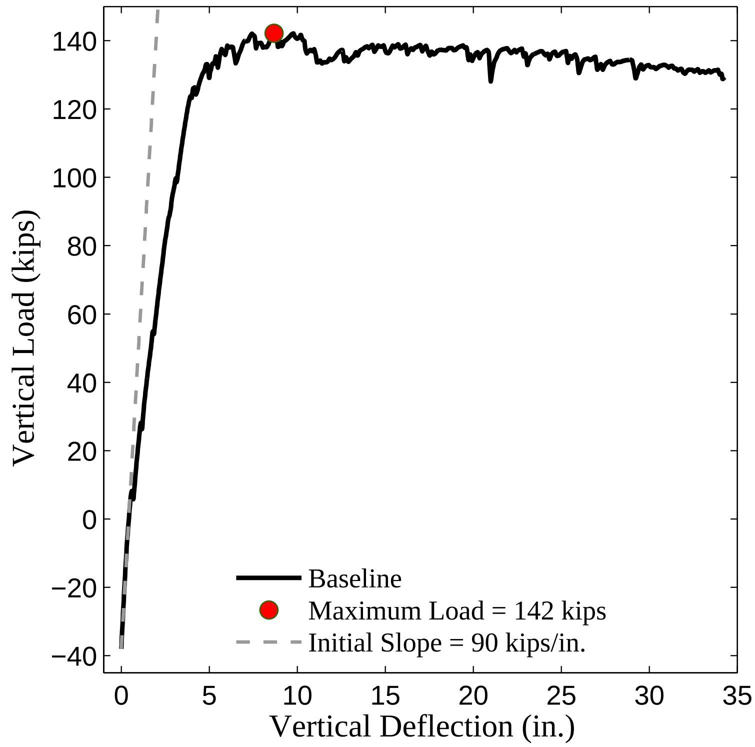

Figure 5.17: Load deflection behavior of the baseline model. Initial negative load at zero deflection is the support reaction due to the self-weight and uniform gravity load applied on the model.

5.3.1.2 Load Redistribution at Supports

Figure 5.18 presents the additional loads transferred from the specimen to the supports due to the push applied at the corner support location. It is noted that the loads presented are the change in load (i.e. loads due to gravity is not included) applied at the top of each support and are presented for only five of the nine supports due to symmetry of the structure and loading.

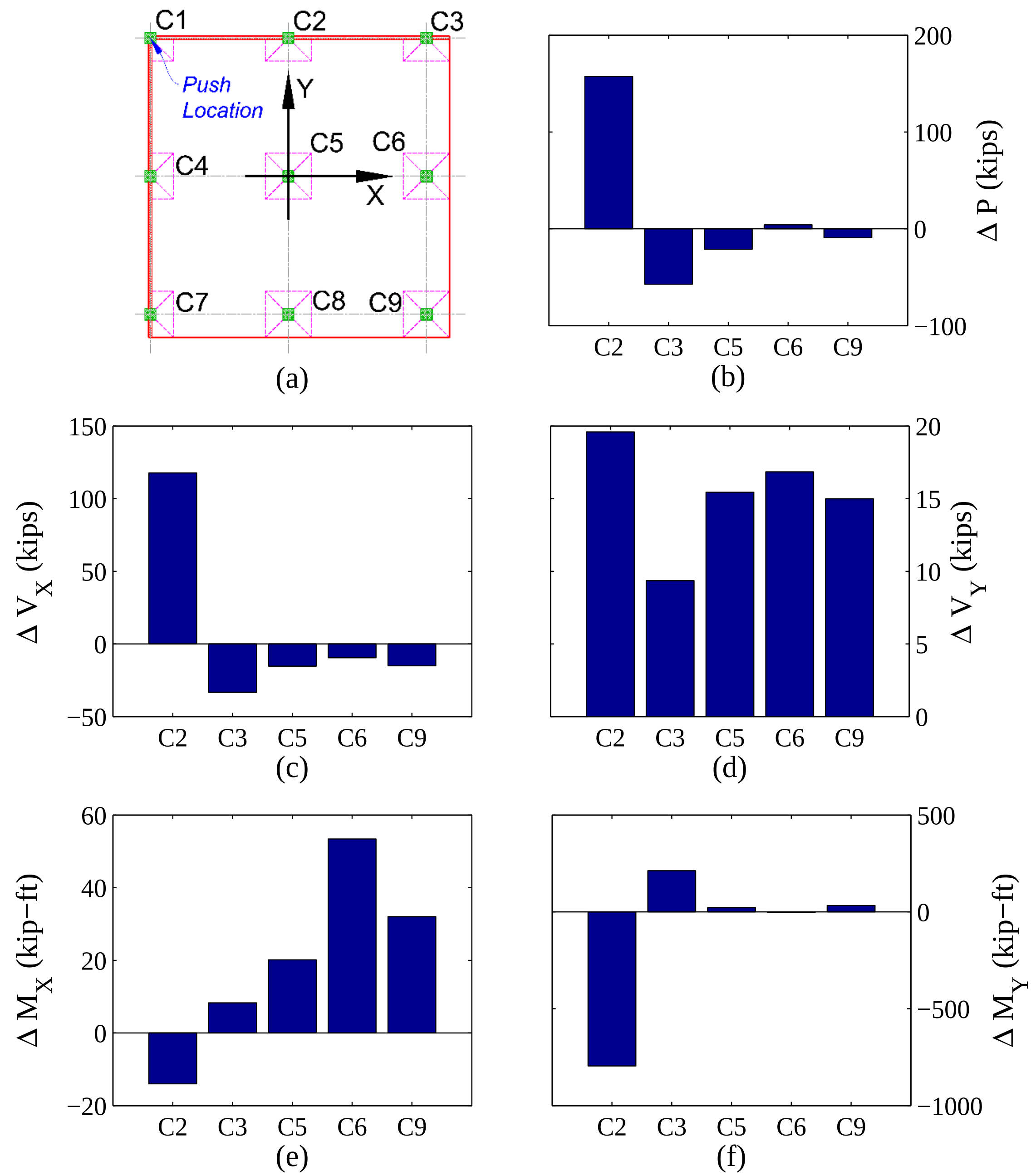

Figure 5.18: Distribution of loads at supports at peak load (142 kips) during the push at the corner support C1, (a) location and naming of the supports, (b) change in axial load, (c) change in X shear force, (d) change in Y shear force, (e) change in X moment, and (f) change in Y moment. Only five of the eight supports are shown due to specimen and loading symmetry. The values presented are additional load at each support due to corner column failure, i.e. load demands due to gravity load is not included.

Figure 5.18 (b) shows the change in axial loads at maximum load condition due to supports removal at C1. It is noted that axial forces acting down on the supports is shown as positive while negative axial force depicts upward force at the support location. As expected, support C2 and C4 experienced the maximum increase in axial load of about 160 kips (additional load demand of approximately $0.03 \times f'c \times Ag$) each. Support C3 (and C7) experienced some reduction in axial load, of about 60 kips, due to beam continuity along C1-C2-C3 and C1-C4-C7. Support C5, placed at the center of the model, experienced an decrease of approximately 20 kips due to negative bending along the failure zone that formed between supports C2 and C4 (see discussion on damage). Other supports, C6, C8 and C9 only experienced very small change of approximately -10 to 5 kips in axial force when the vertical load of 142 kips is applied at the removed column location C1.

Figure 5.18 (c) and (d) present the change in shear force at the support locations C2, C3, C5, C6 and C9. Support C2 experienced an increase in resultant shear of approximately 120 kips (i.e. additional shear stress of approximately 1.7 $\sqrt{f'c}$), mostly directed along the X direction (along the spandrel beam connecting C1 and C2). The direction of the shear force suggests net compression acting along the beam longitudinal axis, pushing the adjacent supports C2 and C4 away from the push location. Other supports also experienced small increase in shear force, ranging from 20 to 35 kips in resultant shear.

Figure 5.18 (e) and (f) presents the additional moments induced at the top of the columns due to the support failure at C1. As expected, most of the moment was induced at support C2 and C4 due to their proximity to the removed column, resulting in an additional resultant moment demand of approximately 820 kip-ft. at top of the column C2 and C4. At support location C2, most of the moment demand was in the –Y direction, i.e. along the spandrel beam transverse axis caused due to the bending along the strong axis of the beam. Support C3 and C7 also experienced an increase in moment demand of approximately 200 kip-ft. along the beam transverse axis. This increase in moment is attributed to the absence of any additional panels, which would provide rotational restraint along the free edges C3-C6-C9 and C7-C8-C9, thus significantly reducing the moment demands along the beam transverse axis at supports C3 and C7. Compared to the moment demands at C2, C3, C4 and C7, other supports experienced little to no change in moment demand due to support failure at C1.

5.3.1.3 Observed Tensile Strain Concentration

This section presents the tensile strain concentration in the model during the column failure at corner support C1 at end of simulation. It is noted that tensile strain is used in the present context as a proxy for damage. Figures 5.19 and 5.20 shows the plot of the *maximum principal strain* (i.e. tension) on the top and bottom surface of the specimen at maximum achieved deflection. As expected, the direction and location of the tensile strain concentration along the adjacent support C2 and C4 is in agreement with the expected yield lines that would form between these supports due to the force applied at support C1 (Figure 5.19). Tensile strain concentrations near C2 and C4 are caused due to the presence of drop panel near the supports. The plot of the maximum tensile strain also suggests some tensile damage away from the yield line due to the presence of in-plane membrane forces in the slab.

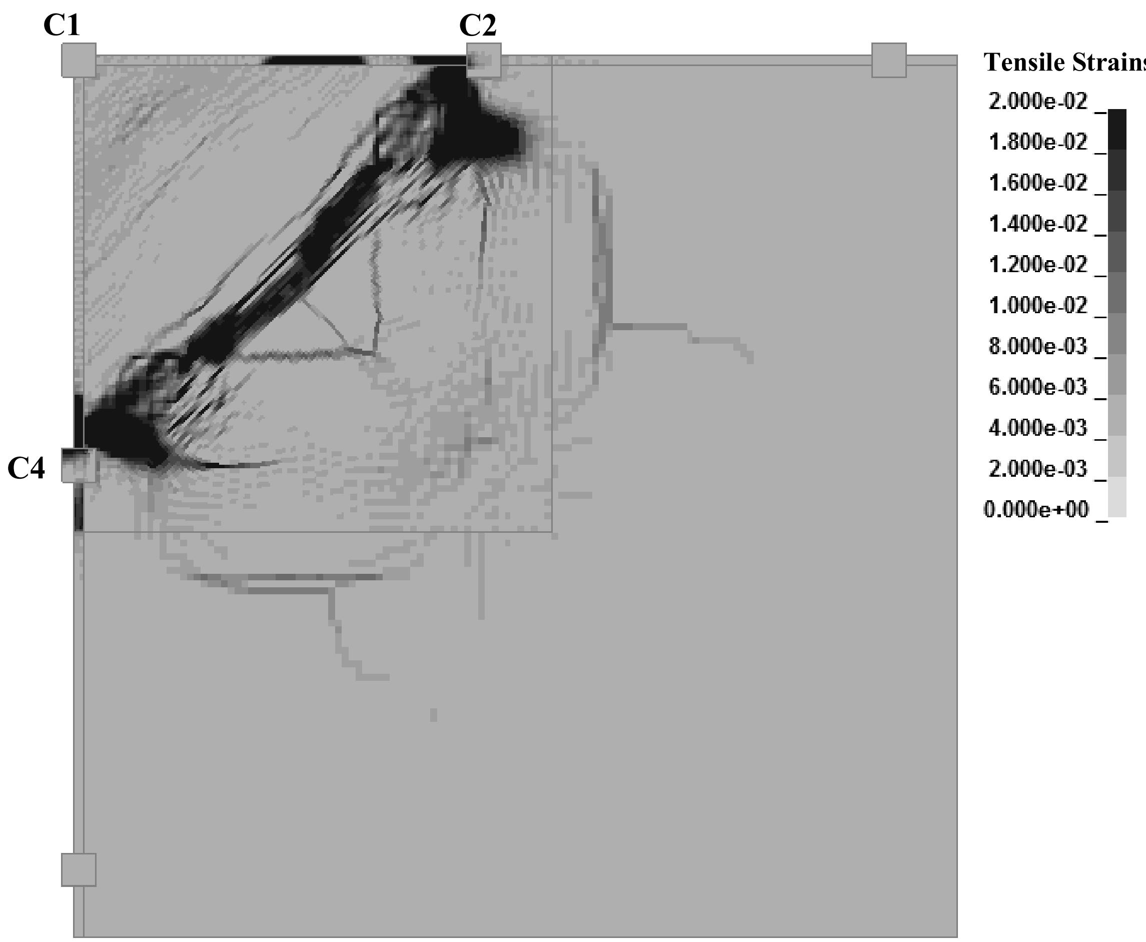

Figure 5.19: Plot of the principal strain (*tension*) on the top surface at end of simulation (i.e. corner deflection of 34.5 in.).

Figure 5.20 shows a similar plot of the tensile strains on the bottom surface of the model. Similar to the observed cracks on the bottom surface during the tests at corner locations (Chapter 3), tensile strains are observed radiating away from the push location, suggesting torsional strain, with some localization observed outside the failure zone suggesting presence of tensile forces inward of the specimen away from the failure zone.

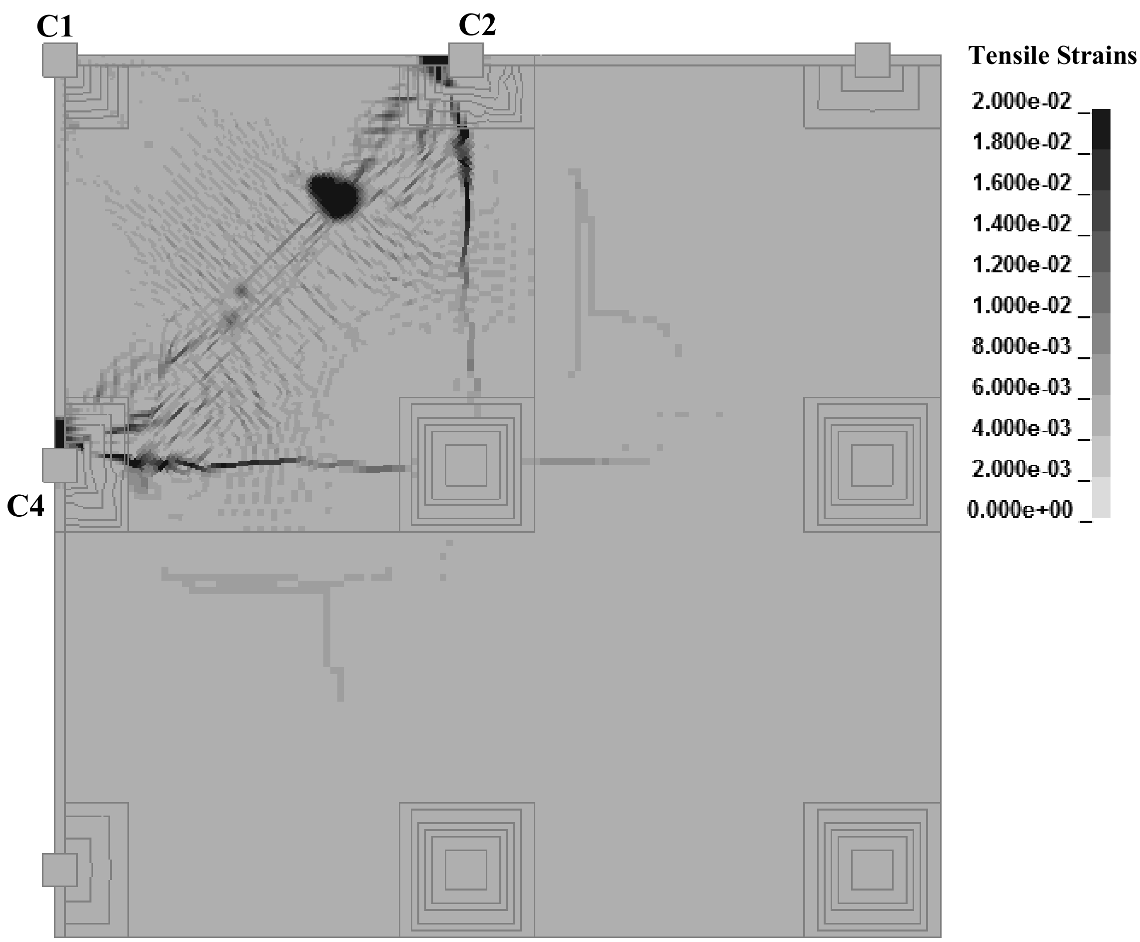

Figure 5.20: Plot of the principal strain (*tension*) on the bottom surface at end of simulation (i.e. corner deflection of 34.5 in.).

A similar profile of principal tensile strains on one of the edge beams is shown in Figure 5.21. As the yield line formed closer to the support location, most of the tension was localized near the support with the damage profile suggesting mostly flexure behavior near the supports. Away from the yield line, the principal strains aligned along 45° angle, suggesting mid-span cracking dominated by shear. Moderately high tensile strains are also observed in the adjacent panel due to beam continuity, similar to the cracking observed during the specimen 1 test program.

Figure 5.21: Plot of the principal strain (*tension*) on the side of the spandrel beam at end of simulation (i.e. corner deflection of 34.5 in.). C1 is the location of push. It is noted that the deflected shape of the specimen is not shown.

5.3.3 Comparison of the Various Parametric Cases with Baseline

5.3.3.1 Load-Deflection Behavior

Additional Restraint Case: Figure 5.22 presents the load-deflection relation of the additional constraint model compared with the baseline model. The model with additional restraint began to deform with an initial tangent stiffness of approximately 90 kips/in., same as the stiffness recorded in the baseline model. Pushed further the stiffness decreased by 50% at a deflection of approximately 0.8in. A significant decrease in stiffness is observed beyond 4.5 in. deflection with the additional restraint model reaching its maximum capacity of 148 kips at a vertical deflection of 9.4 in. Compared with the baseline model, the load capacity was only 4% higher. Similar to the base line model, the additional restraint model continued to deform with small strength degradation, reaching a load capacity of 132 kips at a deflection of 34.5 in. (compared to 129 kips for the base line model at same deflection). Comparing the overall load-deflection relation between the two models, little difference is observed due to the presence of additional in-plane restraint along the interior slab edges away from the push location, suggesting that the presence of additional panels do not significantly affect the load deflection behavior under corner support failure.

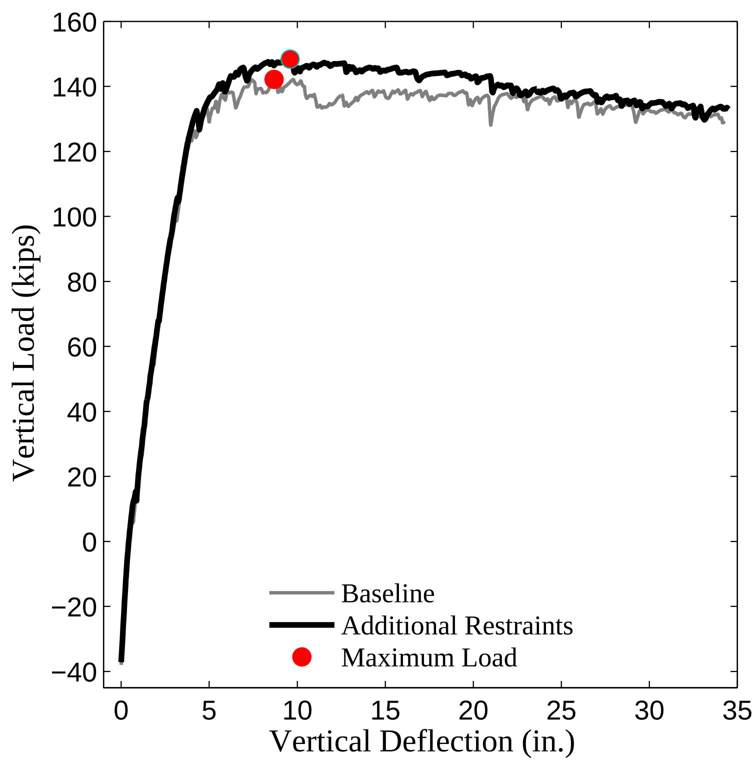

Figure 5.22: Load deflection comparison between the base line case and the two special cases, one with additional restraints and another without the slab.

No Slab Case: Figure 5.23 presents the comparison of the load deflection behavior of the base line model and the no-slab model. For the no-slab case, the model deformed with an initial stiffness of approximately 75 kips/in. When pushed beyond approximately 1 in. vertical deflection at the push location, the stiffness reduced to 25 kips/in. (35% of the initial stiffness), until it reached its peak load of 75 kips at a deflection of 3.8in. Pushed further, the model continued to deform in a plastic manner until it reached a deformation of 25 in., at which point a sudden drop in load was observed due to beam longitudinal rebar fracture near column C2 (Figure 5.24).

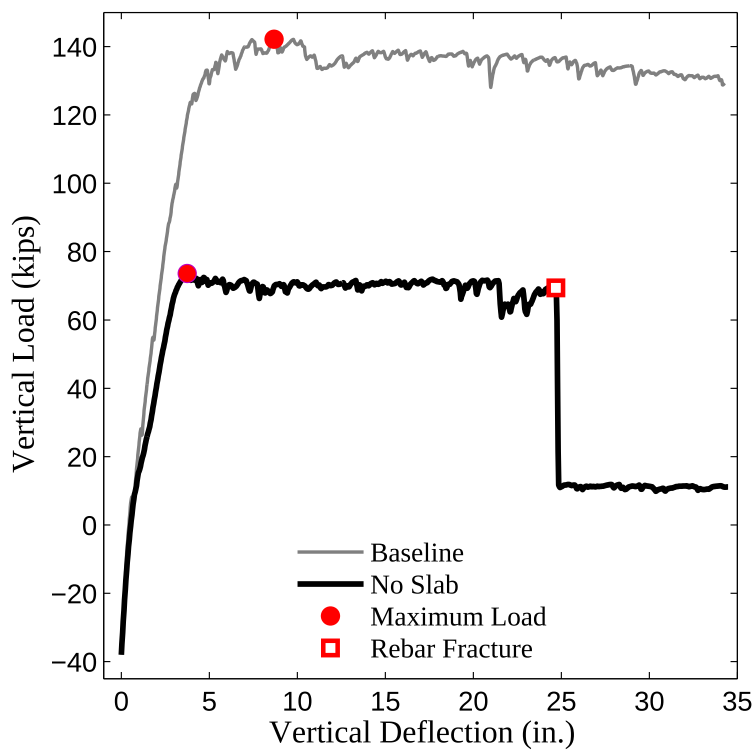

Figure 5.23: Load-deflection behavior comparison between baseline model and no slab model.

As the deflection was further increased the model continued to deform plastically with a load capacity of 11 kips until the simulation was stopped at a deflection of 34.5 in. Compared with the baseline model, the no slab model deformed with a slightly lower initial stiffness (defined as secant stiffness between initial point and zero load) and was only able to achieve 50% of the ultimate load capacity of the baseline model, suggesting load enhancement of almost 100% due to the presence of two-way slab.

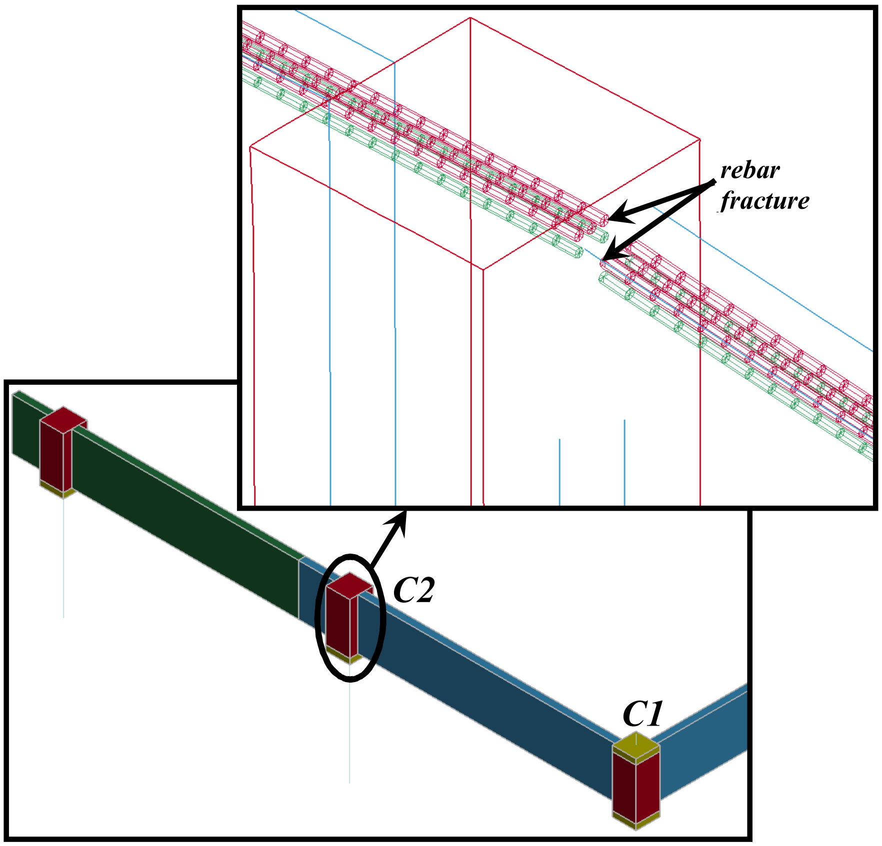

Figure 5.24: Observed rebar fracture near column C2 during push at corner support in no-slab model at 25 in. vertical deflection. Note that only the beam longitudinal rebar are shown in the inset.

Beam Depth: Figure 5.25 presents the load deflection behavior of the models where the depth of the beam is varied between 56 in. and 72 in. It is noted that while the depth of the beam was varied, the total rebar area provided in the beam is not modified from the baseline model, hence a change in beam depth also changes the beam reinforcing ratio by the same factor.

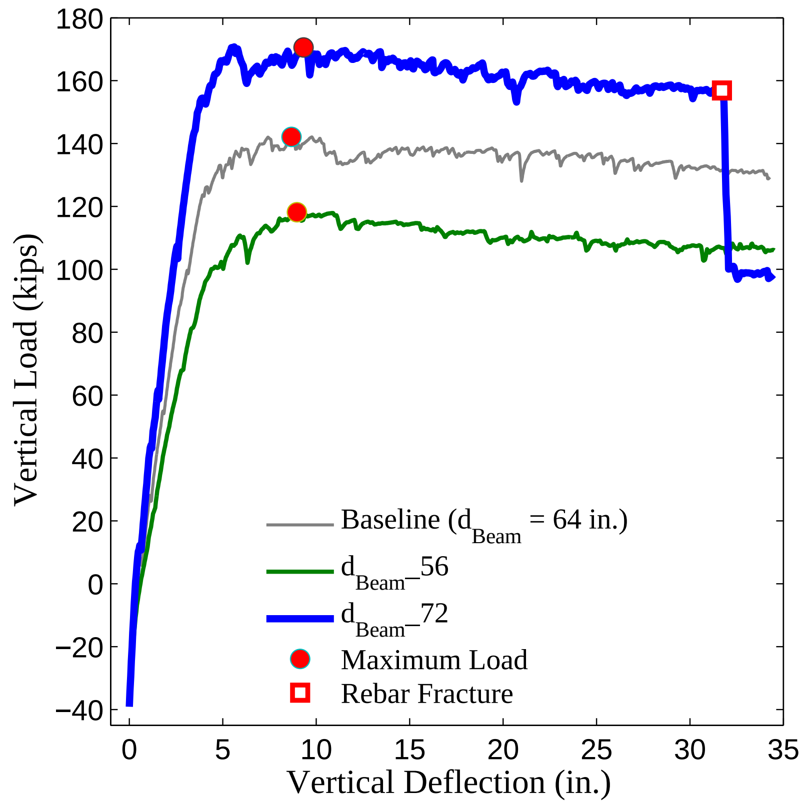

Figure 5.25: Load deflection relation for models with different beam depth. It is noted that total beam longitudinal reinforcement is same between different models.

The two models began to deform with initial stiffness of 65 kips/in. and 120 kips/in. for $d_{Beam\_}56$ and $d_{Beam\_}$ 72, respectively, compared to the initial stiffness of 90 kips/in. for the baseline model (d_{Beam} = 64 in.). As the deflection was increased beyond 0.4 in., all the models experienced softening, and continued to deform with 40% of their initial stiffness. The models attained the peak load of 118 and 170 kips for $d_{Beam\_}56$ and $d_{Beam\_}72$, respectively, at deflections of approximately 9 in., compared to the maximum achieved load of 142 kips for the base line model. Beyond the peak load, all the models experienced small strength degradation of approximately 10%, at maximum achieved deflection of 34.5 in. Unlike the other two models, the model with $d_{Beam\_}72$ experienced a sudden drop in load at a vertical deflection of 32 in. due to beam rebar fracture, lowering the load capacity to 100 kips at a vertical deflection of 34.5 in.

Beam Reinforcing Ratio: Figure 5.26 presents the load deflection behavior of the two models with varying beam reinforcing ratio. The beam reinforcing ratio was varied between 0.5% and 2%, a typical range of reinforcing ratio observed in reinforced concrete construction.

All the models deform with slightly different initial stiffness of 70 kips/in. and 115 kips/in. for $\rho_{Beam\_}0.5$ and $\rho_{Beam\_}2.0$, respectively, compared to the initial stiffness of 90 kips/in. for the base line model (ρ_{Beam} = 1.1 %). This slight difference in initial stiffness was due to the some tensile damage that had already occurred in the beams during gravity loading. When pushed further, the stiffness for the models diverge significantly at a vertical deflection of approximately 0.7 in., reducing the stiffness for each model to approximately 30-40% of their respective initial stiffness. Each model continued to deform with a reduced stiffness until the models became non-linear and achieved their respective maximum capacity of 90 kips and 255 kips for $\rho_{Beam\_}0.5\%$ and $\rho_{Beam\_}2.0\%$, respectively. Beyond the peak load, all the models show some strength degradation. The model with high beam reinforcing ratio (ρ_{Beam} = 2.0%), experienced a sudden drop in vertical load carrying capacity at a vertical deflection of 32.5 in., beyond which the capacity dropped to approximately 150 kips until the end of simulation at a vertical deflection of 34.5 in.

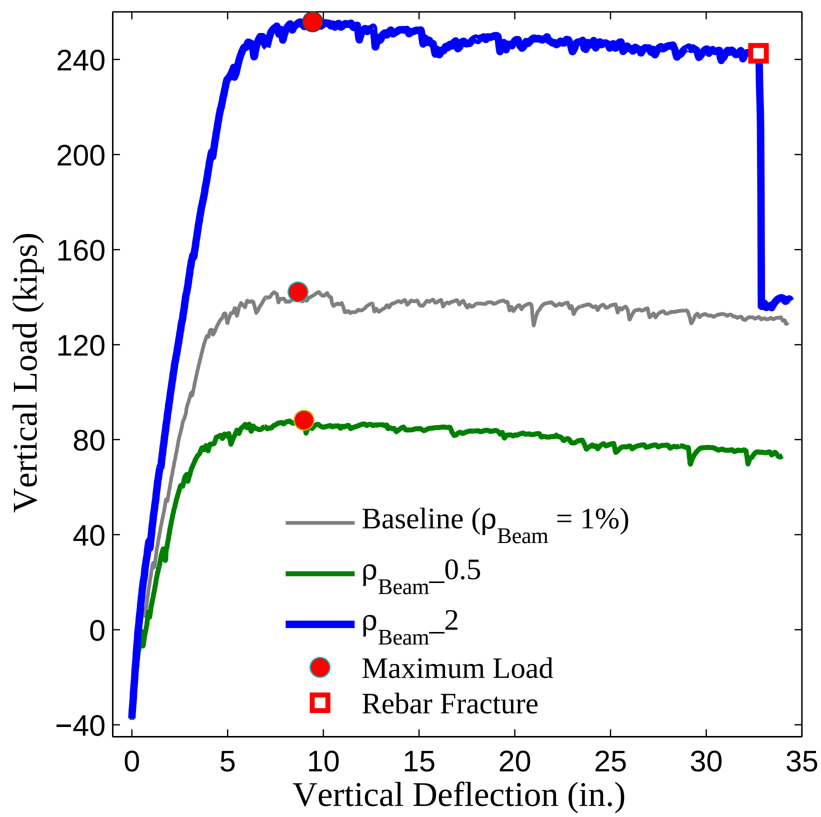

Figure 5.26: Load deflection relation for models with different beam reinforcing ratios.

Slab Reinforcing Ratio: Figure 5.27 presents the load deflection behavior for the three models with varying slab reinforcing ratio. The three models shows a very similar force-deflection behavior with initial stiffness of approximately 90 kips/in. with slight stiffness degradation at vertical deflection of 0.8 in. As the deflections are increase in each model, the behaviors of the models diverge at approximately 3.5 to 4 in. vertical deflection. Beyond this, the models gain little additional strength, reaching their maximum load of 123 and 162 kips for slab reinforcing ratio of 0.25% and 1%, respectively, compared to the maximum capacity of 142 kips for the base line model with slab reinforcing ratio of 0.5%.

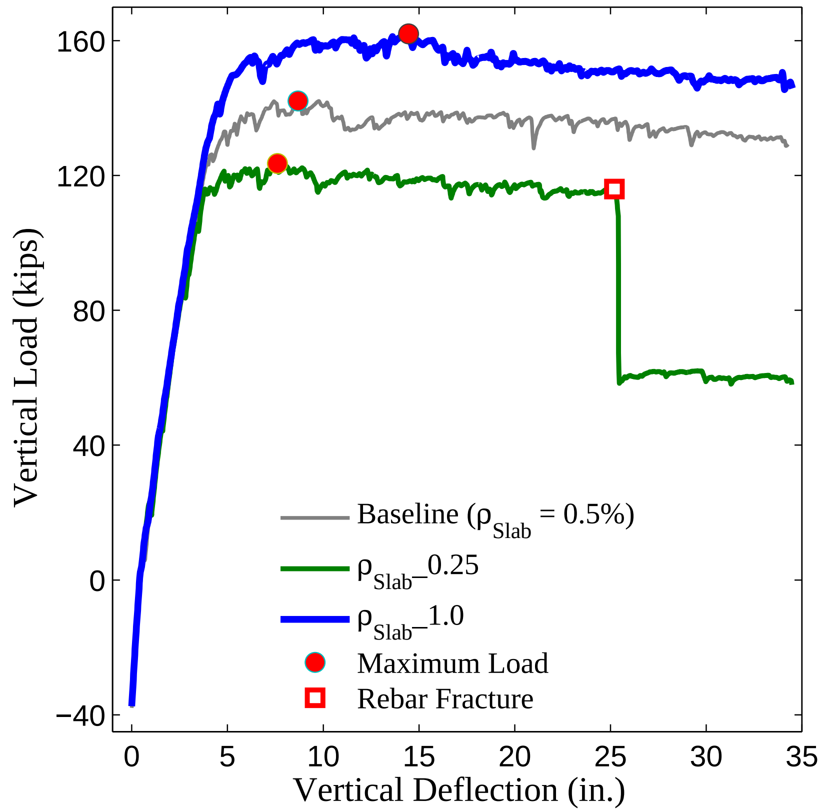

Figure 5.27: Load deflection relation for models with different slab reinforcing ratios.

Beyond the peak, all the models show small strength degradation until the deflection of 34.5 in. vertical deflection, except for the model with low slab reinforcing ratio (ρ_{Slab}=0.25%), which experienced beam rebar fracture at approximately 25 in. vertical deflection.

Span Length: Figure 5.28 presents the comparison of the load deflection curve for the parametric model where the span length of the models is varied. The initial negative loads at zero vertical deflection are the loads at the corner support location due to the model self-weight and applied uniform gravity load. It is noted that as the span length for each of the three models were different, the initial load at support C1 due to self-weight and gravity load are also different, with longer span model experiencing larger initial loads due to increased tributary area.

Models L_{Span}_20 and L_{Span}_40 began to deform with an initial stiffness of approximately 280 kips/in. and 35 kips/in., respectively, compared to 90 kips/in. for the base line model with L_{Span} = 30 ft. When pushed beyond zero load, both models experience small decrease in stiffness, and continue to deform until a vertical deflection of 3 to 5 in. is achieved. Beyond this, the models softened significantly reaching their ultimate capacity of 262 kips and 80 kips at 7.6 in. and 10.9 in. for L_{Span}_20 and L_{Span}_40, respectively. Compared to the base line model, the strengths are 85% higher and 55% lower for L_{Span}_20 and L_{Span}_40, respectively. Beyond the ultimate load capacity, both models experienced some strength degradation, achieving a load capacity of 127 and 75 kips for the L_{Span}_20 and L_{Span}_40 model, respectively.

Unlike the base line model and L_{Span}_40 model, the L_{Span}_20 model experienced rebar fracture of beam longitudinal rebar near support C2 at approximately 23 in. vertical deflection, reducing the capacity to 150 kips. The second set of beam longitudinal rebar fracture was captured near support C4 at approximately 26 in. vertical deflection, resulting in numerical instability. Due to the instability caused by rebar fracture on both the edge beams, the analysis was stopped at 26in. vertical deflection for L_{Span}_20.

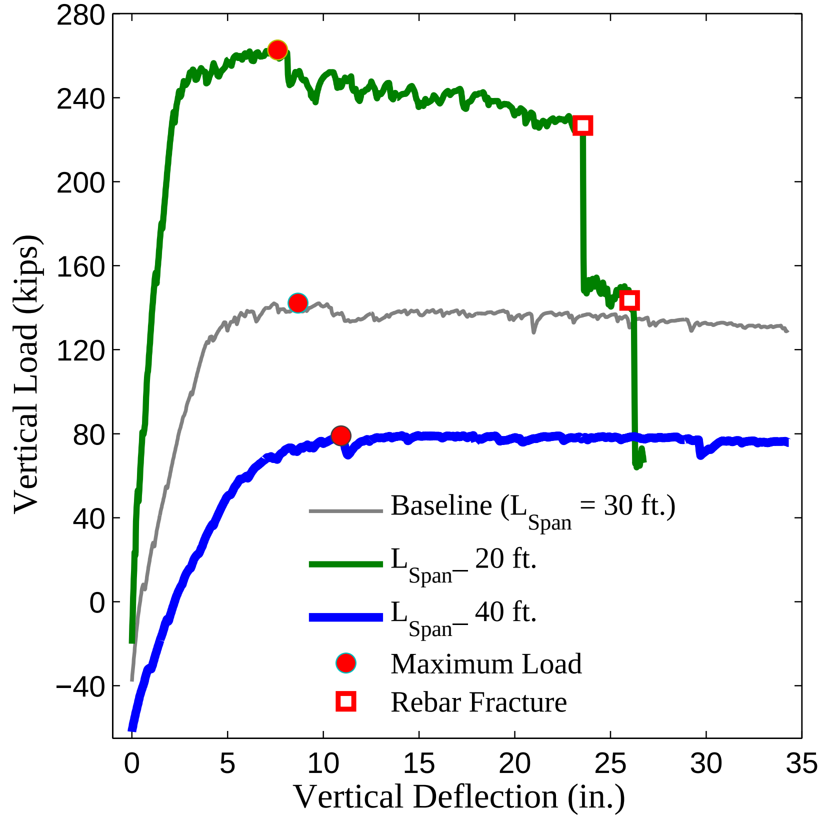

Figure 5.28: Load deflection relation for models with different span length.

Concrete Compressive Strength: Figure 5.29 presents the comparison of load deflection behavior of models with varying concrete strength. The three models began to deform with an initial stiffness of 75, 82 and 90 kips/in. for the 4000 psi, 5000 psi and 6000 psi concrete, respectively. The three models continue to deform with slightly different stiffness until 0.8 in. vertical deflection, beyond which the stiffness reduction is observed for all the models. As the deflection is increased, models experience softening at around 4.5 in. vertical deflection, finally reaching their maximum strength at 11.2, 10.2 and 8.75 in. vertical deflection for 4000 psi, 5000 psi and 6000 psi concrete, respectively. For *f'c*_4000 and *f'c*_5000 the maximum strength is slightly lower, with maximum strength of 127 and 135 kips, respectively, compared to 142 kips for the baseline model with concrete compressive strength of 6000 psi. All the models experience strength degradation, achieving a load capacity of 118, 127 and 129 kips for 4000 psi, 5000 psi and 6000 psi concrete, respectively at maximum applied deflection of 34.5 in.

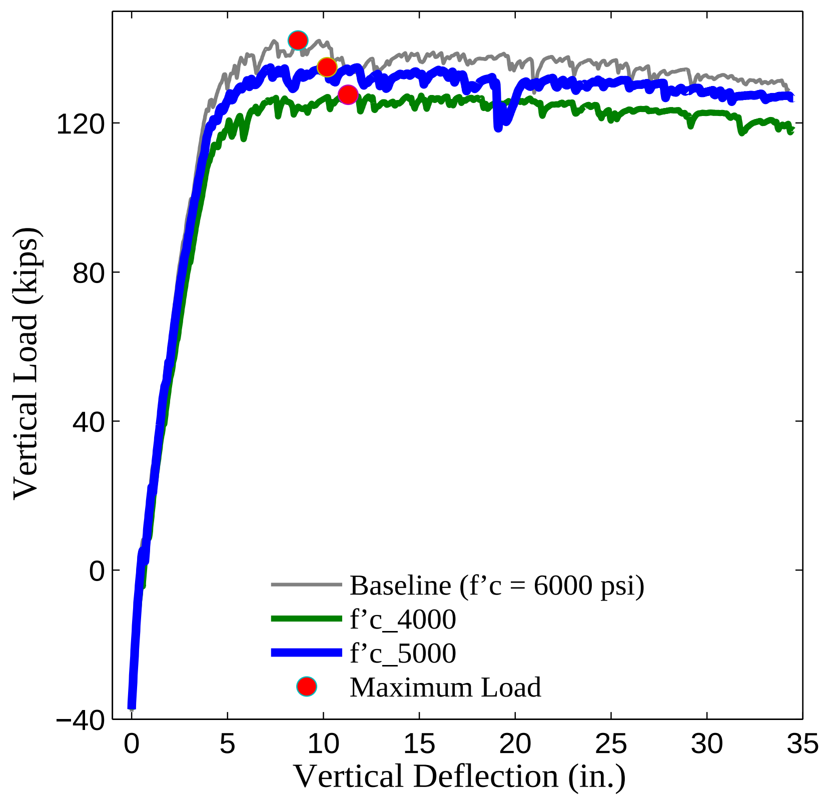

Figure 5.29: Load deflection relation for models with different concrete compressive strengths.

Support Stiffness: Figure 5.30 presents the comparison of the load-deflection behavior of the baseline model with the two models with 25% and 100% of the initial uncracked column stiffness. All the models deformed with an initial stiffness of approximately 90 kips/in. and achieved load capacities between 142 and 143 kips at approximately 8.5 in. vertical deflection. Similar to the baseline case, the other two models showed strength degradation with increase in deflection, with the three models reaching a load of 129-130 kip at maximum vertical deflection of 34.5 in. at the push location. By comparing the load deflection curve for the three models with varying support stiffness, it is evident that the effect of column stiffness on the load-deflection behavior of the system is insignificant.

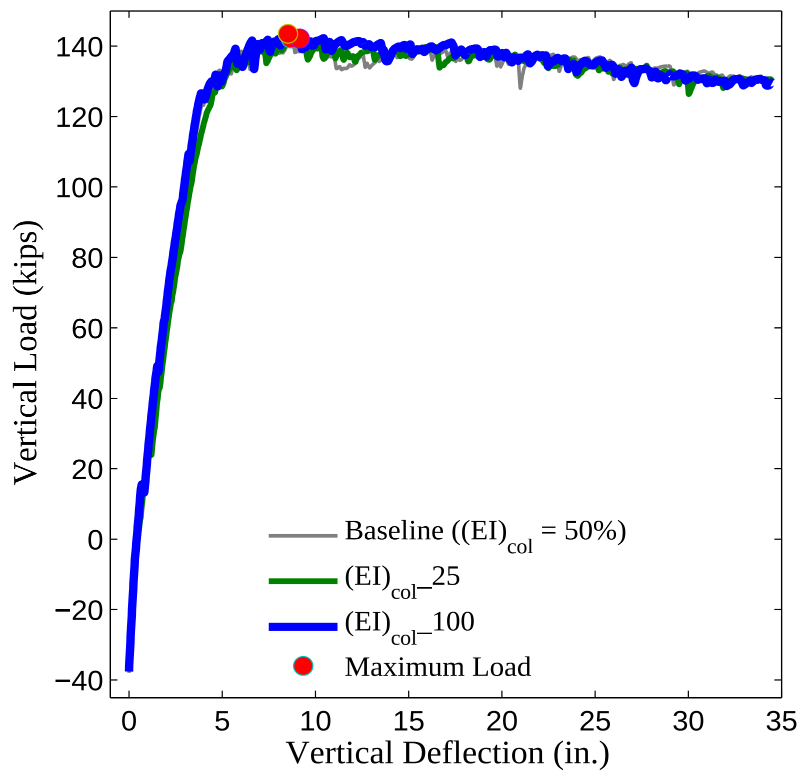

Figure 5.30: Load deflection comparison due to change in column stiffness at support locations.

5.3.3.2 Comparison with Yield Line Theory Estimates

Yield line theory has been widely used to calculate the ultimate load carrying capacity of two-way slab systems under varying load and support conditions. This section compares the capacity of the various parametric models against the values predicted by yield line theory.

Based on the observed damage, idealized yield lines were assumed to coincide with the regions of concentrated physical damage. A rigorous analysis of the system, where different yield line profiles are considered, might result in a slightly different profile of the yield line in the slab, however, it is believed that the effect of such a change would be minimal as the two edge beams contribute to approximately 90% of the overall YLT estimate. The yield lines are simplified into three linear segments, two towards the end (near adjacent supports C2 and C4), and one near the center of the panel as shown in Figure 5.31.

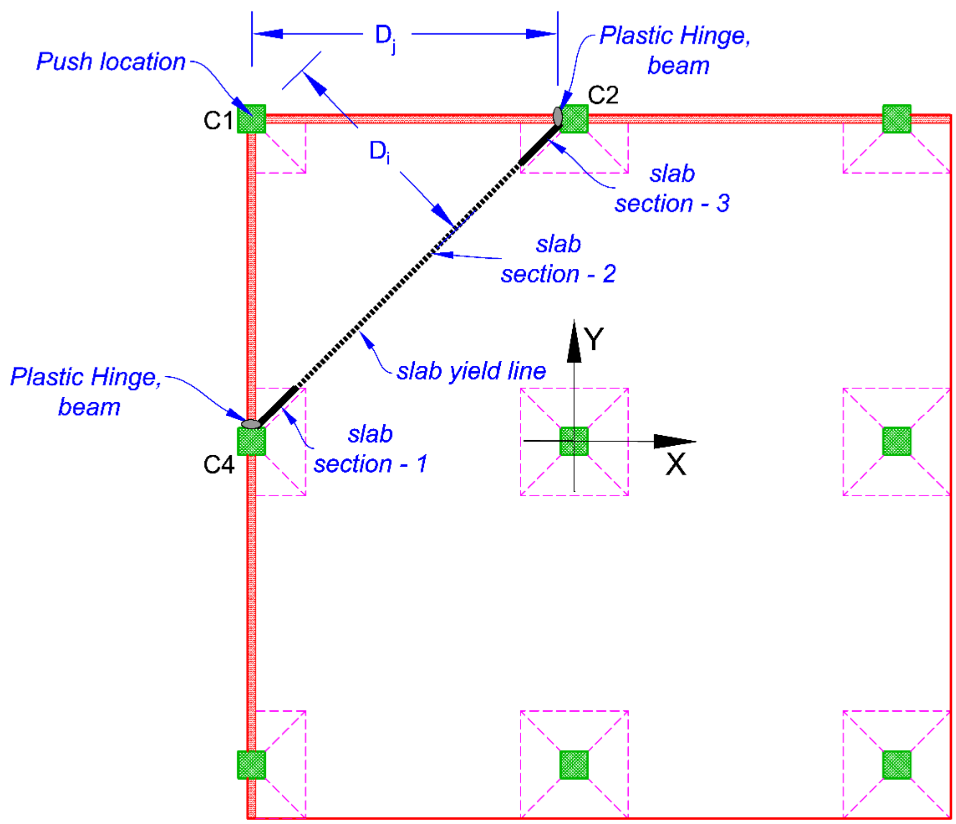

Figure 5.31: Yield line definition characterizing the location and orientation of the yield line on the slab. The location of plastic hinges that form in the beam are also shown.

Slab section 1 and 3 are doubly reinforced slab sections with a thickened drop panel near the ends, and section 2 is a slab section with bottom reinforcement only. For the assumed yield line as shown, using the virtual work method, the following equation may be written by equating the point load applied at the corner support:

$$P_{YLT} = \sum_i \frac{m_i \times \Delta L_i}{D_i} + \sum_j \frac{M_j}{D_j} - W_{Ext} \qquad \text{Equation 5.3}$$

where P_{YLT} is the load capacity based on Yield Line Theory estimates, m_i is the moment capacity per unit length of the i^{th} slab section along the yield line, ΔL_i is the length of the i^{th} slab section of the yield line, D_i is the perpendicular distance of the i^{th} slab section of the yield line from the push location (support C1), M_j is the moment capacity of the j^{th} beam, D_j is the perpendicular distance to the hinge in the j^{th} beam from the push location (support C1) and W_{Ext} is the work done by any external force (self-weight and uniform gravity loads) for unit deflection at the corner support. For the slab section yield lines, as the direction of the yield line is at an angle with the rebar orientation, the moment capacity for each of three sections along the yield line can be calculated using:

$$m_i = m_i^X \times \cos^2 \theta_i + m_i^Y \times \sin^2 \theta_i \qquad \text{Equation 5.4}$$

where m_i is the moment capacity per unit length along the yield line of section i, m_i^X is the moment capacity per unit length of the slab section i along X direction, m_i^Y is the moment capacity per unit length of the section i along the Y direction and θ_i is the angle of the i^{th} yield line section with the X axis.

Figure 5.32 provides a summary of the ratio of the calculated yield line estimates to the recorded ultimate load from the non-linear analysis. It is observed from the comparison that for all the parametric cases, except for the no slab case, the yield line theory underestimates the load capacity by a factor of 1.2 to 1.8. The absence of any load enhancement in the no-slab model and an average ultimate load enhancement of 1.5 for all other cases suggests that the presence of the slab causes significant in-plane membrane forces increasing the load capacity of the system.

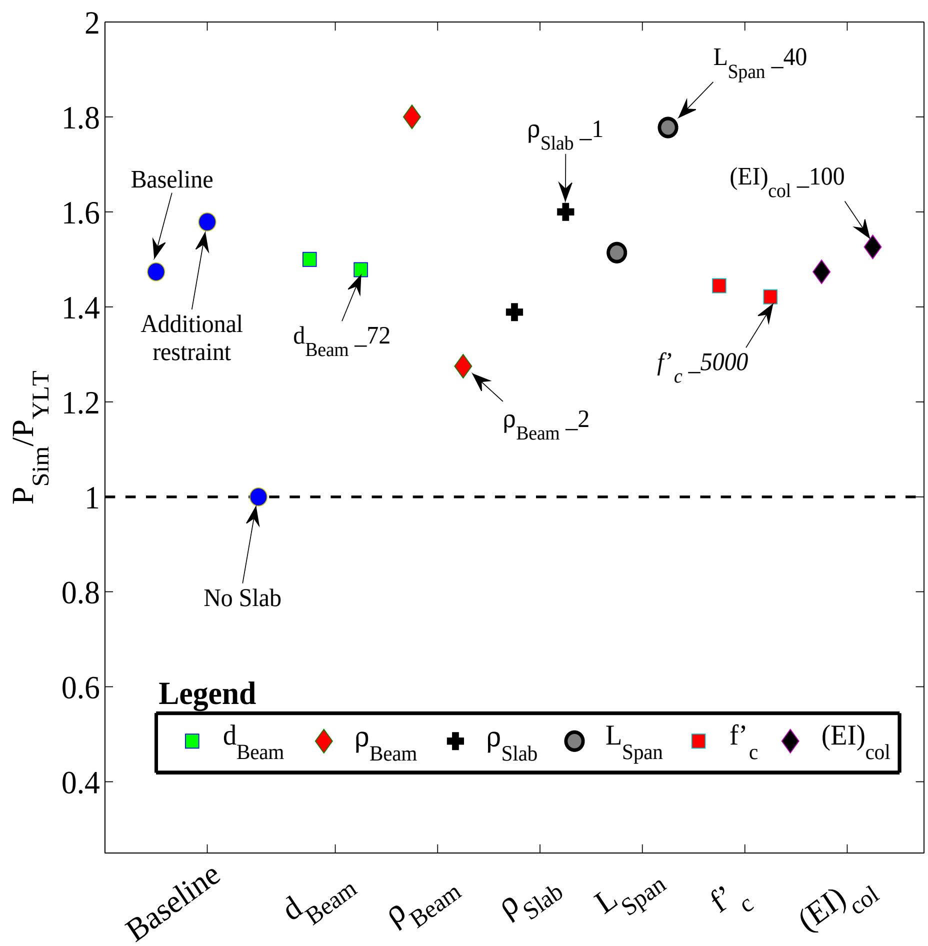

Figure 5.32: Comparison of yield line theory estimates with the calculated ultimate load capacities from the nonlinear finite element model.

5.3.3.3 Redistribution of Loads to Adjacent Supports

Table 5.2 presents the comparison of the additional loads transferred to the two columns C2 and C4, which are placed adjacent to the column failure location at support C1. Focus is given to the forces transferred to the column C2 and C4 due to their proximity to the removed column and lower force demands imposed at other support locations due to failure of the corner column. It is noted that since columns C2 and C4 are placed symmetric to the push location, result from one of the columns is presented. For comparison, the load imposed at the support at the end of gravity loads (i.e. self-weight and uniform load of 70 psf) is shown in parentheses. The force resultants presented are the loads transferred from the beam-slab model onto the column at C2 and C4 and not the reactions at the base of the columns.

For the base line model, at maximum load of 140 kips (approximated to nearest multiple of 5), the removal of the corner column imposed an resultant shear force of 135 kips, 5 times higher than the shear force experienced due to gravity loads. Assuming a 30 in. square column, this increase in shear corresponds to a total shear of approximately $2\times\sqrt{f'_c}\times Ag$. The column removal also increased the axial load demand by 125% to 280 kips ($0.05\times f'_c\times Ag$), compared to 120 kips due to gravity loads only. A similar increase in resultant moment is observed, with the top of the column experiencing a total moment resultant of 820 kip-ft., a 250% increase compared to the 250 kip-ft. moment imposed due to the gravity loads only.

Compared with the models where additional lateral restraint are provided to simulate the presence of additional panels, the model with additional restraint is able to carry an additional 10 kips compared to the base line case (approximately 7% higher), which resulted in a slightly higher demands at the adjacent support location. At maximum load conditions, the model with additional in-plane constraints experienced approximately 5 to 8% higher load demands in resultant shear and moment, while no significant change is observed in the axial load demand at the adjacent support. This proves that the presence of additional panels, apart from the four panels considered, would not result in any significant changes in the additional forces imposed at the adjacent support due to corner support failure.

For the no-slab model, the forces induced at the adjacent supports are small compared to the base line case. At maximum load capacity of 75 kips (approximately 50% of the baseline case), the adjacent support experienced a resultant shear of 45 kips ($0.65\times\sqrt{f'_c}\times Ag$), one-third of the resultant shear in the baseline model. Similarly the axial load and resultant moment demands are approximately half of the demands recorded in the baseline model.

Comparing the base line case with the two models where the depth of the beams are varied (models $d_{Beam\_}56$ and $d_{Beam\_}72$), no significant changes are observed in the imposed resultant shear and moment demands on the adjacent support C2 and C4 even though the overall capacity of the models differed by 20 to 30 kips from the baseline model. Due to the difference in the vertical load capacity at failure support location C1, some changes are observed in the axial load demands at the adjacent support, which varied by -30 and +35 kips for the $d_{Beam\_}56$ and $d_{Beam\_}72$ models, respectively.

Table 5.2: Summary of forces at column C2 after gravity load and maximum load condition during the column failure simulation at support C1.

Case	P_{Max}, kips	$V_{Resultant}$ @ Max Load (Gravity), kips	Axial @ Max Load (Gravity), kips	$M_{Resultant}$ @ Max Load (Gravity), kip-ft.
BL	140	135 (35)	280 (120)	820 (250)
ACons	150	145 (35)	280 (120)	900 (250)
XSlab	75	45 (5)	180 (75)	435 (10)
DB_56	120	125 (40)	250 (120)	815 (255)
DB_72	170	125 (35)	315 (125)	755 (230)
RB_0.5	90	115 (35)	230 (120)	695 (255)
RB_2.0	255	165 (35)	385 (120)	1090 (250)
RS_0.25	125	125 (35)	265 (120)	765 (255)
RS_1.0	160	150 (35)	295 (120)	960 (250)
L_{Span}_20	265	110 (10)	305 (60)	740 (75)
L_{Span}_40	80	185 (70)	325 (200)	1055 (455)
FC_4000	130	125 (40)	265 (125)	780 (260)
FC_5000	135	130 (40)	275 (120)	820 (255)
SS_25	140	105 (30)	285 (120)	690 (220)
SS_100	145	160 (40)	275 (125)	945 (270)

For the two models where the beam reinforcing ratios were changed to 0.5% and 2.0%, a significant change in force and moment demands at the adjacent support location is observed as the ultimate load capacities differed significantly between the models. For the two models, the resultant shear demand at maximum capacity is recorded to be 115 kips ($1.65\times\sqrt{f'_c}\times Ag$) and 165 kips ($2.4\times\sqrt{f'_c}\times Ag$) for ρ_{Beam}_0.5 and ρ_{Beam}_2, respectively. Similarly the axial force demands for the two models increased with the increase in beam reinforcing ratio, ranging between 230 kips and 385 kips for ρ_{Beam}_0.5 and ρ_{Beam}_2, respectively. The resultant moments induced at the adjacent support also increased with the increase in beam reinforcing ratio, with resultant moment demands of 700 kip-ft and 1100 kip-ft. for models ρ_{Beam}_0.5 and ρ_{Beam}_2, respectively.

For the parametric models ρ_{Slab}_0.25 and ρ_{Slab}_1, where the slab reinforcing ratio is varied, the two models shows slight difference in force demands at the adjacent support location. For ρ_{Slab}_0.25 and ρ_{Slab}_1 (i.e. ρ_{Slab}=0.25% and 1.0%), the total resultant shear demand varied by approximately $\pm$10 kips from the base line model, with lower demands for ρ_{Slab}_0.25, while, ρ_{Slab}_1.0 experienced a slightly higher shear demand at support location C2. Similar to the resultant shear demands, no significant variation in axial load demands is observed, with the two models experiencing a change of only 15-20 kips compared with the baseline model.

The models L_{Span}_20 and L_{Span}_40 show significant differences in the loads transferred to the adjacent support location. The resultant shear force and resultant moments transferred to the column C2 increased with increase in the span length although the ultimate capacity of the structure was lower. For L_{Span}_20 and L_{Span}_40, 110 and 185 kips of resultant shear (1.5 and 2.6 $\sqrt{f'_c}\times Ag$) is transferred to the column C2, respectively. A similar difference is also observed in the transferred axial loads and moments, where the models experienced higher load demands for L_{Span}_40. It is noted that for this parametric case, the loads transferred due to gravity loads are significantly different from the base line model as the intensity of gravity load is kept constant, which results in a different loads at supports due to different span length.

For the parametric models *f'c*_4000 and *f'c* _5000 (i.e. *f'c* = 4000 psi and 5000 psi), no significant changes are observed in the load demands at the adjacent support. The force demands for these two models varied from 90 to 95% of the demands recorded for the baseline model. This is likely due to the fact that the overall structural behavior under corner column failure scenario is governed by flexure behavior, which is not greatly affected by small changes in concrete compressive strength.

For the models $(EI)_{col}$_25 and $(EI)_{col}$ _100, where the lateral stiffness of the columns are assumed to be 25% and 100% of the uncracked cross-section, respectively, no significant changes are observed in the axial loads transferred to the adjacent support C2 when compared to the baseline model. Although the overall load capacity at the column failure location is very similar for all the three cases (i.e. baseline, $(EI)_{col}$_25 and $(EI)_{col}$_100), the resultant shear and moment demands differed significantly. For model SS_25, the resultant shear and moment demands were approximately 80% of the baseline model. In contrast, model $(EI)_{col}$_100 with a stiffer column experienced greater demands, approximately 20% and 10% higher shear and moment demands, respectively, compared to the baseline model. Higher load demands on a stiffer section is expected as more load gets transferred to stiffer member.

5.4 Approximate Method for Determining Stiffness and Strength under Corner Column Failure Scenario

5.4.1 Approximation of Initial Stiffness

For the design of two-way slabs, ACI 318-2011 proposes the use of a Direct Design Method or Equivalent Frame Method, where the two-way slab is divided into strips or equivalent frames along the column and/or panel center lines. A similar approach is used where the slab under investigation is divided into column and middle strips and idealized by equivalent beams running along the center line of each strip. The following assumptions are made for the simplified model:

1. As the gravity load does not produce any significant cracking near supports, all section moduli are calculated assuming an un-cracked section.

2. At the support locations, if a drop panel or column capital is present, the section modulus is accordingly updated to account for a thickened cross-section

Figure 5.33 presents a schematic of the discretization of the two-way beam-slab system into equivalent beams. For all beams, the section properties (moment of inertia, torsional constant, etc.) are based on the actual section of the slab it represents. For the edge beams where upturned spandrel beams are present, the section property of the equivalent beam also includes the beam cross section. Table 5.3 provides a summary of the comparison between the calculated initial stiffness from the simple elastic model and the values calculated during the different parametric cases. It can be seen that for all the cases the simple elastic model provides a good approximation of the initial stiffness, with an average error of approximately 4%. A greater error of 20% in L_{Span}_40 is partly due to the smaller stiffness calculated from the LS-DYNA model and the linear model. It is also noted that the stiffness reported by the linear models are tangent stiffness while the stiffness calculated from the LS-DYNA model are secant stiffness.

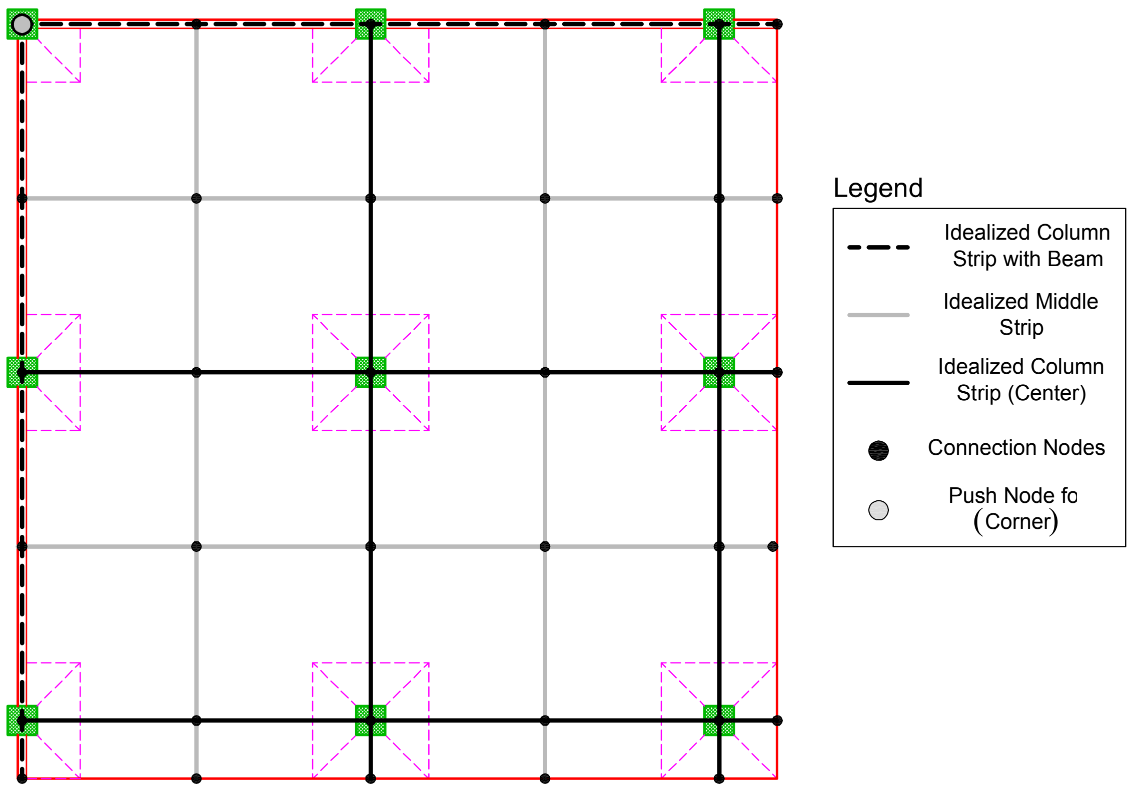

Figure 5.33: Discretization of two-way slab into equivalent beams along the column and middle strip.

Table 5.3: Comparison of initial stiffness obtained from the simplified model (Figure 5.33) and the nonlinear model implemented in LS DYNA

	$K_{Calculated}$ (kips/in.)	**$K_{Parametric}$ (kips/in.)**	**% Error**
BL	94	90	5 %
ACons	98	90	10 %
XSlab	75	75	0 %
DB_56	72	65	10 %
DB_72	125	120	4 %
L_{Span}_20	285	280	2 %
L_{Span}_40	42	35	20 %
FC_4000	75	75	0 %
FC_5000	85	80	6 %
SS_25	85	90	6 %
SS_100	100	90	10 %

A similar model is also implemented for the two test specimens and the recorded stiffness are compared against the stiffness obtained from the simplified models and are summarized in Table 5.4. A large variation is observed in this comparison due to cracks that formed during the actual tests. By reducing the section modulus for beam cross section by 25%, i.e. assuming the beam stiffness is 75% of the uncracked section, a better approximation is obtained for the three corner tests. Similarly for the second specimen where the edge supports were tested, for the beam edge case a better approximation of the system stiffness is obtained if the initial beam stiffness is reduced by 50% to account for the initial damage observed during the experiment.

Table 5.4: Comparison of initial stiffness obtained from the simplified model and the two test specimens (Chapter 3)

	$K_{Calculated}$ (kips/in.)	$K_{Experiment}$ (kips/in.)	Error
Beam-Beam Corner	12.2	9.6	27 %
Slab-Slab Corner	5.6	3.6	50 %
Beam-Slab Corner	8.5	6.5	30 %
Slab Edge	17.3	14.5	20 %
Beam Edge	51.0	34.5	50 %

5.4.2 Estimation of Vertical Load Capacity under Corner Support Failure Considering Membrane Forces

As shown in the previous section, the actual load carrying capacity of the beam-slab system under a column failure scenario is higher than estimations from the classical Yield Line Theory (YLT). To better predict the ultimate capacity of such a system, this section introduces the failure mechanism of a beam-system under corner support failure and the vertical load capacities are calculated and compared with the load capacities for each case from the LS-DYNA model. The same method is also then applied to the test performed on the beam-beam corner location on specimen 1(Chapter 3).

Consider a corner support location where beams are present along the two edges of a two-way slab as shown in Figure 5.34a. As the vertical deformation at the corner push location is increased, the corner will want to move outwards in the X and Y directions due to extension of the beam. Although the beam corner moves outward, this movement will be restrained by (1) out of plane bending of the orthogonal beam(s), and

(2) axial extension of the slab, which in turn will cause compression in the beams. The assumed internal in-plane forces generated in the beam-slab section 1-1 is shown in Figure 5.34b. It is noted that external or internal moments and vertical forces are not shown for clarity, i.e. only in-plane forces are diagrammatically shown.

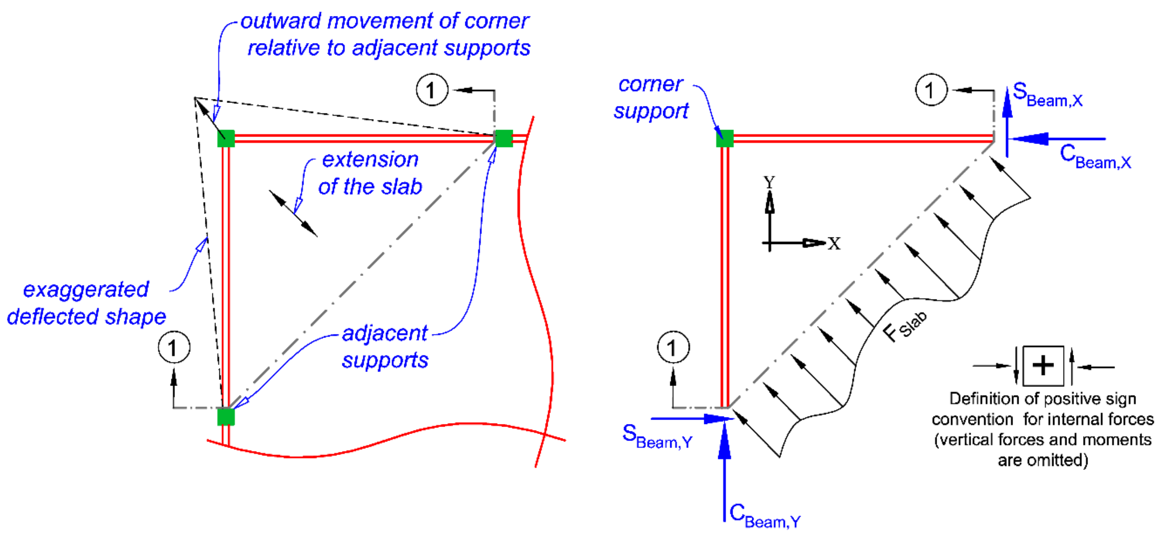

Figure 5.34: Schematic of the beam-slab system under vertical deflection (a) deformed shape of the beam-slab system, and (b) in-plane internal forces along section 1-1. Part b does not show the vertical forces and moments.

Assuming that the forces in the slab are transferred to the nearest beam, which is similar to the assumptions of the Direct Design Method of two-way slabs, the forces along the two edge beams is shown in Figure 5.35. It is noted that in this figure only the forces effective along the two edge beams along their individual longitudinal axis is shown in the figure. Using force balance in the X and Y direction, the compression in each beam in direction *"j"* can be calculated as the sum of the forces in the adjacent half-panel as given by:

$$C_{Beam,j} = \left(T_{Rebar} - C_{Conc}\right)_{\frac{L_{Span}}{2},j} \qquad \text{Equation 5.5}$$

The maximum possible compression in the edge beams occur when the T_{Rebar} is maximum, i.e. all the slab rebar in the half-panel adjacent to the beams has reached their individual yield capacity, and the compression in the concrete is zero (assuming concrete takes no compression due to through cracks along the slab yield line).

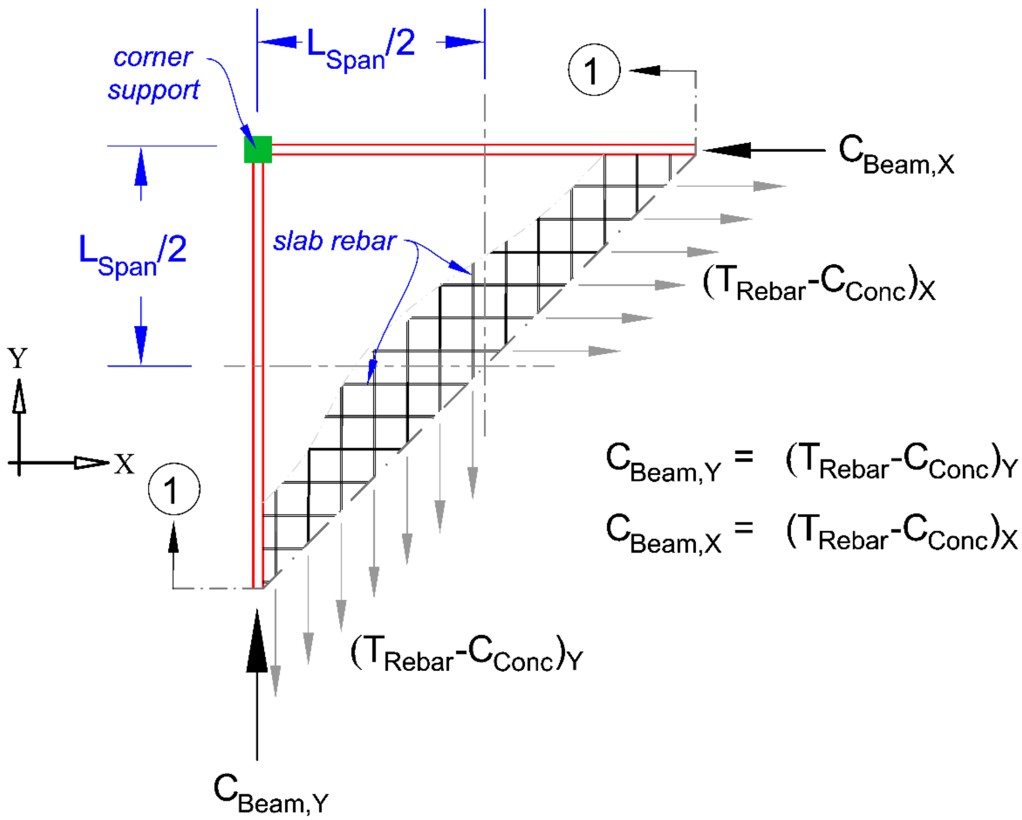

Figure 5.35: In-plane force balance in edge beam. Internal forces which affect the beam axial forces are shown, other forces in the beam and the slab are omitted for clarity. Only a portion of the slab rebar is shown. Both the top and bottom slab rebar mat is shown.

Using the assumptions mentioned, the maximum possible compression in the beam(s) can be approximated if the slab top and bottom rebar layout is known using:

$$C_{Beam,j} = \left(\sum_i A_{i,Rebar} \times f_{y,i}\right)_j \qquad \text{Equation 5.6}$$

where $C_{Beam,j}$ is the beam compression in 'j' direction, $A_{i,Rebar}$ is the area of i^{th} rebar that intersects section 1-1 (either top or bottom mat) in the half panel containing the edge beam and $f_{y,i}$ is the yield stress of the i^{th} rebar, and i is the total number of rebar that cross through section 1-1 in direction j.

It is also noted that depending on the relative location of the slab to the edge beam, this compression might create additional moment in the beam. Assuming that the force transferred from the slab to the beam occurs along the slab centroidal axis, any offset between the slab and beam centroidal axis would result in additional moment in the beams as shown in Figure 5.36. In order to provide a better approximation of the overall capacity, this additional moment caused due to the offset in axial force on the beam can be accounted for using Equation 5.7:

$$M_{Cap} = M_y + \Delta M_{PM} + C_{Beam} \times (\Delta_{NA}) \qquad \text{Equation 5.7}$$

where M_{Cap} is the capacity of the edge beam considering membrane forces and the location of the compression force along the beam depth, M_y is the moment capacity without the membrane forces, ΔM_{PM} is the additional capacity due to P-M interaction, C_{Beam} is the total compression in the edge beam given by Equation 5.6 (taken as negative value for compression), and Δ_{NA} is the distance between the beam neutral axis and the slab neutral axis. The distance Δ_{NA} is taken as positive if the beam neutral axis is above the slab neutral axis.

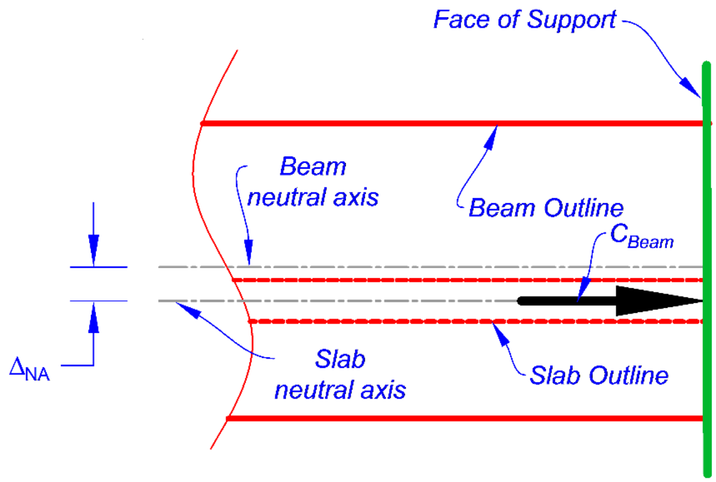

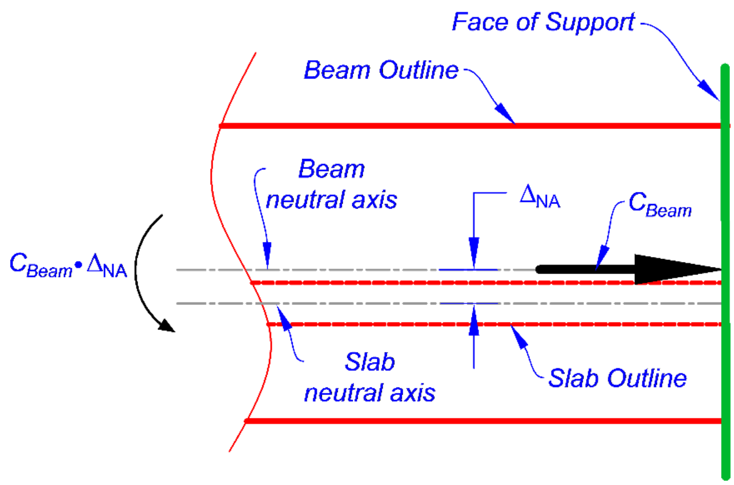

Figure 5.36: Schematic showing the profile view of the additional moment demand due to the offset between beam and slab center lines.

It is noted that since the entire slab is assumed to be under significant tensile strain through its depth, the contribution from the slab can be ignored. Using the assumptions above, and the updated moment capacity of the edge beams, the ultimate capacity of a beam-slab system under corner support failure scenario can be calculated using:

$$P_{Ult} = \sum_{j} \frac{M_{Cap,j}}{D_j} - W_{Ext} \qquad \text{Equation 5.8}$$

Figure 5.37 provides a comparison of the load capacities calculated using the proposed method against the recorded capacities from the parametric study. It is observed that the method provides a good prediction of the ultimate capacity of the beam-slab system under corner column failure scenario for all the cases. The method is able to predict the ultimate capacity of the system with acceptable accuracy with most of the predicted values within 10% of the recorded ultimate capacities from the finite element analysis. Only one case, L_{Span}_40, shows an overestimation of 15% compared to the LS-DYNA results.

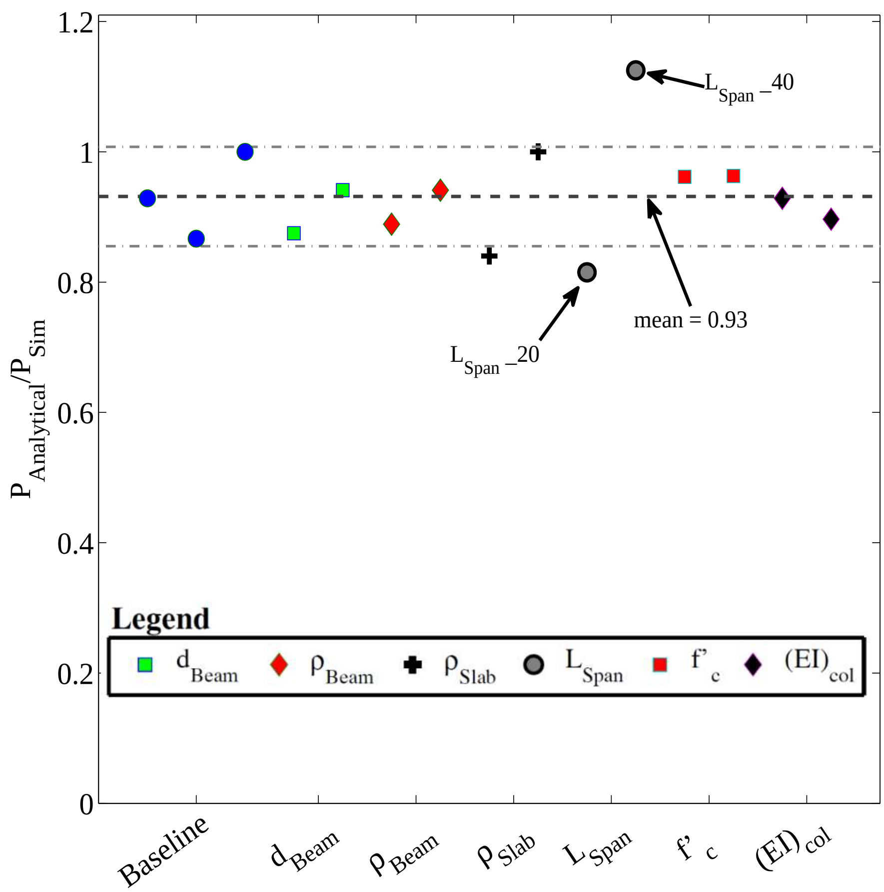

Figure 5.37: Comparison of ultimate load capacity estimates from the analytical model and the values obtained from the non-linear finite element analysis.

For completeness, the same approach was used to recalculate the strength for the beam-beam corner case from specimen 1 presented in Chapter 3. Using the method described above, the analytical method provides a load capacity of 10 kips, which is only 8% higher than the actual recorded ultimate load capacity of 9.3 kips from the experiment.

5.5 Effect of Bond-Slip between Concrete and Rebar

As mentioned in Chapter 4, the current modeling technique assumes a perfect bond between concrete and rebar. The presence of bond-slip between the rebar and concrete not only affects the maximum possible stress development near the end of the rebar, it will also affect the length of the rebar over which strain localization occurs. To investigate the effect of bond-slip between rebar and concrete near the end of the rebar, a model is constructed where the end of the two node beam elements, used to model the slab rebar, are shortened by their individual development length (L_d, calculated based on ACI-318, 2011). Although this method ignores the partial stress that would be generated in these elements, it does provide an approximation of the scenario where the ends of the rebar are assumed to carry lower stresses, should bond-slip occur.

Another aspect that needs to be evaluated is the length of rebar over which plastic deformation is localized and its effect on the overall behavior of the system under corner support removal. If the length of the beam elements used to model the rebar is small, the inelasticity would localize in one element, suggesting large localized strains, while neighboring elements will not experience significant strains, as should happen due to the bond-slip behavior between the concrete and rebar. Therefore, a separate baseline model, termed *relaxed rebar model*, is implemented where the length of the two node beam elements, used to define slab and edge beam rebar, is increased to 10-15×d_b. A similar *relaxed rebar model* is implemented for the no slab case, where only the two edge beams are modeled.

Baseline Model with Rebar Curtailment: Figure 5.38 presents a comparison between the baseline model and the model where the ends of the slab rebar were curtailed by their individual development length (L_d) to implicitly model extreme case of bond-slip behavior. The model with curtailed rebar began to deform with an initial tangent stiffness of approximately 90 kips/in., same as the stiffness recorded in the baseline model. The model continued to deform with small stiffness degradation until it reached a vertical deflection of 4.5 in. Beyond this point, the curtailed rebar model experienced significant change in stiffness, reaching its maximum capacity of 140 kips at a vertical deflection of 9.5 in. Compared with the baseline model, the load capacity is only 1.5% lower. Similar to the base line model, curtailed rebar model exhibits small strength degradation, reaching a load capacity of 125 kips at a deflection of 34.5 in. (compared to 129 kips for the base line model at the same deflection). Comparing the overall load-deflection relation between the two models, little difference was observed due to curtailment of slab rebar.

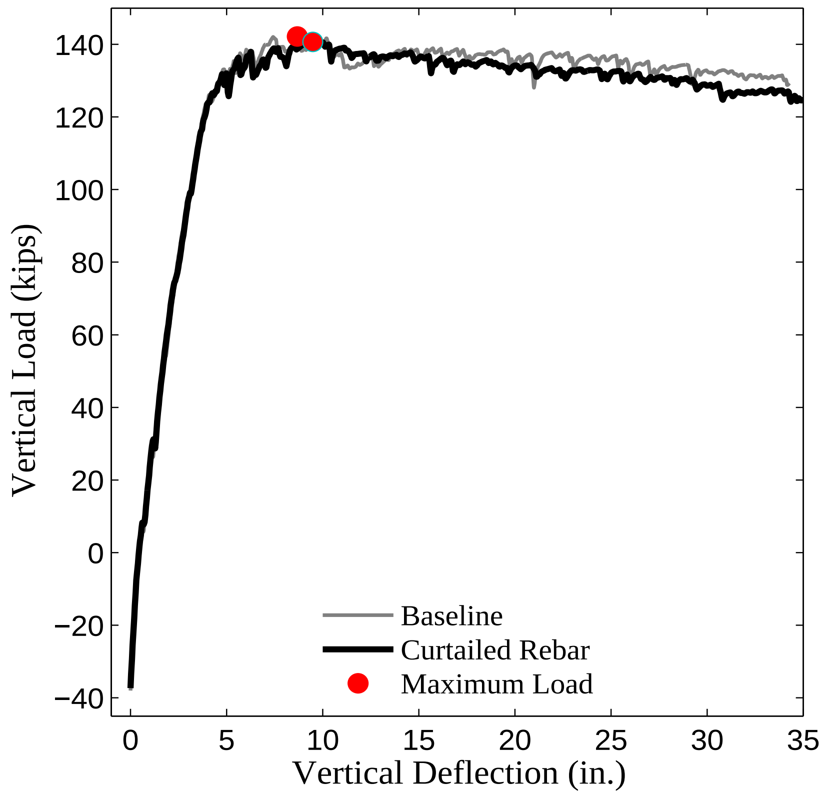

Figure 5.38: Load deflection relation comparison with the baseline model and the model with slab rebar curtailed by their respective development length.

This behavior between the baseline model and the curtailed rebar model is expected to be similar as the number of rebar that contribute to the overall capacity of the system does not change significantly, even if all rebar are curtailed by length of L_d. Figure 5.39 shows an outline of the zone of high nonlinearity in the models overlaid on top of the partial slab rebar layout. It is observed that even after each slab rebar is curtailed, the number of rebar that cross the zone of concentrated nonlinearity does not change significantly; compared with the baseline model with no rebar curtailment, only about 20% of the slab rebar are affected by the reduction in length of the rebar. As the effective number of slab rebar does not change drastically, no significant affect is observed on the load carrying capacity of the beam-slab system due to rebar curtailment.

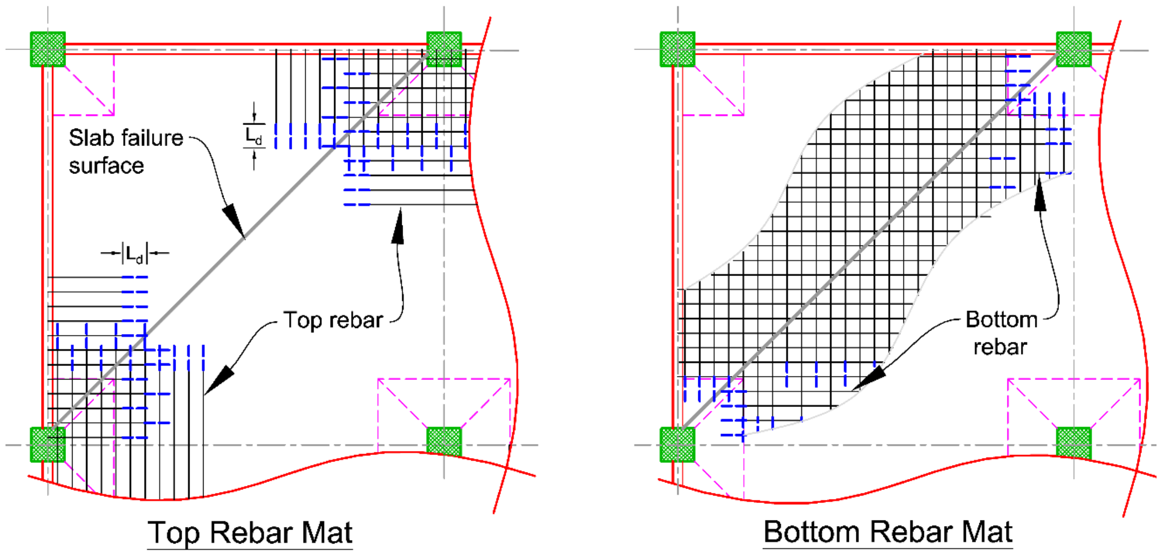

(a) (b)

Figure 5.39: Schematic showing the slab rebar that intersect the slab failure surface due to the push at corner location. (a) top rebar mat, and (b) bottom rebar mat. The portion of the curtailed slab rebar is shown by dashed blue lines. Only the rebar near the failure surface are shown.

Baseline model with Relaxed Rebar: Figure 5.40 presents a comparison of the load deflection behavior of the baseline model to the corresponding relaxed rebar model, where each rebar was modeled using two node beam element of length $L_d/2$. This model began to deform with a slightly lower stiffness of 80 kips/in., 90% of the stiffness calculated for the baseline model. The relaxed rebar model continues to deform with a similar stiffness until a vertical deflection of 4 in. Beyond this, the relaxed rebar model deforms with a slightly lower stiffness compared to the baseline model, eventually reaching its capacity of 142 kips at approximately 10 in. vertical deflection, compared to 142 kips capacity at 9 in. vertical deflection for the baseline model. Pushed beyond its peak, the relaxed rebar model exhibits little strength degradation, similar to the baseline model, reaching a capacity of 133 kips at 22 in. vertical deflection. At this point the numerical analysis suffered convergence errors and was terminated.

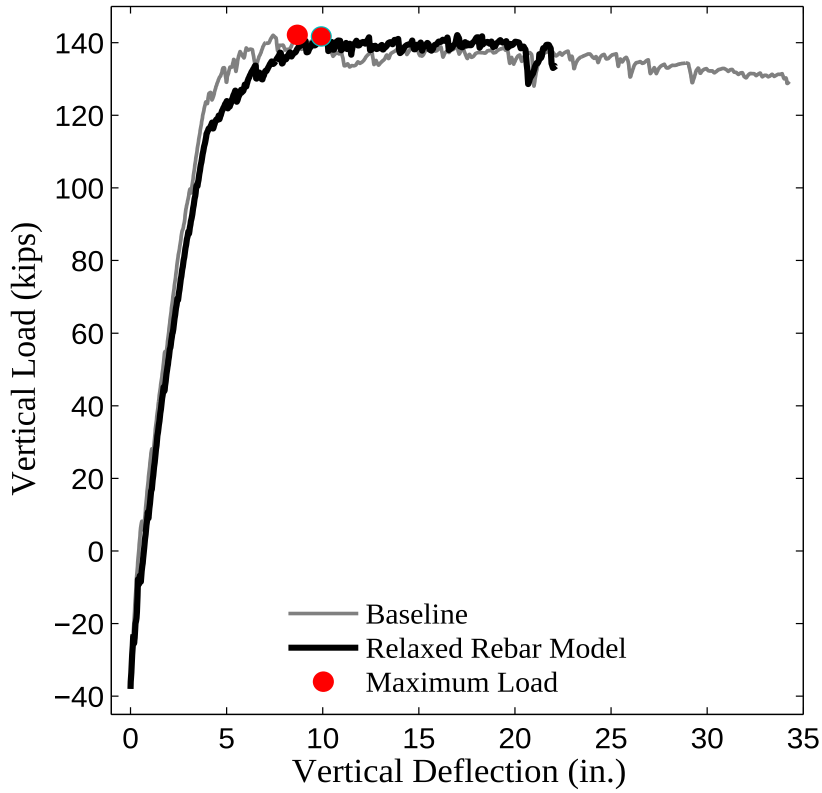

Figure 5.40: Load deflection relation comparison with the baseline model and the relaxed rebar beam-slab model.

Nonetheless, for the range of stable simulation, compared to the baseline model, the model with longer beam elements did not show significant difference in its load-deflection characteristics. The model achieved the same load capacity and exhibited similar post-peak behavior as the baseline model, suggesting that the length of rebar where strain localization occurs does not affect the monotonic load-deflection behavior.

Figure 5.41 presents a similar comparison between the no-slab model and the corresponding relaxed rebar model. The relaxed rebar model deformed with a slightly lower stiffness of 70 kips/in., approximately 95% of the stiffness recorded from the no-slab model, and achieved a similar peak strength of approximately 75 kips. However, rebar fracture in the relaxed rebar no-slab model did not occur until 32 in., 30% greater than calculated by the no-slab model. This difference between the models with varying two-node beam elements length suggests that although bond-slip might not affect the peak strength under corner support failure scenario, it could have a significant effect on the estimation of deformation capacity of the system, assuming flexure dominated mechanism as per the analysis method used in this study.

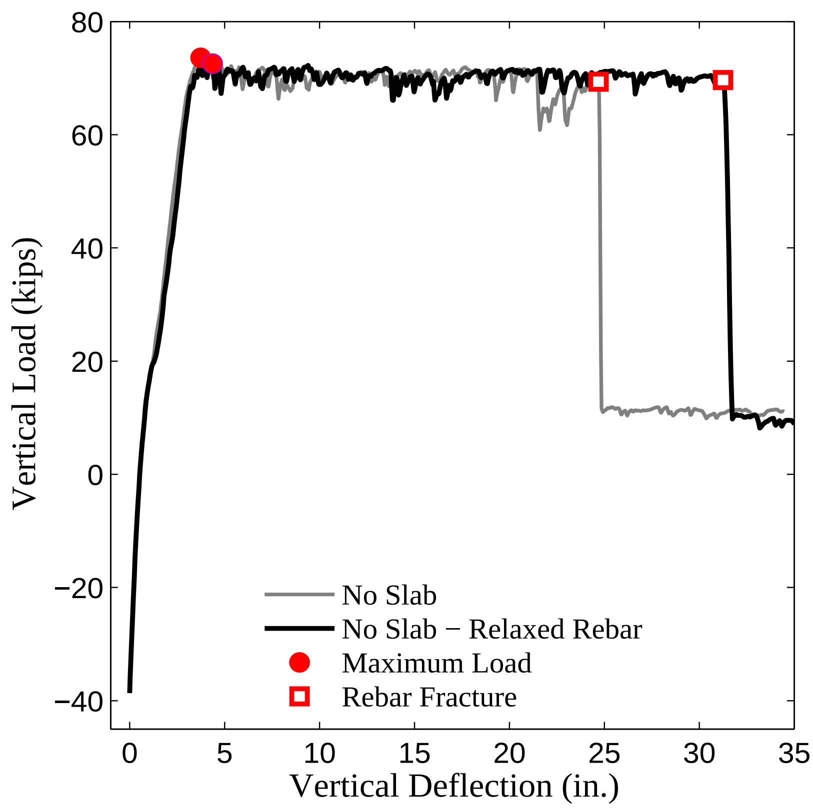

Figure 5.41: Load-deflection relation comparison between the no-slab model and the respective relaxed rebar model.

5.6 Concluding Remarks

This chapter summarizes the findings of a numerical nonlinear parametric study of the behavior of beam-slab system. For this study, numerical models with varying design details, including reinforcing ratio, span length, and concrete strength were constructed within LS-DYNA. Each model was subjected to gravity loads followed by a simulated push at a corner support location. The following conclusions are made based on these analyses:

(1) The presence of additional panels, in addition to the two panels in both directions from the corner location does not significantly affect the load-deflection behavior of the beam-slab system under corner column failure scenario.

(2) The presence of the slab however, as expected, has a pronounced contribution to the ultimate load carrying capacity, increasing the moment capacity of the system considerably. In these analyses, the load carrying capacity of the beam-slab model was approximately 100% higher compared with the no-slab model.

(3) Although the observed damage is in accordance with the predictions made by the yield line theory, the ultimate load carrying capacity is 1.2 to 1.8 times higher than the yield line theory estimates when the slab is present. This is consistent with the tests described in Chapter 3.

(4) Due to corner column removal, two adjacent columns experienced a threefold increase in total axial load demands compared to gravity loads only. The center

support experienced uplift, reducing the axial load demands at this location to approximately 85% of its gravity load demand.

(5) An accurate estimate of the initial stiffness of the various beam-slab systems is obtained by assuming the slabs are equivalent beams.

(6) A simplified model is presented where the load enhancement due to the presence of the slab can be predicted with acceptable accuracy. The observed enhancement is caused due to the presence of compression in the edge beams, resulting in an increase of their moment capacity, largely due to P-M interaction. The magnitude of compression in the edge beam is dependent on the reinforcing steel provided in the slab.

(7) The bond-slip behavior between the concrete and rebar may not affect the monotonic load-deflection behavior of the system significantly for a corner support failure scenario, at least for the models and details considered herein. However, ignoring such a behavior in the finite element model can provide an inaccurate prediction of system's deformation capacity.

******

Portions of the following publication in preparation, for which author is the principal researcher and author, are contained in this chapter:

- Prasad, S. and Hutchinson, T. C., "Behavior of older reinforced concrete beam-slab systems considering a corner support failure scenario: model validation and parametric study".

Chapter 6: Conclusions and Future Work

6.1 Motivation

Older reinforced concrete buildings, built prior to the introduction of seismic guidelines, are susceptible to damage during an earthquake due to lack of adequate detailing of structural members. In particular, older non-ductile columns are particularly susceptible to shear failure. Shear failure of a column could result in loss of its axial load carrying capacity, and subsequently increase the collapse risk in the absence of a secondary load carrying mechanism. Beam-slab systems, being an integral part of the load carrying system within the structure, can act as a secondary load path and redistribute loads to adjacent support locations. However, an accurate assessment of its behavior is needed before the beam-slab can be used in this fashion.

Although several studies have been conducted in the last few decades to understand and prevent progressive collapse potential of structures due to initial support failure, these studies have failed to analyze the contribution of the slab on the overall capacity of the beam-slab system. To this end, an experimental and numerical study is conducted to characterize the behavior of older non-ductile beam-slab systems and the resulting demand distribution on the structure under column failure scenarios. In addition, a simplified analytical method is proposed for estimating the ultimate load capacity of the beam-slab system should a corner failure occur.

6.2 Experimental Program

To better understand the behavior of beam-slab systems under support failure scenarios, a large-scale test program was conducted involving simulated column failure scenarios applied to two 1/3rd scale specimens. The two specimens depict a portion of a floor slab that is typical to buildings common in older construction (pre-1970s). The first specimen, a 2×2 panel or 3×3 support configuration, represents a portion of the floor near the corner of the building, while the second specimen, with similar panel configuration, was constructed to represent the edge of the floor, with and without edge beams. Both specimens incorporate edge spandrel beams and lightly reinforced sloped drop panels at support locations, features commonly observed in older flat slab type construction. The reinforcement in the specimen was detailed according to pre-seismic design guidelines, with approximately 0.5% and 1.0% longitudinal reinforcement provided in the slab and edge beams, respectively. The specimen were supported on axial and custom designed multi-axial load cells at the nine support locations, with multi-axis load cells provided at supports adjacent to the simulated column failure locations.

The first specimen was tested under gravity loads of various patterns followed by simulated column failure at three corner locations, while the second specimen was subjected to uniform gravity loads and simulated column failure at two edge support locations. The findings of the test program are summarized below.

(1) For the tests performed on the three corner locations on the first specimen, the specimen performed extremely well, showing elastic-plastic vertical load-deflection response at the supports with little to no strength degradation. The beam-slab system was able to maintain its load capacity until a deflection equal to 7.5% of the span length.

Similar, reliable vertical load-deflection behavior was observed for the tests performed at the center-edge support locations, where the system was able to deform absent strength degradation to large deflections. During the tests at the beam edge location, the presence of tensile catenary action was observed at large deflections even after initial damage at the beam ends. The final failure of the system occurred due to local punching failure at the push location during the simulated support failure at the beam edge location.

(2) The damage to both specimens was concentrated between the adjacent supports along well defined yield lines spanning from support to support, consistent with the yield line theory (YLT) estimates. However, the ultimate load capacities obtained from the experiments were higher than YLT estimates. This enhancement was due to the presence of in-plane forces in the system, which is not considered in YLT. A load enhancement of about 70-80% was observed in the corner support failure cases where the presence of only one panel prevents the formation of compressive arch or tensile catenary under corner support failures. For the center edge conditions, a load enhancement of 20% and 120% was observed at the beam edge and slab edge, respectively. It is noted that the enhancement at beam edge was lower (only 20%) due to the initial damage that occurred at the beam ends.

(3) For both tests, the simulated support failure resulted in significant load transfer to the adjacent support locations. Supports, which were within one span length of the specimen experienced additional compression, while other supports experienced little to no change in loads. The direction of the shear forces at the adjacent supports suggests the presence of in-plane forces, pushing these supports away from the test location.

(4) To the author's knowledge the data from this test program are the most detailed, publicly available dataset documenting the behavior of the beam-slab system under support failure scenarios. The data from the two test programs are available within NEEShub database: ***DOI:*** *10.4231/D3VH5CJ2N*, and ***DOI:****10.4231/D3M03XX42*.

6.3 Numerical Investigation

A detailed non-linear finite element model of the test specimen 1 was implemented in LS-DYNA and the results obtained from these analyses were compared with the results from the tests. The concrete in this specimen was modeled using eight node hexagonal elements, while embedded reinforcing steel was modeled using two node beam elements, assuming a perfect bond between them. The finite element model was subject to the same sequence of loading (gravity, pattern and corner push) as the actual specimen. Based on numerical validation, the following conclusions and shortcomings are noted:

(1) The finite element model was able to predict the load-deflection response of the beam slab system under corner support failure with acceptable accuracy. In particular, the model was able to capture the initial tangent stiffness, deformation profiles and load distribution quite reasonably. Moreover, the model was able to predict the axial and shear force demands within 10-20% of the recorded values. However, it over predicted the moment demands at the support by as much as 30%. This was partly due to the inability of the model to capture the connection stiffness provided between the specimen and the multi-axis load cells.

(2) The model over predicted the ultimate strength of the test specimen by about 15%. This error is largest for the beam-beam corner condition. This is partly due to the concrete material model, which remains elastic until yield in both compression and tension, and deforms in a relatively ductile manner. This resulted in residual strength at large strains, thus increasing the ultimate load carrying capacity.

Although the finite element model had some deficiencies, it was able to capture the salient and most important characteristics of the beam-slab system behavior. It was also notable that tensile strain patterns of the numerical model matched reasonably well with the damage patterns at the top and bottom of the test specimen. The validated numerical model was subsequently extended to consider beam-slab systems with varying reinforcing ratio, member sizes, span length, concrete strength and support stiffness. The emphasis of this aspect of the study was on the most critical, corner support failure scenario. The key findings from the non-linear parametric study are:

(1) All of the models responded with an approximately elastic-plastic behavior with nominal post-peak strength degradation. The ultimate load capacities for each of the models within the parametric study were larger, by a factor of about 1.5 when compared with their respective yield line theory estimates.

(2) The presence of the slab provided significant contributions to the ultimate load capacity of the system under a corner support failure scenario. The tension in the slab was balanced by the compression induced in the spandrel beams, resulting in increased moment capacity of the beam due to P-M interaction. No load enhancement was observed for the parametric model without the slab.

(3) By considering the force transfer mechanism between the slab and edge beams, the compression in the beam is approximated. This compression is used to update the load capacity of the beam-slab system under corner support failure. The results from this model give a good prediction of the ultimate load carrying capacity for all the parametric cases considered in this study.

(4) The presence of bond-slip between the concrete and rebar may not adversely affect the overall load carrying capacity of the beam-slab system under corner support failure scenario, at least for the models and details considered in the present study. However, ignoring such an affect in numerical analysis could result in an underestimation of the systems ductility.

6.4 Suggestions for Future Work

Although several experimental and numerical studies have been conducted in the past two decades to better understand and mitigate progressive collapse potential, most of this research has focused on removal of columns due to blast or impact loading in beam-frame systems, thus ignoring the slab contribution to system stiffness and strength. Furthermore, apart from a handful of system level studies, very limited research has been conducted on corner support failure, which is more likely to occur during a seismic event. To this end, the following future work is suggested:

(1) Limited research has been conducted to characterize the behavior of the beam-slab system under a corner support failure scenario. Further experimental studies need to be conducted to better characterize the behavior of the beam-slab system under corner support failure. In particular with varied design parameters of slab thickness, reinforcing ratio, beam dimensions and detailing to name a few. Similar studies are needed for characterizing the behavior under edge and center support failures.

- The present experimental program did not account for restraint that could be present due to floors above in a multi-story structure. The presence of additional restraint at support locations may significantly increase the stiffness and strength of the system. Experimental studies are warranted to characterize the effect of additional restraint on the behavior of beam-slab system under support failure scenarios.

- Experimental studies are also needed under lateral load conditions to understand the effects of seismic loading on the structure under support failure scenario.
- This study did not consider any damage that might occur in the beam-slab system due to demands other than column removal. Preexisting damage in the beam-slab system might considerably affect its load carrying capacity, an aspect needing further experimental investigation.
- The supports were provided using elastic load cells, thus precluding any failure at other support locations. Experimental studies are warranted, which account for damage that might occur at other support locations due to initial support failure at one column location.

(2) Simpler non-linear numerical models of the beam-slab system need to be implemented and verified to accurately model the behavior of the slab under large deflections. The current modeling technique presented in this dissertation might not be a feasible method when running a system level study under seismic loading due to the required run time.

(3) The numerical section of this dissertation was focused on failure at corner support locations. Experimental and numerical studies should be extended to consider failure at other support locations. In addition the precipitation of multiple column failure should be assessed, particularly using non-linear analysis.

(4) The present numerical study did not account for bond-slip behavior between the concrete and rebar, which might affect the behavior of the beam-slab system under other support failure scenario. A systematic study needs to be conducted on the effects of bond-slip on the behavior of beam-slab system under different support failure scenarios, particularly under cyclic loading conditions.

REFERENCES

ACI 318 (1956). "Building Code Requirements for Structural Concrete and Commentary (ACI 318-56)" American Concrete Institute, Farmington Hills, Michigan.

ACI 318 (1963). "Building Code Requirements for Structural Concrete and Commentary (ACI 318-63)" American Concrete Institute, Farmington Hills, Michigan.

ACI 318 (2011). "Building Code Requirements for Structural Concrete (ACI 318-11) and Commentary (ACI 318-2011)" American Concrete Institute, Farmington Hills, Michigan.

ACI Committee 209, (1982). "Prediction of Creep, Shrinkage and Temperature Effects in Concrete Structures (ACI 209R-82)," Designing for Creep and Shrinkage in Concrete Structures, SP-76, American Concrete Institute, Farmington Hills, MI, pp. 193-300.

ACI Committee 214, (1977). "Recommended Practice for Evaluation of Strength Test Results of Concrete (ACI 214- 77)," American Concrete Institute, Farmington Hills, MI, 14 pp.

AL-Hassani, H. M., Husain, H. M., and AL-Badri, S. S. A. Q., (2009). "Experimental Tests on Orthotropically RC Rectangular Slabs Having Various Restrained Edges and Subjected to Uniform Load", Journal of Engineering and Technology, 27(5), pp. 913-929.

Anagnos, T., Camerio, M.C., Goulet, C., May, P. J., Greene, M., McCormick, D. L., and Bonowitz, D. (2012) "Developing Regional Building Inventories: Lessons from the Field", Earthquake Spectra, EERI, 2012, 28(4), pp. 1305-1329.

Aoki, Y. and Seki, H. (1971), "Shearing strength and flexural cracking and capacity of two-way slabs subjected to concentrated load", ACI Special Publication, 30, pp. 103-126.

American Society of Civil Engineers (ASCE), (2010), "Minimum design loads for buildings and other structures", ASCE/SEI 7-10, Reston, VA.

Bailey, C. G., White, D. S. and Moore, D. B. (1999), "The tensile membrane action of unrestrained composite slabs simulated under fire conditions", Engineering Structures, 22, pp.1583-1595.

Bailey, C. G. (2001), "Membrane action of unrestrained lightly reinforced concrete slabs at large displacements" Engineering Structures, 23(5), pp. 470–83.

Bailey, C. G. (2002), "Efficient arrangement of reinforcement for membrane behavior of composite floor slabs in fire conditions", Journal of Construction Steel Research, 59(7), pp.931-949.

Bailey, C. G. (2004). "Membrane action of slab/beam composite floor systems in fire" Engineering Structures, 26(12), 1691-1703.

Bailey, C. G., Toh, W. S., and Chan, B. M., (2008). "Simplified and Advanced Analysis of Membrane Action of Concrete Slabs", ACI Structural Journal, 105(1), pp. 30-40.

Bao, Y., Lew, H. S., and Kunnath, S. K., (2014). "Modeling of Reinforced Concrete Assemblies under Column-Removal Scenario" Journal of Structural Engineering, ASCE, 140(1), 04013026.

Bao, Y., Kunnath, S. K., El-Tawil, S. and Lew, H. S. (2008), "Macromodel-Based Simulation of Progressive Collapse: RC Frame Structures", Journal of Structural Engineering, ASCE, 134 (7), pp. 1079-1091.

Bazan, M. L. (2008), "Response of reinforced concrete elements and structures following loss of load bearing elements", Ph.D. Dissertation, Department of Civil and Environmental Engineering, Northeastern University.

Brotchie, J. F., and Holley, M. J., (1971). "Membrane Action in Slabs", ACI Special Publication, 30, pp. 345-377.

CEB-FIP Model Code 1990, Comité Euro-International du Béton, Thomas Telford House, 1993.

Christiansen, K. P., Frederiksen, V. T. (1983), "Experimental investigation of rectangular concrete slabs with horizontal restraints", Material and Structures, 16(3), pp. 179-192.

Comartin, C., Bonowitz, D., Greene, M., McCormick, D., May, P., Seymour, E. (2011) "The Concrete Coalition and the California Inventory Project: An Estimate of the Number of Pre-1980 Concrete Buildings in the State". September, Oakland, CA: The Earthquake Engineering Research Institute.

Elkhoury, E. (Nabih Youssef and Associates); Holmes, W. (Rutherford and Chekene); Mehrain, M. (URS Corp.); Nabih, Y. (Nabih Youssef and Associates); Jack P. Moehle (University of California, Berkeley), Personal Communication (Professional Practice Advisory Committee), 2010-2011.

Fang, I- Kua, Lee, J.H., and Chen, C.R. (1994) "Behavior of partially restrained slabs under concentrated load" ACI Structural Journal, 91 (2), pp. 133–139.

FarhangVesali, N., Valipour, H., Samali, B., and Foster, S. (2013), "Development of Arching Action in Longitudinally-Restrained Reinforced Concrete Beams", Construction and Building Materials, 47(0), pp. 7-19

Foster, S. J., Bailey, C. G., Burgess, I. W., Plank, R. J. (2004) “Experimental behavior of concrete floor slabs at large displacements”, Engineering Structures, 26(9), pp. 1231-1247.

Guice, L.K., and Rhomberg, E.J. (1988), “Membrane Action in Partially Restrained Slabs” ACI Structural Journal, 85(4), pp. 365-373.

Guice, L.K., Slawson, T.R., Rhomberg, E.J. (1989), “Membrane analysis of flat plate slabs” ACI Structural Journal, 86(1), pp. 83–92.

Hawkins, N. M., Mitchell, D. (1979), “Progressive Collapse of Flat Plate Structures” Journal of the American Concrete Institute (ACI), 76(7), pp. 775-808.

Hopkins, D.C. (1969), “Effects of Membrane Action on the Ultimate Strength of Reinforced Concrete Slabs” University of Canterbury, Christchurch, New Zealand, PhD Dissertation.

Hopkins, D.C. and Park, R., (1971), “Test on a Reinforced Concrete Slab and Beam Floor Designed with Allowance for Membrane Action” ACI Special Publication, 30, pp. 223-250

Hung, T. Y., Nawy, E. G. (1971). “Limit strength and serviceability factors in uniformly loaded, isotropically reinforced two-way slabs” ACI Special Publication, 30, pp. 301-24.

Johansen, K. W. (1962). “Yield-line theory”, Cement and Concrete Association, London, 181 pp.

Keenan, W. A. (1969), “Strength and Behavior of Restrained Reinforced Concrete Slabs Under Static and Dynamic Loadings” Technical Report R621, U.S. Naval Civil Engineering Laboratory, Port Hueneme, California, 133 pp.

Khoe, Y. S., and Weerheijm, J., (2012). "Limitations of Smeared Crack Models for Dynamic Analysis of Concrete", 12th International LS-DYNA Users Conference, Dearborn, Michigan, USA, 14 pp.

Kwak, H. G., and Filippou, F. C., (1992). "Finite Element Analysis of Reinforced Concrete Structures under Monotonic and Cyclic Loads", 10th World Conference in Earthquake Engineering, Madrid, Spain, pp. 4227-4232.

Kwak, H. G., and Kim, S. P, (2001). "Bond-Slip Behavior under Monotonic Uniaxial Loads" Engineering Structures, 23, pp. 298-309.

Lahlouh, E. H., and Waldron, P., (1992). "Membrane action in one-way slab strips", Proceedings of the Institution of Civil Engineers, Structures and Buildings, 94(4), pp. 419–428

Lew, H. S., Bao, Y., Sadek, F., Main, J. A., Pujol, S., and Sozen, M. A. (2011), "An Experimental and Computational Study of Reinforced Concrete Assemblies under a Column Removal Scenario", NIST Technical Note 1720, National Institute of Standards and Technology, Gaithersburg, MD.

Li, G. Q., Guao, S. X. and Zhou, H. S. (2006), "Modeling of membrane action in floor slabs subjected to fire", Engineering Structures, 29, pp. 880-887.

Limkatanyu, S., and Spacone, E., (2003). "Effects of Reinforcement Slippage on Non-Linear Response under Cyclic Loadings of RC Frame Structures", Earthquake Engineering and Structural Dynamics, 32(15), pp. 2407-2424.

Liu, R., Davison, B., and Tyas, A., (2005) "A Study of Progressive Collapse in Multi-Storey Steel Frames", Structures Congress 2005, pp. 1-9.

LSTC, "LS-DYNA Keyword User's Manual Volume I", Livermore: Livermore Software Technology Corporation, January 2013.

LSTC, "LS-DYNA Keyword User's Manual Volume II, Material Models", Livermore: Livermore Software Technology Corporation, January 2013.

McConnell, J. M., and Brown, H., "Evaluation of Progressive Collapse Alternate Load Path Analyses in Designing for Blast Resistance of Steel Columns" Engineering Structures, 33(10), pp. 2899-2909.

Mitchell, D., Cook, W. D. (1984), "Preventing Progressive Collapse of Slab Structures" Journal of Structural Engineering, 110(7), pp. 1513-1532.

Mohamed, O. A. (2009), "Assessment of progressive collapse potential in corner floor panels of reinforced concrete buildings", Engineering Structures, 31(3), pp. 749-757.

Morone, D. J. (2012), "Progressive Collapse: Simplified Analysis Using Experimental Data", Masters Thesis, Ohio State University. (Electronic Thesis or Dissertation). Retrieved from https://etd.ohiolink.edu/.

Morone, D. J., and Sezen, H. (2014) "Simplified Collapse Analysis Using Data from Building Experiment", ACI Structural Journal, Vol. 111, No. 4, pp 925-934.

Murray, Y.D. (2007), "User's Manual for LS-DYNA Concrete Material Model 159" Report No. FHWA-HRT-05-062, Federal Highway Administration, McLean, Virginia.

Murray, Y. D., Abu-Odeh, A., and Bligh R. (2007), "Evaluation of Concrete Material Model 159" Report No. FHWA-HRT-05-063, Federal Highway Administration, McLean, Virginia.

Muthu, K. U., Amarnath, K., Ibrahim, A. and Mattarneh, H. (2007), "Load deflection behavior of partially restrained slab strips", Engineering Structures, 29(5), pp. 663-674.

Park, R. (1964), "The Ultimate Strength of Uniformly Loaded Laterally Restrained Rectangular Two-Way Concrete Slabs", Ph.D. Dissertation, University of Bristol.

Park, R. (1971), "Further test on a reinforced concrete floor designed by limit procedures", ACI Special Publication, 30, pp. 251-270.

Park, R. and Gamble, W.L. (2000) "Reinforced concrete slabs", 2nd Edition, John Wiley & Sons Inc, New York.

Pham, X. D., and Tan, K. H. (2010). "Membrane actions of RC slabs in mitigating progressive collapse of building structures", Engineering Structures, 55, pp. 107-115.

Prasad, S. and Hutchinson, T., (2012). "Experimental Evaluation of a 1/3rd scale Lightly Reinforced Concrete Slab under Uniform, Pattern and Concentrated Pull Down Load: Corner Conditions" Structural Systems Research Project (SSRP) Report No. 12/11, Department of Structural Engineering University of California, San Diego.

Prasad, S. and Hutchinson, T. C. (2013) "Behavior of Reinforced Concrete Flat Slab Systems under Corner and Center Support Failure Scenarios", Proceedings of 10th International Conference on Urban Earthquake Engineering (CUEE), Tokyo, Japan.

Prasad, S. and Hutchinson, T., (2014). "Experimental Evaluation of a 1/3rd scale Lightly Reinforced Concrete Slab under Uniform and Pull Down Load: Edge Conditions (Version A)" Structural Systems Research Project (SSRP) Report No. 14/01, Department of Structural Engineering University of California, San Diego.

Prasad, S. and Hutchinson, T., (2014). "Experimental Evaluation of a 1/3rd scale Lightly Reinforced Concrete Slab under Uniform and Pull Down Load: Edge Conditions (Version B)" Structural Systems Research Project (SSRP) Report No. 14/02, Department of Structural Engineering University of California, San Diego.

Prasad, S. and Hutchinson, T. C. (2014), “Evaluation of Older Reinforced Concrete Floor Slabs Under Corner Support Failure”, ACI Structural Journal, Vol. 111, No. 4, pp 839-850.

Prasad, S. and Hutchinson, T. C. (201X), “Evaluation of Older Reinforced Concrete Floor Slabs under Edge Support Failure”, ACI Structural Journal (In review).

Qian, K., and Li, B. (2012), “Slab effects on response of reinforced concrete substructure after loss of corner column”, ACI Structural Journal, 109(6), 845-855.

Qian, K., and Li, B. (2013), “Experimental Study of Drop-Panel Effects on Response of Reinforced Concrete Flat Slabs after Loss of Corner Column”, ACI Structural Journal, 110(2), pp. 319-330.

Qian, K., Li, B., and Ma, J. X., (2014) “Load-carrying mechanism to resist progressive collapse of RC buildings”, Journal of Structural Engineering, ASCE.

Sadek, F., Main, J. A., Lew, H. S. , and Bao, Y. (2011), “Testing and Analysis of Steel and Concrete Beam-Column Assemblies under a Column Removal Scenario”, Journal of Structural Engineering, ASCE, 137 (9), pp. 881-892.

Sasani, M., Bazan, M. and Sagiroglu, S. (2007), “Experimental and analytical progressive collapse evaluation of actual reinforced concrete structures”, ACI Structural Journal, 104(6), pp. 731-739.

Sasani, M. (2008), “Response of a reinforced concrete infilled-frame structure to removal of two adjacent columns”, Engineering Structures, 30(9), pp. 2478-2491.

Sasani, M., Kazemi, A., Sagiroglu, S. and Forest, S., (2011), “Progressive Collapse Resistance of an actual 11-story structure subjected to severe initial damage”, Journal of Structural Engineering, ASCE, 137(9), pp. 893-902.

Sasani, M. and Kropelnicki, J., (2008), “Progressive Collapse Analysis of an RC Structure” Structural Design of Tall and Special Buildings, 17(4), pp. 757-771.

Sasani, M. and Sagiroglu, S. (2010), "Gravity Load Redistribution and Progressive Collapse Resistance of 20-story Reinforced Concrete Structure following loss of interior column" ACI Structural Journal, 107(6), pp. 636-644.

Shetye, G. A. (2013), "Finite Element Analysis and Experimental Validation of Reinforced Concrete Single-Mat Slabs Subjected to Blast Loads", Master's Thesis, University of Missouri-Kansas City.

Spacone, E., and Limkatanyu, S., (2000). "Responses of Reinforced Concrete Members Including Bond-Slip Effects", ACI Structural Journal, 97(6), pp. 831-839.

Su, Y., Tian, Y., and Song, X. (2009), "Progressive Collapse Resistance of Axially-Restrained Frame Beams", ACI Structural Journal, 106(5), pp. 600-607.

Tan, K. H., Yu, J., & Pham, X. D. (2010). "Alternate Load Paths in Mitigating Progressive Collapse of RC Building Structures Subjected to Column Loss Scenarios" Design and Analysis of Protective Structures, 14 pp.

Tong, P. Y., and Batchelor, B. V. (1971), "Compressive membrane enhancement in two-way bridge slabs", ACI Special Publication, 30, pp. 271-286.

UFC-4-023-23 (2005), "Unified Facilities Criteria (UFC): Design of Structures to Resist Progressive Collapse", Department of Defense, Washington, D.C.

United States General Services Administration (GSA), (2003), "Progressive collapse analysis and design guidelines for new federal office buildings and major modernization projects", Washington, D.C.

Usmani, A. S. and Cameron, N. J. K. (2003), "Limit capacity of laterally restrained reinforced concrete floor slabs in fire", Cement and Concrete Composites, 26, 127-140.

Vecchio, F. J. and Tang, K. (1990), "Membrane action in reinforced concrete slabs" Canadian Journal of Civil Engineering, 17(5), pp. 686–697.

Wang, G., Wang, Q. X., and Li, Z. J., (2011). “Membrane Action in Lateral Restraint Resinforced Concrete Slabs”, Journal of Central South University of Technology, 18(2), pp. 550-557.

Wu, Y., Crawford, J. E., and Magallanes, J. M., (2012). “Performance of LS-DYNA Concrete Constitutive modes”, 12th International LS-DYNA Users Conference, Dearborn, Michigan, USA, 14 pp.

Yi, W. J., He, Q. F., Xiao, Y., Kunnath, S. K. (2008), “Experimental Study on Progressive Collapse-Resistant Behavior of Reinforced Concrete Frame Structures” ACI Structural Journal, 105(4), pp. 433-439.

APPENDIX A: Summary of Previous Tests on RC Slabs

Summary of few of the relevant tests performed by other authors is presented in this section. Details provided for each test include: specimen dimensions, load transfer mechanism, loading type, boundary condition, range of steel reinforcing ratio, failure load, and load enhancement compared to Yield Line Theory estimates. Test where slab was tested under concentrated loads, the Failure Load is in **bold**.

Table A.1: Summary of experiments conducted on reinforced concrete slabs.

Reference	Specimen Dimensions L×B×t (in.)	Load transfer	Loading	Boundary Condition	Steel Ratio (range, %)	Failure Load (psi/kip)	Load Enhancement (Exp/YLT)
Powell (1956)	36×20.57×1.286	Two-way	Uniform	Four edges fixed	0.25	41.8 *	7.6 *
					0.45	40.5 *	4.1 *
					0.71	54.0 *	3.5 *
					0.97	50.2 *	2.0 *
					1.53	64.6 *	1.7 *
					Unreinforced	35.7 *	-
Park (1964)	60×40×2	Two-way	Uniform	Four edges fixed	0.19 – 0.41	30.8	3.7
					0.21-0.84	31.3	2.7
					0.22-1.44	37.8	1.8
					0.23-2.42	37.3	1.4
					Unreinforced	24.6	-
	60×40×1.5					12.9	-
	60×40×0.98					4.61	-
	60×40×1.01					4.14	-
	60×40×0.99					4.14	-
	60×40×2			Three edges fixed. One short edge simply supported	0.19 – 0.41	20.2	2.9
					0.21-0.84	24.1	2.2
					0.22-1.44	25.6	1.4
					0.23-2.42	32.9	1.5
				Three edges fixed. One long edge simply supported	0.19 – 0.41	16.7	2.9
					0.21-0.84	18.8	2.1
					0.22-1.44	18.1	1.4
					0.23-2.42	26.6	1.5

Table A.1: Summary of experiments conducted on reinforced concrete slabs (cont.)

Reference	Specimen Dimensions L×B×t (in.)	Load transfer	Loading	Boundary Condition	Steel Ratio (range, %)	Failure Load (psi/kip)	Load Enhancement (Exp/YLT)
Keenan (1969)	72×72×3	Two-way	Uniform	Four edges fixed	0.82	32.2	1.8
					Unreinforced	23.6	-
					0.82	34.6	1.9
					0.82	32.1	1.8
	72×72×4.75				0.89	85.0	1.7
	72×72×6				1.33	182	1.4
Brotchie and Holley (1971)	15×15×0.75	Two-way	Uniform	Four edges fixed	Unreinforced	35.6	-
						25.9	-
					0-1.0	59.5	3.2
					0-2.0	55.0	1.6
	15×15×1.5				Unreinforced	144	-
					0-1.0	209	2.6
					0-2.0	220	1.5
Christiansen and Frederiksen (1983)	49.2×49.2×1.54	Two-way	Uniform	Four edge fixed	0.39-0.66	5.8	1.6
	49.2×49.2×1.54				0.32-0.38	4.6	2.3
	49.2×49.2×1.5				Unreinforced	1.8	-
	49.2×39.4×1.61				0.31-0.36	8.7	2.1
	49.2×39.4×1.54				Unreinforced	4.2	-
	59.1×39.4×1.57				0.29-0.35	6.6	1.7
	59.1×39.4×1.54				0.33-0.35	6.8	1.7
	59.1×39.4×1.85				Unreinforced	4.0	-
	68.9×39.4×1.61				0.30-0.36	6.1	1.8
	68.9×39.4×1.81				Unreinforced	3.2	-
	78.7×39.4×1.57				0.32-0.33	4.9	1.5

Table A.1: Summary of experiments conducted on reinforced concrete slabs (cont.)

Reference	Specimen Dimensions L×B×t (in.)	Load transfer	Loading	Boundary Condition	Steel Ratio (range, %)	Failure Load (psi/kip)	Load Enhancement (Exp/YLT)
Guice and Rhomberg (1986)	24×24×2.31	One-way	Uniform	Partial end restraint provided by support beams along two opposite edges.	0.52	65 *	2.3 *
					0.74	72 *	1.7 *
					1.06	94 *	1.6 *
	24×24×1.62				0.58	28 *	1.5 *
					1.14	40 *	1.4 *
					1.47	34 *	1.0 *
Lahlouh and Waldron (1992)	98.42×11.8×5.90	One-way	Concentrated load at mid-span	Partial end restraint provided by support wall at ends of the long edge. Short edge free.	1.34	**19.0**	1.0
					0.38	**24.7**	1.3
					0.24	**32.2**	1.8
Fang et al. (1994)	90.55×39.37×4.52	One-way	Concentrated load at mid-span	Partial end restraint provided by support beams at ends of the short edge. Long edge free.	0.33	**268 ***	1.9 *
					0.5	**291 ***	2.0 *
					0.67	**310 ***	2.2 *
	90.55×39.37×3.0				0.47	**128 ***	1.4 *
					0.71	**164 ***	1.9 *
Muthu et al. (2006)	35.8×21.6×2.0	One-way	Uniform	Partial end restraint provided by support beams at ends of short edge. Long edge free.	0.26	5.68	1.2
					0.26-0.31	8.35	1.4
					0.26-0.41	10.2	1.5
					0.26-0.52	11.4	1.4
	35.8×21.6×2.6				0.15-0.18	6.09	1.4
					0.15-0.24	9.97	1.4
					0.15-0.32	12.3	1.4

Table A.1: Summary of experiments conducted on reinforced concrete slabs (cont.)

Reference	Specimen Dimensions L×B×t (in.)	Load transfer	Loading	Boundary Condition	Steel Ratio (range, %)	Failure Load (psi/kip)	Load Enhancement (Exp/YLT)
Bailey et al. (2008)	66.94×43.31×0.72	Two-way	Uniform	Simply supported on all edges	0.68	3.01	2.4
	43.31×43.31×0.75				0.64	3.92	2.0
	66.94×43.31×0.87				0.41	1.78	1.9
	43.31×43.31×0.79				0.46	2.65	2.2
	66.94×43.31×0.74				0.97	2.60	2.1
	43.31×43.31×0.85				0.81	3.92	1.7
	66.94×43.31×0.80				0.28	1.25	1.7
	43.31×43.31×0.75				0.31	1.55	1.6
	66.94×43.31×0.87				0.32	1.07	1.4
	43.31×43.31×0.78				0.37	1.43	1.6
	66.94×43.31×0.73				0.94	1.29	1.7
	43.31×43.31×0.76				0.86	2.35	1.8
	66.94×43.31×1.44				0.33	4.22	1.3
AL-Hassani et al. (2009)	36×22×1	Two-way	Uniform	Four edges fixed	0.26-0.52	10.9	1.5
				Three edges fixed, one short edge simply supported		10.5	1.6
				Three edges fixed, one long edge simply supported		9.20	1.7

Table A.1: Summary of experiments conducted on reinforced concrete slabs (cont.)

Reference	Specimen Dimensions L×B×t (in.)	Load transfer	Loading	Boundary Condition	Steel Ratio (range, %)	Failure Load (psi/kip)	Load Enhancement (Exp/YLT)
Wang et al. (2011)	96×12×3.2	One-way	Uniform	Short edges fixed. Long edge free.	1.89	4.09	1.3
	96×12×4.8				1.25	7.43	1.4
	96×12×4.0				1.51	4.83	1.5

Notes:

- Results of Powell (1956) are obtained from Park and Gamble (2000).
- For tests performed by Guice and Rhomberg (1988), load enhancements are calculated based on YLT estimates assuming fixed edge conditions on all edges.
- For Fang et al. (1994), the authors report load enhancement based on theoretical estimates obtained using AASHTO (1989) code recommendations.
- Some failure load and load enhancement values (suffixed by *) are based on average values from multiple specimen with similar detailing as presented in the table.
- For all tests performed with no reinforcement (i.e. Unreinforced), YLT estimates are zero, hence the load enhancement is not defined.

APPENDIX B: Yield Lines from Experiment

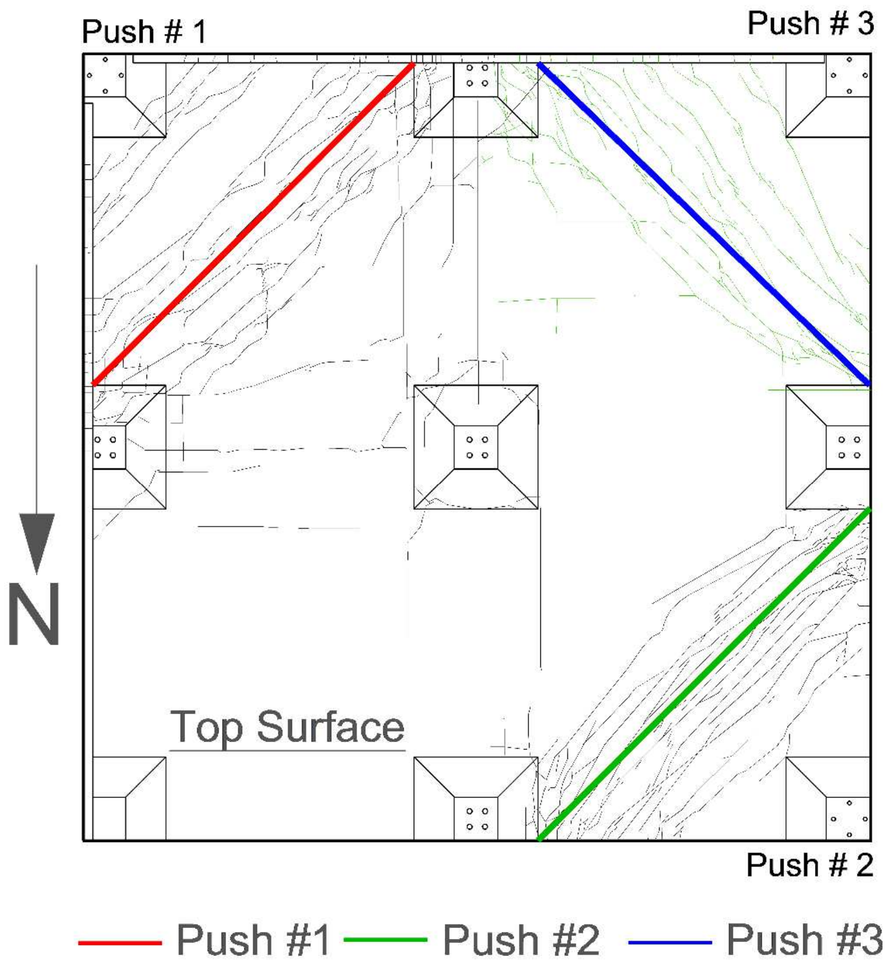

Figure B.1: Idealized yield line for the three corner tests locations on specimen 1. The crack pattern on the top surface is shown. All yield lines are negative, i.e. tension occurs on the top surface.

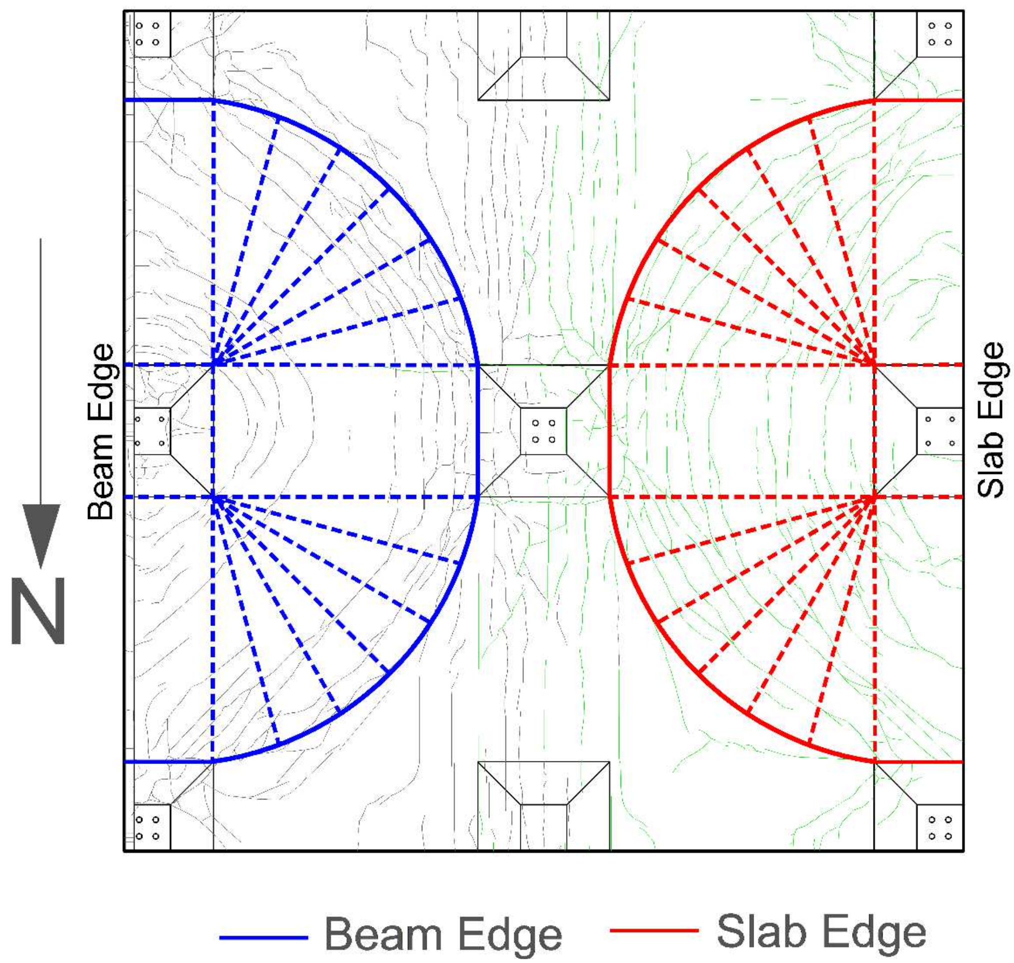

Figure B.2: Idealized yield line for the two push tests at center edge location on specimen 2. The crack pattern on the top surface is shown. Solid lines are yield lines with tension on top, while dashed lines are positive yield lines. The figure shows the circular fan in the panels which resulted in significant cracking on the bottom surface of the specimen during both edge support removal tests.

APPENDIX C: LS-DYNA Steel Stress-Strain Input Curve

LS DYNA input curves used to define the post-yield stress-strain curve of Grade 40 and Grade 60 rebar in Chapter 4. The abscissa is the effective plastic strain and ordinate (o1) is the stress.

```
*DEFINE_CURVE_TITLE
Grade 40 #3 Rebar
$#     lcid      sidr       sfa       sfo      offa      offo    dattyp
          1         0  1.000000 1000.0000     0.000     0.000         0
$#                  a1                  o1
                 0.000           46.500000
              0.002625           46.500694
              0.005250           46.501701
              0.007875           46.502102
              0.010500           46.502102
              0.013125           46.501801
              0.015750           46.501202
              0.018375           46.500301
              0.021000           47.640579
              0.023625           49.164845
              0.026250           50.595657
              0.028875           51.937408
              0.031500           53.194752
              0.034125           54.371811
              0.036750           55.472649
              0.039375           56.501232
              0.042000           57.461369
              0.044625           58.356579
              0.047250           59.190369
              0.049875           59.966045
              0.052500           60.686840
              0.055125           61.355793
              0.057750           61.975761
              0.060374           62.549625
```

0.062999	63.080006
0.065624	63.569534
0.068249	64.020660
0.070874	64.435661
0.073499	64.816948
0.076124	65.166527
0.078749	65.486450
0.081374	65.778809
0.083999	66.045341
0.086624	66.287872
0.089249	66.508095
0.091874	66.707611
0.094499	66.887924
0.097124	67.050461
0.099749	67.196701
0.102374	67.327805
0.104999	67.445091
0.107624	67.549782
0.110249	67.642838
0.112874	67.725288
0.115499	67.798164
0.118124	67.862366
0.120749	67.918709
0.123374	67.967964
0.125999	68.010872
0.128624	68.048042
0.131249	68.080315
0.133874	68.108055
0.136499	68.131836
0.139124	68.152145
0.141749	68.169449
0.144374	68.184128
0.146999	68.196548
0.149624	68.207008
0.152249	68.215790
0.154874	68.223061
0.157499	68.229218
0.160124	68.234283
0.162749	68.238472
0.165374	68.241783
0.167999	68.244499
0.170624	68.246696
0.173249	68.248238
0.175873	68.249001

```
          0.178498          68.250000
          0.181123          68.250999
          0.183748          68.251999
          0.186373          68.252998
          0.188998          68.253998
          0.191623          68.254997
          0.194248          68.255997
          0.196873          68.257004
          0.199498          68.258003
          0.202123          68.259003
          0.204748          68.260002
          0.207373          68.261002
          0.209998          68.262001
          0.212623          68.263000
          0.215248          68.264000
          0.217873          68.264999
          0.220498          68.265999
          0.223123          68.266998
          0.225748          68.267998
          0.228373          68.268997
          0.230998          68.269997
          0.233623          68.271004
          0.236248          68.272003
          0.238873          68.273003
          0.241498          68.274002
          0.244123          68.275002
          0.246748          68.276001
          0.249373          68.277000
          0.251998          68.278000
          0.254623          68.278999
          0.257248          68.279999
          0.259873          68.280998


*DEFINE_CURVE_TITLE
Grade 60 #4 Rebar
$#    lcid      sidr       sfa       sfo      offa      offo    dattyp
         2         0  1.000000 1000.0000     0.000     0.000         0
$#                  a1                  o1
                 0.000           67.750000
              0.001648           68.982140
              0.003296           71.437767
              0.004944           73.784081
              0.006592           76.024055
              0.008241           78.160820
```

0.009889	80.197357
0.011537	82.136520
0.013185	83.981377
0.014833	85.734795
0.016481	87.399445
0.018129	88.978279
0.019777	90.474052
0.021426	91.889542
0.023074	93.227409
0.024722	94.490318
0.026370	95.680832
0.028018	96.801666
0.029666	97.855286
0.031314	98.844238
0.032962	99.770943
0.034611	100.63799
0.036259	101.44760
0.037907	102.20216
0.039555	102.90434
0.041203	103.55549
0.042851	104.15936
0.044499	104.71710
0.046147	105.23092
0.047795	105.70275
0.049444	106.13599
0.051092	106.53149
0.052740	106.89105
0.054388	107.21752
0.056036	107.51273
0.057684	107.77849
0.059332	108.01569
0.060980	108.22761
0.062629	108.41476
0.064277	108.58003
0.065925	108.72491
0.067573	108.85048
0.069221	108.95786
0.070869	109.04947
0.072517	109.12698
0.074165	109.19109
0.075813	109.24450
0.077462	109.28635
0.079110	109.32008
0.080758	109.34588
0.082406	109.36536

0.084054	109.37900
0.085702	109.38831
0.087350	109.39400
0.088998	109.39800
0.090647	109.39900
0.092295	109.40000
0.093943	109.40000
0.095591	109.40000
0.097239	109.40000
0.098887	109.40000
0.100535	109.40000
0.102183	109.40000
0.103832	109.40000
0.105480	109.40000
0.107128	109.40000
0.108776	109.40000
0.110424	109.40000
0.112072	109.40000
0.113720	109.40000
0.115368	109.40000
0.117016	109.40000
0.118665	109.40000
0.120313	109.40000
0.121961	109.40000
0.123609	109.40000
0.125257	109.40000
0.126905	109.40000
0.128553	109.40000
0.130201	109.40000
0.131850	109.40000
0.133498	109.40000
0.135146	109.40000
0.136794	109.40000
0.138442	109.40000
0.140090	109.40000
0.141738	109.40000
0.143386	109.40000
0.145035	109.40000
0.146683	109.40000
0.148331	109.40000
0.149979	109.40000
0.151627	109.40000
0.153275	109.40000
0.154923	109.40000
0.156571	109.40000

0.158219	109.40000
0.159868	109.40000
0.161516	109.40000
0.163164	109.40000